

Yukon
Exploration & Geology
2019



Yukon Geological Survey staff

Left to right: Nicole Eriks, Alex Sadurski, Patrick Sack, Tyler Ambrose, Carolyn Relf, Warwick Bullen, Julie Minor, Panya Lipovsky, Olwyn Bruce, Scott Casselman, Emilie Stewart-Jones, Maurice Colpron, Amanda O'Connor, David Moynihan, Kristen Kennedy, Bailey Staffen, Tiffani Fraser, Derek Torgerson, Leyla Weston, Jeff Bond, Diane Skipton, Justin Emberley and Brett Elliot.

Missing from photo: Rosie Cobbett, Lara Lewis, Karen MacFarlane, Sydney van Loon.

Yukon

Yukon Exploration & Geology 2019

Edited by
K.E. MacFarlane

Yukon Geological Survey
Energy, Mines and Resources
Government of Yukon

Published under the authority of the Department of Energy, Mines and Resources, Government of Yukon, https://yukon.ca.

Printed in Whitehorse, Yukon, 2020.

Publié avec l'autorisation du Ministères de l'Énergie, des Mines et des Ressources du gouvernement du Yukon, https://yukon.ca.

Imprimé à Whitehorse (Yukon) en 2020.

©Department of Energy, Mines and Resources, Government of Yukon

ISSN 1718-8326

Yukon Geological Survey publications can be obtained from:
Yukon Geological Survey
102-300 Main Street
Box 2703 (K-102)
Whitehorse, Yukon, Canada Y1A 2C6

email geology@gov.yk.ca

Yukon Geological Survey website https://yukon.ca/en/science-and-natural-resources/geology.

In referring to this publication, please use the following citation:
Yukon Geological Survey, 2020. Yukon Exploration and Geology 2019, K.E. MacFarlane (ed.), 2020. Yukon Geological Survey, 139 p.

Front cover photograph: Don Murphy (YGS Emeritus Geologist) explains the geology of Tombstone Park during a 'Weekend on the Rocks'.

Preface

Yukon Exploration and Geology (YEG) papers and the Yukon Exploration and Geology Overview are two of the main publications of the Yukon Geological Survey (Energy, Mines and Resources, Government of Yukon). Individual YEG papers, with colour images, are available in digital format and can be downloaded from our website. The YEG Overview is available in digital format and in a limited colour print run.

YEG 2019 contains up-to-date information on mining and mineral exploration activity, studies by industry, and results of recent geological field studies. Information in this volume comes from prospectors, exploration and government geologists, mining companies, and students, all of whom are willing to contribute to public geoscience for the benefit of the scientific community, general public and mineral industries of Yukon. Their work is appreciated.

Once again my colleagues at the Yukon Geological Survey are thanked for their involvement in authoring and reviewing YEG papers. Their commitment to provide geoscience information to support informed decision making is to be commended.

The Queen's Printer ensured that the printing process went smoothly.

We welcome any input or suggestions that you may have to improve future YEG publications. Please contact me at (867) 667-8519, or by email at karen.macfarlane@gov.yk.ca.



Karen MacFarlane

In Memoriam



Julia Lane

1986 – 2019

Julia Lane was an exceptional geologist, widely admired for her ability to manage large and logistically difficult exploration projects in remote areas of Yukon. She tragically passed away on August 6, 2019, at the age of 33, in an aircraft accident during a routine flight from the field.

Julia started her career in 2007, working as a geology student for Archer, Cathro & Associates (1981) Limited on a variety of projects in Yukon. In 2009, she joined Archer Cathro full time as a senior project geologist working at ATAC Resources Ltd. Rackla Gold Project in central Yukon. Her exemplary management skills led to more responsibility the following year as Project Manager for the Rackla project. She was instrumental in ATAC's 2010 discovery and delineation of the Osiris Carlin-type gold deposits. Julia guided her colleagues and ATAC through the steep learning curve of understanding an unfamiliar deposit model in a rugged, remote area that had never previously been explored for gold and had only seen rudimentary geological mapping. In peak exploration years, Julia effortlessly budgeted for and managed up to 5 helicopters, 6 diamond drills, 20 project geologists, a support staff of over 50, as well as ongoing academic research projects while providing a safe working environment and culture.

Julia grew up on a small family farm in the rural town of Summerland, in the Okanagan, where she developed a passion for science and nature at a young age. Her father, David, was a federal government scientist working on development of new varieties of cherries and apples. Her mother, Donna, a landscape architect and keen gardener, conducted business from a home office which gave Julia early exposure to the "work side of things", and kindled her love of gardening. Julia's family went camping and hiking near Rodger's Pass and Banff every summer, where she had very positive experiences in the mountains from a young age; experiences that undoubtedly developed into her passion for geology and working in remote mountain locations. Julia's love of science was truly expressed in her frequent participation in Science Fairs, starting in grade 6. She made several appearances in National Science Fairs in high school, earning a gold medal, and went on to represent Canada at the International Science Fair in Taiwan where she received a bronze medal.

Julia graduated with a Bachelor of Science (B.Sc.) degree in geology from the University of British Columbia (UBC) in 2009. She was a registered Professional Geoscientist and became a partner in Archer Cathro in 2012. In 2015, she was appointed Vice President of Exploration for ATAC Resources Ltd. She was an active volunteer with the Association for Mineral Exploration (AME) as a participant in the mentorship program and as co-chair of the Roundup 2019 BC/Yukon/Alaska technical session. She will be remembered as a skilled communicator with an uncanny ability to simplify even the most complex geological concepts. She was a frequent speaker at conferences and short courses, and authored or co-authored a number of technical papers on the subject of Yukon exploration and Carlin-type deposits. Her work was recognized internationally.

Julia was always supportive of more 'academic' geological studies, whether at the deposit level or at a regional scale. In 2010, the Yukon Geological Survey and the Geological Survey of Canada began coordinated mapping and topical research focused at unravelling the regional geology and documenting the Carlin-type deposits of the Rackla Gold belt. This research was welcomed by Julia and facilitated with her enthusiasm and access to ATAC's logistical assistance and extensive geological and geochemical database. She extended similar support for academic researchers from the Colorado School of Mines, Dartmouth College, UBC, Harvard, McGill and Simon Fraser universities.

Julia was a strong advocate for women in geoscience, standing out as a role model, both to young women and men – not by any specific intention, but by embodying what it means to be professional, accomplished, passionate and dedicated to your work. She was a natural and humble leader who was excited to share her knowledge and encouraged others to excel. While known and respected as a rising star in Canada's mineral exploration industry, she will also be remembered for her kindness, positivity and enthusiasm and, above all, her ability to keep things fun.

Julia lived in the present and took great pleasure in what she called the "simple things in life". She loved the world around her and everything in it. She shared these simple things and a garden (with a house) in Vancouver with her partner of 14 years, Ryan Gandy. She leaves behind her parents Donna and David, her brothers Alex and Malcom, sisters-in-law Marta and Steph, nieces and nephews Emily, Mattie, George and Benjamin, and the many friends she made on her journey through life.

Archer Cathro established The Julia Lane Foundation to continue her passion to encourage young professionals. Its primary intent is to assist and encourage future generations to pursue advanced education in the sciences. Grants made by the foundation will support students pursuing degrees in earth sciences or related programs. Donations can be made at https://tinyurl.com/JuliaLaneFoundation.

Shawn Kitchen

1995–2019



Shawn Kitchen was passionate about flying.

In September 2014, Shawn began his Commercial Aviation diploma at Okanagan College in Kelowna. In the Spring of 2015, after his first year of college, he started working at Alkan Air as a dispatcher and moved to Mayo as Alkan's rampie. Everyone quickly learned that Alkan had hired a keen, positive and energetic individual who truly loved working in aviation. Working for Alkan Air only confirmed Shawn's decision to become a commercial pilot.

Shortly after receiving his diploma and his wings, Shawn purchased a Cessna 120 and took his family and friends flying, while at the same time building up his flight hours. Once Shawn reached the hours he needed to meet the medevac contract requirements in the Yukon, he began flying for Alkan Air as a First Officer medevac pilot on the King Airs. In this position, he flew all around the Yukon and major cities of British Columbia and Alberta. Shawn always prided himself for being able to help the Yukon community as a medevac pilot.

In Winter of 2017, Shawn served as a medevac pilot flying for Alkan Air out of their Nanaimo base. From here, Shawn was able to fly medevacs all across North America.

After flying the King Airs, Shawn became interested in bush flying and, in the Spring of 2017, he progressed onto the Dornier 228, Alkan Air's famous twin engine bush machine. Here he learned to appreciate a whole different aspect of flying. It was flying into remote strips in the most beautiful part of the country where you saw Shawn's smile come out the most.

Shawn progressed onto the Caravan 208 in the Spring of 2019 – and without hesitation relocated to Mayo, where his aviation career started. Shawn's care and professionalism were reflected on the day-to-day operations at the Mayo base and in Alkan as a whole.

Besides flying, Shawn was committed to Scouting. Beginning as a cub, Shawn grew to be a Scout, Venturer and Rover. Through Scouting, Shawn travelled to Germany, Sweden, Iceland, Madagascar and Switzerland, making friends wherever he went. It was through his travels that he became known as "Shawn of the Yukon". Shawn had strong community values and it was important to him to give back to the youth of Yukon. He believed that youth should have a voice in programs geared towards youth. As Area Commissioner for Scouting, Shawn provided leadership to Scouts Yukon as well as being a mentor and role model for many Cubs, Scouts and Leaders throughout the Yukon.

Shawn had an adventurous spirit and a love for the outdoors. His days off from Alkan Air were often spent hiking with friends to some of the most beautiful places around the Yukon. Shawn was always up to new challenges and had recently taken up rock climbing. Shawn was also a budding photographer and took his camera everywhere he went. He was inspired by the scenery, people and events around him and captured much of it with his camera. With a keen sense of perspective, Shawn's photos told stories about the places he visited, the people he met and life happening around him. He had the eye of a professional.

Shawn brought life and energy to everything he did. Shawn passed away on August 6, 2019. At just 24 years of age, he had touched the lives of many people on a personal and professional level. He will be missed and remembered by all who knew him.



Yukon Exploration and Geology 2019

Table of Contents

Preliminary report on the bedrock geology of the Rackla River area, southern Wernecke Mountains, Yukon (parts of NTS 106C/4, 5 and 106D/1, 8)
T. Ambrose and S. Bowie 1

New mineral potential mapping methodology for Yukon: Case studies from the Beaver River and Dawson regional land use planning areas
W. Bullen 23

Preliminary report on the bedrock geology of Castle Mountain area, Yukon (parts of NTS 105D/6)
R. Cobbett 43

Assessment of thermo-hydraulic properties of rock samples near Takhini Hot Springs, Yukon
H. Langevin, T. Fraser, and J. Raymond 57

Updated geology and porphyry copper potential of the Klaza deposit, Mount Nansen district (Yukon MINFILE 115I 067)
W.-S. Lee, D.J. Kontak, J.P. Richards and P. Sack 75

Geochronologic and Pb-isotopic constraints on gold mineralization at the Plateau South property (Yukon MINFILE 105N 034, 035, 036), central Yukon
P. Sack, J. Gabites, J. Crowley, J. Benowitz, C. McFarlane, J. Gobadi and D. Ferraro 99

Upper Triassic to Lower Jurassic stratigraphy of the Faro Peak formation, southern Tay River map area, central Yukon (NTS 105K)
A.C. Wiest, L.P. Beranek and M.J. Manor 121

Preliminary report on the bedrock geology of the Rackla River area, southern Wernecke Mountains, Yukon (parts of NTS 106C/4, 5 and 106D/1, 8)

T. Ambrose*
Yukon Geological Survey

S. Bowie
Simon Fraser University

Ambrose, T. and Bowie, S., 2020. Preliminary report on the bedrock geology of the Rackla River area, southern Wernecke Mountains, Yukon (parts of NTS 106C/4, 5 and 106D/1, 8). *In:* Yukon Exploration and Geology 2019, K.E. MacFarlane (ed.), Yukon Geological Survey, p. 1–21.

Abstract

The Rackla River area is underlain by normal faulted and gently folded sedimentary strata of the Paleoproterozoic Wernecke Supergroup, Mesoproterozoic Pinguicula Group, Neoproterozoic Hematite Creek Group and Windermere Supergroup, and Paleozoic Bouvette Formation. Gabbro dikes and sills that are likely age equivalent to the *ca.* 1380 Ma Hart River Sills cut the Wernecke Supergroup rocks. The presence of a mafic volcaniclastic horizon within the Bouvette allows its informal subdivision into a lower and upper member. These volcaniclastic rocks may the distal equivalent to volcanic rocks near the Tiger deposit, located ~20 km to the southwest. Three major angular unconformities are documented in the map area: at the base of the Rapitan Group, the base of the lower Bouvette, and the base of the upper Bouvette Formation.

* tyler.ambrose@gov.yk.ca

Introduction

This paper presents preliminary results from 1:50 000-scale geological mapping conducted during 2019 in the Rackla River area, southern Wernecke Mountains, east-central Yukon. The mapped area covers ~300 km^2 and includes parts of NTS map sheets 106C/4 (Mount Mervyn), 106C/5 (Rusty Mountain), 106D/1 (Mount Westman) and 106D/8 (Mount Good). Prior to this study, most of the area was mapped at the 1:250 000 reconnaissance scale (Blusson, 1974). The area is host to significant mineralization, including the Val (Yukon MINFILE 106C 085, 116, 117) and Vera (Yukon MINFILE 106C 083, 114) occurrences, that justifies more detailed mapping.

Previous work

Aside from the westernmost part, Blusson (1974) previously mapped the area as part of a series of four 1:250 000-scale maps of the northern Selwyn basin. Delaney (1981 described and subdivided the Wernecke Supergroup into the Fairchild Lake, Quartet, and Gillespie Lake groups. Eisbacher (1981) described the Pinguicula Group and divided it into units A–F. Roots (1990) mapped the adjacent 1:50 000-scale sheets to the west (eastern half of 106D/7 and 106D/8). Abbott (1997) and Thorkelson (2000) mapped similar Proterozoic stratigraphy in the Hart River (116A/10, 11) and northern Wernecke (106D/16, 106C/13, 14) inliers, respectively. Based on the interpretation of an unconformity between Pinguicula C and D of Eisbacher (1981), Thorkelson (2000) reassigned Pinguicula Group units D–F into the newly defined Hematite Creek Group. Morrow (1999) formalized and described the type section of the Bouvette Formation. Turner (2011) formalized the Hematite Creek Group and assigned it to the lowermost Mackenzie Mountains Supergroup. To the south of the map area, in the Rackla belt,

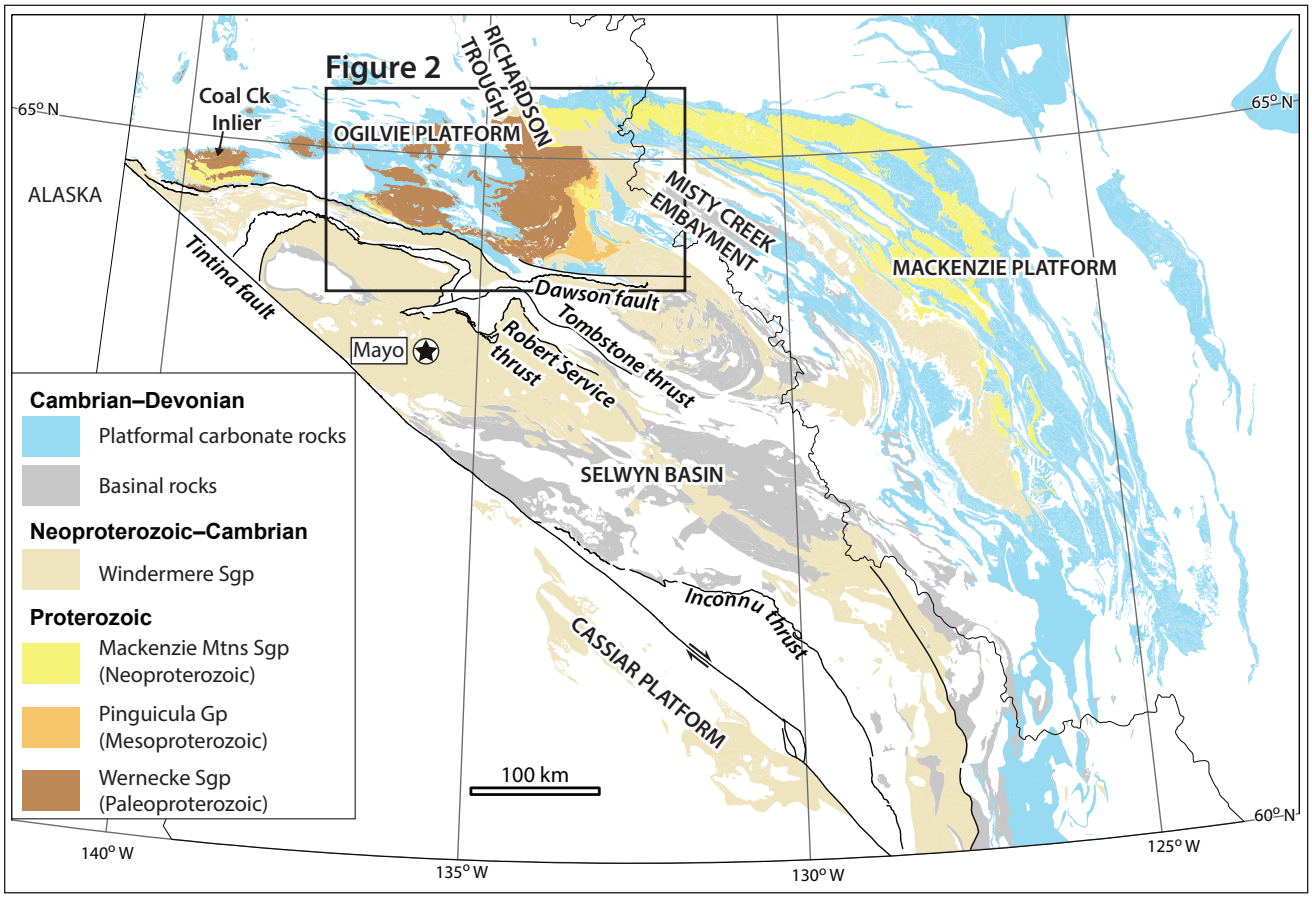


Figure 1. *Simplified geological map of eastern Yukon and western Northwest Territories illustrating the distribution of Proterozoic through to Devonian assemblages (after Moynihan et al., 2019). The study area is located within the Wernecke Inlier, the farthest east, and largest of several erosional windows that expose Paleoproterozoic and Mesoproterozoic rocks.*

Colpron et *al.* (2013) mapped five 1:50 000-scale map sheets (106C/1–4 and D/1), and Moynihan (2014) mapped 106B/4. Medig et *al.* (2016) described and formalized type sections for the Pinguicula Group in the Wernecke Inlier. Moynihan et *al.* (2019) defined the Rackla Group of the Windermere Supergroup. Property-scale mapping, conducted by Sivertz (1980), W.G. Timmins Exploration & Development Ltd. (1983), Waugh (1989) and Eaton (1999), focused on the Val and Vera mineral occurrences.

Location and geological setting

The mapped area is located in the southern Wernecke Mountains, ~120 km NE of Mayo (Figs. 1 and 2). Access is by a fixed-wing flight from Mayo to Rackla airstrip (64.22°N 133.21°W) followed by a helicopter flight to the field area. The map area is located along the southern margin of the Wernecke Inlier (Figs. 1 and 2). Along with the Coal Creek and Hart River inliers to the west, the Wernecke Inlier is an erosional window through the Phanerozoic cover of Ancestral North America into the underlying Proterozoic stratigraphy. The Proterozoic rocks exposed in these inliers include the oldest non-crystalline rocks exposed in the Cordillera and provide clues to the Proterozoic evolution of northwestern Canada. The inliers are located north of the Dawson fault on the relatively thick lithosphere of the Yukon stable block (Lenz, 1972). The Dawson fault marks the northern boundary of the Selwyn basin, a Paleozoic feature that developed on comparatively thin lithosphere.

The map area exposes Proterozoic through Paleozoic rocks (Fig. 3). The southern margin of the map is the Kathleen Lakes fault, which is nearly coincident with the East Rackla River. The Rackla River flows south through the central part of the map. The oldest rocks exposed in the Wernecke Inlier are Paleoproterozoic rocks of the Wernecke Supergroup and Mesoproterozoic Rocks of the Pinguicula Group. Overlying these successions are the Neoproterozoic Hematite Creek Group, the Neoproterozoic to earliest Cambrian Windermere Supergroup, and the Cambrian to Devonian Bouvette Formation (Fig. 4).

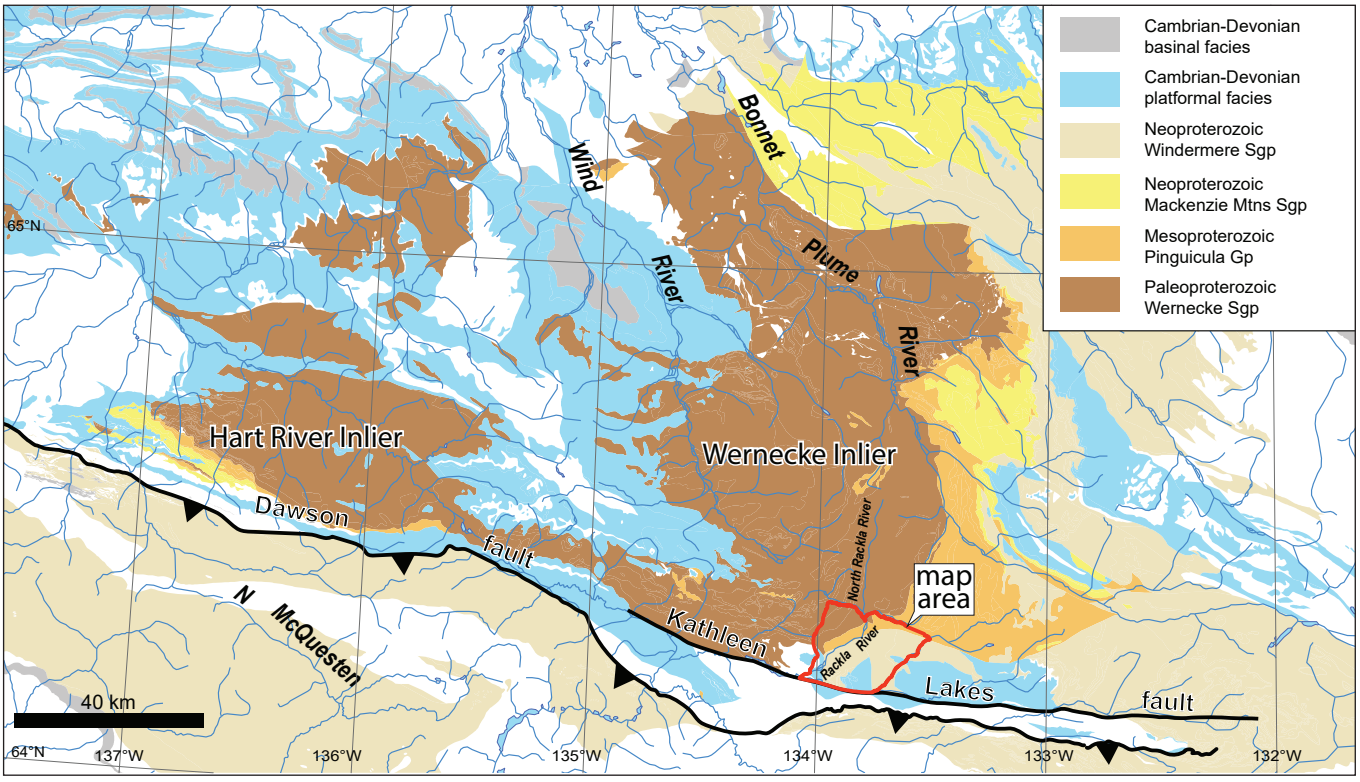
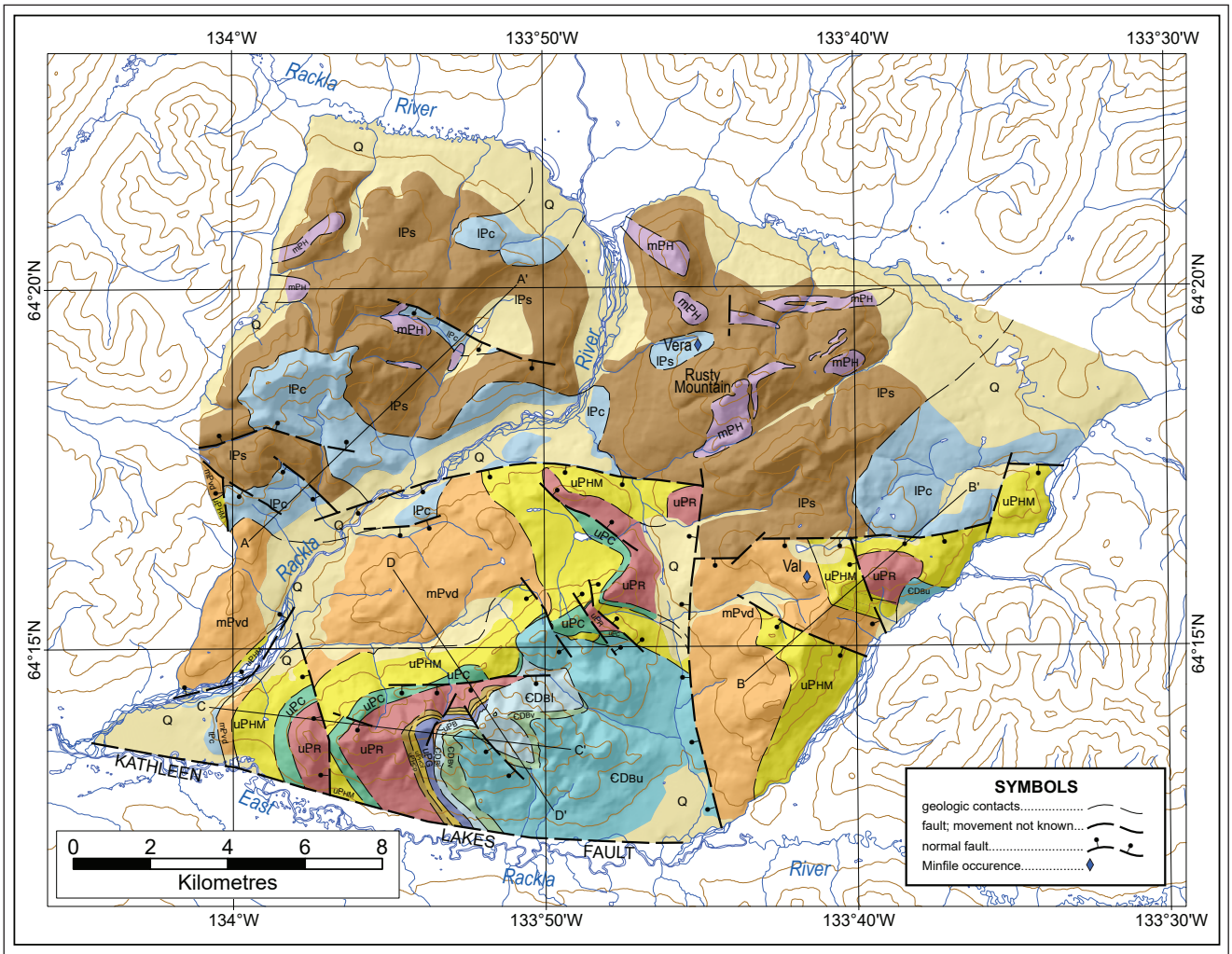


Figure 2. *Simplified geological map of the Wernecke and Hart River inliers. Location is shown in Figure 1. The map area (outlined in red) is located north of the Dawson and Kathleen Lakes faults, and across the southern margin of the Wernecke Inlier. Geology from Colpron et al. (2016).*



QUATERNARY

Q — unconsolidated alluvial, colluvial, fluvial, and glacial deposits

CAMBRIAN TO DEVONIAN

BOUVETTE FORMATION

ЄDBu — UPPER MEMBER: light to medium grey weathering dolostone; commonly thickly bedded; locally fossiliferous

ЄDBv — VOLCANICLASTIC MEMBER: grey, green and orange weathering volcaniclastic sandstone and conglomerate; locally fossiliferous

ЄDBl — LOWER MEMBER: light to medium grey weathering sugary dolostone

EDIACARAN

RACKLA GROUP

uPB — BLUEFLOWER FORMATION: brown weathering shale and siltstone

uPG — GAMETRAIL FORMATION: Well bedded and laminated grey, buff, maroon, yellow-orange, and green weathering silty lime- and dolo-mudstone

CRYOGENIAN–EDIACARAN

HAY CREEK GROUP

uPHCr — RAVENSTHROAT FORMATION: grey and cream weathering dolostone, gray and black chert; local chaotic bedding and tepee structures

uPHCp — MOUNT PROFEIT DOLOSTONE/ICE BROOK FORMATION: grey and cream weathering dolostone; light-grey weathered carbonate-clast diamictite

CRYOGENIAN

RAPITAN GROUP

uPR — orange, maroon, and brown weathering clast- to matrix-supported diamictite; maroon and green shale, siltstone and sandstone intervals

TONIAN

CALLISON LAKE FORMATION

uPC — light to medium grey weathering dolostone with irregular chert layers; commonly laminated; locally silica replaced oolitic grainstone; locally hematite-cement conglomerate

NEOPROTEROZOIC

HEMATITE CREEK GROUP

uPHM — laminated, medium to very thickly bedded grey, purple, and orange weathering quartz sandstone, with subordinate shale, siltstone, limestone, red-weathering stromatolitic dolostone, and orange-weathering dolostone and dolomitic siltstone

MESOPROTEROZOIC (?)

"VAL DOLOSTONE"

mPvd — dark and light grey laminated dolostone with local zebra textures

MESOPROTEROZOIC

HART RIVER SILLS

mPH — medium-grey weathering fine- to medium-grained greenish-grey gabbro sills and dikes

PALEOPROTEROZOIC(?)

LOWER CARBONATE UNIT

lPc — well-bedded, laminated, grey and orange weathering dolostone and limestone that is commonly cross-laminated; dolomitic/calcareous shale, siltstone, sandstone and intraclast rudstone

LOWER CLASTIC UNIT

lPs — grey, brown, black, terracotta, green and blue weathering shale, siltstone and sandstone; locally phyllitic and slatey; locally conglomerate;

Figure 3. *Simplified geological map of the Rackla River area.*

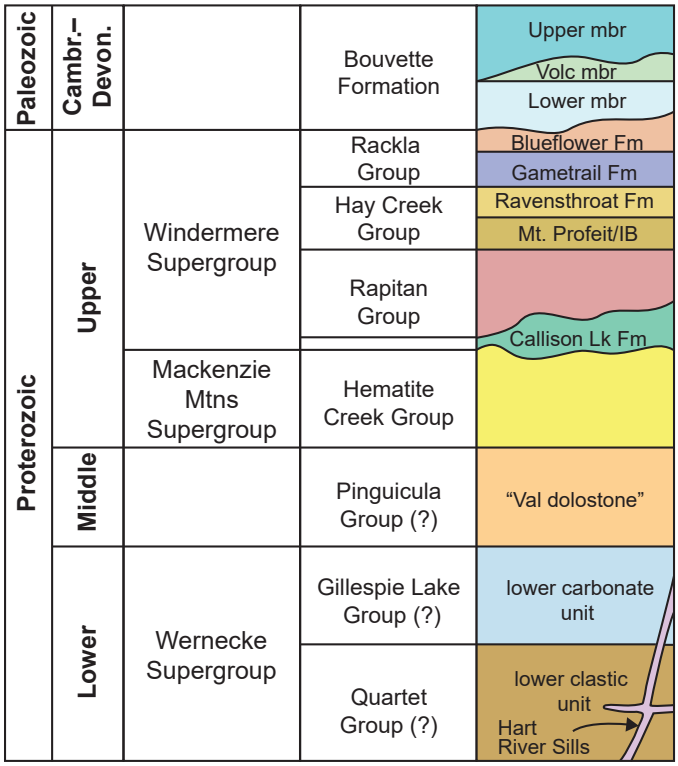


Figure 4. *Stratigraphy and tentative correlations of the Rackla River area.*

Stratigraphy

Lower clastic unit

The oldest unit (lower clastic unit) is exposed in the northern and central part of the map area and consists of brown, blue, green, black, terracotta and grey weathering laminated shale, siltstone, and sandstone (Figs. 3–5). Planar parallel laminations are common (Fig. 5a,b) and wavy laminations are locally observed. An interval of sandstone interbedded with matrix to clast-supported conglomerate containing clasts of limestone, siltstone, and chert is present at one locality west of Rusty Mountain. Siltstone and sandstone beds are locally cross-laminated (Fig. 5c,d). A pencil cleavage is commonly well-developed (Fig. 5e) and a slatey to phyllitic cleavage is locally developed. At one locality, on a ridge ~3 km NNW of Rusty Mountain, dark and light grey finely crystalline limestone with 5 mm-thick dark-grey chert nodules is present. At this same locality, chert also occurs as interbeds and nodules within orange-weathering dolostone.

Lower carbonate unit

The lower carbonate unit gradationally overlies the lower clastic unit and consists primarily of well-bedded and commonly cross-laminated, grey and orange weathering limestone and dolostone (Fig. 6a–c) and relatively minor shale, siltstone, dolomitic and calcareous siltstone, and silty dolostone (Fig. 6d). The contact between the lower carbonate unit and the underlying lower clastic unit is particularly well exposed in the western part of the map area (Fig. 7). Here, the upper most ~10 m of the lower clastic unit becomes slatey and phyllitic, and the overlying basal ~10 m of the lower carbonate unit comprises tan weathering dolomitic shale and platy silty dolostone that passes up section into orange weathering dolostone and limestone more typical of the unit. A distinct lithology that consists of very thickly bedded, commonly intensely calcite-veined, dark-grey, micritic limestone occurs at various stratigraphic levels within this unit (Figs. 6e and 8). An interval, a few metres thick, of intraclast conglomerate–breccia containing clasts of limestone in an orange weathering dolomitic matrix occurs locally in the northwest quadrant of the map area (Fig. 6f).

Outcrop-scale evidence for tectonic deformation is not common in the lower carbonate unit. A cleavage is developed in siliciclastic intervals and minor (10s of cm in scale) folds are rarely observed in carbonate beds.

Hart River Sills

The lower clastic and lower carbonate units are cut by medium-grey weathering, fine to medium-grained, greenish-grey gabbro sills and dikes (Figs. 3, 4, 9 and 10). These intrusions are most likely equivalent to the Mesoproterozoic (ca. 1.38 Ga) Hart River Sills that have been described elsewhere in the Wernecke Inlier (*e.g.*, Abbott 1997; Thorkelson, 2000; Verbaas *et al.*, 2018). The distribution of the intrusions is variable, being most abundant near Rusty Mountain, yet absent to the southeast despite similar host rocks. Whereas intrusions are locally abundant in the lower clastic unit, there is only one locality, in the northwestern part of the map area, where metamorphism of the lower carbonate unit indicates that it was also intruded (Fig. 3). Although this relationship is not directly observed, gabbro is exposed within a hundred metres of hornfelsed siliciclastic rocks and marble.



Figure 5. *Select field photographs of the lower clastic unit.* ***(a–c)*** *Laminated shale and siltstone. Dark lenses in (c) are cross-laminated.* ***(d)*** *Cross-bedded sandstone with dewatering/soft-sediment deformation structure.* ***(e)*** *Pencil cleaved siltstone.* ***(f)*** *Minor fold in slatey siltstone and fine-grained sandstone.*



Figure 6. *Representative field photographs of the lower carbonate unit.* ***(a–c)*** *Typical orange and grey weathering laminated dolostone and limestone.* ***(d)*** *Siltstone interbedded with orange weathering dolostone.* ***(e)*** *Dark grey micritic limestone containing abundant calcite veins.* ***(f)*** *Carbonate-intraclast conglomerate with orange dolomitic matrix.*

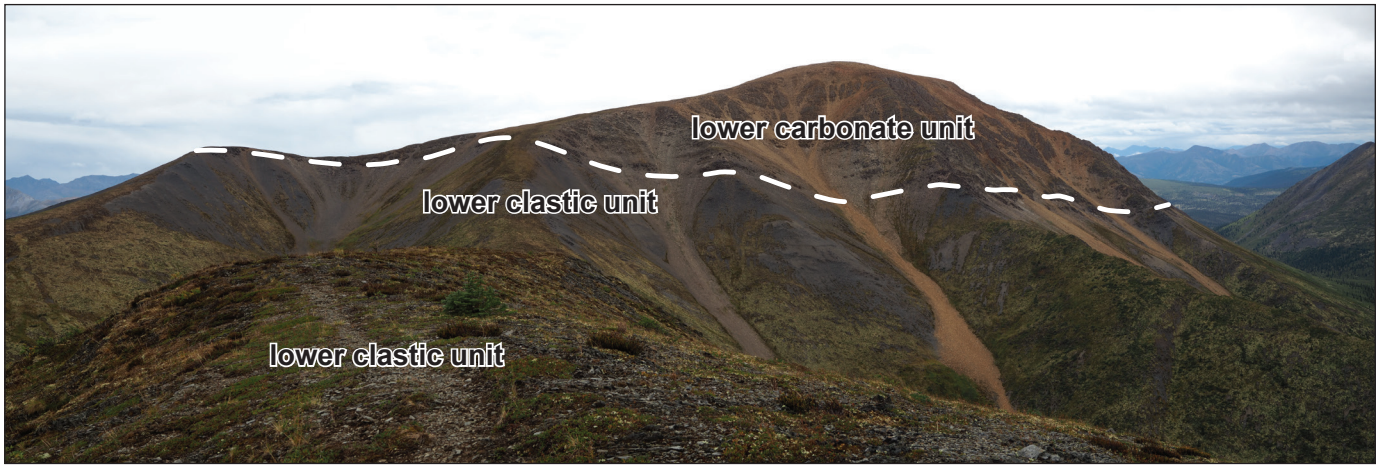


Figure 7. *Panoramic field photograph of the resistant orange weathering lower carbonate unit underlying recessive shale and siltstone of the lower clastic unit.*

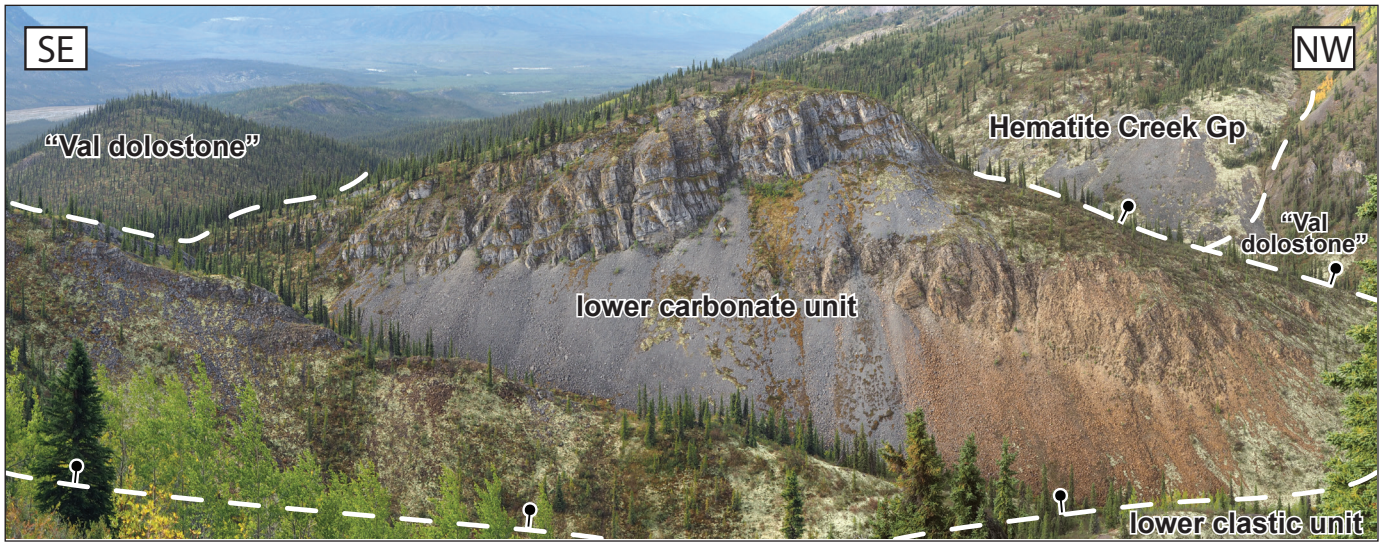


Figure 8. *Panoramic field photograph from the westernmost extent of the map area illustrating the relationship between laminated dolostone of the "Val dolostone" and very thickly bedded carbonate of the underlying lower carbonate unit. In the top right of the frame, quartz arenite of the Hematite Creek Group, and underlying "Val dolostone", are both in fault contact with the lower carbonate unit. Photo is taken from shale and siltstone of the lower clastic unit.*



Figure 9. *Hand sample photograph of greenish altered gabbro. Scale bar is in mm.*



Figure 10. *Field photograph of a gabbro dike, cutting fine-grained clastic rocks of the lower clastic unit on Rusty Mountain.*

"Val dolostone"

The "Val dolostone" is informally named after the host lithology at the Val occurrence (MINFILE 106C 085). It consists of dark and light grey laminated dolostone (Fig. 11a). Laminations are typically planar parallel and, in places, wavey and discontinuous. The "Val dolostone" is in fault contact with the lower clastic unit north of the Val occurrence (Fig. 3). On the western edge of the map area, the "Val dolostone" apparently overlies thickly bedded limestone of the lower carbonate unit (Fig. 8). The orientation of bedding in both units is consistent, but the exact nature of the contact is uncertain as it occurs undercover in a small gulley and, as elsewhere in the map area, may be a fault.

The "Val dolostone" is commonly replaced by mm to cm-scale bands of orange and white sparry dolomite that commonly occur as en échelon arrays, a feature commonly described as zebra texture (Fig. 11b,c). This texture is common in hydrothermal dolomite associated with base metal deposits (e.g., Wallace et *al.*, 1994). Occurrences of zebra textures are typically associated with brecciation and disruption of layers (Fig. 11d–f). The degree of dolomitization and brecciation is variable. Weakly brecciated zones locally preserve tepee-like structures (Fig. 11d).

In the southeastern part of the map area (near the Val occurrence), the top ~100 m of the "Val dolostone" becomes progressively more quartzose and eventually grades into overlying siliciclastic rocks of the Hematite Creek Group. At this same locality, east of the Val occurrence, the "Val dolostone" contains a several tens-of-metres thick horizon of orange weathering dolostone. Neither the increasing quartz content nor the orange-weathering dolostone were observed in other regions of the map area.

Hematite Creek Group

The "Val dolostone" is gradationally overlain by a heterolithic succession dominated by thickly bedded quartz arenite of the Tonian Hematite Creek Group (Figs. 12 and 13; Thorkelson 2000; Turner, 2011; Gibson et *al.*, 2019). The quartz arenite typically weathers light to medium grey, less commonly purple and, when iron oxides are present, orange (Fig. 13b). The Hematite Creek Group also contains interbedded limestone, grey, orange, and maroon shale and siltstone, orange weathering dolostone and silty dolostone, and red weathering stromatolitic dolostone (Fig. 13). These carbonate and shale intervals are similar to parts of the lower carbonate unit, although they are always associated with quartz arenite in the Hematite Creek Group. Planar parallel laminations, and less commonly cross-laminations, occur in quartz arenite, limestone and siltstone of the Hematite Creek Group.

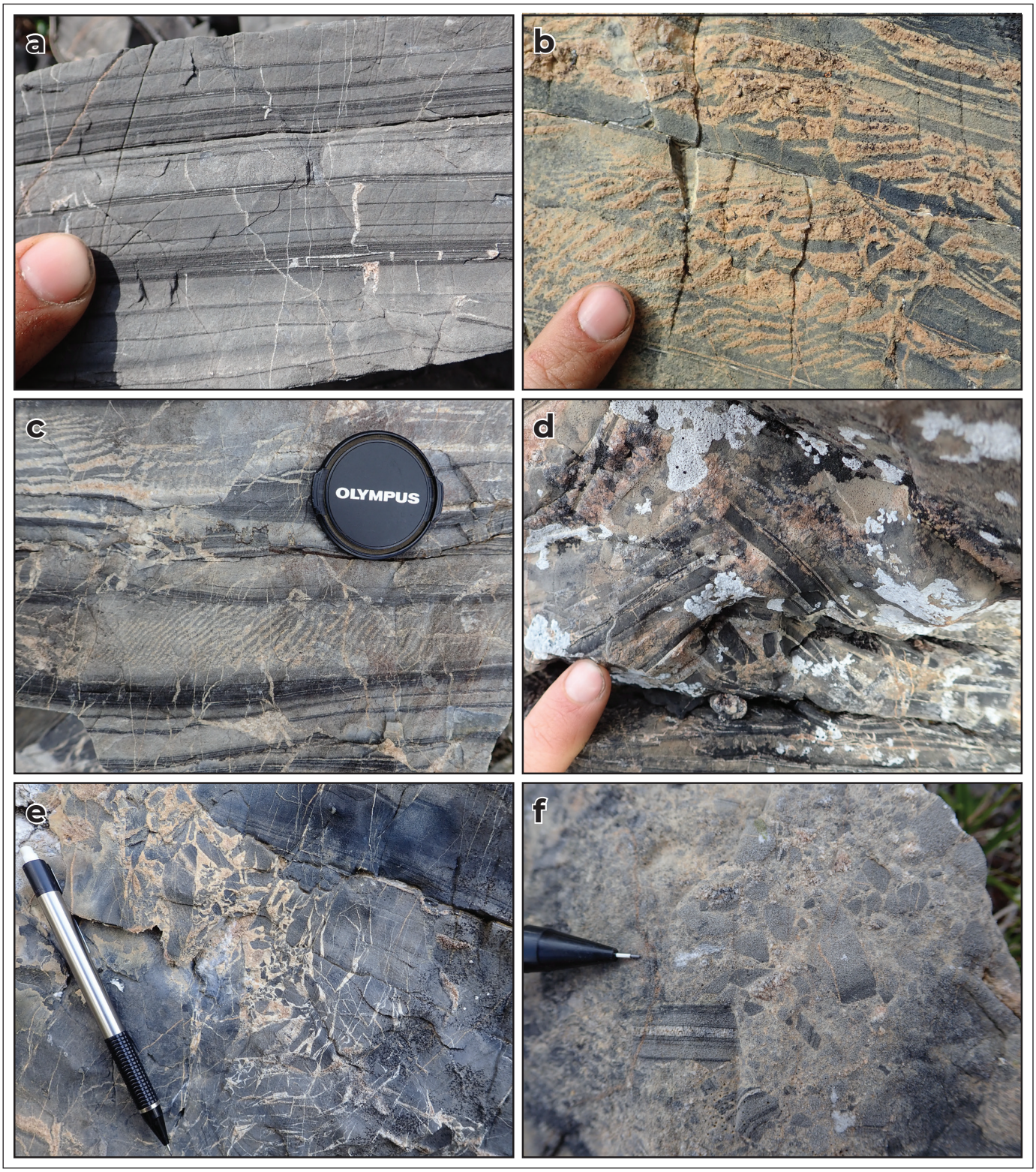


Figure 11. *Representative field photographs of the "Val dolostone".* ***(a)*** *Typical pin-stripe laminated dolostone.* ***(b–c)*** *Zebra dolostone, characterized by orange and white sparry dolomite that occurs as en échelon bands.* ***(d)*** *Tepee structure in brecciated "Val dolostone".* ***(e)*** *Brecciated fluid pathway in laminated dolostone.* ***(f)*** *Breccia with angular clasts of laminated dolostone.*

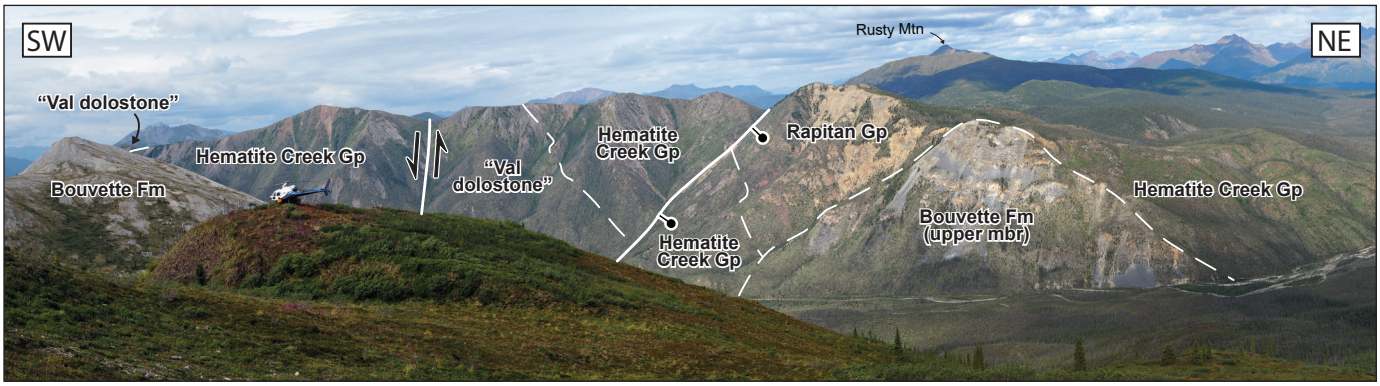


Figure 12. *Panoramic field photograph illustrating field relationships along the ridge at the eastern margin of the map area. Two unconformities are visible, one at the base of the Bouvette Formation, and another at the base of the Rapitan Group. The peak of Rusty Mountain is visible in the background.*

Windermere Supergroup

Callison Lake Formation

The Tonian Callison Lake Formation (Abbott, 1997; Strauss *et al.*, 2015) constitutes the base of the Windermere Supergroup in the area (Fig. 4). In the Coal Creek and Hart River inliers, the Callison Lake Formation rests with angular unconformity on older strata (Abbott, 1997; Strauss *et al.*, 2015). In the map area, however, it always overlies the Hematite Creek Group and thus evidence for an angular unconformity is lacking (Figs. 3 and 14). The Callison Lake Formation consists of light to medium-grey weathering, thin to thickly bedded, cliff-forming dolostone with irregular mm to few-cm-thick chert layers (Fig. 15). It is commonly laminated (Fig. 15b) and includes discontinuous intervals of grey to black chert (Fig. 15c) and silicified oolitic grainstone (Fig. 15d). A several metre-thick interval of matrix to clast-supported hematite-cemented conglomerate containing clasts of carbonate, chert and jasper is present at the easternmost exposure of the unit (Fig. 15e). Locally, the Callison Lake Formation also contains a matrix to clast-supported conglomerate with intraformational clasts of chert, carbonate and silicified oolitic grainstone (Fig. 15f). The identification of the Callison Lake Formation in the map area extends its geographic range significantly farther east than has previously been recognized.

Rapitan Group

The Cryogenian Rapitan Group (Yeo, 1981) consists of orange, maroon and brown weathering, very poorly sorted, clast to matrix-supported conglomerate and diamictite, and maroon, orange and green shale, siltstone and fine-grained sandstone (Fig. 16). The base of the Rapitan Group is an unconformity that cuts the stratigraphic section from the Callison Lake Formation in the west (Fig. 14) to as deep as the Hematite Creek Group in the east (Fig. 12). Sandstone and siltstone are commonly laminated (Fig. 16f), and all rock types locally exhibit a well-developed tectonic foliation (Fig. 16e,f). Clasts within the conglomerate are angular to rounded and include chert, jasper, siltstone, dolostone, limestone, and mafic volcanic rocks. The upper contact of the Rapitan Group is observed at two localities: at the southern edge of the map sheet where it underlies the Mount Profeit dolostone, and along the eastern margin of the map area, where it unconformably underlies the upper member of the Bouvette Formation. A fine-grained mafic dike cutting maroon siltstone and sandstone is present at one locality near the southern extent of the map area.



Figure 13. *Representative field photographs of the Hematite Creek Group.* ***(a)*** *Thickly bedded light grey weathering quartz arenite.* ***(b)*** *Iron-oxides in quartz arenite that cause red to orange weathering.* ***(c)*** *Interbedded calcareous shale-siltstone and limestone.* ***(d)*** *Red weathering stromatolitic dolostone.* ***(e)*** *Interbedded orange weathering dolostone, dolomitic siltstone and quartz arenite.* ***(f)*** *Interbedded dolomitic siltstone-sandstone, dolomitic quartzite and quartzite.*

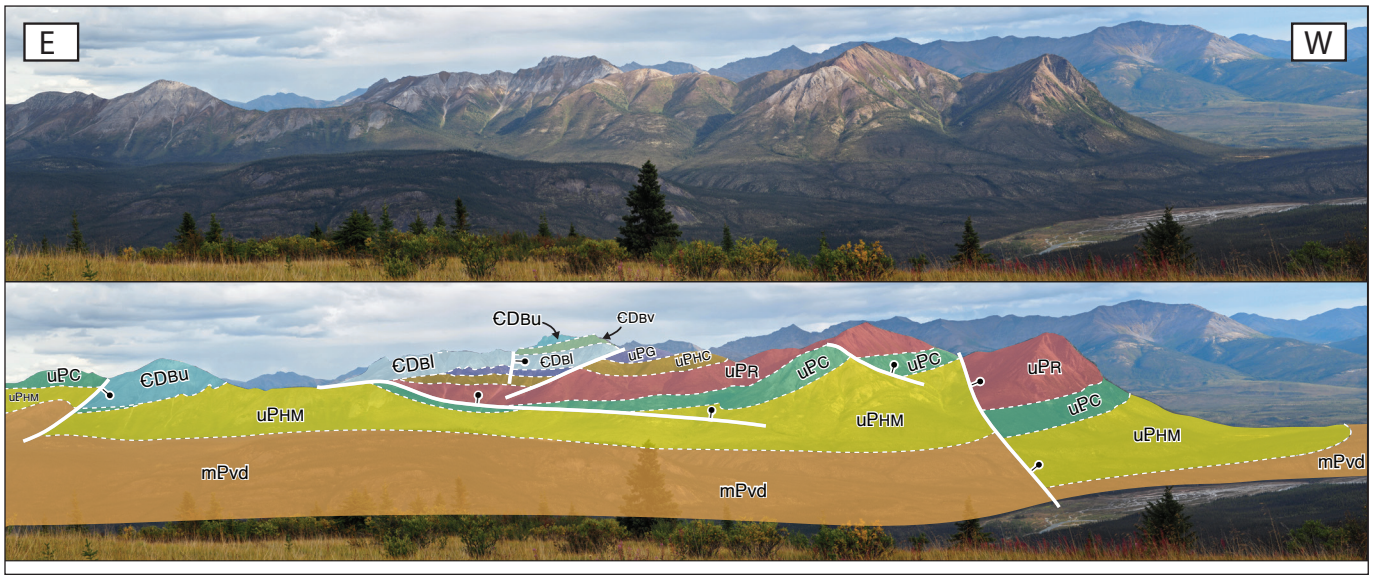


Figure 14. *Panoramic field photograph of an east-west trending ridge in the southwestern part of the map area that illustrates the stratigraphic relationship between Mesoproterozoic and younger units. Rackla River is in the valley bottom. See Figure 3 for legend.*

Hay Creek Group

In the map area, the Hay Creek Group (Yeo, 1978) comprises the Cryogenian Mount Profeit dolostone and Ice Brook Formation, and the Ediacaran Ravensthroat formation (Figs. 3, 4 and 17a–d). An ~200 m-thick section of the Hay Creek Group is exposed along a ridge in the southern part of the map area (Figs. 3 and 14). The Mount Profeit dolostone, which constitutes the base of the Hay Creek Group in the area and overlies the Rapitan Group, consists of grey and cream weathering dolostone with irregular chert intervals (Fig. 17a). The Mount Profeit dolostone is overlain by a several metre thick interval of light grey weathering, carbonate-clast diamictite of the Stelfox member of the Ice Brook Formation (Fig. 17b). The Ice Brook Formation is overlain by the Ravensthroat formation, which consists of grey and cream weathering dolostone containing chert layers that highlight chaotic layering, tepee-shaped structures and sheet-cracks (Fig. 17c,d).

Rackla Group

In the map area, the Ediacaran Rackla Group (Moynihan *et al.*, 2019) comprises the Gametrail and Blueflower formations (Figs. 3, 4 and 14). As with the Hay Creek Group, the Rackla Group is only exposed in a small area near the southern extent of the map area (Fig. 3). The Gametrail Formation consists of grey, buff, maroon, yellow-orange, and green weathering, well-bedded and laminated, silty lime and dolo-mudstone (Fig. 17e,f). The Blueflower Formation unconformably underlies the lower member of the Bouvette Formation and consists of brown shale and siltstone containing Ediacaran trace fossils (Fig. 17e).



Figure 15. *Field photographs presenting key characteristics of the Callison Lake Formation.* **(a)** *Thickly-bedded dolostone.* **(b)** *Lamination in dolostone.* **(c)** *Discontinuous black chert layering in light grey dolostone.* **(d)** *Silicified oolitic grainstone.* **(e)** *Hematite cemented conglomerate.* **(f)** *Conglomerate containing dolostone matrix and clasts of light grey dolostone, black chert and silicified oolitic grainstone.*



Figure 16. *Field photographs of the Rapitan Group.* ***(a)*** *Cliff of maroon weathering diamictite. Arrow points to geologist for scale.* ***(b–d)*** *Orange and maroon weathering diamictite.* ***(e)*** *Orange weathering, matrix supported, well-foliated conglomerate.* ***(f)*** *Maroon-weathering siltstone exhibiting shallow laminations and a steeply dipping cleavage.*

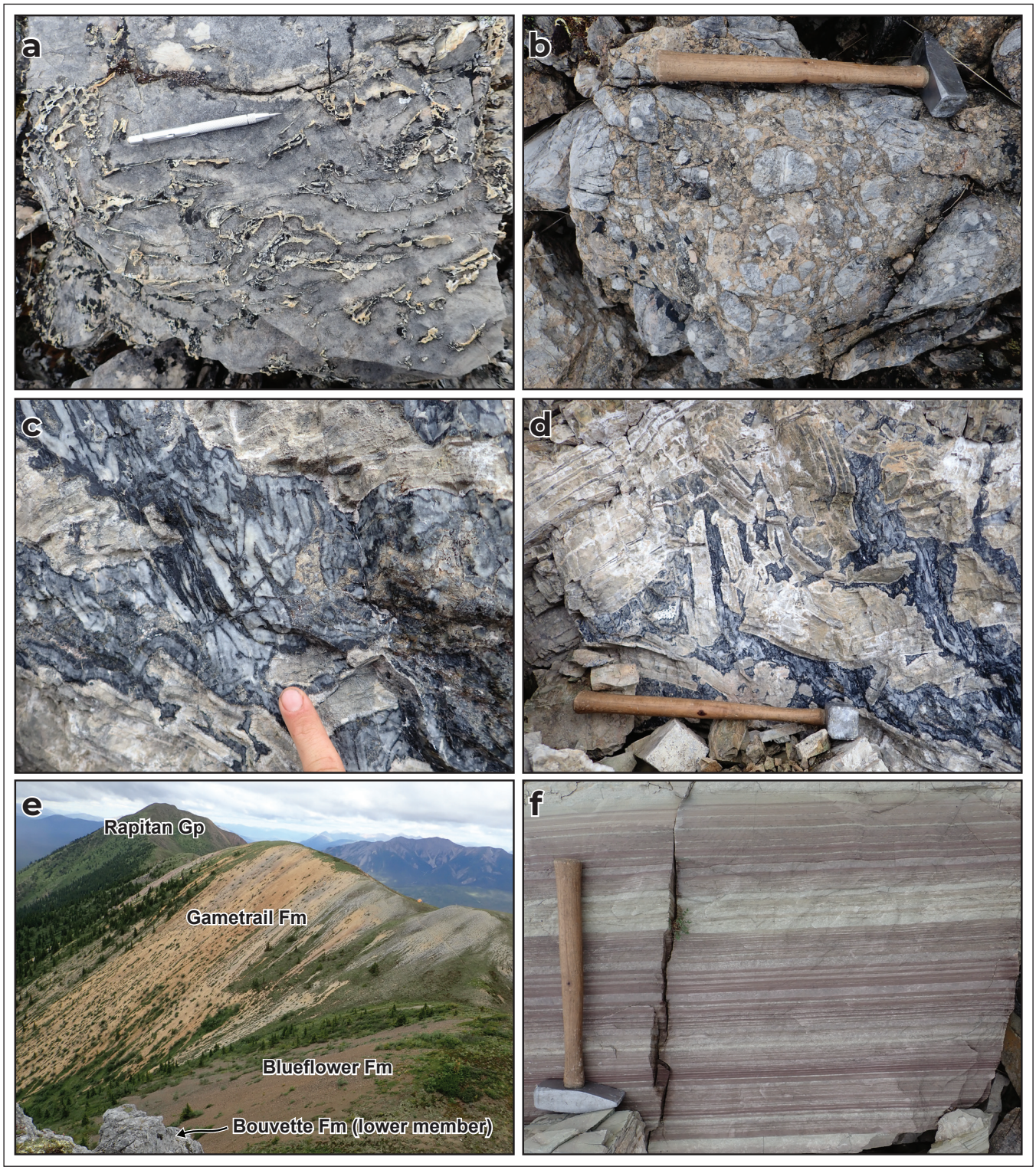


Figure 17. *Select field photographs of the Hay Creek Group (a–d) and Rackla Group (e–f).* ***(a)*** *Dolostone containing irregular cream-coloured chert layers of the Mount Profeit dolostone.* ***(b)*** *Carbonate-clast diamictite, Stelfox Member of the Ice Brook Formation.* ***(c–d)*** *Chaotic bedding, sheet crack and tepee-shaped structures in the Ravensthroat formation.* ***(e)*** *View from Bouvette Formation (grey dolostone at very base of photo) of brown shale of the Blueflower Formation and underlying yellow-orange, silty lime mudstone of the Gametrail Formation. Peak at end of ridge is Rapitan Group. Hay Creek Group is hidden from view. Looking west.* ***(f)*** *Laminated maroon and grey silty lime mudstone in the Gametrail Formation.*

Bouvette Formation

The Cambrian to Devonian Bouvette Formation (Morrow, 1999) overlies older successions along an unconformity that cuts stratigraphy from as young as the Blueflower Formation to as old as Hematite Creek Group (Figs. 3, 4, and 18a). We informally divide the Bouvette Formation into a lower, volcaniclastic, and upper member. The lower member consists of light grey weathering, saccharoidal dolostone with minor grey chert (Fig. 18a). The volcaniclastic member consists of thin to medium-bedded grey, green, and orange weathering volcaniclastic sandstone and conglomerate (Fig. 18). Clasts and grains include fragments of mafic volcanic rocks, fossils, and limestone in a predominantly carbonate matrix (Fig. 18b,c,e). Intervals of the volcaniclastic member are extensively bioturbated (Fig. 18f). Fossils are locally abundant and include graptolites, brachiopods, trilobites, sponges, crinoids, bryozoans and echinoids. The volcaniclastic member may be a more distal equivalent of the mafic volcanic rocks exposed ~20 km WSW at the Tiger deposit.

The upper member of the Bouvette Formation consists of light to medium grey weathering dolostone (Figs. 12 and 14). Unlike the lower member, the upper member is commonly bedded and locally fossiliferous, with corals being most common. The base of the upper Bouvette is an unconformity that, in the field area, cuts from the volcaniclastic member in the west, down through the stratigraphy to the Hematite Creek Group in the east (Figs. 3, 12 and 14). A preliminary assessment of the fossil assemblages indicates a late Ordovician to earliest Silurian age for the volcaniclastic member, and a Silurian age for the upper member of the Bouvette (R.B. Blodgett, pers. comm., 2019).

Structure

In the map area the strata are inclined and gently folded (Fig. 19). Outcrop-scale minor folds are rare and are best developed in the lower clastic unit, lower carbonate unit, and "Val dolostone". An axial planar cleavage is commonly well developed in the lower clastic unit and Rapitan Group, and in fine-grained clastic intervals in the lower carbonate unit. The relatively incompetent shale and siltstone of the lower clastic unit exhibit the most deformation and, in places, may be overturned on the short limbs of asymmetric folds (see cross section A-A' in Fig. 19). Normal faults are the dominant structure in the map area (Figs. 3 and 19). A major normal fault runs east-west for ~20 km across the centre of the map area and separates old, Paleoproterozoic strata to the north from Mesoproterozoic and younger rocks to the south. Another major fault runs north-south through the centre of the map area and down-drops strata to the west. A series of shorter, generally NNW–WNW striking, normal faults were also identified.

Correlation of older units

The lithology and stratigraphic relationships of the lower clastic unit, lower carbonate unit, and "Val dolostone" indicate that they may be correlative with the Mount Landreville (formerly Pinguicula A of Eisbacher, 1981), Pass Mountain (formerly Pinguicula B of Eisbacher, 1981), and Rubble Creek (formerly Pinguicula C of Eisbacher, 1981) formations of the Pinguicula Group (Medig *et al.*, 2016). However, as discussed above, the lower clastic and the lower carbonate units are cut by mafic dikes that are likely equivalent to the *ca.* 1380 Ma Hart River Sills (e.g., Abbott, 1997; Thorkelson, 2000; Verbaas *et al.*, 2018). Based on contact relationships observed elsewhere in the Wernecke Mountains, Medig *et al.* (2010) interpreted the Hart River Sills to have intruded the Wernecke Supergroup prior to the deposition of the overlying Pinguicula Group. This suggests that the lower clastic and carbonate units are more likely correlative with the Quartet and Gillespie Lake groups of the Wernecke Supergroup, a plausibility also supported by their lithological characteristics.

Two other explanations can account for the geological relationships observed: (1) the intrusions may be younger than the Hart River Sills and thus it would be permissible that the section is all part of the Pinguicula Group. (2) Another less likely explanation is that the Hart River Sills intruded the Pinguicula Group, up to, at minimum, the Pass Mountain Formation. Thorkelson (2000) and Thorkelson *et al.* (2005) reported that the base of the Mount Landreville Formation was cut by a diorite dike correlative with the Hart River Sills.

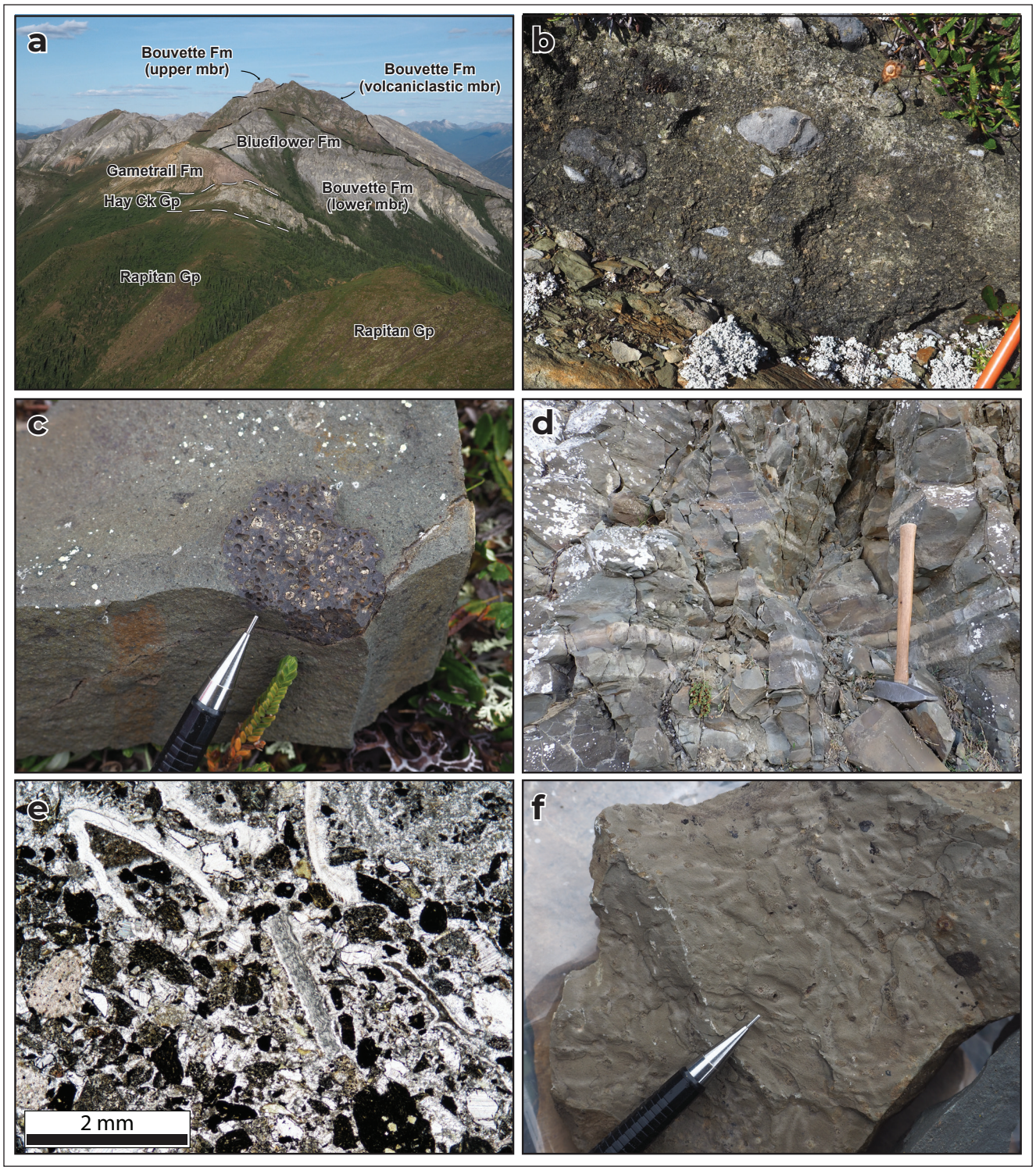


Figure 18. *Select field photographs of the lower, volcaniclastic and upper members of the Bouvette Formation.* ***(a)*** *Field photograph illustrating the stratigraphy of the Windermere Supergroup overlain by the Bouvette Formation along a ridge at the southern extent of the map area.* ***(b)*** *Conglomerate from the volcaniclastic member with grey limestone clasts and a green-weathering sandy matrix. Pencil for scale in bottom right if frame.* ***(c)*** *Scoria clast in green weathering volcaniclastic sandstone.* ***(d)*** *Well-bedded, green-weathering volcaniclastic sandstone.* ***(e)*** *Photomicrograph (PPL) of sandstone from the volcaniclastic member, comprising fragments of mafic volcanic rocks (dark clasts) and fossils in a carbonate matrix.* ***(f)*** *Burrows in green-weathering sandstone from the volcaniclastic member.*

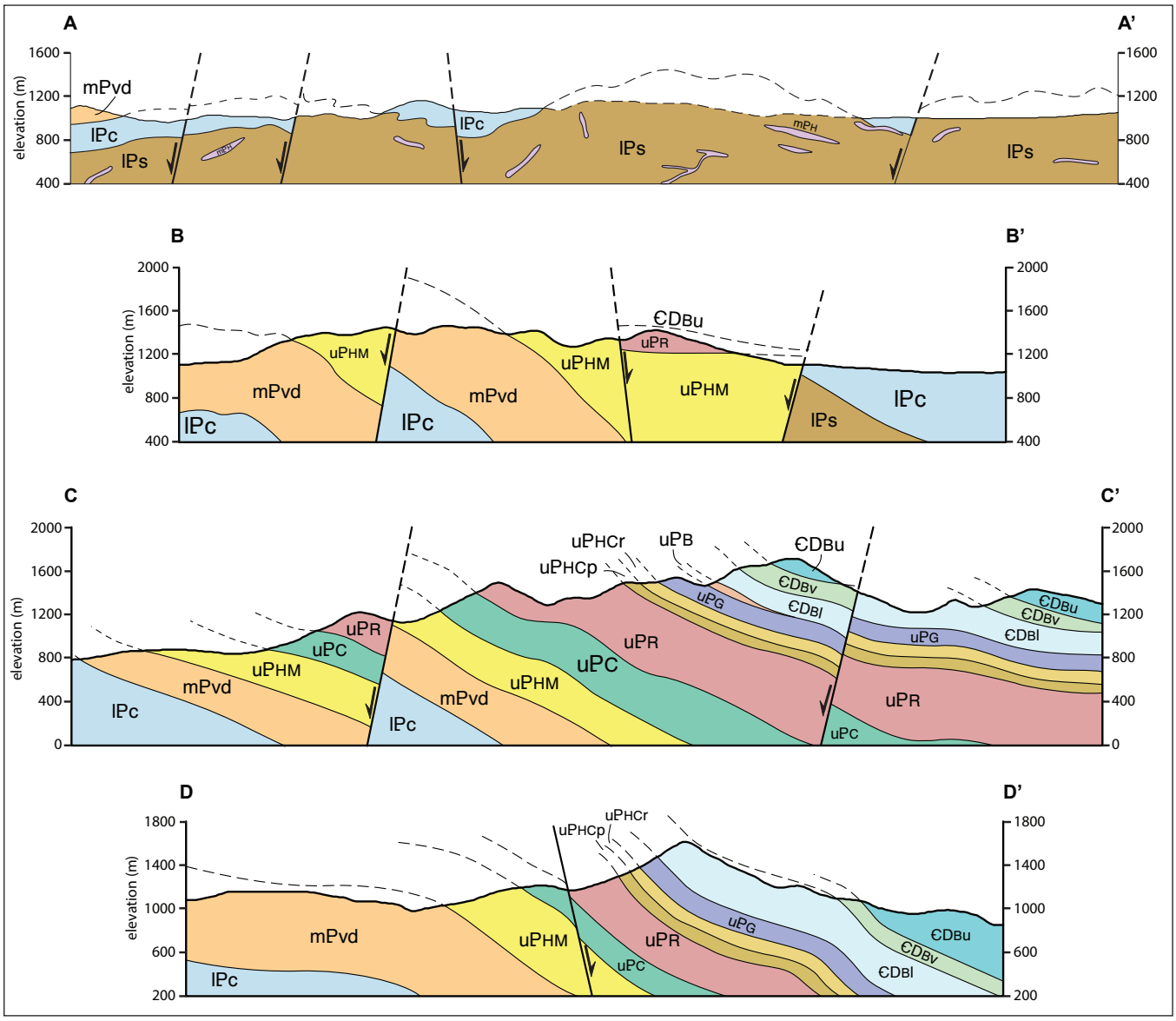


Figure 19. *Cross sections illustrating the geological and stratigraphic relationships. Locations are indicated in Figure 3. See Figure 3 for legend.*

However, these authors have since reinterpreted the host rock as being part of the Wernecke Supergroup, not the Pinguicula Group (Medig et *al.*, 2010). Moreover, Thorkelson (2000) only ever interpreted the Hart River Sills to have intruded the lowest levels of the Mount Landreville Formation. The field relationships described herein would require that Hart River Sills intrude through the Mount Landreville Formation and into the Pass Mountain Formation. Based on this line of reasoning, the most likely explanation is that the lower clastic and carbonate units correlate to the Quartet and Gillespie Lake groups, respectively, of the Wernecke Supergroup.

Mineralization

The map area includes several mineral occurrences that are mostly located in the eastern half of the map area (see Eaton, 1999 and Kammerer and Eaton, 2010 for a summary). The most significant mineralization is centred at the Vera (Yukon MINFILE 106C 083 and 114) and Val (Yukon MINFILE 106C 085, 115, 116, and 117) occurrences (Fig. 3). The Vera occurrence, located on the north slope of Rusty Mountain, consists of Ag-Pb-Zn mineralization in brecciated orange weathering stromatolitic dolostone of the lower carbonate unit (Sinclair, 1981). The Val occurrence

consists of Ag-Pb-Zn mineralization in breccia zones and sparry dolomite veins in the 'Val dolostone' unit (Sivertz, 1980). Vera has a historical resource estimate of 392 667 t at 607.0 g/t Ag, 3.18% Pb and 3.47% Zn, and Val has a historic resource estimate of 19 964 t at 1029 g/t, 26.7% Pb and 7.3% Zn (Casselman, 2018). In addition to the Val and Vera occurrences, Ag-Pb-Zn mineralization also occurs across the eastern half of map area in veins and breccia in the lower clastic unit, Hart River Sills, and the Hematite Creek Group (e.g., Kammerer and Eaton, 2010).

Acknowledgements

David Moynihan, Maurice Colpron and Rosie Cobbett are thanked for insightful discussion and field visits. Thanks also to Maurice Colpron and David Moynihan for reviewing an earlier version of this manuscript, Horizon Helicopters and Alkan Air for transport to the field, and Cantex for logistical support.

References

Abbott, G., 1997. Geology of the upper Hart River area, eastern Ogilvie Mountains, Yukon Territory (116A/10, 116A/11). Exploration and Geological Services Division, Yukon Region, Indian and Northern Affairs Canada Bulletin 9, 92 p.

Blusson, S.L., 1974. Five geological maps of northern Selwyn Basin (Operation Stewart), Yukon Territory and District of Mackenzie (105N, O; 106A, B, C). Geological Survey of Canada, Open File 205, scale 1:250 000.

Casselman, S. (compiler), 2018. Yukon Mineral Deposits Summary 2018. Yukon Geological Survey, 30 p.

Colpron, M., Moynihan, D., Israel, S. and Abbott, G., 2013. Geological map of the Rackla belt, east-central Yukon (NTS 106C/1-4, 106D/1). Yukon Geological Survey, Open File 2013-13, 1:50 000 scale, 5 maps and legend. (2018 Update).

Colpron, M., Israel, S., Murphy, D., Pigage, L. and Moynihan, D., 2016. Yukon bedrock geology map. Yukon Geological Survey, Open File 2016-1, scale 1:1 000 000.

Delaney, G.D., 1981. The mid-Proterozoic Wernecke Supergroup, Wernecke Mountains, Yukon Territory. *In:* Proterozoic Basins of Canada, F.H.A. Campbell (eds.), Geological Survey of Canada, Paper 81-10, p. 1–23.

Eaton, J., 1999. Geochemical, Geological and Geophysical Assessment Report for the Val, Vera, Rusty, KLA, Nad and Craig Claims, Manson Creek Resources Ltd., February 1999. Yukon Energy, Mines and Resources Assessment Report 093968.

Eisbacher, G.H., 1981. Sedimentary tectonics and glacial record in the Windermere Supergroup, Mackenzie Mountains, northwestern Canada. Geological Survey of Canada, Paper 80–27, 40 p., https://doi.org/10.4095/119453.

Gibson, T.M., Halverson, G., Macdonald, F., Cumming, V., Kunzmann, M., Wörndle, S., Lechte, M., Maloney, K., Millikin. A., Murphy, J. and Wallace, M., 2019. Tectono-stratigraphy and facies architecture of the Tonian Hematite Creek and Katherine groups, Wernecke Mountains, Yukon: *In:* Abstracts with Programs, GAC–MAC Conference 2019, Québec City, QC.

Kammerer, M., and Eaton, W.D., 2010. Geological mapping, prospecting and geochemical sampling at the Rusty Property. Yukon Energy, Mines and Resources Assessment Report 95720.

Lenz, A.C., 1972. Ordovician to Devonian history of northern Yukon and adjacent District of Mackenzie. Bulletin of Canadian Petroleum Geology, vol. 20, p. 321–361.

Medig, K.P.R., Thorkelson, D.J. and Dunlop, R.L., 2010. The Proterozoic Pinguicula Group: Stratigraphy, contact relationships and possible correlations. *In:* Yukon Exploration and Geology 2009, K.E. MacFarlane, L.H. Weston and L.R. Blackburn (eds.), Yukon Geological Survey, p. 265–278.

Medig, K.P.R., Turner, E.C., Thorkelson, D.J. and Rainbird, R.H., 2016. Rifting of Columbia to form a deep-water siliciclastic to carbonate succession: The Mesoproterozoic Pinguicula Group of northern Yukon, Canada. Precambrian Research, vol. 278, p. 179–206, https://doi.org/10.1016/j.precamres.2016.03.021.

Morrow, D.W., 1999. Lower Paleozoic stratigraphy of northern Yukon Territory and northwestern District of Mackenzie. Geological Survey of Canada Bulletin 538, 202 p., https://doi.org/10.4095/210998.

Moynihan, D., 2014. Bedrock Geology of NTS 106B/04, Eastern Rackla Belt. *In:* Yukon Exploration and Geology 2013, K.E. MacFarlane, M.G. Nordling and P.J. Sack (eds.), Yukon Geological Survey, p. 147–167.

Moynihan, D.P., Strauss, J.V., Nelson, L.L. and Padget, C.D., 2019. Upper Windermere Supergroup and the transition from rifting to continent-margin sedimentation, Nadaleen River area, northern Canadian Cordillera. GSA Bulletin, vol. 131, issue 9–10, https://doi.org/10.1130/B32039.1.

Roots, C.F., 1990. New geological maps for the southern Wernecke Mountains, Yukon. In: Current Research Part E, Geological Survey of Canada, Paper 90-1E, p. 5–13.

Sinclair, A.J., 1981. Report on the Vera, South Rusty Mountain and Siltstone mineral occurrences. Yukon Energy, Mines and Resources Assessment Report 062146.

Sivertz, G.W., 1980. Assessment Report on Geology, Geochemistry and Drilling at Val 1-318 Claims 1980. Yukon Energy, Mines and Resources Assessment Report 090511.

Strauss, J.V., MacDonald, F.A., Halverson, G.P., Tosca, N.J., Schrag, D.P. and Knoll, A.H., 2015. Stratigraphic evolution of the Neoproterozoic Callison Lake Formation: Linking the break-up of Rodinia to the Islay carbon isotope excursion. American Journal of Science, vol. 315, p. 881–944, https://doi.org/10.2475/10.2015.01.

Thorkelson, D.J., 2000. Geology and mineral occurrences of the Slats Creek, Fairchild Lake and "Dolores Creek" areas, Wernecke Mountains, Yukon Territory (106D/16,106C/13, 106C/14). Exploration and Geological Division, Yukon Region, Indian and Northern Affairs Canada, Bulletin 10, 73 p.

Thorkelson, D.J., Abbott, J.G., Mortensen, J.K., Creaser, R.A., Villeneuve, M.E., McNicoll, V.J. and Layer, P.W., 2005. Early and Middle Proterozoic evolution of Yukon, Canada. Canadian Journal of Earth Sciences, vol. 42, p. 1045–1071, https://doi.org/10.1139/e04-075.

Turner, E.C., 2011. Stratigraphy of the Mackenzie Mountains supergroup in the Wernecke Mountains, Yukon. *In:* Yukon Exploration and Geology 2010, K.E. MacFarlane, L.H. Weston and C. Relf (eds.),Yukon Geological Survey, p. 207–231.

Verbaas, J., Thorkelson, D.J., Milidragovic, D., Crowley, J.L., Foster, D., Daniel Gibson, H. and Marshall, D.D., 2018. Rifting of western Laurentia at 1.38 Ga: The Hart River sills of Yukon, Canada. Lithos, vol. 316–317, p. 243–260, https://doi.org/10.1016/j.lithos.2018.06.018.

Wallace, M.W., Both, R.A., Ruano, S.M., Fenoll Hach-Ali, P. and Lees, T., 1994. Zebra textures from carbonate-hosted sulfide deposits; sheet cavity networks produced by fracture and solution enlargement. Economic Geology, vol. 89, p. 1183–1191, https://doi.org/10.2113/gsecongeo.89.5.1183.

Waugh, D.H., 1989. A Preliminary Diamond Drilling and Trenching Report on the Val-Vera Quartz Claims (Rusty Mountain-Kathleen Lakes Area). Yukon Energy, Mines and Resources Assessment Report 092725.

W. G. Timmins Exploration & Development Ltd., 1983. Summary Report on the Val-Vera Property: Kathleen Lakes, Yukon Territory. Yukon Energy, Mines and Resources Assessment Report 062185.

Yeo, G.M., 1978. Iron-formation in the Rapitan Group, Mackenzie Mountains, Yukon and Northwest Territories. DIAND Mineral Industry Report, Economic Geology Series 1978-5, p. 170–175.

Yeo, G.M., 1981. The Late Proterozoic glaciation in the northern Cordillera. *In:* Proterozoic basins of Canada, F.H.A. Campbell (ed.), Geological Survey of Canada, Paper 81-10, p. 25–46.

Yukon MINFILE, 2019. Yukon MINFILE – A database of mineral occurrences. Yukon Geological Survey, https://data.geology.gov.yk.ca, [accessed November 2019].

New mineral potential mapping methodology for Yukon: Case studies from the Beaver River and Dawson regional land use planning areas

W. Bullen*
Yukon Geological Survey

Bullen, W., 2020. New mineral potential mapping methodology for Yukon: Case studies from the Beaver River and Dawson regional land use planning areas. *In:* Yukon Exploration and Geology 2019, K.E. MacFarlane (ed.), Yukon Geological Survey, p. 23–42.

Abstract

Territory-wide mineral potential mapping in Yukon was last conducted 18 years ago. An updated suite of maps for land use planning is, therefore, necessary. Yukon Geological Survey has developed a new GIS-based mapping process for this purpose. Industry-based applications using the new method will be developed going forward.

The approach makes use of mineral system components that potentially contribute to metal accumulations in an area. The method is a hybrid between a classic data-driven probabilistic approach and an expert-driven fuzzy logic approach. It is non-specific in terms of commodity and/or deposit type–however, the claim and assessment report footprint data that are integral to the mapping process capture these important components.

The procedure makes use of block modeling techniques where each block is assigned a prospectivity and (bedrock mapping) confidence score. Calculations are based on the presence or absence of categorical features within unit cells, and the scores represent the posterior favourability of each cell. Evidential layers are weighted according to buffer distance and/or through the application of knowledge-based factors. Lithology classes are factored using a multiclass weights-of-evidence approach.

Mineral potential and confidence scores are converted to either a 1, 2 or 3 according to a defined mathematical schema. The values are then combined–blocks with scores of 1:1 have the lowest mineral potential/lowest confidence whereas blocks with scores of 3:3 have the highest mineral potential/highest confidence. Nine possible combinations exist. Mineral potential maps containing measures of both potential and confidence are generated based on the cumulative contrast values.

Areas cut by major structures along which significant displacement has occurred need to be evaluated separately, and then stitched back together at the end of the assessment process. Concurrently, the mineral potential data need to be levelled to account for prospectivity differences across the structure concerned.

* warwick.bullen@gov.yk.ca

Introduction

After a five-year hiatus, the Yukon Government is getting back into land use planning. The Beaver River watershed and Dawson regional land use plans (BRLUP and DRLUP, respectively; Fig. 1) are currently underway. The BRLUP was initiated in response to a proposal from ATAC Resources for the construction of an all-season, single-lane tote road from the existing Hanson Lakes road to the Tiger deposit located on the Rau property. The original completion date for the BRLUP was March 31, 2020; however, the date has been pushed back to November 2020.

Land use planning for the Dawson region commenced in 2011 but was suspended in 2014. During this time, the commission consulted on, and drew up, a comprehensive resource assessment report, generated a number of plan alternatives, and commenced work on a draft land use plan. Planning recommenced in early 2019 with the establishment of a new commission. The (revised) terms of reference of the reconstituted commission call for the completion of a Recommended Plan by March 2021 and a Final Recommended Plan by September 2021.

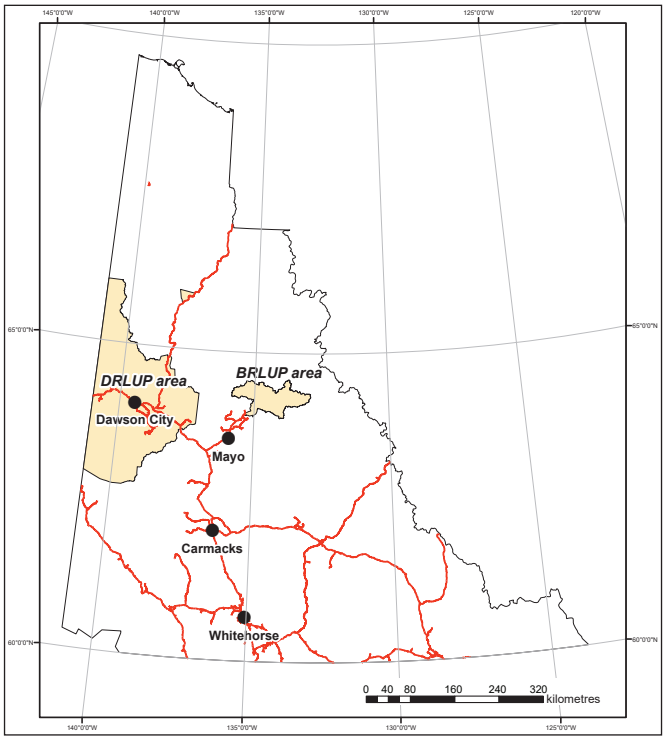


Figure 1. *Map of Yukon illustrating the boundaries of the BRLUP and DRLUP areas.*

Mineral potential mapping in Yukon

Previous mapping

Territory-wide mineral potential mapping for Yukon was last carried out over the period 1999 to 2001 (Bradshaw and VanRanden, 2003). The mapping was conducted using a quantitative method for prediction of undiscovered deposits developed by the United States Geological Survey (USGS) and first described by Singer (1993). Popularly known as the "three-part method for quantitative mineral resource assessment", it is based on mineral deposit models described by Cox and Singer (1986) and their probability of being hosted in a particular geological environment. To better accord with the metallogenic setting of the southern Canadian Cordillera (Lefebure and Ray, 1995; Lefebure and Hoy, 1996) the mineral deposit models used for the Yukon assessment were modified and added to by the British Columbia Geological Survey. To ensure all deposits in the territory were incorporated (Fonseca and Bradshaw, 2005) further modifications were made to the deposit models for the Yukon assessments.

Systems-based mineral potential mapping

Earlier mineral potential maps are now considered dated given advances in both Yukon Geological Survey (YGS) work and industry exploration. An updated suite of maps is, therefore, necessary for land use planning in the territory to ensure decisions are based on the most current data available, particularly in respect of the pending BRLUP and DRLUP. Furthermore, to be effective, design of the mineral potential maps should resonate with land use planning stakeholders. This is important as overly complicated representations of mineral potential data, or maps that do not appear spatially logical to land use planners, may not gain the necessary traction in the land use planning process.

Mineral potential maps of the territory should:

1. Be simple, easy to understand and easy to relate to.
2. Minimize subjective input to the extent possible.
3. Be based primarily on actual rather than hypothesized data. In practice, this means moving

away from the three-part, deposit model-based method where the primary inputs are subjective estimations of mineral occurrence probability. Mineral potential mapping for land use planning should, in any event, not focus on deposit models as their predictive power is limited at larger scales (McCuaig and Hronsky, 2014), as required by land use planners. Deposit models focus on features at the deposit scale with the deposit model approach ascribing equal probability to the presence of deposits of all possible sizes in a geologically favorable tract. Additionally, the evidence suggests that larger mineral deposits tend to be discovered first with later discoveries being smaller in size (Ellefsen, 2019). According to Ellefsen, such "size biased" sampling may have "adversely affected the resource predictions of previous U.S. Geological Survey assessments that were conducted with the three-part method". There are other potential problems with using deposit types for mineral potential mapping:

   a. missing deposits or generating "false positives" given too strict a focus on the analogue;
   b. the ongoing generation of additional model variations for the same commodity as new deposits in different settings are discovered; and
   c. the inability of deposit models to distinguish large and/or high quality occurrences from small and/or low quality ones (McCuaig and Hronsky, 2014).

4. Differentiate between mineral potential categories in a clear, transparent, and mathematically defined manner.
5. Contain mathematically defined measure(s) of confidence in relation to the mineral potential categories in order to facilitate land use planning decisions.
6. Be presented as a single map to avoid confusion.

To this end, YGS has developed a generalized mineral system approach to prospectivity mapping for land use planning. The process is based on actual data, and while the amount, quality and vintage of data in different parts of Yukon varies, the fundamental principles utilized in prospectivity mapping going forward will remain the same to ensure uniformity and consistency of output.

The generalized mineral system approach adopted by YGS makes use of mineral system components that may contribute to the development of metal accumulations in an area, in this case the area in which land use planning activities are taking place. Although conceptually similar to the mineral systems-based exploration targeting approach advocated by McCuaig and Hronsky (2014), the YGS method has been explicitly designed to accommodate land use planners in the territory. It is non-specific in terms of commodity (suite) and/or deposit type continuums, hence the generalized designation. These important components are fully captured, however, in the Placer/Quartz claim and assessment report footprint data that is integral to the mapping process. YGS has embarked on the process to develop the method such that the focus shifts to private sector applications. Commodity suite and deposit type continuums, together with newly developed features, will form an important component of these applications.

Wyborn *et al.* (1994), in a seminal paper, defined mineral systems as "all geological factors that control the generation and preservation of mineral deposits, and stress the processes that are involved in mobilizing ore components from a source, transporting and accumulating them in a more concentrated form and then preserving them throughout the subsequent geological history". The authors list the important controlling geological factors as sources of mineralizing fluids and transporting ligands, sources of metals, fluid migration pathways, energy sources and thermal gradients, focusing mechanisms (mechanical/structural), and precipitation mechanisms (chemical/physical).

Mineral potential mapping for land use planning in Yukon makes use of the above factors and incorporates additional criteria relevant to the prospectivity of the area concerned:

1. the occurrence and spatial distribution of known mineral deposits/mineralization;
2. aeromagnetic geophysical data;
3. claim data (Placer and Quartz, current and historical), the rationale being that resource companies stake ground deemed, after careful study, to be prospective for the minerals being sought. Companies also take practical (*i.e.*, economic) and political (*i.e.*, prevailing and probable future sentiment around commodity type) considerations into account when staking ground;

4. assessment report footprints, in order to highlight areas lying within claim boundaries that are considered more prospective than the claim as a whole; and
5. stream sediment sample data, the rationale being that watersheds upstream of anomalous sample data are potentially prospective for the metal(s) concerned.

The assessments use geophysical data, in the form of airborne magnetics, primarily implicitly–in the sense that other inputs, (faults, folds, bedrock contacts) are based on/corroborated by this information. The airborne magnetic data however, is used explicitly to assess the possible extent of the influence of plutonic intrusions on surrounding rocks.

New mapping principles employed by YGS

Mineral potential maps have been completed for the BRLUP and DRLUP areas using ArcGIS. The maps are based on quantifiable, spatially referenced categorical features buffered and/or weight-factored as required using a knowledge-based approach. The process is iterative in nature and relies on existing rather than hypothetical data.

The procedure makes use of block modeling techniques where each block (unit cell) is assigned a prospectivity score and, separately, a confidence score. Scores are calculated based on the presence or absence of categorical features within unit cells and represent the posterior favourability of each unit cell relative to other unit cells. The posterior favourability refers to mineral potential and confidence scores after all evidence has been taken into account. Evidential layers are weighted according to buffer distance and/or through the application of knowledge-based factors. Lithology classes are an exception–these features are factored using a multiclass weights-of-evidence (WofE) approach with known mineral deposits used as training points.

The process thus differs to pure data-driven mineral prospectivity mapping, where known mineral deposits are used to establish the relative importance each input (evidential) layer plays in the outcome. In data-driven mapping, the "weight" of each input layer is established using the spatial relationship between mineral deposits, referred to as the training population or data set, and evidential map features. Mineral potential maps generated by YGS, on the other hand, are based on cumulative contrast values (*i.e.*, the relative, between-block, prospectivity and confidence score totals).

The method is somewhat of a hybrid between a classic data-driven probabilistic WofE approach (which uses a binary value assessment, *i.e.*, 0/1) and an expert-driven fuzzy logic approach, the latter providing the advantage of allowing the user to assign a membership value anywhere between 0 and 1 (*i.e.*, 0, 0.01, 0.02,...0.98, 0.99, 1) for any predictive input parameter. This also allows for the integration of continuous data where, for example, the weighted importance of 'buffer' distance from a certain feature may be expressed in numerical terms.

While some similarities exist between data/knowledge-driven mapping methodologies and the mineral potential assessment process adopted by YGS, the YGS approach differs in a number of key respects and has been designed to fulfil a different function. The process does not rely, in contrast to standard WofE mapping, on training data, which may be lacking in less well-mapped/explored areas. A second important advantage is that the process is independent of the number of parameters (categorical features) entered. Parameters may vary from one (in theory) to as many as might be deemed relevant by the user. The resulting output is fundamentally useful irrespective of the number of parameters used; standard mineral prospectivity mapping methodologies can also generate output from just one or two predictor maps, although the results from such an exercise tend to be inaccurate and of limited use. A third difference relates to practicality and ease of use, and the fact that the method is dynamic–*i.e.*, new/revised/updated spatial data can be input as soon as it becomes available and the mineral potential map updated at short notice. Finally, the method itself does not require the generation of complex models or processing steps, and as such can be used by anyone with a moderate understanding of GIS software. However, expert knowledge is required to generate meaningful outcomes and this input is integral to the entire process.

Factors and buffers are an important fuzzy logic (*i.e.*, non-Boolean) component of the mineral potential mapping process. The choice of buffer distance in the case of point, line (and less commonly polygonal) data, and the selection of weighting factors in the case of polygonal data, is critical to a successful outcome. Expert input is key in this respect.

New mapping methodology

Mineral potential and confidence

The YGS has a detailed procedure for determining mineral potential. The steps involved are laid out in order below. Several of the steps are iterative, and some of the inputs, while adequate, are known to be imperfect–notably with regard to confidence. This aspect will be improved on in future maps.

1. All available geological information pertaining to the area of interest (AOI) is captured in a standard GIS environment either as polygons (*e.g.*, favorable host lithology, zones of hydrothermal alteration, watersheds), polylines (*e.g.*, thrusts, faults, fold axes) or points (*e.g.*, mineral deposits). As noted above, the procedure is independent of the amount of geological information available. However, quality of information is critical and data, as it pertains to mineral systems, is considered key.
2. The AOI includes the assessment area itself (*i.e.*, the BRLUP and DRLUP areas) plus a zone around it that may have a bearing on the mineral potential within the planning area. An exception occurs when planning boundaries are coincident with Yukon borders, an example being the western margin of the DRLUP area that marks the boundary between Yukon and Alaska.
3. The AOI is then subdivided into blocks of equal size using an ArcGIS fishnet overlay–a 2 by 2 km polygon grid was used in the BRLUP and DRLUP areas (Fig. 2). The grid forms the basis for the computational process so it is important that grid dimensions are neither too large (will cause excessive smoothing of the mineral potential scores) or too small (results in very long computational times without meaningful enhancements to the overall mineral potential profile of the AOI). The underlying logic to the gridding process is a follows:
   a. if the AOI is encompassed by a single grid square, then the mineral potential of the AOI will be represented by a single score (the overall or average mineral potential) and the entire area will be, for example, highly prospective, moderately prospective, *etc.* Such a map would be of no use to land use planners, as they must be able to distinguish between areas of differing mineral potential to be able to make decisions;
   b. subdividing the AOI into four grid squares, for example, has no effect on the overall mineral potential, but results in contrasting scores for each of the four blocks. While there is a non-linear relationship between the four mineral potential scores, the overall score remains static; and

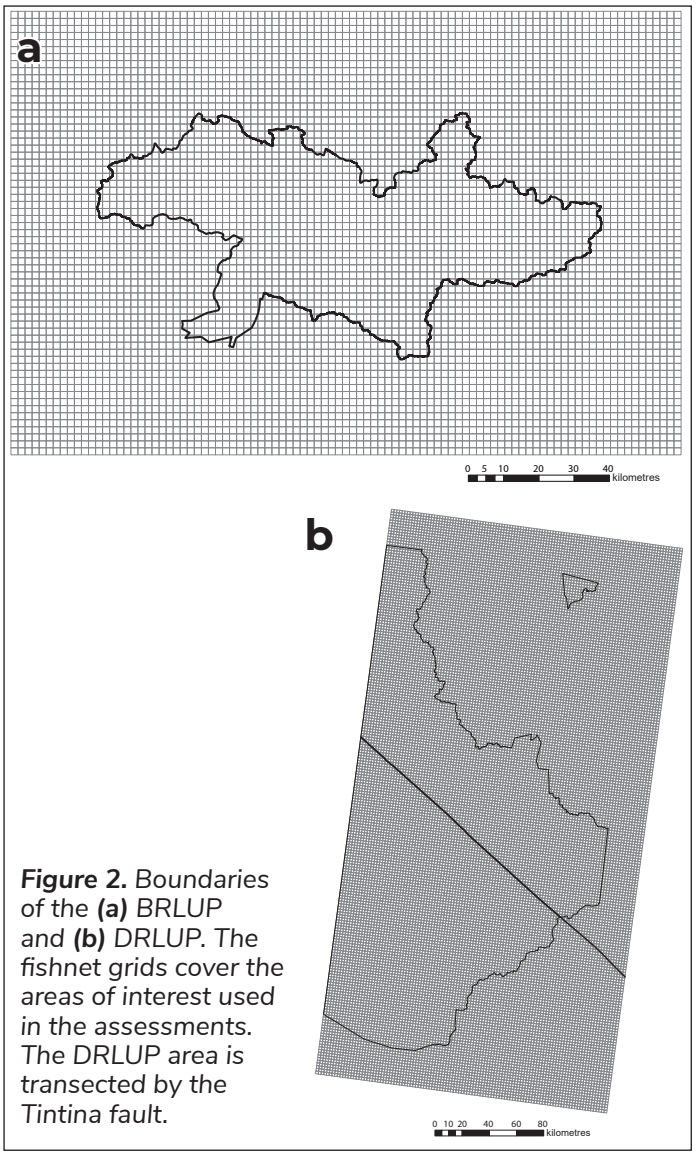


Figure 2. *Boundaries of the* **(a)** *BRLUP and* **(b)** *DRLUP. The fishnet grids cover the areas of interest used in the assessments. The DRLUP area is transected by the Tintina fault.*

c. continued subdivision of the AOI into smaller and smaller grid squares results initially in more detailed and practically useful prospectivity scores. However, once the block size drops below a certain threshold, prospectivity scores in areas of similar potential start to repeat themselves as the contrast between the data elements informing those scores becomes less pronounced.

Different grid sizes were applied to the Beaver River watershed to assess the impact of cell size variation on prospectivity score maxima and the average number of categorical elements used to calculate block potential. The following grid sizes were applied: 8 × 8 km, 7 × 7 km, 6 × 6 km, 5 × 5 km, 4 × 4 km, 3 × 3 km, 2 × 2 km, 1 × 1 km, 500 × 500 m and 250 × 250 m. The following metrics were used to quantify the impact:

a. the ratio of the highest block score to the lowest for each grid size; and
b. the between grid differences of the average of the number of elements used to calculate each cell's prospectivity score divided by that cell's block score.

Figure 3 depicts the outcome.

For block score ratios, there is a natural break in values at a grid size of 3 km, at which point the ratios increase markedly. The scores level out again, at a significantly higher level, at a grid size of 1 km. For the average of the number of elements divided by the block potential metric there is a natural break at a grid size of 2 km with values appearing to level out below 1 km. Based on these metrics, a 2 × 2 km grid size was chosen. It is suggested, however, that a 1 × 1 km grid might be more applicable for smaller-scale industry-sector targeting purposes. In any event, grid sizes below 1 km require excessive computational times making their use impractical from both a land use planning and targeting perspective.

4. Data are simplified to facilitate the assessments. For example, for the BRLUP area, bedrock geology was "dissolved" into similar lithologic/stratigraphic units, and unnamed, but clearly contiguous, fault segments were extrapolated, where necessary, into major (named) faults so that these structures were continuous. For the Dawson region, rock types were simplified and grouped based on rock class and subclass (the "Rock_CLASS" and "ROCK_SUBCL" fields, respectively, in the bedrock geology ArcGIS table; Table 1).
5. All point and line data are buffered to varying degrees in line with standard mineral potential mapping procedures (e.g., Porwal, 2006; Harris, et al., 2001; Schmitt, 2010). This is important because while this data is effectively dimensionless

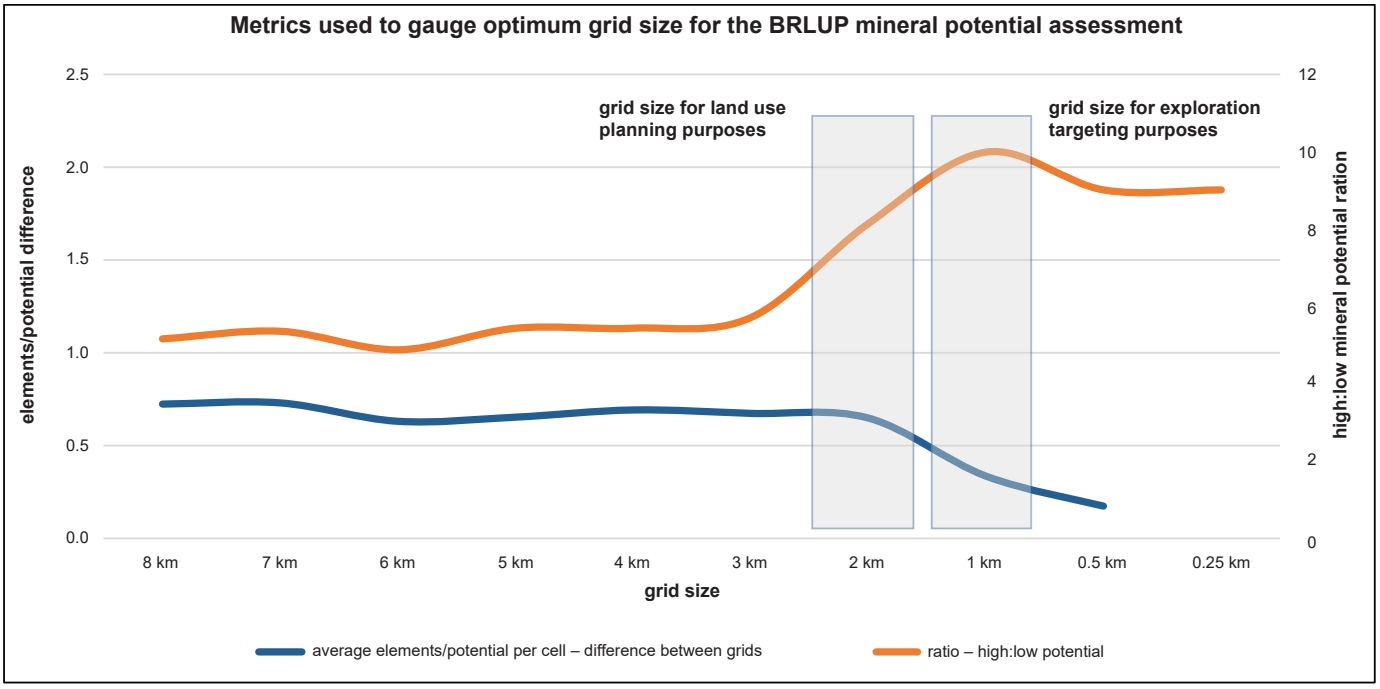


Figure 3. *Graph illustrating the ratio of the highest/lowest block scores for each grid size, and the between grid differences of the average of the number of elements used to calculate each cell's mineral potential score divided by that cell's score.*

Table 1. *Simplified bedrock geology for the BRLUP* ***(top)*** *and DRLUP* ***(bottom)*** *areas.*

Stratigraphic/lithologic simplification	Rock unit(s)
Cretaceous granite intrusions	LKM?, mKM
Phanerozoic volcanic/plutonic rocks	CSM, TrG
Phanerozoic sandstone/siltstone	TrJ, lmCS, PCB
Phanerozoic limestone/dolostone	CDB, CH, DB, DG, ICl, ICS, OSK, PJC, uCT
Phanerozoic shale ± other seds	CPMC, CT, DME, ICG, ODR
Proterozoic sandstone/shale/limestone	PCH
Proterozoic diorite/gabbro	mPH
Proterozoic black shale	lPQ, uPFl, uPS
Proterozoic siltstone/conglomerate	uPCl, uPP, uPR
Proterozoic limestone/dolostone	lPG, uPB, uPG, uPH, uPHC, uPN, uPRi

Rock class	Rock subclass
Sedimentary	Clastic
	Carbonate
	Clastic/carbonate
	Clastic/carbonate/chert
Volcanic	Hydrothermal
	Felsic/intermediate
	Mafic/ultramafic
Plutonic	Felsic/intermediate
	Intermediate/mafic
	Mafic/ultramafic
Metamorphic	Carbonate
	Clastic
	Mixed igneous/sedimentary
	Volcanic felsic/intermediate
	Volcanic mafic/ultramafic
	Plutonic felsic/intermediate
	Plutonic mafic/ultramafic

it has a strong influence on potential mineralization in 3D-space. The extent of buffering depends on the perceived mineral system "weight" of the data element concerned. For example, in the case of mineral deposits, the buffer distance is based on deposit status (Table 2). Once completed, all point and line data are represented as polygons, the relative size of each class feature component being a function of its perceived importance vis-à-vis the mineral system concept.

6. Factors are applied to polygonal data if deemed necessary to account for the perceived "weight" of the various class feature components relative to mineral systems generally (in certain instances) and critically, to each other. For example, for the Beaver River area, lithology/stratigraphic bedrock geology "packages" were weighted (factored) downwards or upwards depending on, among other things, their perceived favorability for mineralization, possible source of metals, heat engines, etc. For the Dawson region, rock subclasses were assigned a factor using a multiclass WofE approach, with known mineral occurrences used as training data. A unit cell size of 4 km^2 was used, equivalent to the fishnet grid size, with each deposit assumed to occupy one cell.

   Calculation of quantities used to estimate the WofE were as follows:

   a. Number of cells in the AOI occupied and not occupied by a deposit.
   b. Number of cells occupied and not occupied by each rock subclass.
   c. Number of cells within each rock subclass occupied and not occupied by a deposit.
   d. Number of cells outside each rock subclass occupied and not occupied by a deposit.

   W^+ and W^- pairs for each class feature (*i.e.*, rock subclass) were estimated using Bayes' theorem (*e.g.*, Harris, et *al.*, 2001; Porwal, 2006). For each class feature, positive weights indicate that more deposits are associated with the class than simply due to chance, with the inverse applying to negative weights (Raines, et *al.*, 2000).

   Contrast values, *i.e.*, $W^+ – W^-$, were calculated for each class feature. This metric provides an overall measure of the spatial association between the rock subclass and mineral deposits. The contrast values were converted to a standardized normal distribution and factors were determined based on the deviation of the normalized contrast value from the mean (ranging from 1.5 for deviations greater than +2 standard deviations (StDev) to 0.5 for deviations less than –2StDev; Table 2).

Table 2. *Class elements, factors and buffers used in the BRLUP and DRLUP mineral potential assessments.*

Dawson region

	Rock subclasses*		Factor	Buffer	Rationale
north of Tintina fault	Felsic to intermediate, igneous plutonic rocks of Jurassic age and younger		1	4000 m	Estimate of potential influence of intrusion away from contact from aeromagnetic surveys.
	Sedimentary	Carbonate	0.9	none	Using a multiclass WofE approach (see text for explanation), factors determined as follows:
					StDev > 2.0 = 1.5
		Clastic	0.8		1.5 < StDev ≤ 2.0 = 1.4
		Clastic/carbonate	0.8		1.0 < StDev ≤ 1.5 = 1.3
		Clastic/carbonate/chert	0.9		0.5 < StDev ≤ 1.0 = 1.2
	Volcanic	Hydrothermal	1.3		0.0 < StDev ≤ 0.5 = 1.1
		Felsic/intermediate	0.6		-0.5 < StDev ≤ 0.0 = 0.9
		Mafic/ultramafic	0.9		-1.0 < StDev ≤ -0.5 = 0.8
	Plutonic	Felsic/intermediate	1.3		-1.5 < StDev ≤ -1.0 = 0.7
		Intermediate/mafic	1.3		-2.0 < StDev ≤ -1.5 = 0.6
		Mafic/ultramafic	1.2		-2.0 > StDev = 0.5
south of Tintina fault	Felsic to intermediate, igneous plutonic rocks of Jurassic age and younger		1	4000 m	Estimate of potential influence of intrusion away from contact from aeromagnetic surveys.
	Sedimentary	Clastic	1.1	none	Using a multiclass WofE approach (see text for explanation), factors determined as follows:
	Volcanic	Felsic/intermediate	0.8		StDev > 2.0 = 1.5
		Mafic/ultramafic	0.9		1.5 < StDev ≤ 2.0 = 1.4
	Plutonic	Felsic/intermediate	1.1		1.0 < StDev ≤ 1.5 = 1.3
		Mafic/ultramafic	0.9		0.5 < StDev ≤ 1.0 = 1.2
	Metamorphic	Carbonate	0.7		0.0 < StDev ≤ 0.5 = 1.1
		Clastic	0.9		-0.5 < StDev ≤ 0.0 = 0.9
		Mixed igneous/sedimentary	1.4		-1.0 < StDev ≤ -0.5 = 0.8
		Volcanic felsic/intermediate	0.9		-1.5 < StDev ≤ -1.0 = 0.7
		Volcanic mafic/ultramafic	1.1		-2.0 < StDev ≤ -1.5 = 0.6
		Plutonic felsic/intermediate	0.8		-2.0 > StDev = 0.5
		Plutonic mafic/ultramafic	1.4		

Beaver river watershed

Stratigraphy/lithology	Factor	Buffer	Rationale
Cretaceous granite intrusions	1	5000 m	Width of Rau intrusive contact aureole as mapped.
Phanerozoic volcanic/plutonic rocks	1.1	None	Estimated relative importance to mineralizing process (observational/knowledge-based).
Phanerozoic sandstone/siltstone	0.5		
Phanerozoic limestone/dolostone	1.5		
Phanerozoic shale ± other seds	1.3		
Proterozoic sandstone/shale/limestone	1		
Proterozoic diorite/gabbro	1.1		
Proterozoic black shale	1.3		
Proterozoic siltstone/conglomerate	0.3		
Proterozoic limestone/dolostone	1.5		

Beaver River watershed and Dawson region

Deposit type	Buffer	Rationale
Past producer/producer	2000 m	Estimated relative importance of categorical features
Deposit	1000 m	
Anomaly/drilled prospect/prospect	500 m	
Showing	250 m	
Staked – no work recorded/Unknown	100 m	

Beaver River watershed and Dawson region

Fault category	Buffer	Rationale
Tintina	2000 m	Estimated relative importance of categorical features
Major	1000 m	
Minor	500 m	

Beaver River watershed

Fold category	Buffer	Rationale
Major	500 m	Estimated relative importance of categorical features
Minor	250 m	

Beaver River watershed

	Claim category	Factor	Buffer	Rationale
placer claims not material to assessment	Historic Quartz and Placer claims	0.5	None	Previously staked, not re-staked.
	Current Quartz and Placer claims	0.75		Not upgraded to higher class.
	Current Quartz and Placer claims – Class 3	1		Prospective.
	Current Quartz and Placer claims – Class 4	1.5		Highly prospective.
	Current Quart claims – Class 5	2		Potentially economic.
	Assessment report footprints (dissolved)	1		Superimposed on current/historical claims.

Dawson region

	Claim category	Factor	Buffer	Rationale
placer: claims highly material to assessment, factors increased accordingly	Historic Placer claims	1	None	Previously staked, not re-staked.
	Current Placer claims (incl. mineral lease and lake)	1.5		Not upgraded to higher class.
	Current Placer claims – Class 3	2		Prospective.
	Current Placer claims – Class 4	2.5		Highly prospective.
	Assessment report footprints (dissolved)	1		Superimposed on claims.
quartz: numerous advanced projects, factors increased accordingly	Historic Quartz claims	1		Previously staked, not re-staked.
	Current Quartz claims (incl. mineral lease)	1		Not upgraded to higher class.
	Current Quartz claims – Class 2	1.25		Known to be prospective.
	Current Quartz claims – Class 3	1.5		Known to be significantly prospective.
	Current Quartz claims – Class 4	1.75		Known to be highly prospective.
	Current Quart claims – Class 5	2		Potentially economic.
	Assessment report footprints (dissolved)	1		Superimposed on current/historical claims.

Stream sediment geochemistry

	Commodity	Factor	Buffer	Rationale
Beaver River watershed	Ag	1	None	Upstream watershed polygons cover anomalous area, no factor or buffer required. Thresholds calculated at 2 StDev's.
	Au			
	Cu			
	Pb			
	Zn			
	W			
Dawson region	Ag	1	None	Upstream watershed polygons cover anomalous area, no factor or buffer required. Thresholds calculated graphically using histograms, resultant threshold percentiles for Ag, Au, Cu, Mo, Ni, Pb, W and Zn = 98, 96, 98, 97, 98, 98, 97 and 97, respectively. Re-assayed data used for area south of the Tintina fault; re-assayed plus original assay data used for area north of the Tintina fault (latter used where re-assayed data not available). For the original assays, instrumental neutron activation "INA" data used when available (superior detection limits). Watershed polygons not available for extreme northwest portion of DRLUP area.
	Au			
	Cu			
	Mo			
	Ni			
	Pb			
	W			
	Zn			

Dawson region

Placer potential	Factor	Buffer	Rationale
Probability 5	5	500 m	From Placer Gold Potential Map (J Bond), estimated relative significance of probability categories.
Probability 4	4	400 m	
Probability 3	3	200 m	
Probability 2	2	100 m	
Probability 1	1	50 m	

The application of factors to bedrock geology is an important component of the mineral potential assessment process. For example, while many mineral deposits may be structurally hosted, or spatially associated with structures, lithology plays a critical role in determining whether the structures will be mineralized, notably in terms of competency and/or chemical reactiveness of the host. The Keno Hill silver district serves to illustrate this point. While the silver mineralization is clearly structurally hosted, there is a marked spatial association with quartzite rocks of the Keno Hill Quartzite Formation. A multiclass bedrock WofE estimation for this area would ascribe positive factors to these rocks as expected (and required).

In addition to applying bedrock factors, felsic to intermediate, mainly Cretaceous and younger, igneous plutonic rocks in the Dawson and Beaver River areas were buffered to account for the potential influence of these intrusive rocks on mineralization in surrounding rocks–in terms of both fluid supply and source of metals. Intrusive rocks in the Beaver River area were buffered by 5,000 m in line with the mapped extent of the contact aureole around the Rau intrusive. In the Dawson region, Jurassic and younger intrusive rocks were buffered by 4,000 m, based on an assessment of the aeromagnetic geophysical data available for the area.

7. The area of each fishnet grid square occupied by each class element polygon (using the "intersect" function in ArcGIS) is then calculated. This process takes the buffers, but not the factors, into account. Multiple instances of the same class feature occurring within a single grid square are captured separately (*i.e.*, as separate records)–e.g., different mineral deposit status types. In addition, intersections between same-class polygons within a grid square (e.g., mineral "showings") give rise to new polygons, which are captured as separate records. This "reinforcement" process is a required outcome as it takes into account the cumulative effect of the clustering of discrete, closely spaced categorical features within unit cells. For example, if two mineral "deposits" occupy the same grid square, their buffered areas will likely intersect. This will give rise to four records within the intersect table:
   a. the buffered area of the first deposit minus the intersection with the second deposit;
   b. the buffered area of the second deposit minus the intersection with the first deposit; and
   c. the area of the intersection between deposits one and two (with one of the records relating to deposit one, and the other to deposit two).
8. The proportion of each grid square occupied by each class feature polygon is then calculated. This is done by dividing the area occupied by each class element polygon by the grid area (4 km^2 in the case of the Beaver River and Dawson region areas) and multiplying the outcome by the class feature factor, if relevant–*i.e.*, when the factor is either greater or lesser than one.
9. The various attribute tables are then dissolved for simplification purposes if need be, keeping, at minimum, the grid square (fishnet) IDs, the class feature names, and the calculated proportion fields.
10. The dissolved tables are then merged into a single table. Each record in the merged table, which will consist of tens to hundreds of thousands of records, contains, among other things, the proportion data for each polygon class feature present in each grid square.
11. The various class feature proportions within each grid cell are then summed using the summary statistics function in ArcGIS. The StDev of class feature proportions within each grid cell is calculated at the same time–this parameter allows for the calculation of block standard errors (StErr) which are a potentially useful confidence and block selection metric. A summary statistics table is generated with the output constrained against the fishnet polygon IDs. The resultant table contains one record for each fishnet polygon (grid square) with each record containing the sum (and StDev) of the class feature proportions within each square. The process is shown schematically in Figure 4.
12. The summary statistics table is then joined to the original fishnet polygon attribute table and a preliminary mineral potential map is created showing the fishnet polygons coloured according to the sum of the proportions calculated for each grid square (with warmer colours corresponding to higher values, etc.). The warmer colours, therefore, represent the prospective portions of the mineral potential map (and so on), and the output provides a first-pass overview of the mineral potential of the AOI as a whole. This map is used for initial verification purposes (figs. 5 and 6).
13. Mineral potential confidence is then assessed. Two measures are used for this purpose, namely

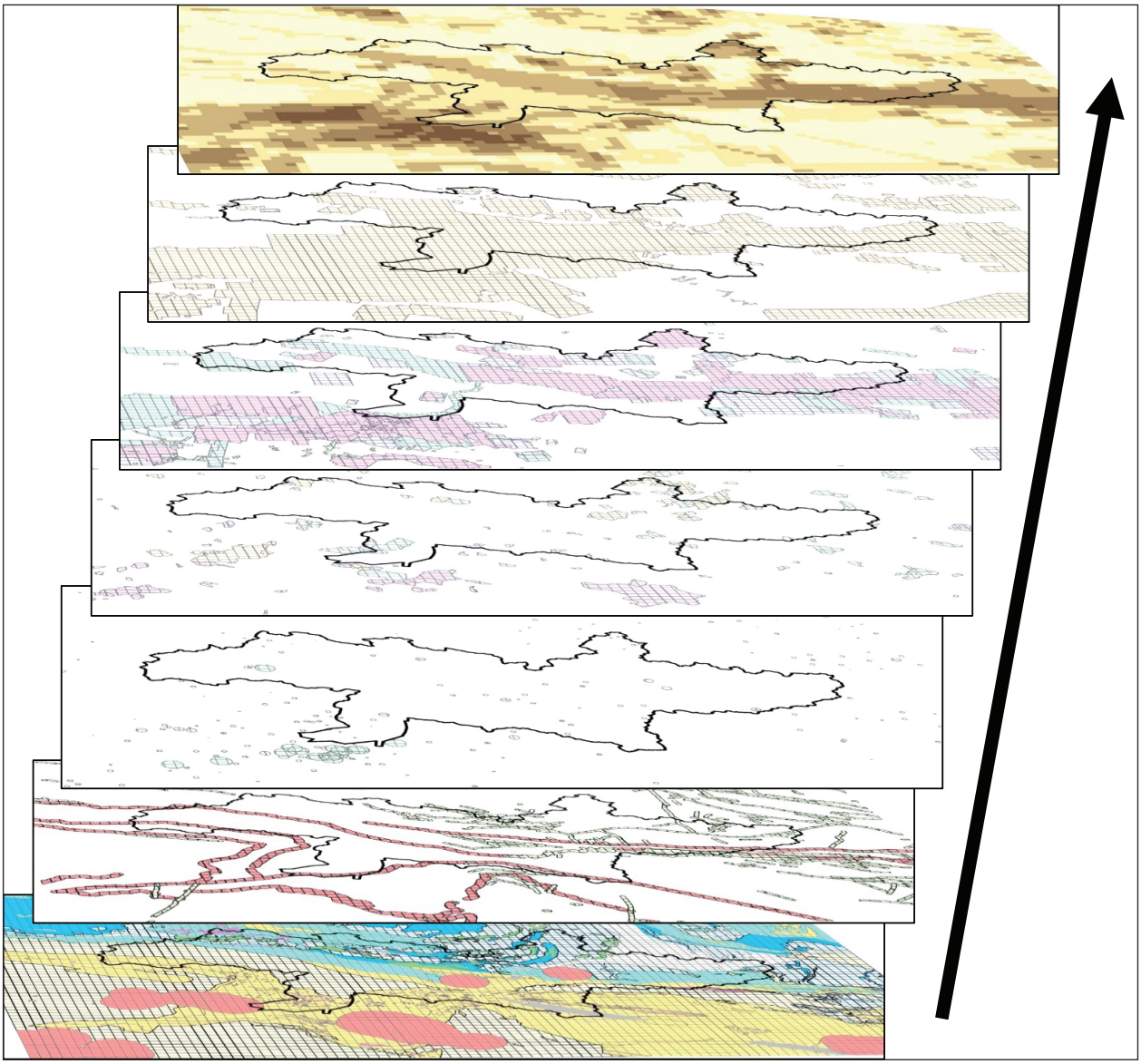


Figure 4. *Schematic representation of layers (simplified for presentation purposes) used to produce the Beaver River mineral potential map. More than 30 layers were used to produce the Beaver River map, while 92 were used to produce the Dawson Regional map.*

bedrock mapping confidence and block StErr. The bedrock mapping confidence metric is considered more appropriate for mineral potential maps for land use planning purposes, whereas both metrics are useful for maps produced for exploration targeting (*i.e.*, for industry use). Confidence metrics are required in order to distinguish between, well-mapped areas that might be deemed highly prospective from poorly mapped areas that might also be rated as highly prospective.

Bedrock mapping "confidence" for Yukon has been assessed based on the amount of mapping undertaken in an area and scores, ranging from one to six, assigned (with six being ascribed to the highest confidence areas and one to the least):

1 = unknown or poorly defined at any level (Supergroup/Group/Formation/ Member);
2 = mapped to the Supergroup level only;
3 = mapped to the Group level;
4 = mapped to the Formation level;
5 = mapped to the Member level; and
6 = mapped in sufficient detail to confirm and confine a mineralized horizon, either at the Member or Facies level.

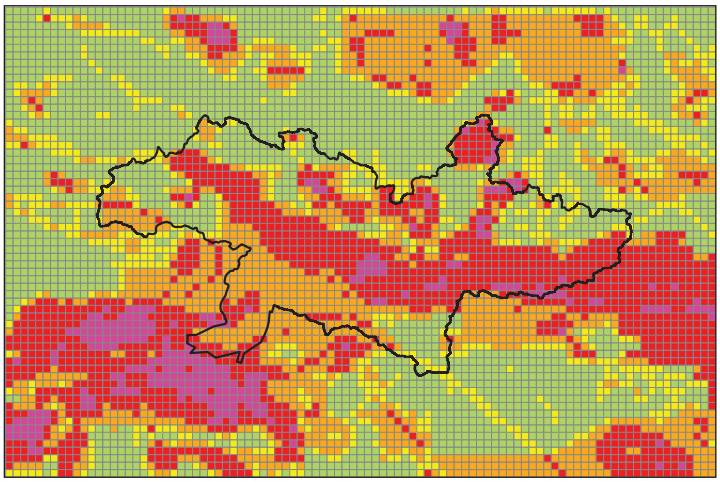


Figure 5. *Preliminary, fishnet-based, mineral potential map (excluding measures of confidence) for the BRLUP area of interest. ArcGIS-ascribed Jenks Natural Breaks used.*

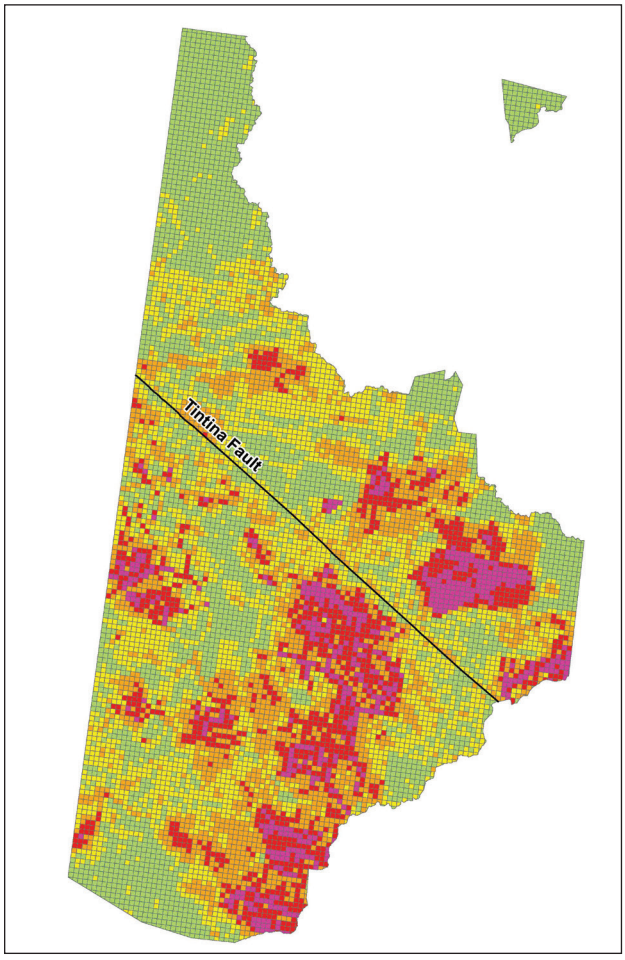


Figure 6. *Preliminary, fishnet-based, mineral potential map (excluding measures of confidence) for the DRLUP area of interest. ArcGIS-ascribed Jenks Natural Breaks used.*

For plutonic rocks, the following "confidence" schema has been introduced:

1 = undated, no geochemical data;
2 = undated, geochemical data;
3 = other dating method, no geochemical data;
4 = other dating method, geochemical data;
5 = zircon dating, no geochemical data; and
6 = zircon dating, geochemical data.

14. The procedure used to apportion the bedrock mapping confidence values to grid scores follows that described above–*i.e.*, the confidence scores for each rock unit within the AOI are incorporated into the fishnet grid using ArcGIS's intersect function and the proportions calculated accordingly (Fig. 7). No factors or buffers are used. The fishnet-based output for the Beaver River AOI is depicted in Figure 8, with the warmer colours representing areas of higher bedrock mapping confidence etc., as per the aforementioned methodology.

Claim and assessment report footprint data

Claim and assessment report footprint data represent an important store of intellectual capital and form an important component of the mineral potential mapping process. Companies and private individuals that stake claims do so on the basis of the perceived prospectivity for the commodities of interest to them. Staking is only done after considerable research and after due consideration of the practicalities concerned.

For example, consider a bulk tonnage commodity (e.g., an iron deposit) in an area with little to no infrastructure, or an "out-of-favor" commodity within the context of the prevailing political climate (e.g., coal or uranium). The mineral occurrences will reflect positively on the mineral potential map before claim data are taken into account. However, companies interested in these commodities will think twice before staking ground in this area as the likelihood of a return on investment, at any stage of the exploration/development phase, would be very low. Even if a company does elect to stake, the likelihood of upgrading claims to Class 3 or 4 status is even more improbable given the significant expense that would need to be committed to the program and the minimal return on investment that could reasonably be expected to accrue. Incorporating claim data in the mineral potential assessment would, therefore, downgrade the mineral potential of the area

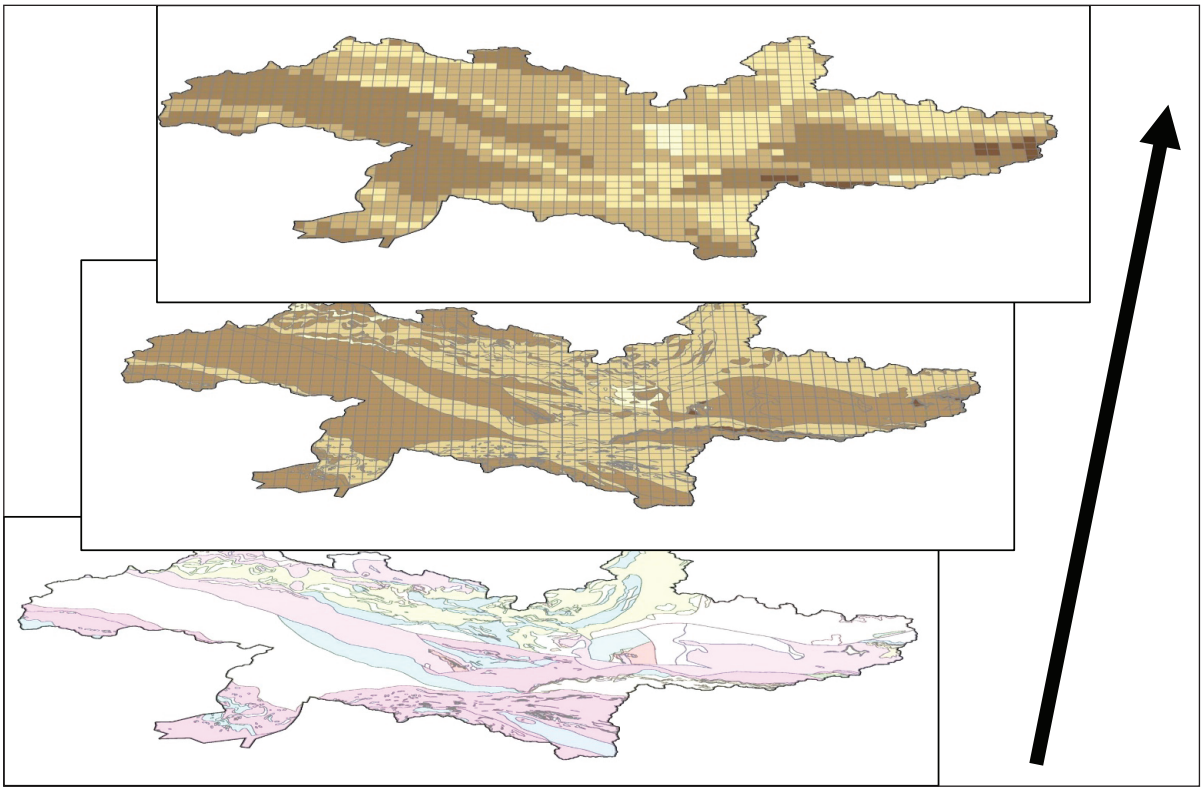


Figure 7. *Schematic representation of layers used to produce the bedrock confidence map for the Beaver River watershed and Dawson Regional mineral potential maps (simplified for presentation purposes).*

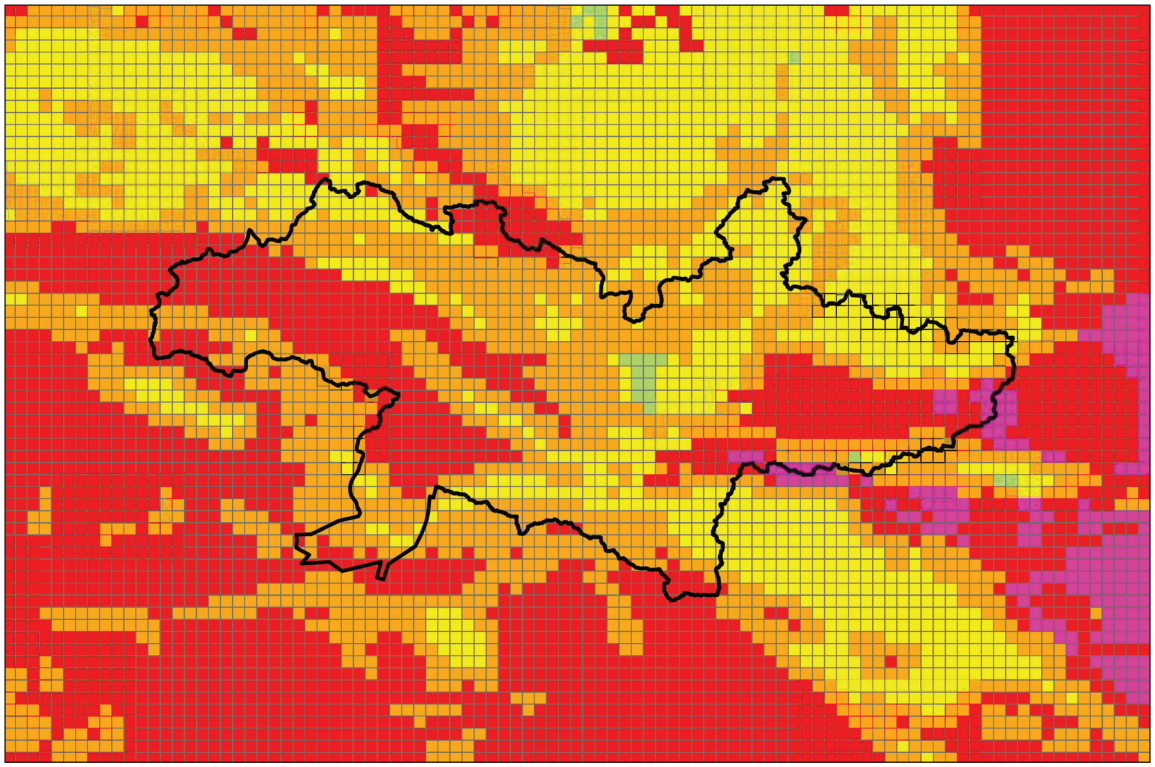


Figure 8. *Preliminary, fishnet-based, bedrock confidence map (excluding measures of mineral potential) for the BRLUP area of interest.*

encompassed by, in this example, the iron/uranium/coal mineralization, as the area would either not be staked, or contain no upgraded claims.

In contrast, claim data covering precious metal mineral deposits would have the opposite effect, reinforcing areas previously determined to be prospective using other data.

Obviating the edge effect

The assessment process for a mineral potential map ideally needs to include the actual assessment area plus a zone around it (*i.e.*, the AOI) for two reasons:

1. Areas of high (or low) mineral potential immediately adjacent to the assessment area influences the potential of the area itself. For example, the Keno area immediately southwest of the BRLUP is exceptionally prospective based on a number of factors. Cretaceous granite intrusions in this area, while lying outside the BRLUP, have a direct and materially positive impact on the prospectivity of the BRLUP and must, therefore, be taken into account when determining the area's mineral potential; and
2. Clipping the assessment area (prior to calculation of the final mineral potential and confidence scores) truncates the grid squares along the margin of the area. Polygon proportions in these marginal blocks will be reduced by the degree of truncation and the blocks will not, therefore, accurately reflect potential and confidence around the margins of the area. For example, a polygon occupying 100% of a block which has been truncated by 50% will be ascribed a proportion of 0.5, rather than 1. For that reason, assessment areas are clipped only right at the end of the assessment process, rather than at the beginning of, or during, the process.

Processing the mineral potential and confidence data

The mineral potential and bedrock mapping confidence data are clipped to the planning area itself and then exported to Excel for processing. The exported data contain, as a minimum, the summed proportions of the mineral potential categorical features for each fishnet square, and the bedrock confidence data for each fishnet square (expressed as a weighted average score when two or more confidence values are present in a square). The StDev for each fishnet square may also be exported, should the StErr be used as a measure of confidence.

The mineral potential and StErr (if used) confidence data are assessed for skewness. If the skewness is <-1 or >1 (*i.e.*, highly skewed) the data are transformed to reduce the distortion. For mineral potential, a log-transformation is suitable. Log-transformations for StErr data are not suitable given that StErr values of zero occur and log 0 is undefined. Consequently, a square root transformation is applied to StErr values for highly skewed data. Note that negatively skewed data must first be converted to positively skewed data prior to transforming by way of a reflection. The data can then be back-transformed for further processing if need be (or simply assessed as is in reverse).

The transformed mineral potential and StErr data are then converted to standardized normal distributions, each with a mean of zero and a StDev of one. The normalized scores for the mineral potential and StErr metrics are then assigned values of 1, 2 or 3:

1. Scores falling below a StDev of −1 are assigned a value of 1 (encompassing approximately 16% of the data, designated "Moderately prospective" in the final mineral potential map);
2. Scores falling between a StDev of −1 and +0.5 are assigned a value of 2 (approximately 53% of the data, designated "Significantly prospective" in the final mineral potential map); and
3. Scores falling above a StDev of +0.5 are assigned a value of 3 (approximately 31% of the data, designated "Highly prospective" in the final mineral potential map).

The weighted average scores for the bedrock mapping confidence metric are assigned values of 1, 2 or 3:

1. Block values ≤ 2.6665 (*i.e.*, lower third of values) are assigned a value of 1;
2. $2.6665 <$ Block values ≤ 4.3335 (middle third of values) receive a score of 2; and
3. $4.3335 <$ Block values (upper third of values) receive a score of 3.

The result is the conversion of mineral potential and confidence scores to either a 1, 2 or 3 according to a defined mathematical schema. The scores are then combined such that fishnet blocks with scores of 1:1,

for example, have the lowest mineral potential and the lowest confidence whereas blocks with scores of 3:3 have the highest mineral potential and the highest confidence. Combining the revised prospectivity and confidence scores will, therefore, give rise to (up to) nine possible combinations ranging from 3:3 (most potential, highest confidence) to 1:1 (least potential, lowest confidence). The combined scores are best understood when viewed graphically (Fig. 9).

The data, together with the associated scores, are imported from Excel into ArcGIS and joined to the fishnet attribute table. Two contour maps are then constructed using the normalized mineral potential scores and the confidence scores (*i.e.*, the 1, 2, 3 values). Three ArcGIS functions are implemented:

1. polygon to raster using a cell size of 250 m and the proportion and confidence as the value fields, respectively;
2. focal statistics, which calculates for each raster input cell location a statistic of the values within a specified neighborhood around it thereby helping to smooth the final contours (circle neighborhood, radius = 20 (raster pixels); and
3. contour, to create contours from the focal statistics raster grid (contour type = "CONTOUR_POLYGON"). A contour interval of 0.6667 and a base contour of 1 are selected. The process is shown schematically in Figure 10.

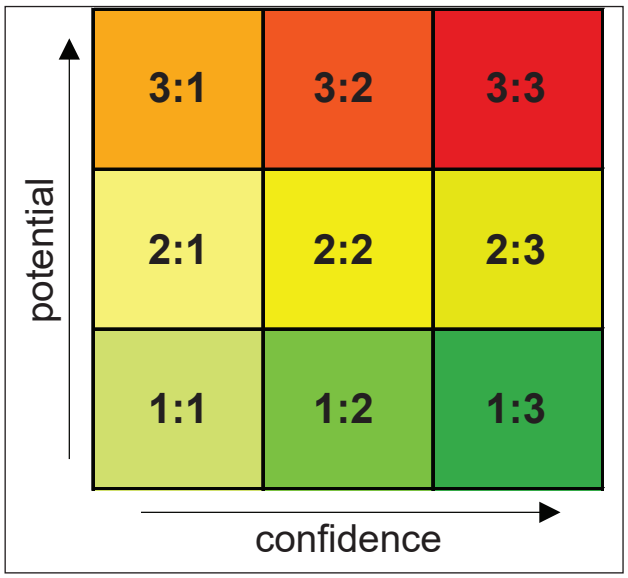


Figure 9. *Graphic representation of colour-coded mineral potential/confidence scores as used in YGS mineral potential maps. The colours are incorporated into the final map and the mineral potential and confidence metrics interpreted accordingly.*

The potential and confidence contour maps are then combined using the "union" function in ArcGIS. The result is a single map divided into polygons based on the different combinations of the mineral potential/confidence scores–*i.e.*, 3:3, 3:2, 3:1, 2:3, 2:2, 2:1, 1:3, 1:2, and 1:1. The polygons are coloured according to Figure 9 to produce a combined mineral potential/confidence map for land use planning purposes.

Levelling mineral potential data across major structures

Areas cut by major structures along which significant displacement has occurred need to be evaluated separately, and then stitched back together at the end of the assessment process. Concurrently, the mineral potential data need to be levelled to account for prospectivity differences across the structure concerned.

The DRLUP area serves as a case in point. The AOI is cut by the Tintina fault (Fig. 6) along which 430 km of displacement has taken place (Israel, *et al.*, 2019). Rocks of the Selwyn basin (Ancestral North America) to the north are juxtaposed against rocks of the Yukon-Tanana terrane (Intermontane) to the south. Assessing mineral potential across the fault is neither logical nor feasible and hence the two terranes need to be evaluated separately.

Mineral potential scores for the DRLUP area shows that the Yukon-Tanana terrane is, on average, 2.066 times more prospective than the area north of the Tintina fault. This difference needs to be captured in the final mineral potential map for the Dawson region by levelling the data across the Tintina fault so that the mineral potential of the two terranes is correctly reflected when viewed holistically. The following process was used to achieve this:

1. The area under a standardized normal distribution curve below a StDev of -1 was divided by the difference in average mineral potential between the rocks of the Selwyn Basin and the Yukon-Tanana terrane–*i.e.*, 15.87/2.066 = 7.68%.

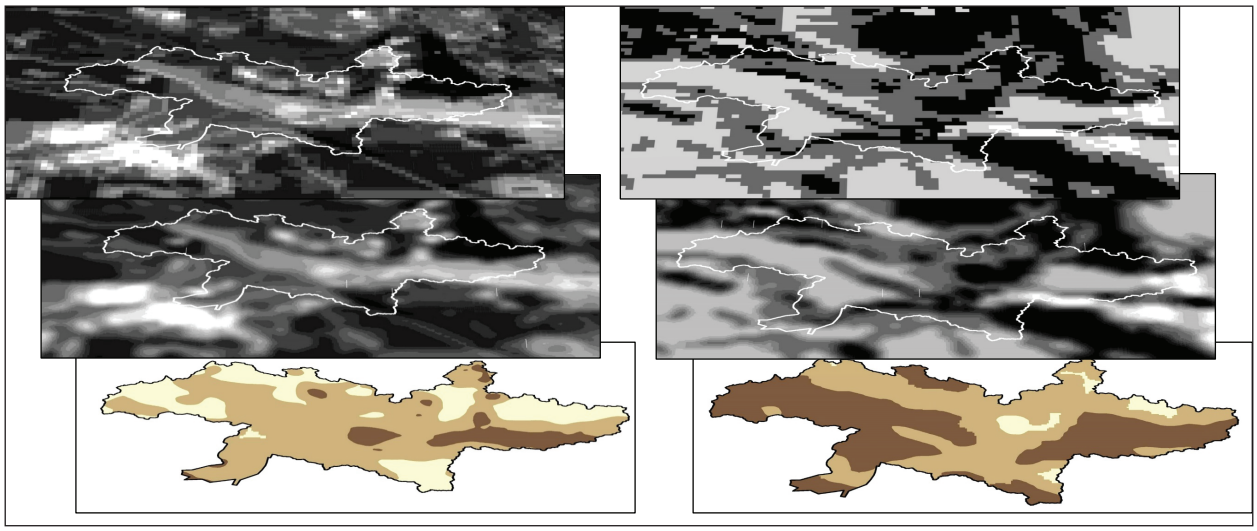


Figure 10. *Schematic representation of layers used to produce the bedrock confidence map for the Beaver River watershed and Dawson Regional mineral potential maps.*

2. For the Selwyn basin component: a mineral potential of 1 was ascribed to the area falling under the normal curve of 23.55% (*i.e.*, 15.78 + 7.68, which corresponds to a StDev = -0.72);
3. For the Yukon-Tanana terrane: a mineral potential of 1 was ascribed to the area falling under the normal curve of 8.19% (*i.e.*, 15.78 - 7.68, which corresponds to a StDev = -1.39);
4. For the Selwyn basin for mineral potential scores of 2 and 3: the areas under the normal curve were reduced by 3.84% (*i.e.*, 7.68/2) to 49.44% and 27.01%, respectively, and the StDev dividing the two areas determined–StDev = 0.61; and
5. For the Yukon-Tanana terrane for mineral potential scores of 2 and 3: the areas under the normal curve were increased by 3.84% (*i.e.*, 7.68/2) to 57.12% and 34.69%, respectively, and the StDev dividing the two areas determined–StDev = 0.39.

For the Selwyn basin component, mineral potential values therefore were apportioned as follows:

1. Scores falling below a StDev of -0.72 = 1;
2. Scores falling between a StDev of -0.72 and 0.61 = 2; and
3. Scores falling above a StDev of 0.61 = 3.

For the Yukon-Tanana terrane, mineral potential values were apportioned as follows:

1. Scores falling below a StDev of -1.39 = 1;
2. Scores falling between a StDev of -1.39 and 0.39 = 2; and
3. Scores falling above a StDev of 0.39 = 3.

Fair copy output

The final mineral potential/confidence maps for the Beaver River watershed and Dawson region are depicted in Figs. 11 and 12. Note that the BRLUP mineral potential map contains eight combinations of prospectivity/confidence scores, rather than the maximum of nine. There is no 1:3 category (*i.e.*, lowest potential/highest confidence), meaning that there are no areas on the BRLUP map that we can be very sure are not prospective.

With respect to the Dawson region, the relatively higher mineral potential of the Yukon-Tanana terrane south of the Tintina fault is clearly reflected in the overall mineral potential map.

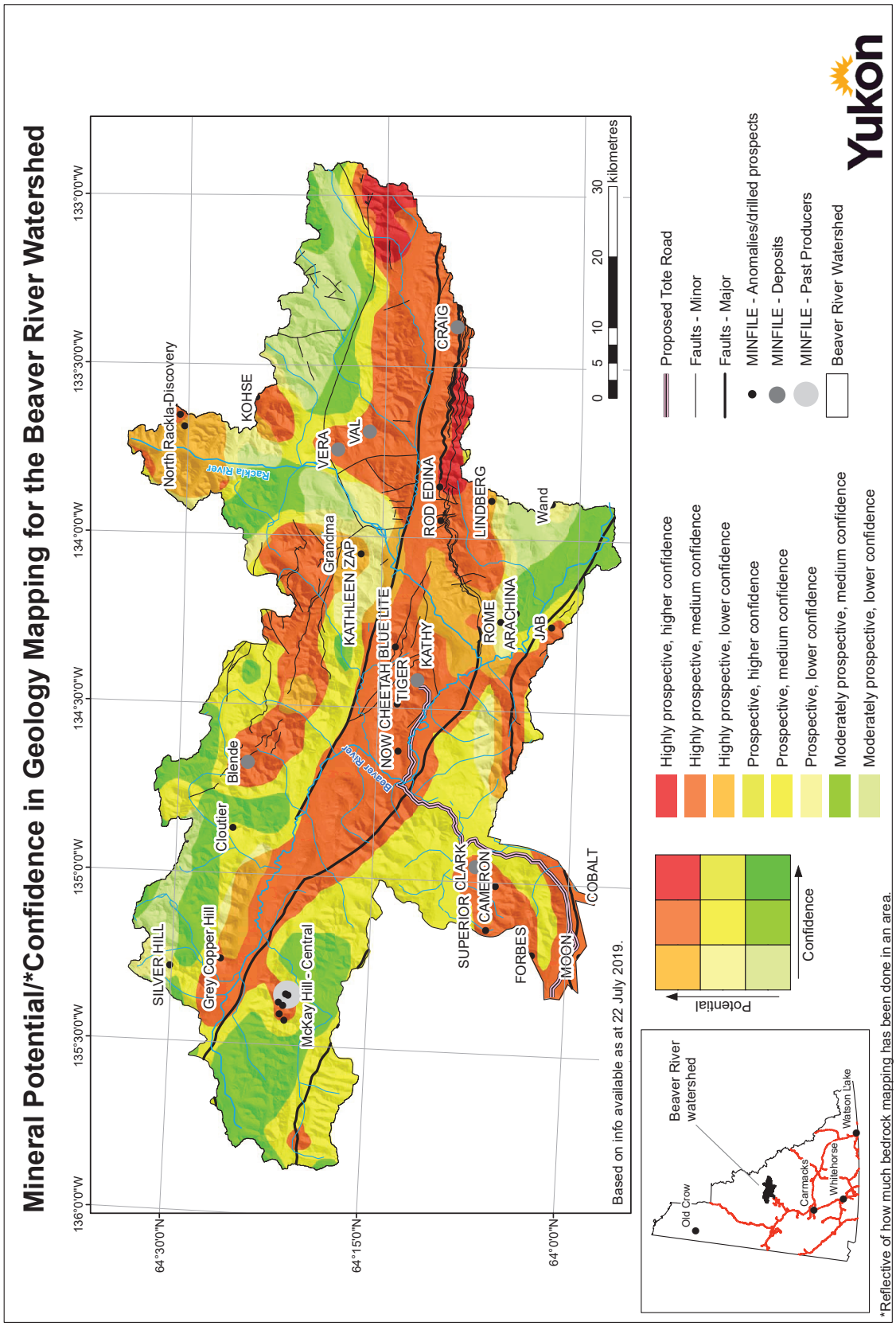


Figure 11. *Mineral potential versus geology mapping confidence map for the BRLUP area.*

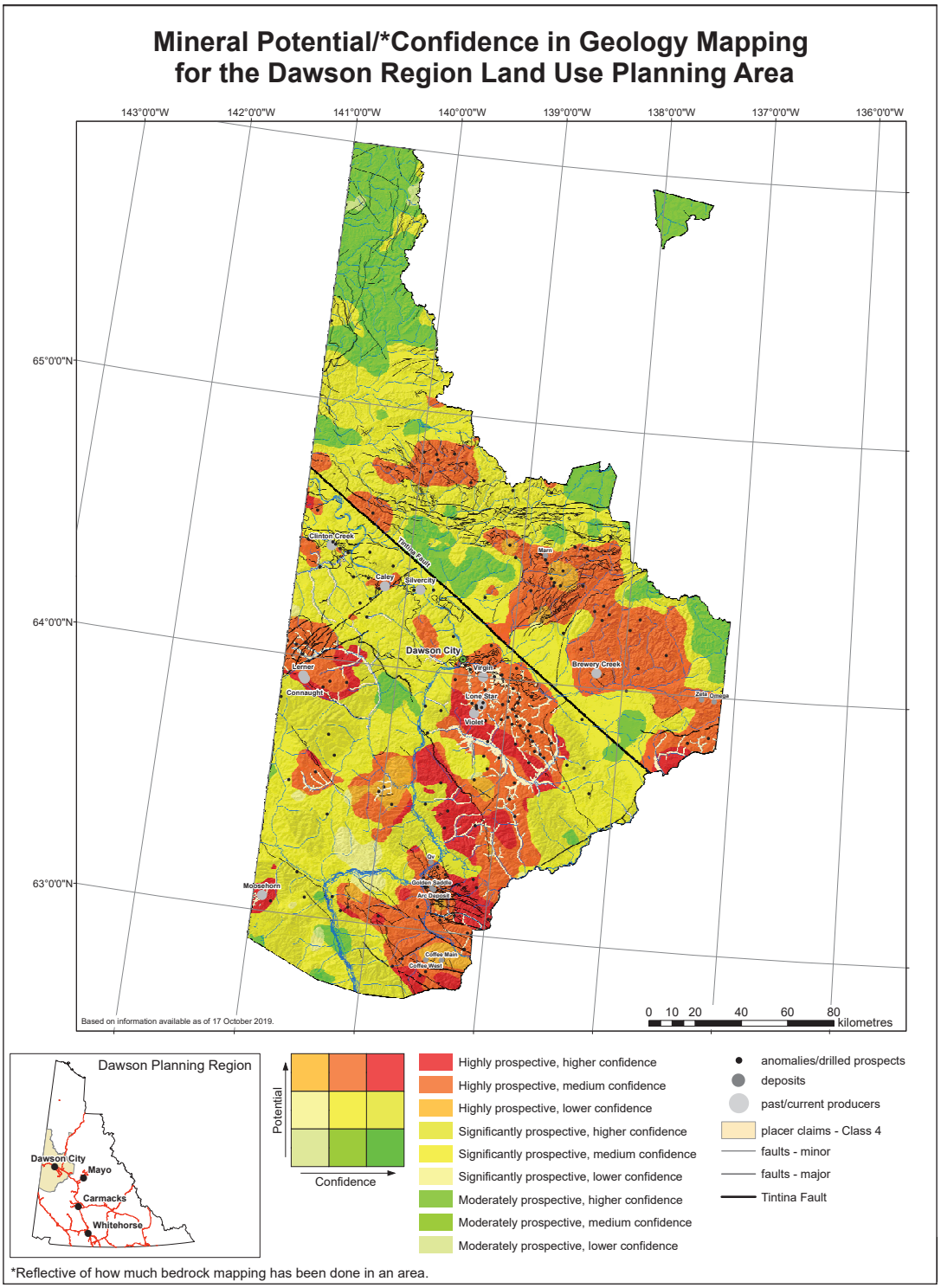


Figure 12. *Mineral potential versus geology mapping confidence map for the DRLUP area.*

Conclusion

Mineral potential maps for land use planning in Yukon will be generated using the process described above. Maps developed for the Beaver River watershed and Dawson region have been well received by land use planners as:

1. they are simple to use and easily understandable, helping with decision-making;
2. they are based on hard data;
3. they are presented as a single map containing all relevant mineral potential data, rather than as separate maps highlighting individual items;
4. uncertainty is built in to the process; and
5. they offer up areas for removal from exploration that minimize impacts on future economic opportunities.

References

Bradshaw, G. and VanRanden, J. (comp), 2003. Yukon regional mineral potential by deposit models 2003. Yukon Geological Survey, Open File 2003-11(D).

Cox, D.P. and Singer, D.A. (eds.), 1986. Mineral deposit models. U.S. Geological Survey, Bulletin 1693, 379 p.

Ellefsen, K.J., 2019, Effect of size-biased sampling on resource predictions from the three-part method for quantitative mineral resource assessment – A case study of the gold mines in the Timmins-Kirkland Lake area of the Abitibi greenstone belt, Canada. U.S. Geological Scientific Investigations Report 2018–5149, 15 p.

Fonseca, A. and Bradshaw, G., 2005. Yukon mineral deposit profiles. Yukon Geological Survey, Open File 2005-5, 163 p.

Harris, J.R., Wilkinson, L., Heather, K., Fumerton, S., Bernier, M.A., Ayer, J., Dahn, R., 2001. Application of GIS processing techniques for producing mineral prospectivity maps—a case study: Mesothermal Au in the Swayze Greenstone Belt, Ontario, Canada. Natural Resources Research, vol. 10, p. 91–124.

Israel, S., Colpron, M., Roots, C. and Fraser, T., 2015. Overview of Yukon geology. Yukon Geological Survey, internal document.

Lefebure, D.V. and Ray, G.E. (eds.), 1995. Selected British Columbia mineral deposit profiles, Volume I – Metallics and Coal. British Columbia Ministry of Energy, Mines, and Petroleum Resources, Open File 1995-20, 136 p. 8

Lefebure, D.V. and Höy, T. (eds.), 1996. Selected British Columbia mineral deposit profiles, Volume 2 – Metallic Deposits. British Columbia Ministry of Energy, Mines, and Petroleum Resources, Open File 1996-13, 172 p.

McCuaig, T. and Hronsky, J., 2014. The mineral system concept: The key to exploration targeting. Society of Economic Geologists, Special Publication 18, p. 153-175.

Porwal, A., 2006. Mineral potential mapping with mathematical geological models. PhD Dissertation, Univ. Utrecht, 277 p. (Plus related course in presentation format.)

Raines, G. L., Bonham-Carter, F. and Kemp, L., 2000. Predictive probabilistic modeling: Using ArcView GIS. ArcUser April-June 2000, p. 45–48.

Schmitt, E., 2010. Weights of Evidence mineral prospectivity modelling with ArcGIS. EOSC 448 Directed Studies.

Singer, D.A., 1993, Basic concepts in three-part quantitative assessments of undiscovered mineral resources: Nonrenewable resources, vol. 2, no. 2, p. 69–81.

Wyborn, L.A.I., Heinrich, C.A. and Jaques, A.L., 1994. Australian Proterozoic mineral systems: Essential ingredients and mappable criteria. Australian Institute of Mining and Metallurgy Annual Conference, Melbourne, Proceedings, p. 109–115.

Preliminary report on the bedrock geology of Castle Mountain area, Yukon (parts of NTS 105D/6)

R. Cobbett*
Yukon Geological Survey

Cobbett, R., 2020. Preliminary report on the bedrock geology of Castle Mountain area, Yukon (parts of NTS 105D/6). *In:* Yukon Exploration and Geology 2019, K.E. MacFarlane (ed.), Yukon Geological Survey, p. 43–55.

Abstract

Carbonate strata of the Cambrian to Devonian Bouvette Formation underlies the Castle Mountain area in central Yukon. Locally, within the Bouvette Formation, calcareous, fossiliferous clastic rocks are interstratified with volcaniclastic and volcanic rocks. The volcanic rocks are inferred to be post-early Silurian based on preliminary fossil ages of graptolites found in underlying limestone. I propose extensional tectonism temporarily disrupted carbonate platform development in the early Silurian in this area. Crustal extension resulted in normal faulting and local subsidence. Thermal uplift, related to underplating of igneous bodies, resulted in subaerial exposure and subsequent erosion of chert, carbonate and volcanic rocks. Basins and slopes (areas between thermally uplifted blocks and subsiding areas) collected material eroding from exposed strata and volcanic rocks deposited during eruptions.

* rosie.cobbett@gov.yk.ca

Introduction

Detailed mapping centred on Castle Mountain provides geologic context to Paleozoic volcanic rocks exposed in this area of central Yukon (Fig. 1). The volcanic rocks here are one of many occurrences of early to mid-Paleozoic magmatic rocks exposed in North American continental margin strata that are poorly characterized in terms of their age, environment of eruption and magma source (Goodfellow *et al.*, 1995; Colpron et al., 2016).

Published bedrock maps for this region are limited to 1:250 000 scale reconnaissance maps by Green (1972). In 2012, the Yukon Geological Survey initiated a targeted study aimed at better characterizing Paleozoic volcanic rocks exposed in Yukon. Since this project began, it has turned into a PhD project at Memorial University of Newfoundland undertaken in collaboration with the Yukon Geological Survey. The scope of the project has expanded outside Yukon to include Northwest Territories and Alaska as the ancient passive margin of western North America extends into these jurisdictions where notable Paleozoic volcanic rocks are exposed. This report summarizes the results of ten days of fieldwork, including geological mapping and sampling, from the Castle Mountain area (NTS 105D/6) in the summer of 2019, and represents the first publication of this multi-year project.

Geologic framework

Castle Mountain is located in the southern Ogilvie Mountains, between Hart River and Elliott Creek, approximately 200 km east-northeast of Dawson City (Fig. 1). In this area, a carbonate-dominated succession of relatively flat lying strata are part of the Ogilvie Platform, an arch that existed as part of the western Laurentian passive margin during the Cambrian to Devonian periods (Abbott, 1997; Cecile *et al.*, 1997). The Selwyn basin is located approximately 50 km to the south of Castle Mountain and is a deep water equivalent to the Ogilvie platform (Fig. 1a). The boundary between the two coincides with the Dawson fault, an east-west striking imbricated thrust fault. North of the Dawson fault, open folds, north and northwest trending steep faults, and a significant unconformity beneath the Cambrian to Devonian Bouvette Formation accounts for much of the map pattern in the area (Fig. 1b; Green, 1972).

Stratigraphy

Dolostone and limestone, and calcareous and volcanic-derived clastic rocks and minor mafic volcanic rocks of the Cambrian to Devonian Bouvette Formation and Cambrian to Silurian Marmot Formation, respectively, underlie the entire map area (Fig. 1b; Colpron *et al.*, 2016; Green, 1972).

In this report, we subdivide the Bouvette Formation into carbonate and deep water facies including three informal formations. Starting at the lowest stratigraphic level, these comprise 1) dolostone, 2) limestone, and 3) dolostone (Fig. 2). The Marmot Formation, termed the volcano-sedimentary facies below, forms an intermediate unit within the Bouvette Formation and is subdivided into sandstone, agglomerate, volcanic breccia, basalt and tuff (Fig. 2).

Dolostone–ЄOd, ЄOs

Buff and light grey weathering, thick-bedded to massive dolostone comprise the lower slopes of Castle Mountain and adjoining ridges (Figs. 2 and 3a). One distinct horizon of silicified stromatolite occurs approximately 90 m from the top of the dolostone and is an important marker bed (Fig. 3b and 4). The stromatolite structures range in size from 10–30 cm in diameter and form a bed approximately 30 cm thick (Fig. 3b). Locally, on the north side of Castle Mountain, orange-buff weathering, grey fresh, medium-bedded, quartz-rich dolomitic sandstone interbedded with orange weathering, green fresh, laminated mudstone crops out structurally below the dolostone and has been included within this member, although it may represent an older formation.

A minimum thickness of this unit is approximately 365 m. The base of the member is not exposed except where the dolomitic sandstone and mudstone crop-out, but the relationship between these rocks and the dolostone is unclear. The upper contact with limestone and chert is conformable and abrupt (Fig. 4).

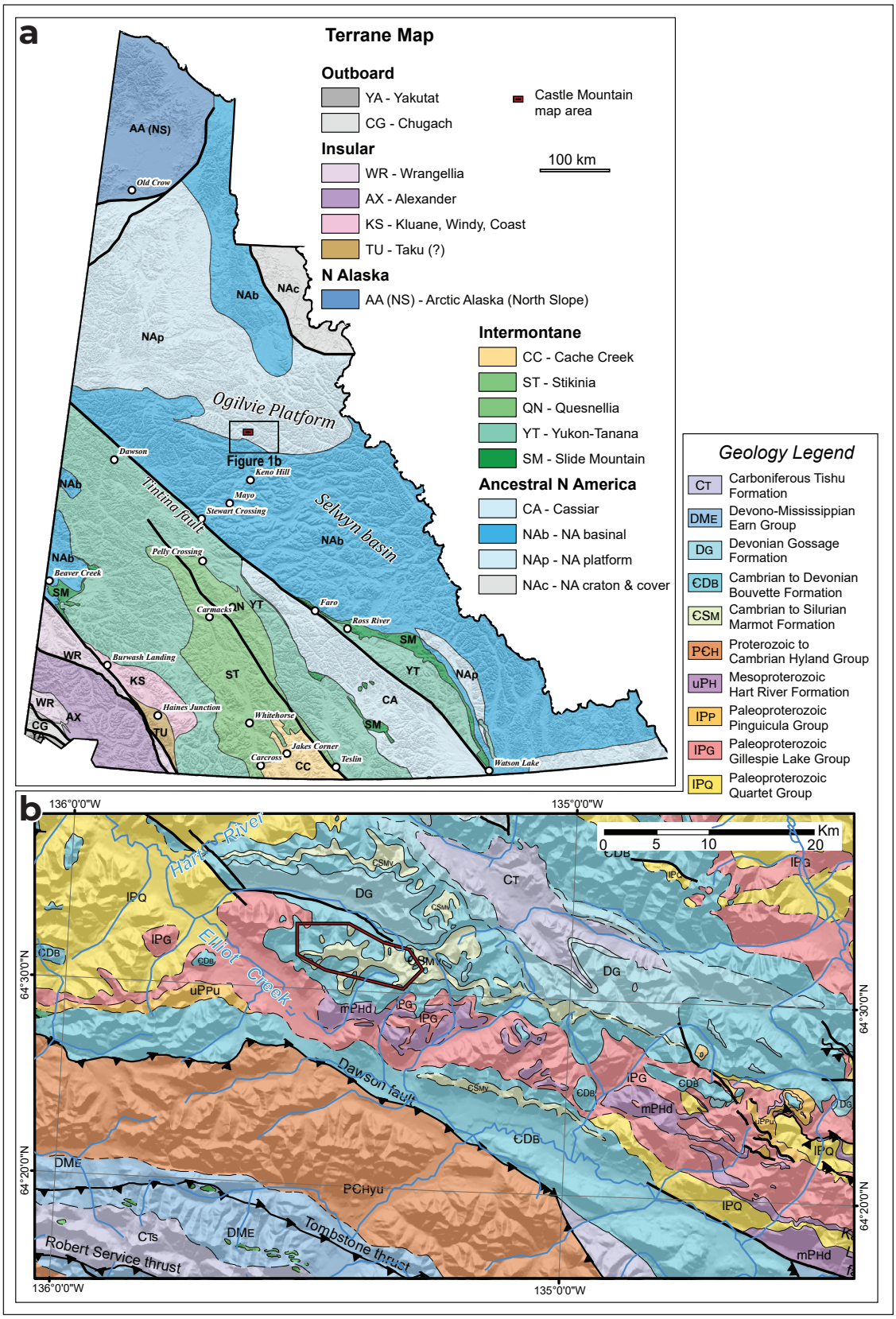


Figure 1. ***(a)*** *Terrane map of Yukon illustrating the location of map area presented in this report. Modified from (Colpron and Nelson, 2011).* ***(b)*** *Inset provides regional geology of the Castle Mountain area (Colpron et al. 2016).*

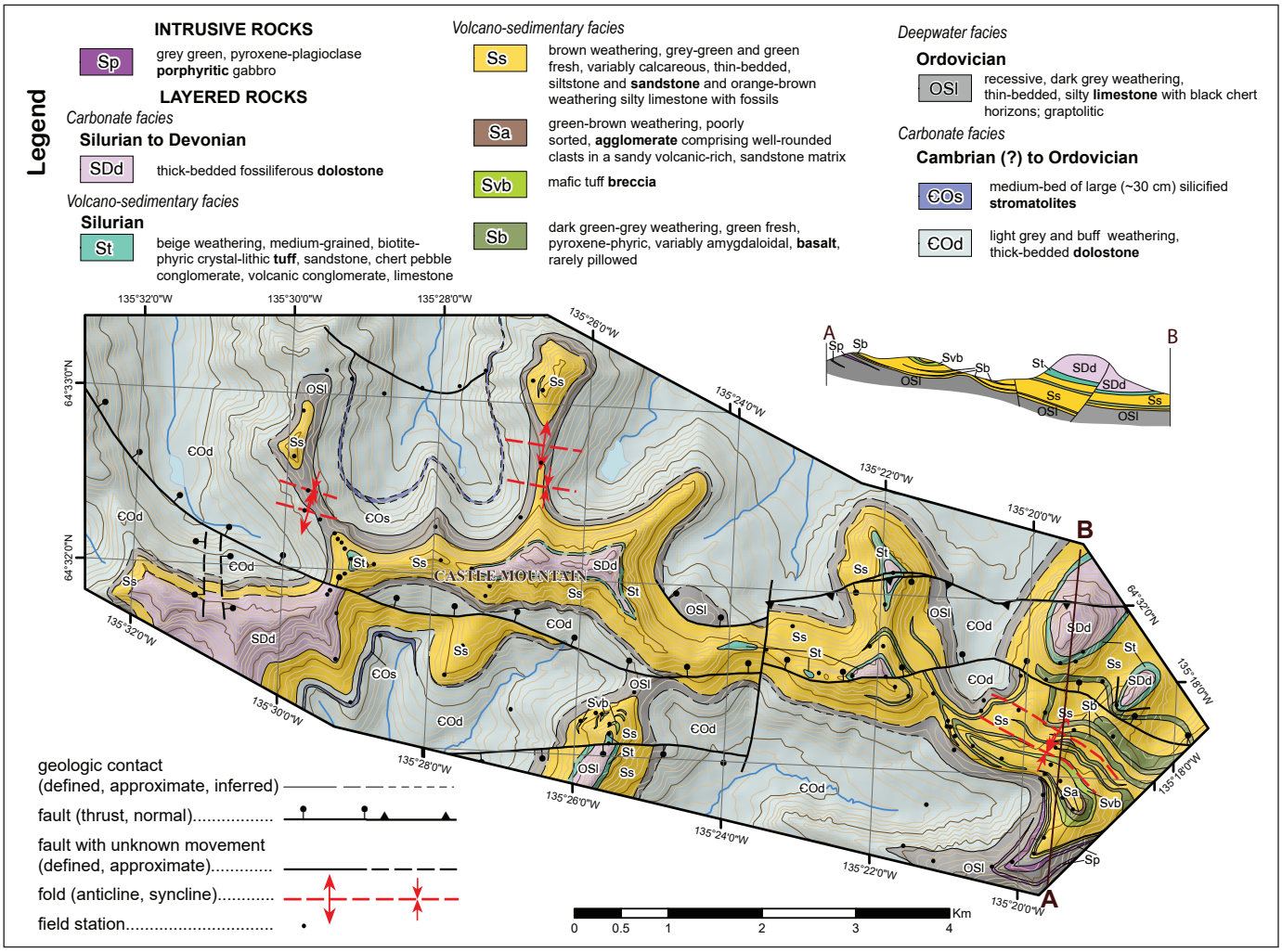


Figure 2. *Geologic map and cross section of the Castle Mountain area.*

Limestone–OSl

Dark, soil-rich scree slopes form a recessive band above the dolostone on all sides of Castle Mountain. Outcrop exposures of this unit comprise dark grey and light grey, recessive weathering, thin and medium-bedded, dark grey, silty limestone with black chert horizons (Fig. 3c). The chert forms continuous beds in some localities and elongate nodules in others. Graptolites are common both in the silty limestone and preserved on top of chert horizons (Fig. 3d). Locally, slump-folds on the ten-centimetre scale occur in the limestone layers (Fig. 3e).

Thickness for this unit ranges from zero to sixty metres throughout most of the map area. In the very southeastern part of the map, the limestone attains thicknesses of up to 200 m but in this area, several sills over-thicken the unit, exaggerating its true thickness (Figs. 4 and 7). Both upper and lower contacts are conformable and abrupt. The occurrence of graptolites of the form *Monograptus* and *Diplograptus*, collected from this unit in the southeastern edge of the map area, suggests an early Silurian age for the limestone (Blodgett, R., pers. comm.; Fig. 3f).

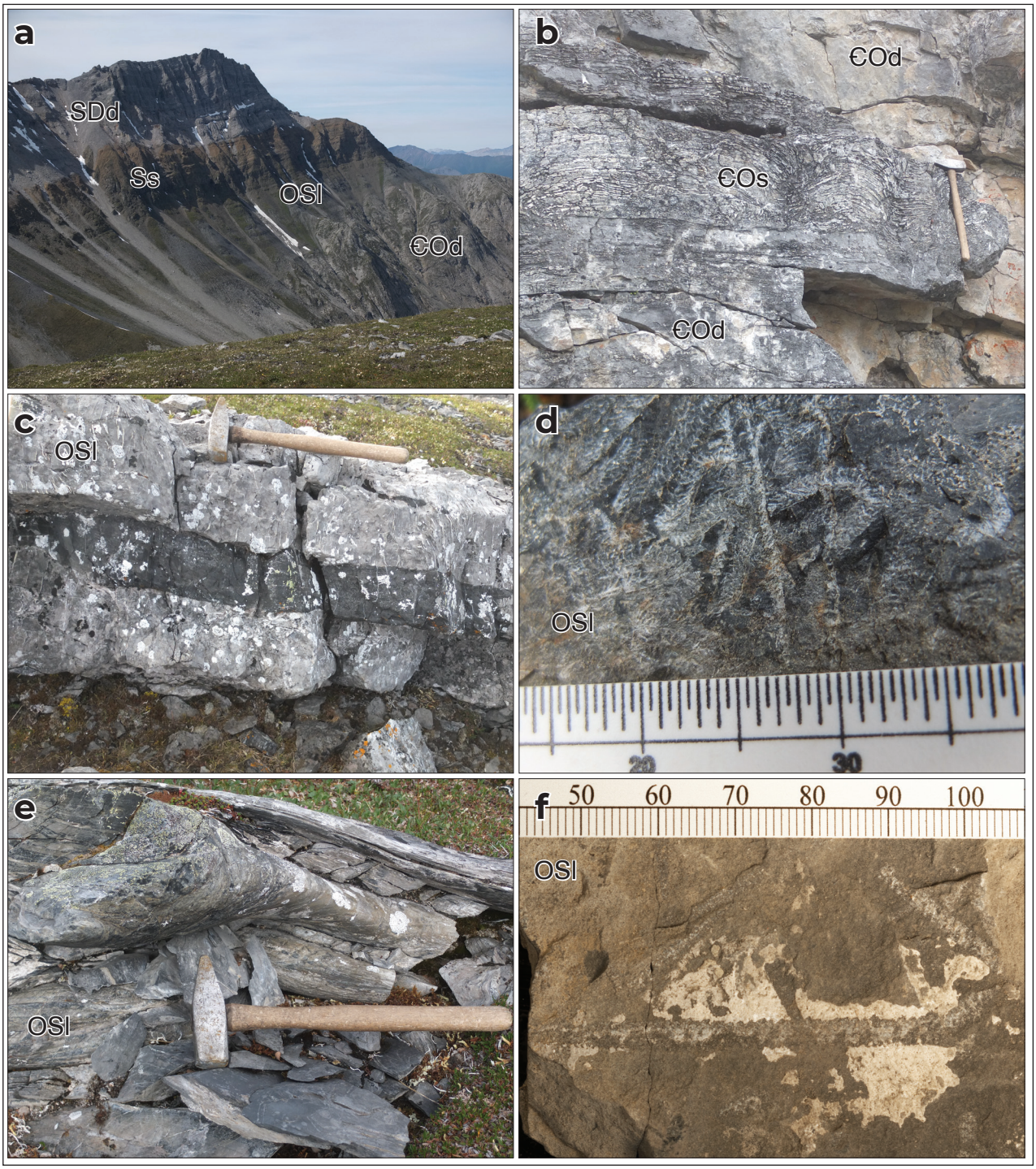


Figure 3. *Photographs of rock exposures from the lower dolostone unit (ЄOd) and the limestone unit (Sl).* ***(a)*** *Buff weathering dolostone typical of the ЄOd unit comprise the band of rock in the lower right hand corner of the map. Above this dark weathering rocks are unit Ss. Grey weathering band forming the top of the ridge is upper dolostone unit (SDd). Photograph was taken from 476549E 7156920N looking southward.* ***(b)*** *Silicified stromatolites within thick-bedded dolostone (ЄOs) in the western part of the map area (476798E, 7155126N).* ***(c)*** *Thin-bedded silty limestone interbedded with black chert of the Sl unit (476393E, 7157064N).* ***(d)*** *Graptolites preserved on the top of the bed of black chert from the Sl unit (476403E, 7158654N).* ***(e)*** *Slump folds within the silty limestone layers of the Sl unit (476393E, 7157064N).* ***(f)*** *Early Silurian graptolites from 484158 E 7153799N.*

Volcano-Sedimentary Succession–Ss, St (west Castle Mnt)–section with minor volcanic rocks

Dark weathering, well-bedded, fine to coarse clastic sedimentary rocks form a distinct, relatively flat lying band below the castellated peak of Castle Mountain and adjoining ridges in the western half of the map area (Fig. 3a). Within this unit, a lower section, dominated by dark green-brown weathering clastic rocks, comprises approximately half the unit thickness and occurs directly below an upper section of orange-brown weathering calcareous rocks capped by quartz-rich sandstone, limestone and tuff (Fig. 4).

The lower part of Ss lies directly on the lower silty limestone unit where it dominantly comprises dark greenish-brown weathering, thin to medium-bedded, calcareous, grey siltstone and calcareous, fossiliferous sandstone. Light green and brown weathering, fossiliferous, calcareous siltstone is interbedded with buff-grey limestone with rare interbeds of cross-bedded calcareous sandstone (Fig. 5a). Medium-beds of dark weathering sandstone contain approximately 5% volcanic clasts. These beds weather into distinct lens shaped cobbles and are a minor part of the lower section. Also in minor proportion, fine-grained lithic sandstone, fossiliferous sandstone, siltstone and conglomerate with carbonate clasts and shell fragments, occur in this section in order of decreasing abundance. North of Castle Mountain, boulders of volcanic breccia comprise angular cobble-size clasts of volcanic rock in a sandy matrix, are anomalous within the well-bedded clastic succession. Gradationally overlying this lower succession, a distinctly orange-brown weathering, medium-bedded, highly fossiliferous, grey silty and sandy limestone occupies most of the upper half of unit Ss (Fig. 4). Typical fossils in this part of the section include ammonites, trilobites, crinoids and bi-valves (Fig. 5b,c). A single thick bed of bright orange weathering limestone occurs near the top of the orange-brown weathering rocks.

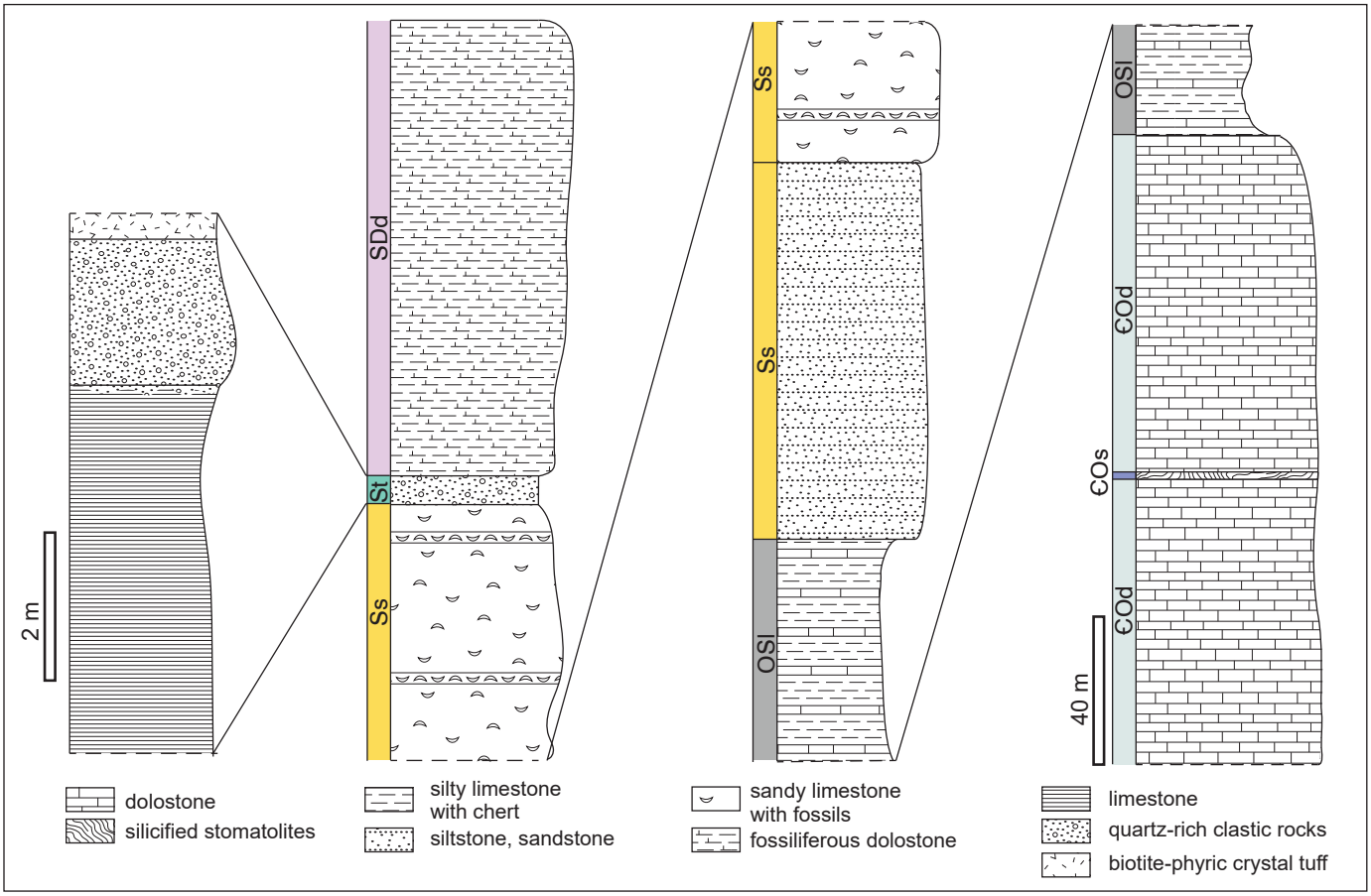


Figure 4. *Schematic stratigraphy from the western part of the Castle Mountain area.*

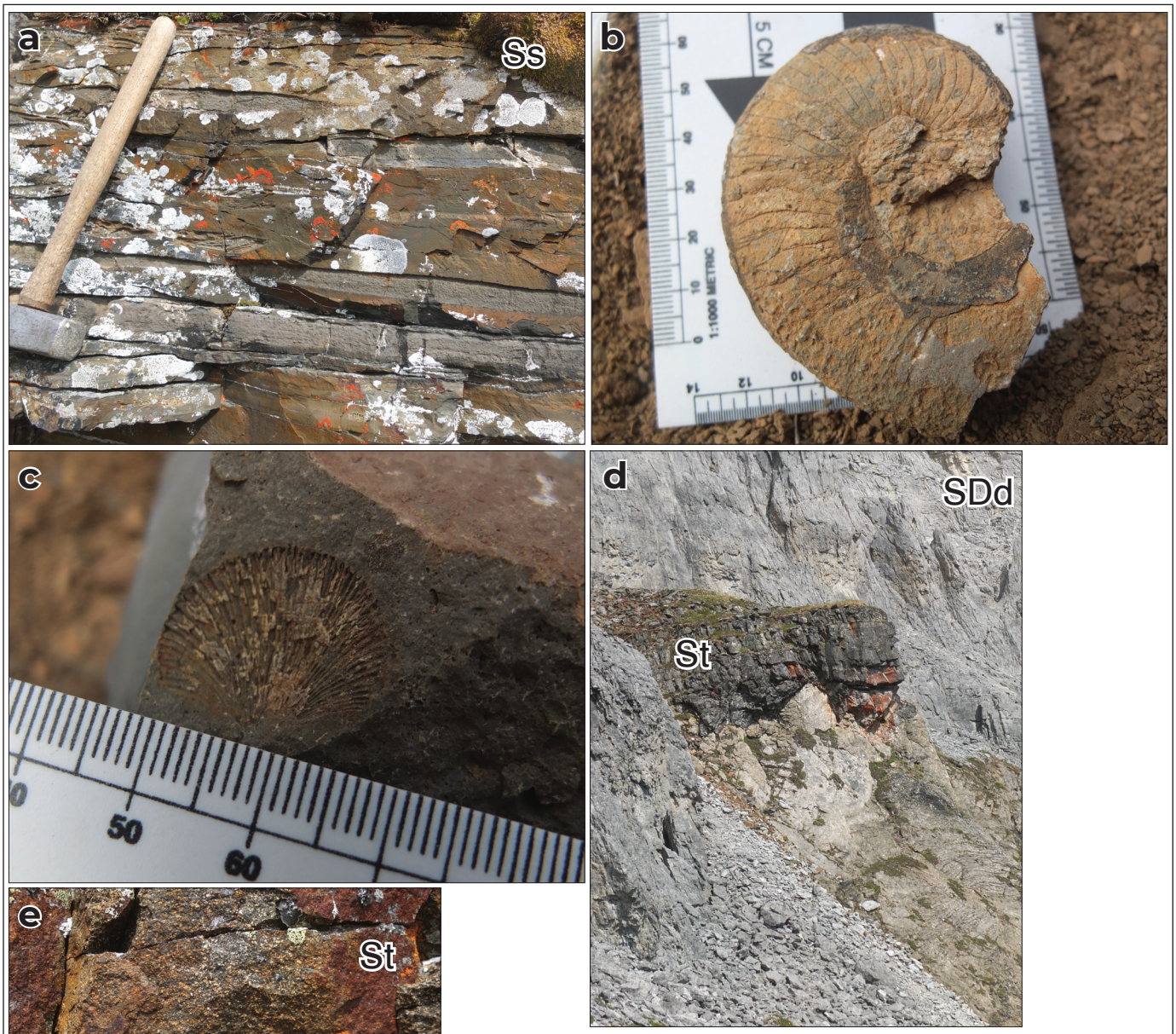


Figure 5. *Photographs of rock exposures from the volcano-sedimentary facies units from the western part of the Castle Mountain area.* **(a)** *Brown weathering calcareous sandstone interbedded with grey weathering limestone (***Ss***). Cross-bedding in a calcareous sandstone lens can be seen near the centre of the photograph (476549E, 7156920N);* **(b)** *ammonite fossil found in the scree of the orange-brown weathering, silty limestone unit (***Ss***) (476988E, 7156605N);* **(c)** *unidentified fossil from the same, orange-brown weathering, silty limestone unit (***Ss***) (476988E, 7156605N);* **(d)** *buff weathering limestone in contact with dark weathering siltstone and chert-rich lithic sandstone and chert pebble conglomerate of (***St***). Notice the undulating nature of the contact between these two units (478240E, 7156501N); and* **(e)** *lower half of the photograph is quartz-rich siltstone overlain by feldspar rich sandstone of the (***St***) unit (478036E, 7156608N).*

An approximately ten metre thick section of limestone, greywacke and tuff caps the upper part of the Ss section, and is identified separately on the geologic map (St; Figs. 2 and 4). This unit has been included in the volcano-sedimentary formation because it comprises these two rock types but is distinct from the underlying strata. At the base of this section, a reddish and buff weathering, fossiliferous limestone commonly has dark grey, wavy laminations throughout. The top surface of the limestone is irregular and undulating, and the troughs filled with grey-brown weathering chert-pebble conglomerate or quartz-rich siltstone (Fig. 5d). The conglomerate grades upwards into a quartz-rich greywacke, into a black weathering and fresh tuffaceous siltstone that is highly magnetic, into a coarse-grained, feldspar-rich sandstone with a dark, silty matrix (Fig. 5e). Above this, more chert pebble conglomerate and greywacke are common. The top of this sub-unit everywhere within the map area is a beige weathering and fresh, medium-grained, biotite-phyric, crystal-lithic tuff.

The thickness of this entire succession in the western part of the map area, including both Ss and St is approximately 200–250 m. It sits abruptly and conformably above the limestone unit (OSl). Its contact with the overlying dolostone is also conformable and abrupt. The calcareous clastic section makes up almost the entire thickness because the upper section contains approximately 5 m of limestone, 2 m of quartz-rich siltstone, sandstone and conglomerate and 30 cm or less of crystal-lithic tuff (Fig. 4).

Volcano-Sedimentary Succession–Ss, St, Sb, Sa, Svb **(east Castle Mnt)–section with abundant volcanic rocks**

The eastern part of the map contains at least three separate coherent mafic volcanic horizons and abundant volcaniclastic and tuffaceous rocks. In general, the volcanic component over the map area increases eastwards (Fig. 2). The more easily erodible nature of the volcanic rocks has created more recessive weathering than in the western part of the map and therefore many sections are covered. The following is a description derived from several different traverses through this unit and may not reflect the exact stratigraphy at any one location.

The base of the succession comprises a mixture of mafic to intermediate volcanic rocks interlayered with volcaniclastic and calcareous fine to coarse clastic rocks. The volcanic rocks include dark green-grey mafic tuff breccia (Svb), amygdaloidal, pyroxene-phyric basalt (Sb; forms pillows in some localities), bedded vitric tuff and a singular thin-bed of welded tuff. Green-grey weathering, thin-bedded volcaniclastic sandstone and siltstone, thinly interbedded with calcareous sandstone, mainly occurs above the volcanic rocks (Ss). This succession grades upwards into brown-grey weathering, thin-bedded, mildly calcareous sandstone interbedded with siltstone with occasional beds of fossiliferous sandstone (Ss). A second volcanic horizon comprises up to five metres of dark green-grey weathering volcaniclastic sandstone interbedded with siltstone (Ss) and capped by a five-metre thick amygdaloidal, pyroxene-phyric, basalt flow (Sb) that is locally overlain by mafic tuff breccia (Svb; Fig. 6a). Laterally this horizon comprises up to 40 m of coherent dark green-grey basalt (Sb) interlayered with both mafic tuff breccia (Svb) and green-weathering agglomerate (Sa). Above the basalt is an approximately one-metre thick bed of volcanic breccia with minor limestone cobbles that eastwards is replaced by orange-grey weathering, thick-bedded, grey, quartz-phyric, welded crystal tuff. Grey-brown weathering, thin-bedded, calcareous sandstone, interbedded with calcareous, fossiliferous siltstone, occurs above the welded tuff and breccia (Ss). An upper (third) volcanic horizon, mapped in the eastern part of the map, comprises two coherent basaltic to andesitic flows (Sb) separated by several metres of mafic tuff breccia (Svb; Fig. 6b). The flows and breccia reach a maximum thickness of thirty metres and taper to less than ten metres over one kilometre. Dark brown and green weathering, sandy, matrix-supported conglomerate, dominated by well-rounded cobbles of mafic to intermediate volcanic rock, occur stratigraphically above this volcanic horizon. Farther west, well-bedded, dark grey, thin to medium-bedded, lithic siltstone, interbedded with light purple-grey weathering, coarse-grained fossil-rich sandstone, lies above the uppermost volcanic horizon and may be a lateral equivalent to the conglomerate (Ss; Fig. 6c).



Figure 6. *Photographs of rock exposures of the volcano-sedimentary facies from the eastern part of the Castle Mountain area.* ***(a)*** *Pyroxene-phyric basalt flow comprising a lower, coherent section overlain by brecciated basalt (*Sb*; 484949E, 7155078N).* ***(b)*** *Weathered surface of mafic tuff breccia (*Svb*; 484341E, 7154941N).* ***(c)*** *Purplish grey weathering coarse-grained, fossil-rich sandstone interbedded with dark grey weathering siltstone (*Ss*; 479575E, 7155013N).* ***(d)*** *Ridge on the right side of the photograph comprises a lower section of purple-maroon weathering volcanic conglomerate overlain by quartz-rich clastic rocks, limestone and biotite-phyric tuff (*St*) and an upper section comprising light grey weathering dolostone (*SDd*). Photograph taken at location 484975E 7155419N looking northwest.* ***(e)*** *Volcanic conglomerate comprising well-rounded clasts in a calcareous, sandy matrix of the* St *unit (484354E, 7155845N).* ***(f)*** *Red weathering, thin-bedded sandstone of the* St *unit (484975E, 7155419N).*

Similar to the western part of the map the top of the volcano-sedimentary succession comprises quartz-rich clastic rocks, conglomerate and tuff (St). Unlike in the west, this unit is much thicker in the east where it attains thicknesses of up to fifty metres (Figs. 6d and 7). The base of this stratigraphy comprises grey weathering limestone overlain by maroon-purple weathering volcanic conglomerate. The conglomerate has well-rounded clasts of intermediate and mafic volcanic rocks in a calcareous, sandy matrix (Fig. 6e). Shell fragments and crinoids are common within more sandy lenses of the conglomerate. Farther up section, thin and medium beds of red weathering, sandstone and pebble conglomerate lie above the volcanic conglomerate (Fig. 6f). Dark grey weathering, quartz-rich lithic sandstone, highly magnetic siltstone, and chert pebble conglomerate sit between the red weathering clastic rocks and a beige, highly fossiliferous bed of limestone. Above the limestone, a bed of biotite-phyric crystal lithic tuff caps the entire volcano-sedimentary succession.

Fossiliferous dolostone (SDd)

Light grey weathering, thick-bedded to massive, fossiliferous dolostone cap the castellated peaks of Castle Mountain and adjoining ridges. Thick beds taper and pinch out in some areas (Fig. 8a). Stromatolites, corals and many unidentifiable fossils and fossil fragments are common within this dolostone (8b). Locally, patchy, laminated dolostone occurs between coral-rich sections (Fig. 8c).

The dolostone is in direct, conformable contact with the underlying crystal-lithic tuff. The upper contact is not exposed within the map area, allowing a minimum thickness estimate for this unit of 150 m.

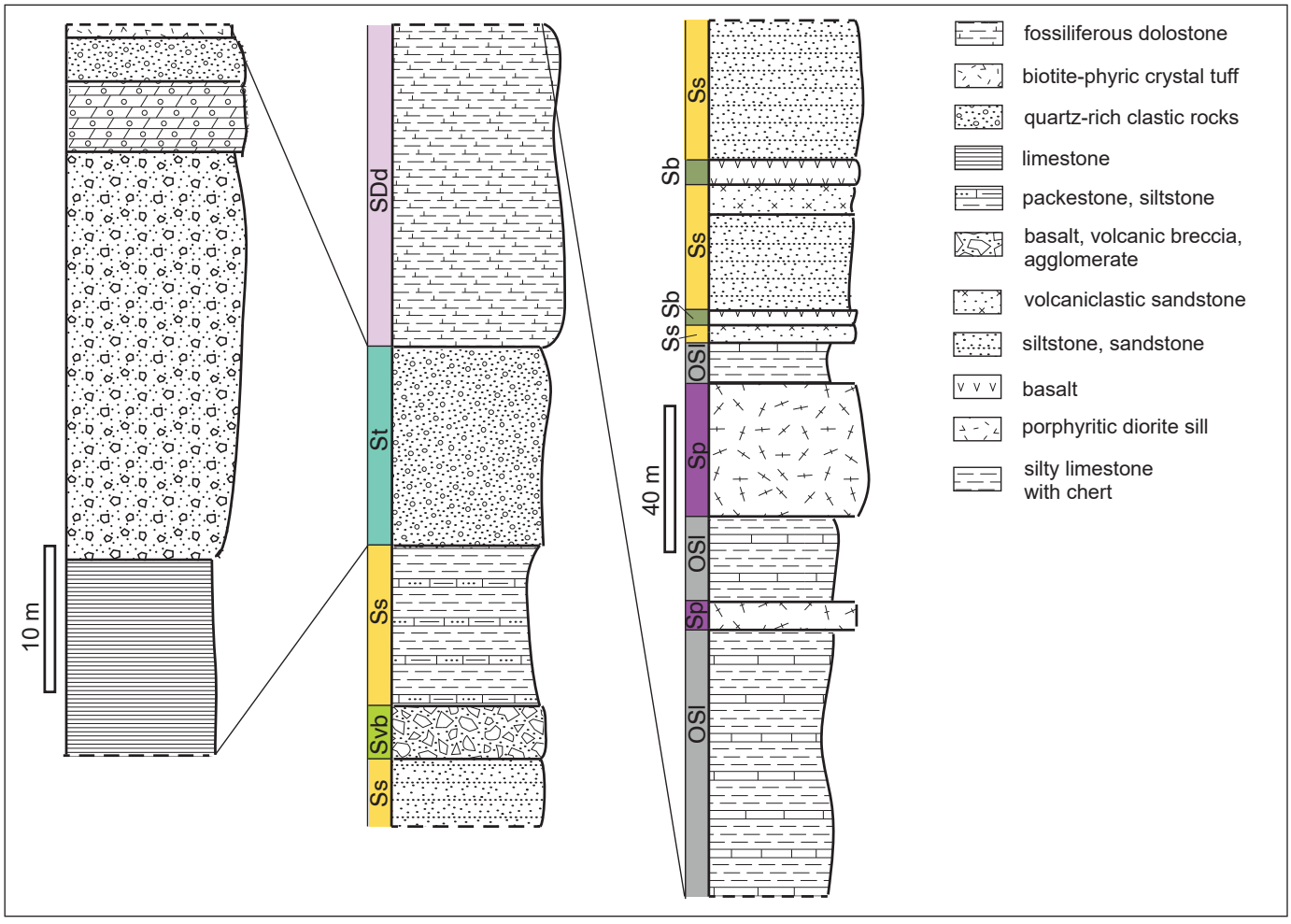


Figure 7. *Schematic stratigraphy from the eastern part of the Castle Mountain area.*

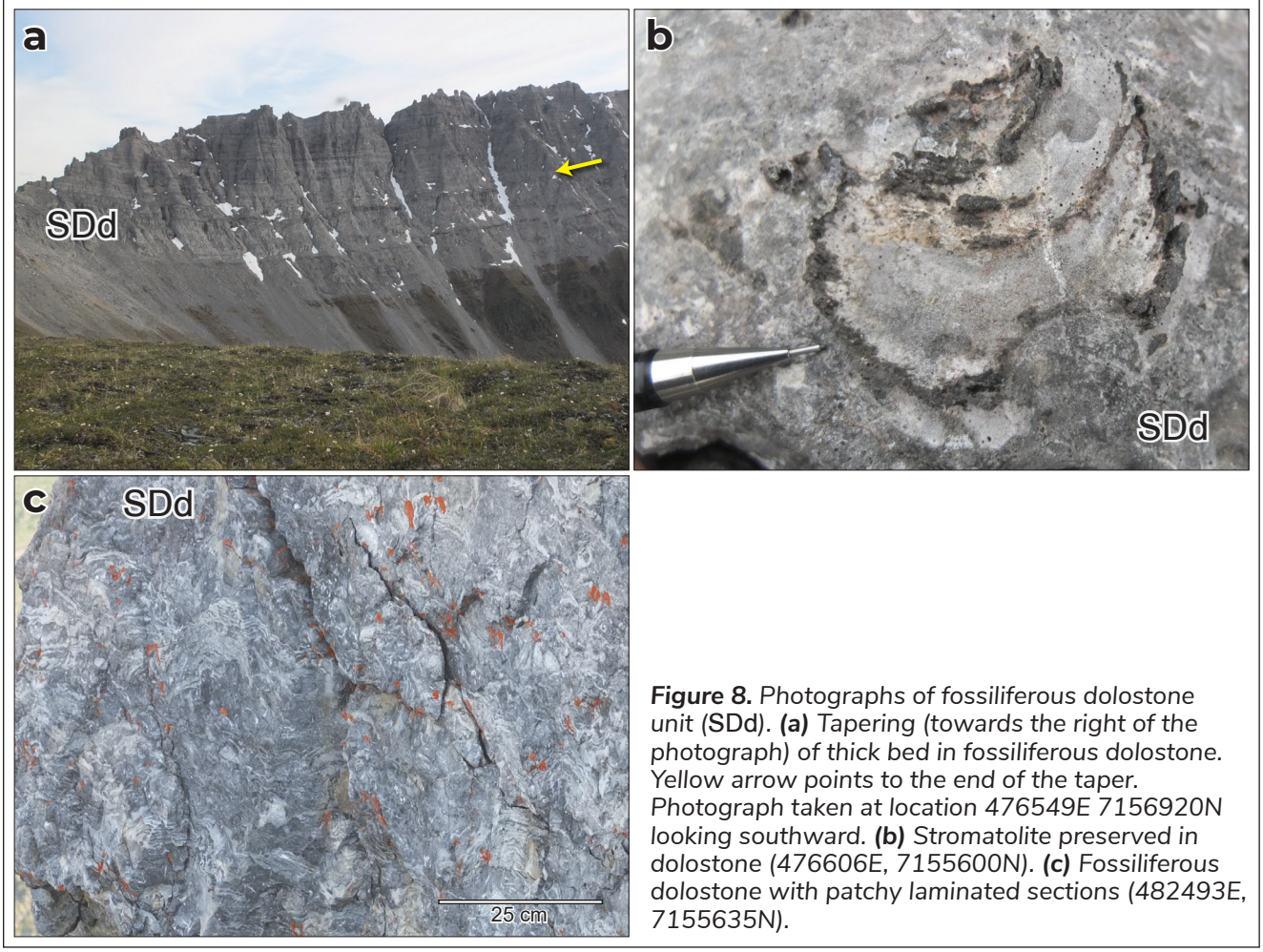


Figure 8. *Photographs of fossiliferous dolostone unit (SDd).* ***(a)*** *Tapering (towards the right of the photograph) of thick bed in fossiliferous dolostone. Yellow arrow points to the end of the taper. Photograph taken at location 476549E 7156920N looking southward.* ***(b)*** *Stromatolite preserved in dolostone (476606E, 7155600N).* ***(c)*** *Fossiliferous dolostone with patchy laminated sections (482493E, 7155635N).*

Structure

Strata across the Castle Mountain area are relatively flat lying. Small but systematic changes in dip of beds characterize east-west oriented open folds (Fig. 2). Steeply dipping normal faults oriented both north-south and east-west have measureable offsets that range from 60 to 100 m. Alteration and brittle deformation of strata delineate faults with unknown movement but offset along these are structures appear to be minor.

Discussion

Depositional environments of carbonate and basin facies

Deposition of the older dolostone (ЄOd) in shallow water, along an epeiric or detached platform, is consistent with the lack of siliciclastic sediment, thick-bedded nature of the carbonate rocks, and the presence of stromatolites (Tucker, 2009). A shift from shallow to deeper water is suggested by deposition of overlying thin-bedded graptolite-bearing, silty limestone (OSl). The synsedimentary folding within the deeper water unit suggests deposition on a slope in an intermediate environment between a shelf and a basin (Tucker, 2009).

Following the transgressive period, the Castle Mountain area must have been situated proximal to a sediment source as it subsequently filled with well-bedded clastic strata comprising carbonate, arkosic and volcanic detritus as well as fossils (Ss). For example, the strata at the top of the St unit contains chert-rich sandstone and conglomerate, as well as conglomerate with well-rounded volcanic clasts. Cross-bedding and silty limestone containing ammonites, trilobites and crinoids suggest deposition in relatively shallow water close to shore (Tucker, 2009), and are evidence that the Castle Mountain area was a catchment for sediment sourcing eroding chert, carbonate and volcanic rocks.

A return to a shallow water environment with limited clastic input occurs immediately after the deposition of a felsic, crystal-lithic tuff (top-most unit in St), as indicated by the build-up of carbonate rocks (SDd). The presence of coral fossils with very patchy laminated sections is interpreted to represent infilling of carbonate sediment between reef frame builders that were bound together during deposition suggesting they may be boundstone (Tucker, 2009). The thick-bedded nature of the dolostone in combination with the tapering of individual thick beds suggests local patch reef buildups were common.

Volcanism

Volcanism appears to be simultaneous with calcareous, clastic rock (Ss) deposition as flows are interbedded with the base of these strata in the eastern part of the map area. In addition, the basal clastic rock package contains many mafic volcanic clasts, which are interpreted to be sourced from nearby, eroding volcanic piles linked to the same magmatic episode as the flows and tuffs that are deposited within the clastic rock succession. Crystal-lithic tuff is deposited across the entire map area and marks the last episode of volcanism before carbonate build-up resumes.

Tectonic implications

Abbott (1997), who documented rift-related volcanic rocks overlying shale containing Early Silurian graptolites in the Upper Hart River area, reports one of the few notable occurrences of Silurian volcanic rocks in the northern Cordillera. Other workers attribute lower Paleozoic volcanism within the North American continental margin to rift-related extension but do not specifically recognize Silurian volcanic rocks (e.g., Cecile, 1982).

At Castle Mountain, extension related faulting resulting in local tectonic subsidence would drown parts of the carbonate platform and explain the deposition of deeper water facies on top of dolostone. Decompressional melting due to lithospheric thinning associated with crustal extension may have resulted in underplating of igneous rocks and local thermal uplift. This model is one way of explaining the local exposure and subsequent erosion of chert, carbonate and volcanic rocks. Crustal breaks from uplift induced normal faulting or faulting related to crustal extension would facilitate the rise of magmas through the upper crust. Regional, thermal subsidence following volcanism is consistent with a return to carbonate facies at Castle Mountain and surrounding areas.

Future work

Detailed work east of the mapped area is essential for full characterization of the volcanic rocks exposed here. This summer's fieldwork captured the details of the stratigraphy and provided many samples for fossil, geochemical and geochronological analyses. Due to time constraints, it did not include areas where the volcanic rocks reach maximum thickness. East of the map area, it appears that the volcanic rocks overwhelm the section and become much thicker and future work will involve geological mapping in these areas.

Acknowledgements

I would like to thank Heather Clarke for her excellent assistance in the field. I owe many thanks to Archer Cathro and Associates Ltd. (1981), specifically Julia Lane and Adam Coultier, for accommodating us in their camp and provided essential logistical support during field work. Tiffani Fraser and Luke Beranek provided meaningful and thorough comments during review of this report.

References

Abbott, G., 1997. Geology of the Upper Hart River area, Eastern Ogilvie Mountains, Yukon Territory (116A/10, 116A/11). Exploration and Geological Services Division, Yukon, Indian and Northern Affairs Canada, Bulletin 9, 92 p.

Cecile, M.P., 1982. The Lower Paleozoic Misty Creek Embayment, Selwyn Basin, Yukon and Northwest Territories. Geological Survey of Canada, Bulletin 335, 78 p.

Cecile, M., Morrow, D. and Williams, G., 1997. Early Paleozoic (Cambrian to Early Devonian) tectonic framework, Canadian Cordillera. Bulletin of Canadian Petroleum Geology, vol. 45, p. 54–74.

Colpron, M. and Nelson, J., 2011. A digital atlas of terranes for the northern Cordillera. BC GeoFile 2011-11.

Colpron, M., Israel, S., Murphy, D., Pigage, L. and Moynihan, D., 2016. Yukon bedrock geology map. Yukon Geological Survey, Open File 2016-1, scale 1:1 000 000.

Goodfellow, W.D., Cecile, M.P. and Leybourne, M.I., 1995. Geochemistry, petrogenesis, and tectonic setting of lower Paleozoic alkalic and potassic volcanic rocks, Northern Canadian Cordillera Miogeocline. Canadian Journal of Earth Sciences, vol. 32, p. 1236–1254.

Green, L.H., 1972. Geology of Nash Creek, Larsen Creek, and Dawson map areas, Yukon Territory. Geological Survey of Canada, Memoir 364, 157 p.

Tucker, M.E., 2009. Sedimentary petrology: an introduction to the origin of sedimentary rocks. John Wiley & Sons.

Assessment of thermo-hydraulic properties of rock samples near Takhini Hot Springs, Yukon

H. Langevin* and J. Raymond
Institut national de la recherche scientifique, Québec

T. Fraser
Yukon Geological Survey

Langevin, H., Fraser, T. and Raymond J., 2020. Assessment of thermo-hydraulic properties of rock samples near Takhini Hot Springs, Yukon. *In:* Yukon Exploration and Geology 2019, K.E. MacFarlane (ed.), Yukon Geological Survey, p. 57–73.

Abstract

The Takhini Hot Springs area north of Whitehorse, Yukon overlies a geothermal heat source that manifests as a 46°C water seep at surface. Despite its long-term use as a tourist swimming facility, the origins and geological setting of the hot spring remains poorly understood. The objective of this study is to assess the thermo-hydraulic properties of rock samples from drill core and outcrops near Takhini Hot Springs to better explain the presence of this hydrothermal system. A moderate rock thermal conductivity (average of ~3 W $m^{-1} K^{-1}$) and a low matrix hydraulic conductivity for consolidated rocks (on the order of 10^{-9} m s^{-1}) corresponding to a linear geothermal gradient of 16°C km^{-1} in the upper part of the Takhini well indicate conductive heat transfer between 50 and 450 m depth. Hydraulic conductivity of fractured and brecciated rocks on the order of 10^{-5} m s^{-1}, and topographic contrasts affecting the hydrostatic pressure driving groundwater flow in the area suggest that forced convective heat transfer in the bottom of the Takhini well is responsible for the strong geothermal gradient of 250°C km^{-1} observed between 450 and 500 m depth. Steep faults appear to be a key pathway for deep groundwater to seep to surface and can explain the geothermal context in the vicinity of the Takhini well. Such a framework is a typical geothermal play type in orogenic belts. This research, therefore, helps to characterize the subsurface and provides critical information needed for a successful exploration of geothermal energy resources.

* hubert.langevin@ete.inrs.ca

Introduction

As part of the Yukon government's initiative to find green energy solutions, the Yukon Geological Survey (YGS) is researching geothermal energy potential in the territory. Despite minimal subsurface temperature data, there is evidence for potential geothermal resources in Yukon due to its proximity to the Pacific Ring of Fire, the presence of hot springs and seeps, as well as the existence of major crustal-scale structures such as the Tintina and Denali faults (Fig. 1). Regional studies conducted by the YGS, including Curie Point mapping (Witter *et al.*, 2018) and heat potential studies from radioactive granitoid rocks (Colpron, 2019), show potential for geothermal resources. Together, these studies indicate that the southern part of Yukon is expected to have the highest geothermal heat potential in the territory, however, subsurface temperature data to validate this interpretation are sparse.

The YGS initiated their geothermal research program in 2016 using funding from both the Yukon and Canadian governments. Two temperature gradient (TG) wells were drilled in 2017 and 2018: the first near Takhini Hot Springs in south–central Yukon, and the second in the Tintina fault zone near Ross River (Fraser *et al.*, 2019; Fig. 1). The present study provides baseline thermo-hydraulic characterization of rock units in the Takhini well and from proximal outcrops in order to understand heat transfer mechanisms controlling the geothermal resource in the region. This study includes lithology, thermal conductivity, fracture spacing and hydraulic conductivity of the rocks, as well as a regional assessment of groundwater flow, with the objective of providing a conceptual hydrothermal model. Provision of such baseline data can help understand the geological controls on the geothermal system and can reduce future exploration risk in the territory.

Background

YGS' Geothermal Research Program

The Government of Yukon (YG) is committed to reducing greenhouse gas emissions from transportation, heating, electricity generation and waste with a target of a 30% reduction in GHG emissions by 2030 (Government of Yukon, 2019). Further, over the next 10 years, YG is committed to ensuring Yukoners have access to reliable, affordable and renewable energy. Geothermal energy fits into this climate change strategy, however, it is a resource yet to be delineated in Yukon. In 2016, the YGS initiated a geothermal research program which, to date, includes a number of technical studies (*e.g.*, Colpron, 2019; Witter *et al.*, 2018; Fraser *et al.*, 2019) and a community outreach engagement program. As part of this initiative, the YGS drilled two 500 m TG wells to evaluate the geothermal gradient in specific geological settings. The first well, which is the focus of this paper, was drilled in the Takhini River valley, northwest of the city of Whitehorse, ~2 km from hot springs having a surface water outflow measuring 46°C (Fig. 1). This area is proximal to a granitoid intrusion having an average potential radiogenic heat production value of 4.1 μW m^{-3} (Colpron, 2019), which is a greater than an average granitoid (2.5 μW m^{-3}; Rybach, 1981; Hasterok and Webb, 2017; Artemieva *et al.*, 2017). The second well is located ~15 km from the village of Ross River, in central Yukon, in a crustal-scale strike-slip fault zone known as the Tintina fault (Fig. 1). Drilling program details and TG results are summarized in Fraser *et al.* (2018), and highlights from the Takhini well are provided herein.

Stabilized downhole temperature was measured at intervals of 50 m in the Takhini well, with finer resolution in the uppermost part of the well. A variable geothermal gradient was found, with the upper 450 m of the well measuring 16°C km^{-1} and the bottom 50 m measuring 250°C km^{-1} (Fig. 2; Fraser *et al.*, 2018). This increase in temperature at the base of the well has been interpreted variably as warm groundwater flow along a fault plane or permeable layer, or an impermeable zone of conductive heat transfer from a deeper aquifer (Fraser *et al.*, 2018). Further drilling is required to determine the thickness and extent of this area of elevated temperature gradient.

Regional geology

The Whitehorse trough is an elongated northwest-trending Early to Middle Jurassic sedimentary basin that extends 650 km from northern British Columbia to central Yukon (Fig. 1; Colpron *et al.*, 2015). Sediments here record synorogenic marine to fluvial sedimentary

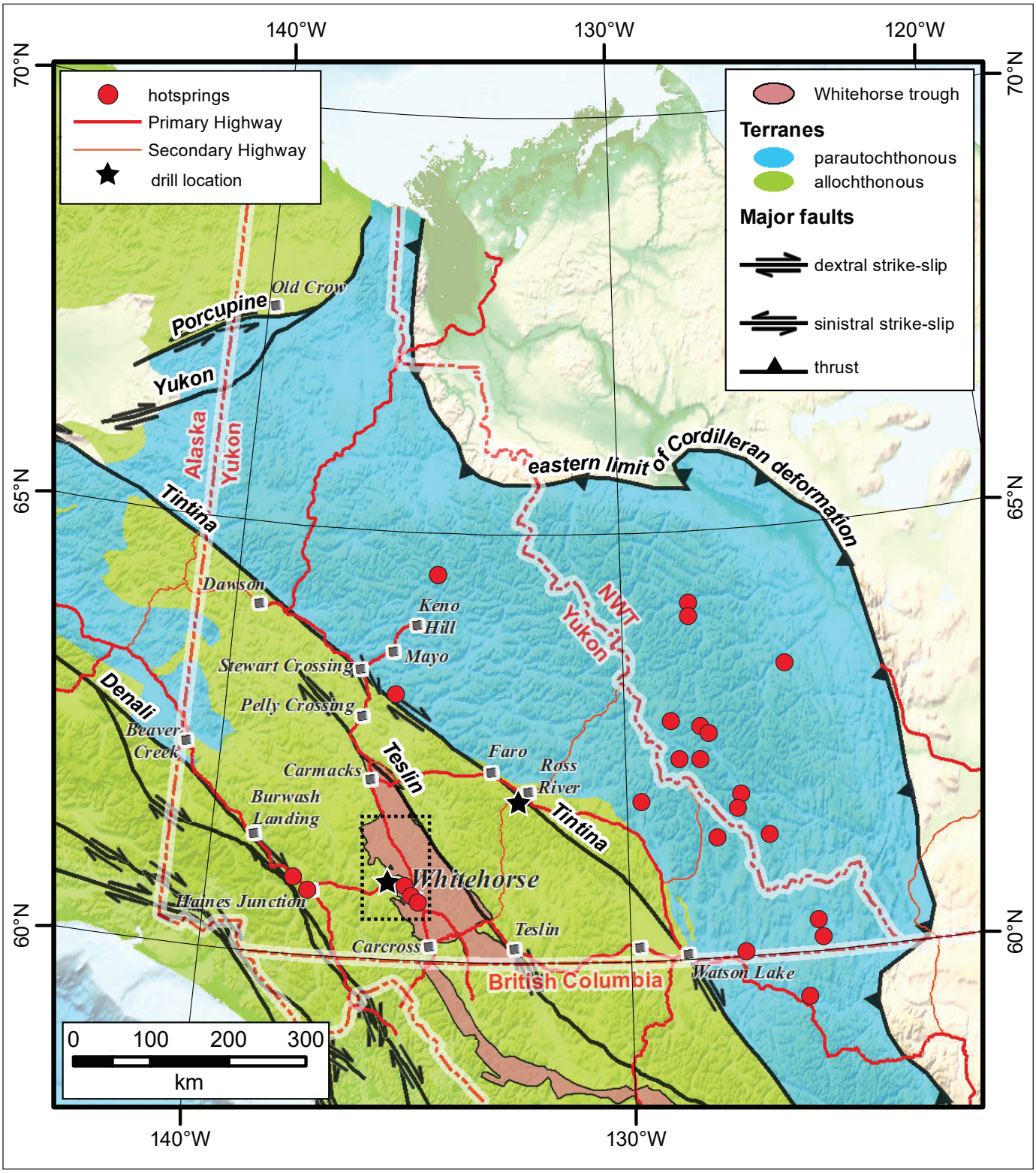


Figure 1. *Terrane map of Yukon illustrating locations of major faults, hot springs, and the Whitehorse trough (orange polygon). Box indicates location of Figure 5.*

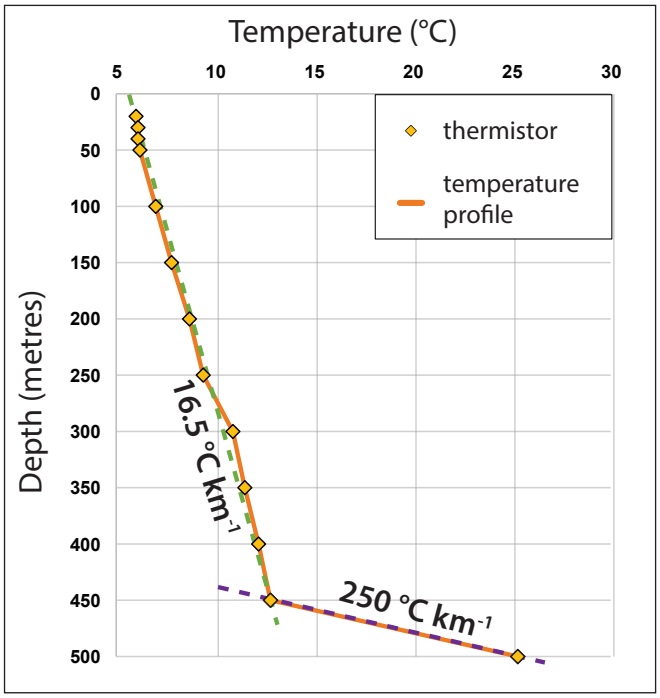


Figure 2. *Downhole temperature data in the Takhini well (after Fraser et al., 2018).*

and volcanic rocks in a forearc basin overlying parts of the Stikinia, Quesnellia and Cache Creek parautochthonous terranes. In the vicinity of the Takhini drill site locality, Whitehorse trough rocks include Laberge Group marine siliciclastic strata (Richthofen formation) and volcanic and volcaniclastic rocks (Nordenskiöld formation), which unconformably overlie Upper Triassic Lewes River Group siliciclastic (Casca and Mandanna members), and carbonate stratigraphy (Fig.3; Hancock member; Hart, 1997). Middle Jurassic to Paleogene granitoid plutons intruded Whitehorse trough and older strata, including an Eocene (54 Ma; Hart, 1997; Fig. 4) granitoid pluton ~2 km west of the drill site.

Methods

Core logging and field sampling

Logging of the Takhini core was undertaken at the YGS' Bostock Core Library in Whitehorse where the core is in storage. From this core, 38 thin sections were made

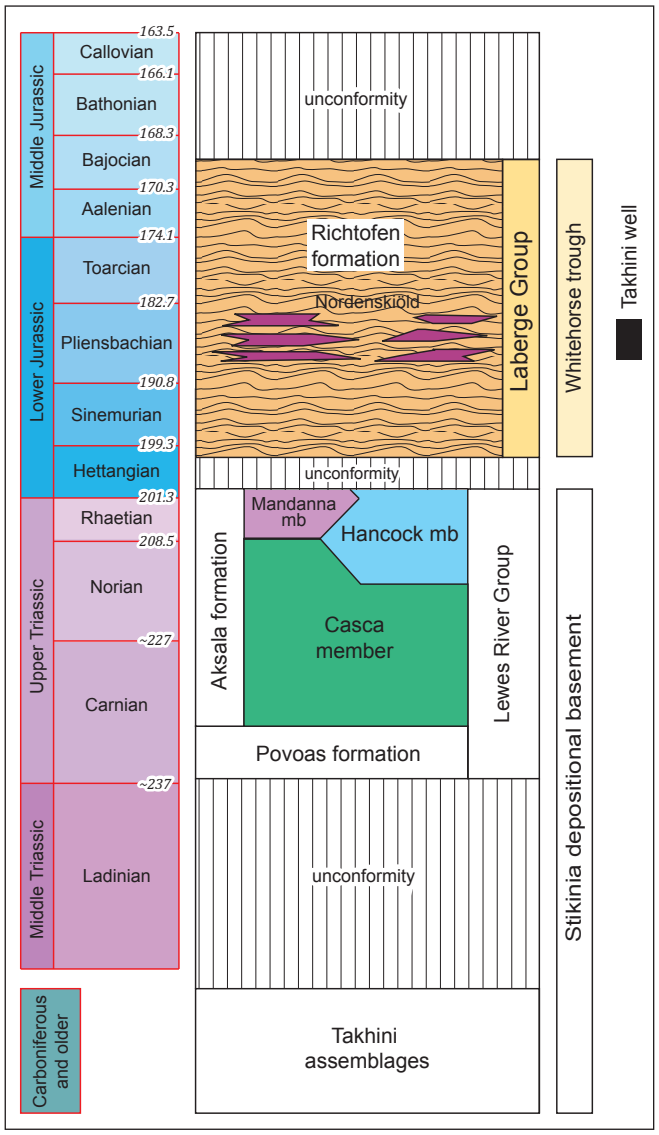


Figure 3. *Sedimentary units of the Takhini well area (modified from Colpron et al., 2015). Note that Mesozoic–Cenozoic intrusive rocks are not shown.*

to help define lithology and to create lithology logs. Rock outcrops found in the vicinity of the Takhini well (Fig. 4) were visited to get a better sense of stratigraphic relationships and variability in lithology to improve the number of samples for the thermo-hydraulic property analysis, and to compile geological cross sections through the well to help to define a conceptual hydrothermal system model.



Figure 4. *Sampling of the Flat Creek pluton ~2 km west from the Takhini well.*

Thermal conductivity

Thermal conductivity measures the amount of energy required to transfer a unit of heat through a unit distance of solid material (SI unit $W\,m^{-1}\,K^{-1}$). This property affects the geothermal gradient when conduction is the dominant heat transfer mechanism. Forty-three well samples were analyzed for thermal conductivity on one of two instruments at the Laboratoire ouvert de géothermie (LOG) at INRS, Québec City, depending upon the nature of the rock. The instruments include: (a) a Lippmann and Rauen thermal conductivity scanner (TCS, 2017; Popov *et al.*, 1999) used at ambient temperature for 41 consolidated rock samples; and (b) a K2D Pro needle probe from Decagon Devices Inc. (Decagon Devices Inc., 2012) used at ambient temperature for 2 unconsolidated rock samples. Thermal conductivity values are reported as ranges ± 2 standard deviations of the lithological unit averages. The units with a single sample have a range of ± 10% considering the relative error of the measurement and the small number of samples.

Hydraulic conductivity

Hydraulic conductivity measures the ability of a fluid to move through a material's pores or fractures (SI unit in $m\,s^{-1}$). For this study, three different methods to evaluate hydraulic conductivity were used to account for variability in the mechanical properties of different rock types including consolidated, unconsolidated/brecciated and fractured rocks.

Consolidated rocks

For consolidated rocks, air permeability (measured in milliDarcies or mD) of core plugs was evaluated using a transient gas permeameter (PPP-250; Core Lab Instruments, 2016) at the LOG. This instrument forces compressed air through 4 cm diameter and 8 cm long cores, and measures the pressure decay as the air infiltrates the rock. Recorded pressures are then plotted as a function of time to calculate air permeability. Permeability values are converted to hydraulic conductivity using a factor $1\ mD = 9.6 \times 10^{-9}\ m\,s^{-1}$ (Duggal and Soni, 1996), assuming water density and viscosity at ambient temperature. The PPP-250 was used to analyze 19 cores from the well and 16 outcrop samples. The instrument has a permeability measurement range of 0.01 to 5000 mD (9.6×10^{-11} to $4.8 \times 10^{-5}\ m\,s^{-1}$) under ideal operating conditions. However, measurements in the range of 1 to 2 mD (9.6×10^{-9} to $1.9 \times 10^{-8}\ m\,s^{-1}$) were assigned a value of <1 mD ($<9.6 \times 10^{-9}\ m\,s^{-1}$) due to difficulties in keeping rock surfaces pressurized. The hydraulic conductivity values for plugs analyzed by the PPP-250 are related to primary porosity, or porosity that existed when the rock was originally formed.

Unconsolidated rocks

Two unconsolidated rock samples were evaluated for hydraulic conductivity from a major breccia/fault zone in the well at a depth of 345 m. Hydraulic conductivity (K) was evaluated from the grain size distribution of the rock fragments (Alvarado Blohm *et al.*, 2016) using the following empirical equation (Beyer, 1966):

$$K = \frac{g \cdot 6\times10^{-4} \cdot log\left(\frac{500}{d_{60}/d_{10}}\right)}{\nu} \cdot d_{10}^{\,2} \qquad (1)$$

where g is the gravitational acceleration ($m\,s^{-2}$); v is the kinematic viscosity of water ($10^{-6}\ m^2\,s^{-1}$); d_{10} is the

diameter of the 10% passing particle size (mm); and d_{60} is the diameter of the 60% passing particle size (mm). The method assumes that the hydraulic conductivity of unconsolidated rocks is related to grain size distribution affecting pore connections, where smaller grains can fill voids in between larger grains. The hydraulic conductivity reported using this method represents a bulk value for the unconsolidated rocks that have been brecciated.

Fractured rocks

Natural open fractures provide preferential paths for groundwater flow. Fracture aperture and spacing can be used to calculate hydraulic conductivity associated with secondary porosity using the Cubic Law (Witherspoon *et al.*, 1979):

$$K = \frac{\rho \cdot g \cdot b^3 \cdot N}{12\,\mu} \qquad (2)$$

where ρ is the density of the rock matrix (kg m^{-3}); g is the gravitational acceleration (m s^{-2}); *b* is the width of the fracture (m); *N* is the total number of fractures per unit metre (m^{-1}); and μ is the dynamic viscosity of water (10^{-3} kg s^{-1} m^{-1}).

This method requires a manual count of natural fractures per unit distance (*N*) on cores and an estimation of fracture aperture (*b*). With this method, care must be taken not to count fractures that have occurred during or post drilling. For the Takhini core, each open fracture having mineral deposits (e.g., calcite, pyrite or chlorite precipitate) was assumed to be natural. Fracture aperture was not measured in core, as the measurements would not reflect the *in situ* conditions. Instead, aperture was assigned a constant value for the entire wellbore and the equation run for three aperture types: superfine, fine, or moderate-large. For this study, superfine was assigned apertures of 0.2 to 4 µm; fine assigned apertures of 4 to 100 µm; and moderate to large assigned a range of 100 to 3000 µm, based on studies by Witherspoon *et al.* (1979). Hydraulic conductivity values therefore are reported as ranges for each aperture type, with number of fractures per unit distance (*N*), which is the only variable in the equation. Further, this method assumes that fractures are interconnected and groundwater is flowing in every fracture observed.

Geological cross sections

Two cross sections were developed through the wellbore to help understand groundwater flow and heat transfer in the Takhini area.

Cross sections were made using data from existing geological maps (Yukon Geological Survey, 2018a,b), core from the Takhini well, and select outcrop samples. The extent of the cross sections was determined by the position of strategic water bodies such as the Takhini River, Takhini Hot Springs, Lake Laberge and Kusawa Lake as they represent flow boundaries (Fig. 5). Thermo-hydraulic properties measured from samples in the well and from outcrops were used to define potential regional ranges of values. All data were interpreted to define a conceptual hydrothermal model of the region.

Results

Takhini well lithology

The Takhini well is collared in volcanic and volcaniclastic rocks of the Jurassic (Pliensbachian) Nordenskiöld facies which occurs at varying stratigraphic levels within the Richthofen formation (Fig. 3). At the drill site, surface samples consist of medium to thickly bedded, poorly sorted, medium to coarse-grained sandstone having angular to subrounded grains consisting primarily of anhedral quartz and plagioclase, with up to 20% hornblende and minor chlorite. Surface bed orientation is ~162°/75° SW. In the vertical wellbore, bedding dips vary from 45 to 85° from horizontal.

The top 55 m of the well were drilled using a reverse circulation drill rig and therefore no core exists from this interval. The well can be divided into 6 main lithostratigraphic units–A to F (Fig. 6). Unit A (55.0–82.9 m depth) consists of volcaniclastic sandstone and basaltic tuff, which has been intruded by mafic dikes (gabbroic–monzodioritic) between 67.5 and 77.4 m depth. Volcaniclastic sandstone (Fig. 7a) has a distinctive green color, is mainly coarse grained, locally containing pebbles and granules, poorly sorted, and is either disorganized or massive in structure, although in areas some crude reverse grading is observed. Clasts are mainly subangular to subround and dominated by mafic volcanic grains, quartz and plagioclase. Tuff is

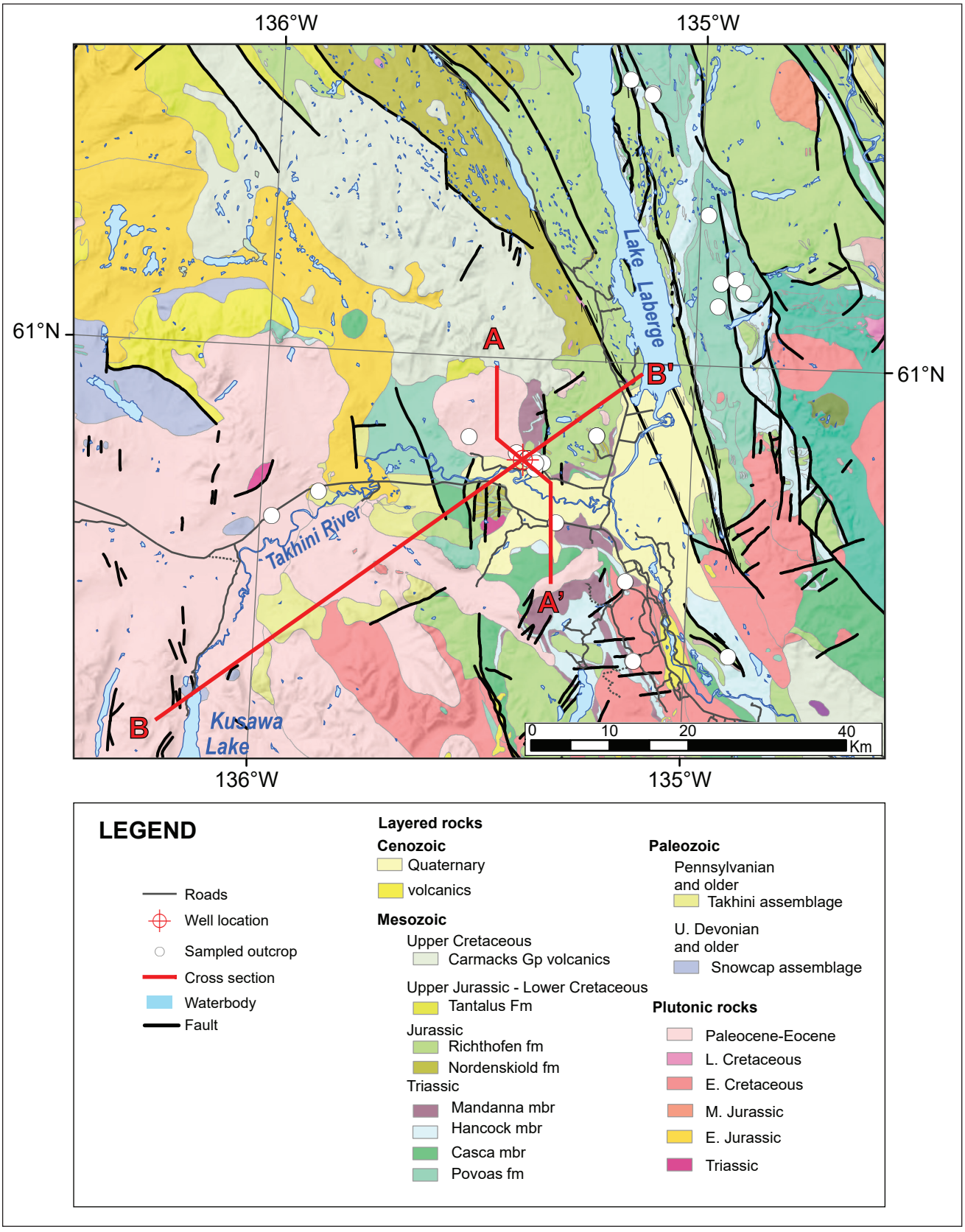


Figure 5. *Geology map in the vicinity of the Takhini well, and location of cross sections shown in Fig. 9. Geology from Yukon Geological Survey (2019a).*

olive green with black phenocrysts (carbonate and chlorite-replaced amphibole; Fig. 7f). Mafic dikes are dark grey with up to 25% black phenocrysts (altered plagioclase and hornblende).

Unit B (82.9–167.1 m) consists of medium and coarse volcaniclastic sandstone and minor shale. Sandstone is medium to olive-grey in color, poorly sorted, and similar in lithology to those of Unit A. Sandstone grain sizes range from fine to very coarse with coarse dominant, and shapes range from angular to subround. Pebbles and granules are rare in this unit. Crude normal grading can be observed as well as massive bedding. Shale occurs in an interval between 114.6 and 120.0 m and is black in colour, variably fractured, and cross cut by veins of calcite. The base of the unit is defined by a 10.8 m unit of highly deformed sandstone and mudstone, which shows evidence of synsedimentary deformation including load and flame structures and rip-up clasts.

Unit C (167.1–258.1 m) is a coarser grained version of Unit B that contains zones of pervasive carbonate alteration. Non-altered zones comprise mainly medium to coarse sandstone and pebbly sandstone that are medium grey to bluish grey in color. Clasts are mafic volcanic, quartz and plagioclase. Normal grading is observed in some intervals, while others have no apparent sedimentary structures. Carbonate altered zones are distinctively 'bleached' in appearance (Fig. 7b), are pale grey/green or grey/orange in color, and are either highly fractured or prominently cross cut with pale yellowish orange calcite veins. Carbonate is observed as matrix cement within these altered intervals.

Unit D (258.1–347.0 m) is a bluish-grey medium to very coarse volcaniclastic sandstone, variably granular, and lesser fine sandstone, siltstone and shale that is interspersed with brecciated fault zones. Sandstones

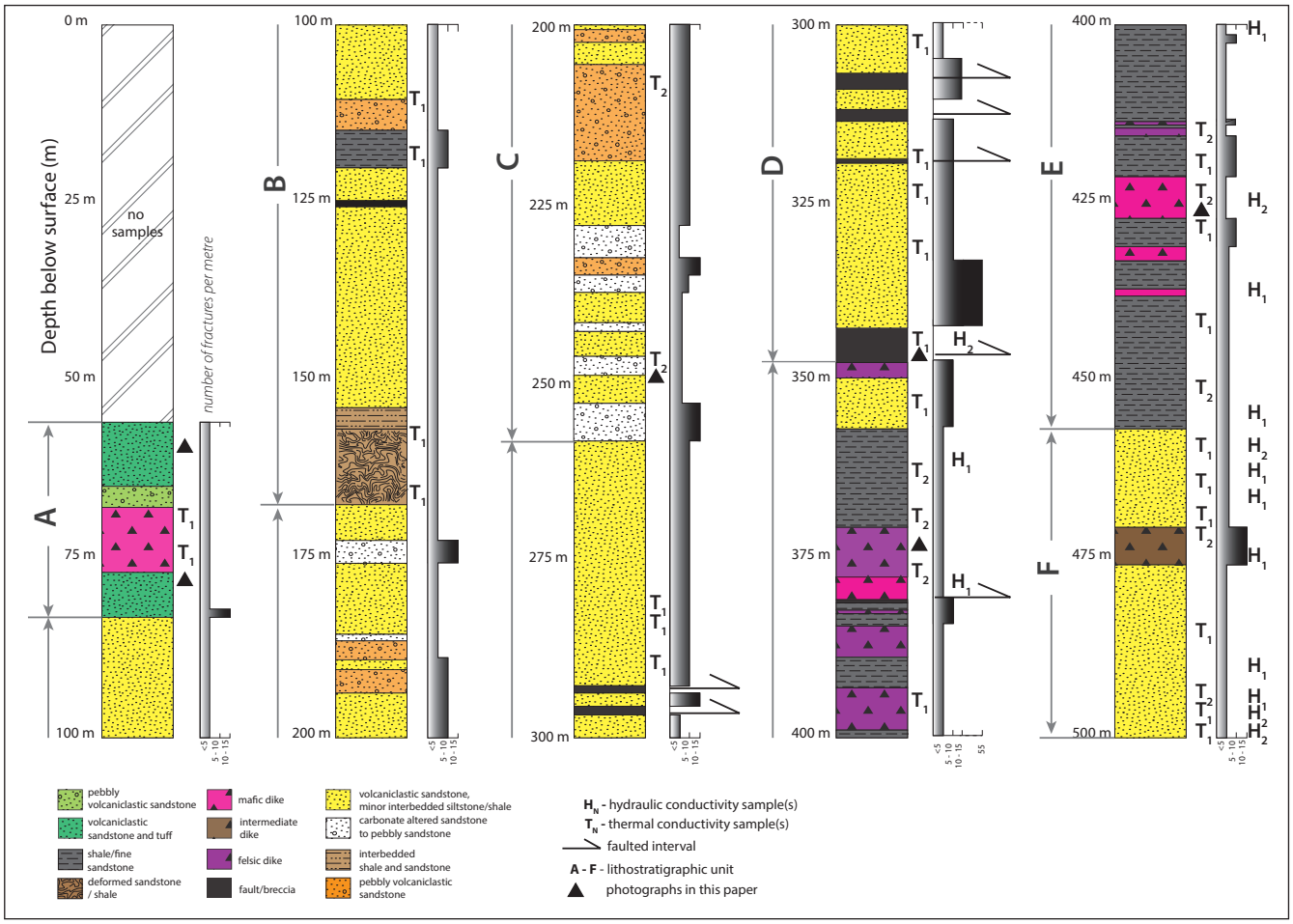


Figure 6. *Lithostratigraphy of the Takhini well including fracture density, and locations of samples for thermal and hydraulic conductivity measurements.*

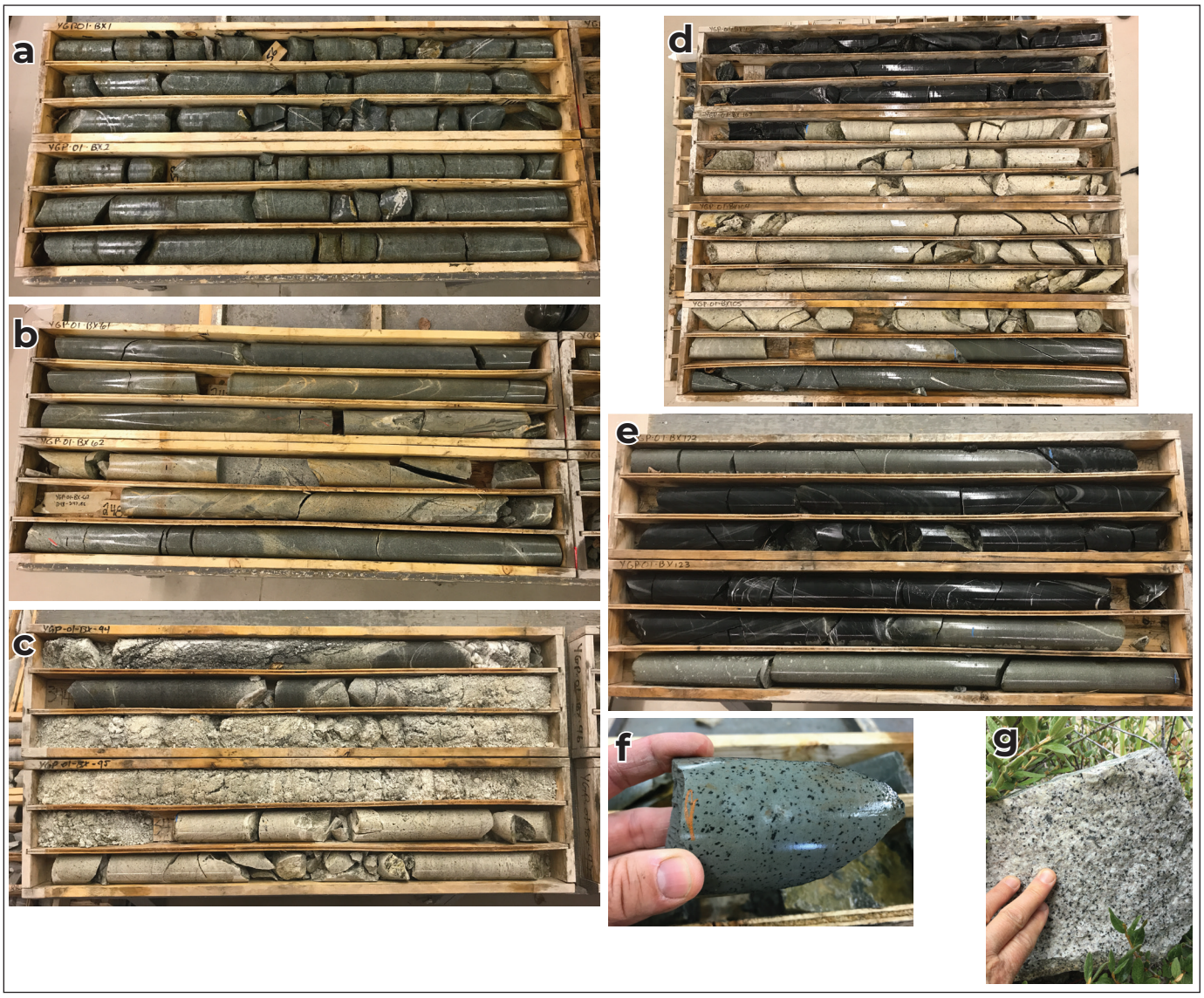


Figure 7. (a) *Volcaniclastic sandstone section from top of Unit A; depth shown 55.5–62.0 m.* ***(b)*** *Volcaniclastic pebbly sandstone (medium to dark grey) and carbonate altered volcaniclastic pebbly sandstone (light grey and Unit C depth (~243.5–250.1 m).* ***(c)*** *Fault zone at the base of Unit D depth (~343.0 – 348.8 m depth).* ***(d)*** *Shale host rock (dark rock in top box) cut by felsic dike (light colored rock) and a mafic dike (dark colored rock at base of Box 105) in Unit E. Depth interval shown ~366.5–379.0 m.* ***(e)*** *Shale host rock (dark rock in box) cut by mafic dikes (lighter colored rocks at top and bottom of boxes shown) in Unit E. Depth interval shown 426.5–433.2 m.* ***(f)*** *Basaltic tuff observed at 82.5 m depth in Unit A.* ***(g)*** *Granite outcrop from ~1.5 km NW of the Takhini well. This granite forms part of the Flat Creek pluton which is part of the Nisling Range plutonic suite.*

are poorly to moderately sorted, and comprise angular to subrounded altered quartz, plagioclase and mafic volcanic grains. Normally graded beds are pervasive in this unit. A thick (4.6 m) fault gouge interval defines the base of this unit (Fig. 7c), which comprises very soft and non-cohesive granular coarse sandstone containing considerable carbonate (in veins, where more cohesive, and in matrix).

Unit E (347.0–462.5 m) is a shale unit containing lesser interbedded siltstone and sandstone, which is cut by a series of mafic and felsic dikes. Felsic dikes occur above 414.1 m, are very light grey to yellowish-grey in color with black phenocrysts (Fig. 7d), and are granitic and fine-grained, with quartz and plagioclase minerals dominant, occurring as either phenocrysts or spherules. Plagioclase is often altered to carbonate. Minor minerals include white mica and scant cubic pyrite. Mafic dikes

are light bluish grey in color, gabbroic to monzogabbroic and occur more commonly below 421 m depth (Fig. 7e). These dikes are fine-grained, plagioclase-rich (in part altered to epidote) with minor hornblende (variably altered to chlorite) and biotite and up to 10% opaque minerals.

Unit F (462.5–500.0 m) is predominantly a coarse volcaniclastic sandstone succession and lesser fine sandstone and siltstone, which is cut by an intermediate dike. Sandstone is medium grey in color, and consists of poorly sorted angular to subangular quartz and plagioclase grains and minor plagioclase feldspar, mica, carbonate and chlorite. The core surface has a distinctive mottled appearance. Sedimentary structures can be observed where sandstone is interlaminated with silt and shale, as well as crude normal grading in some sandstone beds with scoured bed bases. An intermediate (borderline diorite/monzodiorite/monzogabbro) dike cross cuts the sandstone between 470.3 and 475.8 m. The dike comprises fine-grained plagioclase lathes and minor phenocrysts, as well as carbonate and mica, and rare opaque minerals. (Fig.6).

Thermal conductivity

Thermal conductivity averages and ranges for each lithology type in the Takhini well are reported in Table 1, and complete data sets are in Appendix A. Note that there is no data for the 'pebbly volcaniclastic sandstone' and 'volcaniclastic sandstone and mafic tuff' units (green units in Fig. 6), as the rock properties were deemed similar to the volcaniclastic sandstone, minor interbedded siltstone and shale unit (yellow unit in Fig. 6) of which 14 samples were taken. Thermal conductivity values in the well range from 0.63 to 4.19 $W\,m^{-1}\,K^{-1}$; the highest average value is in the deformed sandstone and shale unit (3.81 $W\,m^{-1}\,K^{-1}$),

Table 1. *Thermal conductivity of rock formations in the Takhini well.*

Lithology description	Lithology graphic	Average thermal conductivity ($W\,m^{-1}\,K^{-1}$)	Thermal conductivity (low; high) ($W\,m^{-1}\,K^{-1}$)	Number of samples
Deformed sandstone and shale		3.81	[3.43; 4.19]	1
Carbonate altered sandstone to pebbly sandstone		3.47	[3.05; 3.89]	3
Felsic dike		3.38	[3.18; 3.58]	5
Interbedded shale and sandstone		3.28	[2.95; 3.61]	1
Shale and fine sandstone		3.16	[2.32; 4.00]	7
Pebbly volcaniclastic sandstone		3.16	[3.02; 3.30]	3
Intermediate dike		3.06	[3.04; 3.08]	2
Volcaniclastic sandstone, minor interbedded siltstone and shale		2.94	[2.64; 3.24]	14
Mafic dike		2.39	[2.15; 2.63]	5
Fault/breccia		0.98	[0.63; 1.33]	2
Pebbly volcaniclastic sandstone		-	-	0
Volcaniclastic sandstone and mafic tuff		-	-	0

and the lowest average value is in the breccia unit (0.98 W m^{-1} K^{-1}). Generally, average values are between 3.0 and 4.0 W m^{-1} K^{-1}, except for the mafic dike and the fault/breccia units, which have values ≤ 2.4 W m^{-1} K^{-1}.

Hydraulic conductivity

Consolidated and unconsolidated rocks

Table 2 includes average hydraulic conductivity derived for consolidated and unconsolidated rocks. Figure 6 displays sample locations in the well and the comprehensive results are in Appendix B. Measurements made using the PPP-250 indicate a hydraulic conductivity generally $<9.6 \times 10^{-9}$ m s^{-1} for consolidated rocks, and having a maximum of 1.6×10^{-7} m s^{-1}.

For brecciated rock samples at a depth of 345 m, hydraulic conductivity measures 8.3×10^{-4} and 2.9×10^{-4} m s^{-1} (Table 2), which were averaged to 5.6×10^{-4} m s^{-1} for comparison with results obtained from other methods.

Fractured rocks

Fracture spacing ranges from 2 to 52 fractures per metre along the well, with most values <10 (Fig. 6). Ranges of hydraulic conductivity of fractured rocks are shown in Figure 8. Overall values for the entire well are on the order of 10^{-14}–10^{-10} m s^{-1} for superfine apertures, 10^{-10}–10^{-6} m s^{-1} for fine apertures, and 10^{-6}–10^{-1} m s^{-1} for moderate to large apertures. For fractures having ~100 µm apertures (lower part of moderate), the values are on the same order of magnitude as the unconsolidated rocks of the breccia/fault zone in the well at a depth of 345 m (~10^{-4} m s^{-1}; Table 2).

The highest value of hydraulic conductivity related to fracture porosity is in a well-fractured interval (52 fractures per metre) at a depth of 332–341 m in a volcaniclastic sandstone with minor siltstone and shale unit (yellow on Fig. 6). For this interval, hydraulic conductivity is: 3.4×10^{-13} to 2.8×10^{-9} m s^{-1} for a superfine fracture aperture (0.2–4 µm); 2.8×10^{-9} to 4.3×10^{-5} m s^{-1} for fine fracture aperture (4–100 µm); and 4.3×10^{-5} to 1.2×10^{0} m s^{-1} for a moderate to large fracture aperture (100–3000 µm; Fig.8). The lowest hydraulic conductivity related to fracture porosity occurs in the lower part of the well at a depth of 465 m in a volcaniclastic sandstone with minor siltstone and shale unit having 2.2 fractures per metre. Hydraulic conductivity calculated for a superfine fracture aperture at this depth ranges from 1.4×10^{-14} to 1.2×10^{-10} m s^{-1}, for fine fracture apertures range from 1.2×10^{-10} to 1.8×10^{-6} m s^{-1} and for moderate to large fracture aperture from 1.8×10^{-6} to 4.9×10^{-2} m s^{-1} (Fig. 8). Results are subject to an important variability since fracture aperture is hardly measurable on core samples.

Table 2. *Hydraulic conductivity of consolidated and unconsolidated rocks in the Takhini well.*

Rock Type	Lithology	Well Depth (m)	Hydraulic conductivity (m s^{-1})
Consolidated		302.83 - 303.07	$<9.6 \times 10^{-9}$
		325.16 - 325.34	$<9.6 \times 10^{-9}$
		363.17 - 363.32	$<9.6 \times 10^{-9}$
		378.89 - 379.09	$<9.6 \times 10^{-9}$
		401.86 - 402.08	$<9.6 \times 10^{-9}$
		423.03 - 423.18	$<9.6 \times 10^{-9}$
		424.58 - 424.76	1.6×10^{-7}
		439.86 - 440.00	7.4×10^{-8}
		455.00 - 455.25	$<9.6 \times 10^{-9}$
		459.27 - 459.43	$<9.6 \times 10^{-9}$
		461.44 - 461.59	$<9.6 \times 10^{-9}$
		462.85 - 463.00	$<9.6 \times 10^{-9}$
		467.00 - 467.15	$<9.6 \times 10^{-9}$
		475.00 - 475.28	$<9.6 \times 10^{-9}$
		485.95 - 486.10	$<9.6 \times 10^{-9}$
		493.10 - 493.25	$<9.6 \times 10^{-9}$
		496.40 - 496.50	$<9.6 \times 10^{-9}$
		497.00 - 497.15	$<9.6 \times 10^{-9}$
Uncon-solidated		497.84 - 498.00	$<9.6 \times 10^{-9}$
		345.32 - 345.52	2.9×10^{-4}
		346.00 - 346.20	8.3×10^{-4}

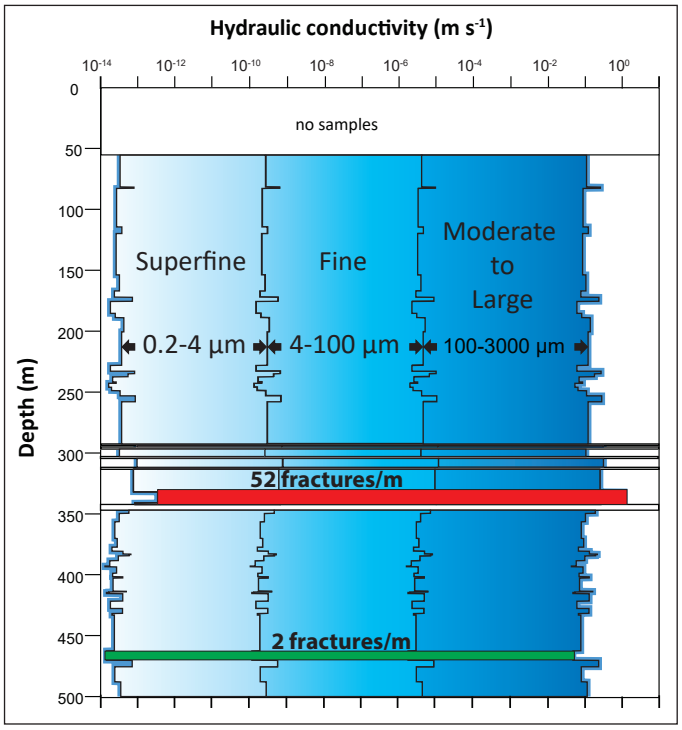


Figure 8. *Hydraulic conductivity of fractured rocks in the Takhini well analyzed for superfine, fine, and moderate-to-large fracture aperture.*

Geological cross sections

Interpreted cross sections A–A' and B–B' (Figs. 5 and 9a,b) show the distribution of geological units influencing heat transfer and groundwater flow in the vicinity of the Takhini well. Basement rocks consist of variably deformed and metamorphosed greenschist of the Takhini assemblage. Triassic-Jurassic sedimentary sequences and volcaniclastic strata overlie the Takhini assemblage. Steeply dipping north trending normal faults separate the sedimentary basin into segments as a result of regional tectonic activity in pre-Late Cretaceous time (Hart, 1997). Eocene granitic and granodioritic plutons intruded Triassic-Jurassic sedimentary sequences and volcaniclastic strata (Hart, 1997). Fault extensions and thickness of rock units at depth are interpretive due to the lack of geophysical or deep well data in this area.

Discussion

Geological interpretation of the Takhini well

Lithology in the Takhini well is assigned to Lower Jurassic Laberge Group sediments that have been intruded by younger plutonic rocks and subjected to faulting. Sandstones are immature and have a high concentration of poorly sorted angular to subrounded volcanic fragments, feldspar and quartz, and have crude sedimentary structures, both primary and secondary. These rocks are similar in description to sandstones interpreted as distal Laberge Group exhibiting characteristics of deposition from turbidity currents and subject to substantial post-depositional reworking based upon outcrop on the shore of Lake Laberge (Hutchison, 2017), ~30 km northwest of the Takhini site. Laberge Group sediments were deposited in a forearc basin derived from the exhumation of flanking arc terranes when orogenesis was beginning in the southern Canadian Cordillera (Pliensbachian and later; Colpron *et al.*, 2015). The majority of the sandstone and shale in the well is currently assigned to the Richthofen formation. However, the immaturity of the sandstone and the presence of crystal tuff, particularly in the upper part of the well (55–80 m), suggests a proximal volcanic source and some of these units may be assigned to the Nordenskiöld formation. The Nordenskiöld formation is defined by a series of crystal tuff layers within the Laberge Group varying from 50–350 m thick that are Jurassic in age (Sinemurian to Pliensbachian; 190.5 ± 1.5 Ma weighted average; Colpron *et al.*, 2015). The tuff layers comprise mainly coarse-grained (2–4 mm) euhedral feldspar, quartz, having broken corners, and fewer fine-grained (1–2 mm) hornblende and biotite crystals containing sparse lithic grains (Hart, 1997). Part of this unit may have a strong sedimentary character, which is interpreted as reworked older tuff horizons. Further studies are required to delineate the exact assignment of these rocks to either the Nordenskiöld or the Richthofen formations.

Cross cutting the Laberge Group sediments are felsic and mafic dikes most commonly observed in the lower part of the well in Unit E, but there is also an intermediate dike in Unit F, and a mafic dike in Unit A.

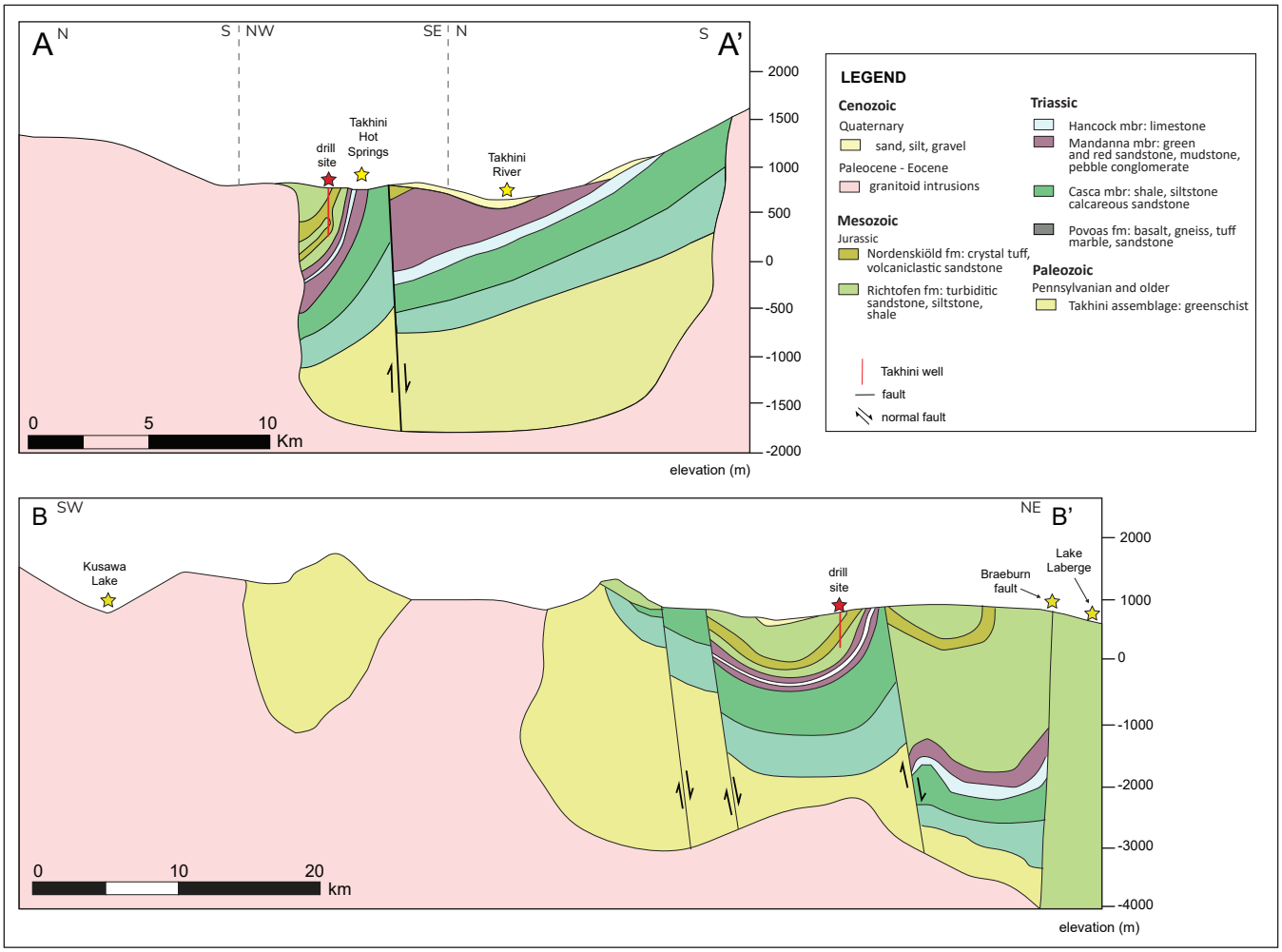


Figure 9. (a) *Cross section A-A' showing the geological interpretations in the vicinity of the Takhini well. Location of cross section in Figure 5. Geology after Hart (1997) and Colpron et al. (2015).* ***(b)*** *Cross section B-B' showing the geological interpretations in the vicinity of the Takhini well. Location of cross section in Figure 5. Geology after Hart (1997) and Colpron et al. (2015).*

It is unknown at this time if these intrusive rocks are coeval, or if they are related to the pluton that crops out to the west of the well (Fig. 5), which is Eocene in age (53.6 ± 0.2 Ma) and associated with older fault reactivation due to regional tectonic stress (Hart, 1997). There is evidence in the well that faulting occurred post dike emplacement. For example, there is a faulted upper contact of a felsic dike interval at a depth of 342 m. However, cross cutting relationships are not always observed, and future radiogenic dating of the rocks would provide meaningful age constraints.

Heat Transfer Mechanisms

Temperature measurements and analysis of thermo-hydraulic properties in the Takhini well indicate that conduction and forced convection are the main heat transfer mechanisms occurring in the upper and lower parts of the well, above and below 450 m, respectively.

The faint thermal conductivity contrasts among units associated with a smooth and near-linear temperature profile above 450 m depth is characteristic of heat conduction. Thick formations of low thermal conductivity, generally <2 $W\,m^{-1}\,K^{-1}$, can induce a thermal blanket effect and increase the geothermal gradient. This insulating effect is not observed in the well because there is no lithology that has such a low thermal conductivity, except for the breccia unit (0.98 $m^{-1}\,K^{-1}$) that only covers 2% of the well length.

Conductive heat transfer cannot explain the high temperature gradient of 250°C km^{1} observed below 450 m depth as thermal conductivity contrasts of the host rock are similar to the rocks above. The temperature anomaly in the lower part of the well is instead interpreted as forced-convective heat transfer due to deep groundwater rising along fractures. The assessment of hydraulic properties confirms this hypothesis. Sass and Götz (2012) suggest that transitional states of natural convective to forced convective heat transfer can occur in rocks within high (10^{-5} m s^{-1}) to low (10^{-9} m s^{-1}) hydraulic conductivity, while conductive heat transfer mostly occurs in rocks of low hydraulic conductivity (<10^{-9} m s^{-1}; Fig. 10). The matrix hydraulic conductivity of rock samples in the Takhini well and surrounding outcrops commonly have values <9.6×10^{-9} m s^{-1} which indicates that heat convection can only occur in fractured and unconsolidated rocks, where hydraulic conductivity was confirmed higher. Figure 10 shows that fine to large fracture apertures can be sufficient to allow different transitional states of forced convective to auto convective heat transfer. A large aperture for all fractures is, however, unlikely.

Natural or auto convection responsible for groundwater movement can only occur under significant temperature contrasts in rocks having high hydraulic conductivity (Sass and Götz, 2012). For example, this can occur in a volcanic environment, where deep groundwater flow in permeable formations is driven by fluid buoyancy due to shallow magmatic intrusions. On the other hand, forced convection implies groundwater flow driven by hydrostatic pressure variations in an aquifer system that can be of moderate hydraulic conductivity. An example of this scenario is where topographic highs in a mountain range act as a recharge zone for water that discharges in lower altitude valleys. Groundwater flow can thus be controlled by the regional hydraulic gradient caused by topography when there is adequate fracture connectivity in the host rock. Fractures and unconsolidated rocks in the well have a hydraulic conductivity that is at least greater than 10^{-9} m s^{-1}. This can lead to forced convective heat transfer and trigger the formation of a hydrothermal system giving rise to hot springs, provided that fractures are interconnected. The Takhini well and the hot spring are located in a trough having important topographic contrasts (Fig. 9a,b), where the difference in elevation (~500 m over ~15 km distance) can cause such a strong hydraulic gradient. However, the Takhini well represents a relatively small window to assess hydraulic properties and does not provide sufficient information to evaluate fracture connectivity. Consequently, it is difficult to correlate any permeable zones observed in the core samples of the Takhini well with the high geothermal gradient at the bottom of this well (>450 m). The forced convective heat transfer hypothesis remains the most plausible. Assuming that faults and fractures are interconnected, regional groundwater flow can be directed toward the Takhini River and upflow can occur along faults, creating resurgence under the Takhini well near the river, a major waterbody collecting groundwater.

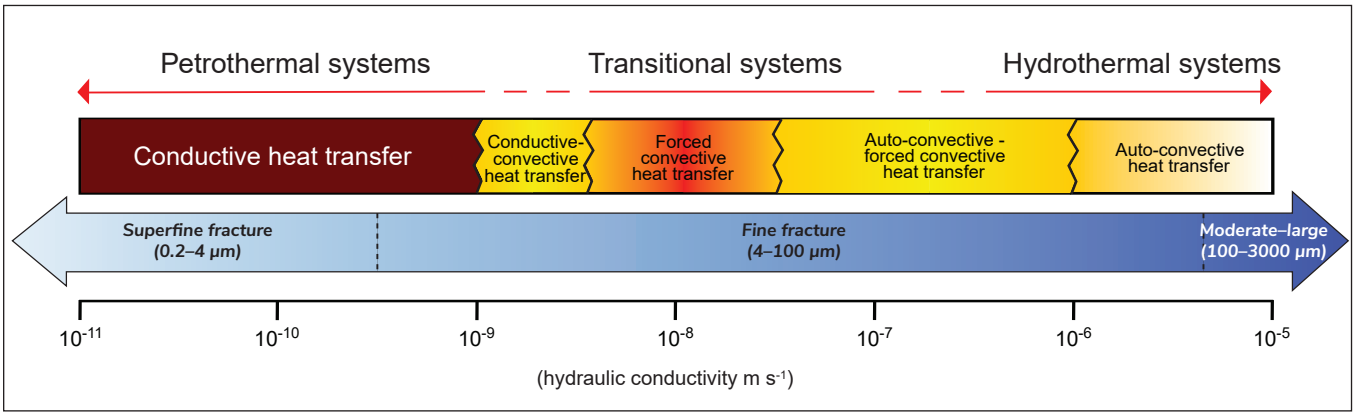


Figure 10. *Generalized characterization of geothermal systems based on major mechanism of heat transfer (convective vs conductive; after Sass and Götz, 2012).*

Conceptual Hydrothermal Model

The geological setting in the Takhini area is typical of an orogenic belt, where conductive and forced convective heat transfer can occur (Moeck et al. 2014). Geological features, such as steeply dipping crustal faults, can favour forced convective heat transfer as they are preferential paths for rising warm groundwater. Figure 11 shows schematic isotherms and water flow line interpretations based on the main recharge areas and major faults. The primary groundwater recharge areas are associated with elevated mountainous regions and the discharge dominantly occurs near the Takhini River. From recharge to discharge, groundwater tends to flow through permeable rocks. Several north-trending steep normal faults cut strata in the Takhini area (Hart, 1997). One of these faults is at the center of the hydrothermal model. This major feature can affect the groundwater flow path as it is believed to be more fractured and permeable than rocks outside the fractured zone. Due to the hydraulic head difference between the top and the base of the fracture, deep water can rise along the fault to create shallower isotherms. This can form hot springs like Takhini Hot Springs where well-connected fractures allow a constant groundwater discharge.

Conclusions

This study has defined the thermo-hydraulic properties of rocks in, and within, the vicinity of the Takhini temperature gradient well in southern Yukon. These data are co-interpreted with the measured temperature gradient at this well and offers explanations for mechanisms of heat transfer in the subsurface. In addition, a conceptual hydrothermal model of the Takhini area is presented. The thermal conductivity results show that conductive heat transfer dominates the well to a depth of 450 m, as the temperature profile is near-linear and thermal conductivity contrasts are faint. The elevated geothermal gradient observed at the bottom of the Takhini well (250°C km^{-1}) and the thermal manifestations at Takhini Hot Springs are likely caused by forced convective heat transfer associated with deep groundwater flow in permeable fractures generating a hydrothermal system typical of a geothermal play type in an orogenic belt (Fig. 11).

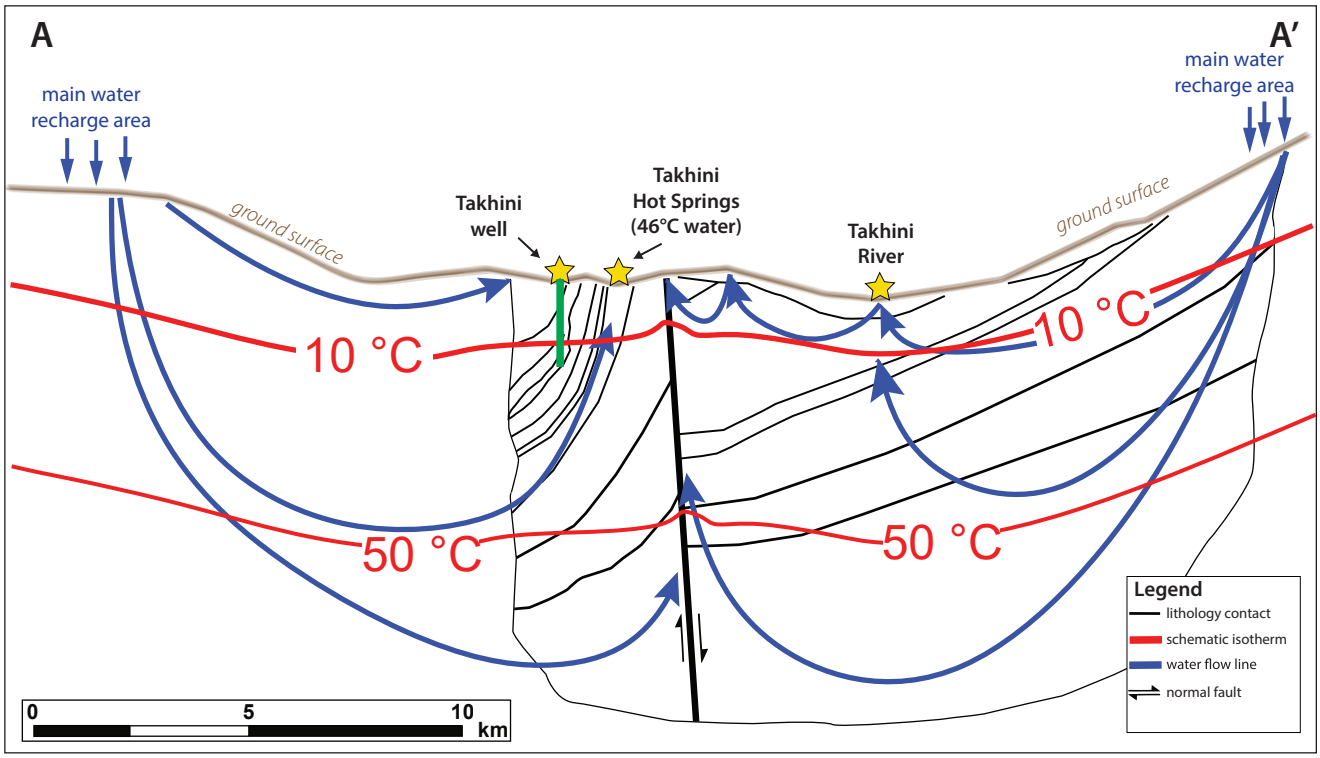


Figure 11. *Interpreted hydrothermal system of the Takhini Hot Springs area according to geothermal play types in orogenic belts; after Moeck, (2014).*

The ~2 km lateral distance between warm water at the bottom of the Takhini well and the Takhini Hot Springs can give an idea about the potential extent of this warm fluid reservoir, assuming there is interconnectivity of fractures between those sources. However, further work is needed to assess the extension and the interconnectivity of those water sources.

Assessment of the thermal conductivity can be used with additional calculated radiogenic heat values from intrusive bodies in the region as a next step to evaluate heat flow and extrapolate temperature at depth. Quantifying the natural amount of heat originating from the Earth interior and based on Fourier's Law, the heat flux density is needed to define boundary conditions of numerical groundwater flow and heat transfer models to quantitatively confirm the heat transfer hypotheses formulated in this work. Such an approach would be helpful to improve understanding of the origin of the Takhini Hot Springs. These models can be used to reproduce the temperature measured in the Takhini well or at the hot spring to better explain the factors controlling the formation of the hydrothermal system.

The Yukon geological context shows potential for geothermal energy with many hot springs like Takhini. Geothermal exploration done by the YGS provides more data to evaluate this potential around the hot springs. Further calculation and simulations with the measurements obtained with this study will bring a better comprehension of resources to move towards the exploitation of geothermal energy in this region.

Acknowledgements

The Takhini well was drilled on Category A land of the Ta'an Kwäch'än Council. We are grateful for the opportunity to work with this Yukon First Nation, and for access to their land in summer 2019 to evaluate outcrops. This work was funded by a Discovery grant from the Natural Sciences and Engineering Research Council of Canada awarded to INRS and a scholarship from the Armand-Frappier Foundation awarded to the first author. Jeff Witter of Innovate Geothermal Inc. is acknowledged for reviewing this paper. Maurice Colpron (YGS) provided field, technical, and GIS guidance for which we are appreciative. Liam Maw is acknowledged for thin section descriptions.

References

Alvarado Blohm F.J., Urzua, A., Ebel, J. and Kafka, A., 2016. Determination of hydraulic conductivities through grain-size analysis. MSc thesis, Boston College University Libraries, Chestnut Hill, United States, p. 102.

Artemieva, I.M., Thybo, H., Jakobsen, K., Sørensen, N.K. and Nielsen, L.S.K., 2017. Heat production in granitic rocks: Global analysis based on a new data compilation GRANITE2017. Earth Science Reviews, vol. 172, p. 1–26.

Beyer, W. 1966. Hydrogeological investigations in the deposition of water pollutants. Journal of Applied Geology, vol. 12, p. 599–606.

Colpron, M., Crowley, J.L., Gehrels, G.E., Long, D.G.F., Murphy, D.C., Beranek, L.P. and Bickerton, L., 2015. Birth of the northern Cordilleran orogen, as recorded by detrital zircons in Jurassic synorogenic strata and regional exhumation in Yukon. Lithosphere, vol. 7, p. 541–562.

Colpron, M., 2019. Potential radiogenic heat production from granitoid plutons in Yukon. Yukon Geological Survey, Open File 2019-16, 1 map and data.

Core Lab Instruments, 2016. PPP-250 Portable probe permeameter operations manual. Core Lab Instruments. Tulsa, United States, p. 6.

Decagon Devices Inc., 2012. KD2 Pro Thermal properties analyser: operator's manual, version 12. Decagon Devices Inc., Pullman, United States, p. 68.

Duggal, K.N. and Soni, J.P., 1996. Elements of Water Resources Engineering. New Age International (P) Limited, p. 270.

Fraser, T.A., Grasby, S.E., Witter, J.B., Colpron, M. and Relf, C., 2018. Geothermal studies in Yukon-collaborative efforts to understand ground temperature in Canadian North. GRC Transactions, vol. 42, 20 p.

Fraser, T., Colpron, M. and Relf, C., 2019. Evaluating geothermal potential in Yukon through temperature gradient drilling. *In:* Yukon Exploration and Geology 2018, K.E. MacFarlane (ed.), Yukon Geological Survey, p. 75–90.

Hart, C.J.R., 1997. A transect across northern Stikinia: Geology of the northern Whitehorse map area, southern Yukon Territory (105D/13-16). Yukon Geological Survey, Bulletin 8, p. 112.

Hasterok, D. and Webb, J., 2017. On the radiogenic heat production of igneous rocks. Geoscience Frontiers, vol. 8, https://doi.org/10.1016/j.gsf.2017.03.006

Hutchison, M.P., 2017. Whitehorse trough: Past, present and future petroleum research – with a focus on reservoir characterization of the northern Laberge Group. Yukon Geological Survey, Open File 2017-2, 48 p. plus appendices and plates.

Moeck, I.S., 2014. Catalog of geothermal play types based on geologic controls. Renewable and Suitable Energy Reviews, vol. 37, p. 867–882. https://doi.org/10.1016/j.rser.2014.05.032

Popov, Y.A., Pribnow, D.F.C., Sass, J.H., Williams, C.F. and Burkhardt, H., 1999. Characterization of rock thermal conductivity by high-resolution optical scanning. Geothermics, vol. 28, p. 253–276.

Rybach, L. 1981. Geothermal systems, conductive heat flow, geothermal anomalies. In: Geothermal systems: principles and case histories, Muffler LJP. Rybach, L. (eds), John Wiley & Sons, New York.

Sass, I. and Götz, A.E., 2012. Geothermal reservoir characterization: a thermofacies concept. Blackwell Publishing: Terra Nova, vol. 24, p. 142–147, https://doi.org/10.1111/j.1365-3121.2011.01048.x.

TCS, 2017. Thermal Conductivity (TC) and Thermal Diffusivity (TD) Scanner, manual. Lippmann and Rauen, Schaufling, Germany, p. 53.

Witherspoon, P.A., Wang, J.S.Y., Iwai, K. and Gale, J.E., 1979. Validity of Cubic law for fluid flow in a deformable rock fracture. University of California, Berkeley, p. 28.

Witter J.B., Miller C.A., Friend M. and Colpron, M., 2018. Curie Point Depths and Heat Production in Yukon, Canada. Proceedings of the 43rd Workshop on Geothermal Reservoir Engineering, Stanford University, Stanford, California, February 12–14, 11 p.

Yukon Geological Survey, 2018a. Bedrock geology data set. Yukon Geological Survey, https://data.geology.gov.yk.ca/Compilation/3, accessed Nov. 2019.

Yukon Geological Survey, 2018b. Surficial geology data set. Yukon Geological Survey, https://data.geology.gov.yk.ca/Compilation/33, accessed Nov. 2019.

Government of Yukon, 2019. Draft of our clean future: a Yukon strategy for climate change, energy and a green economy. Government of Yukon, Whitehorse, Canada, p. 61.

Appendices

The appendices are only available as digital files. They are included in a .zip file that accompanies this document, and are available from https://data.geology.gov.yk.ca/.

Appendix A. (1) Thermal conductivity scanner measurements for consolidated rocks using a Lippman and Rauen thermal conductivity scanner (TCS, 2017). **(2)** Thermal conductivity needle probe measurements for unconsolidated rocks with the K2D Pro needle probe (Decagon Devices Inc., 2012).

Appendix B. (1) Hydraulic conductivity measurements for consolidated rocks using a transient gas permeameter (PPP-250; Core Lab Instruments, 2016). **(2)** Hydraulic conductivity measurements for unconsolidated rocks from the grain size distribution (Beyer, 1966).

Updated geology and porphyry copper potential of the Klaza deposit, Mount Nansen district (Yukon MINFILE 115I 067)

W.-S. Lee*, D.J. Kontak and J.P. Richards†
Harquail School of Earth Sciences, Laurentian University

P. Sack
Yukon Geological Survey

Lee, W.-S., Kontak, D.J. Richards, J.P. and Sack, P., 2020. Updated geology and porphyry copper potential of the Klaza deposit, Mount Nansen district (Yukon MINFILE 115I 067). *In:* Yukon Exploration and Geology 2019, K.E. MacFarlane (ed.), Yukon Geological Survey, p. 75–97.

Abstract

Porphyry to epithermal deposit models are inferred to best describe the Late Cretaceous Klaza Au-Ag-Pb-Zn-(Cu) deposit. Here we report evidence for a protracted and complex magmatic-hydrothermal system typical of porphyry-epithermal deposits (e.g., multiple magmatic events, magma mingling, relevant vein-alteration types). In the Klaza area, there are at least four compositionally and texturally distinct intrusions interpreted as part of the Casino intrusive suite (ca. 80–76 Ma) that intrude granodiorite country rock of the Whitehorse suite (ca. 105 Ma). A ca. 72 Ma dike swarm (likely Prospector Mountain suite) was emplaced approximately 4–5 m.y. after emplacement of the Casino suite. Evidence of high-T hydrothermal activity consists of early dark micaceous (EDM) veins, sinuous and planar A-type veins, B-type, and D-type veins, and molybdenite-quartz veins. Composite epithermal-type sulphide veins cut high-T Cu-Au-Mo mineralization associated with phyllic and lesser potassic alteration assemblages. The age of porphyry-type mineralization is constrained by ^{187}Re-^{187}Os molybdenite dating to ca. 77 Ma (Kelly) and ca. 71 Ma (Cyprus). The ^{40}Ar-^{39}Ar muscovite dates from phyllic alteration in the Central Klaza zone yield ages of ca. 77 Ma. These field observations, integrated with archival Cu-Au-assay data, suggest the Klaza epithermal veins are located in the phyllic alteration shell of a two-stage Cu-Au-Mo porphyry system. It is possible that the Klaza epithermal veins represent a Prospector Mountain-age porphyry–epithermal system overprinting a Casino-age porphyry system.

* wlee1@laurentian.ca

† deceased, June 7, 2019

Introduction

The Late Cretaceous Klaza Au-Ag-Pb-Zn-(Cu) deposit is located within the historic Mount Nansen gold camp (MNGC; Fig. 1), 70 km from the village of Carmacks, Yukon. It has a current combined (indicated and inferred) mineral resource of 4.457 Mt of 4.8 g/t Au, 98 g/t Ag, 0.7% Pb, and 0.9% Zn (Ross et *al*., 2018). The dominant mineralization style at Klaza consists of 0.2 to 8 m wide polymetallic veins having drill-indicated strike lengths of 300 to 2500 m and vertical depths from surface of at least 500 m (Turner and Dumala, 2016). This vein system has been compared to the past-producing Brown McDade/Mount Nansen veins and to a porphyry to epithermal model for the MNGC (Hart and Langdon, 1997; Mortensen et *al*., 2016). This paper provides new geological insights into the current understanding of the Klaza deposit model as supported by new geochronologic data and supporting field constraints (work done in 2017 and 2019), with derived paragenetic reconstructions based on field and petrographic observations in addition to assessing metal zonation at the deposit scale. This information is collectively used to assess the metal endowment of Klaza and its potential as a porphyry-type deposit.

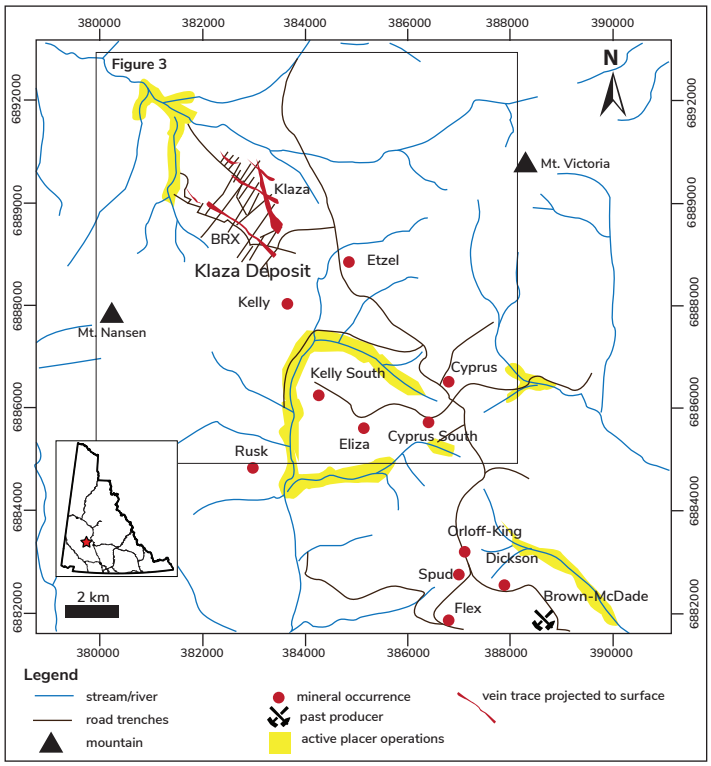


Figure 1. *Geographic map of Klaza–Mt. Nansen district displaying placer-bearing streams (Yukon Mining Recorder placer claim map sheet 115I03P), mineral occurrences, and roads.*

Regional geology

The MNGC is located in the southeastern end of the Dawson Range gold belt (Fig. 2) which stretches from the Yukon-Alaska border to within 50 km of the town of Carmacks, Yukon (Allan et *al*., 2013). Basement rocks in the MNGC comprise Devonian and older metamorphosed volcaniclastic and sedimentary rocks of the parautochthonous Yukon-Tanana terrane, accreted to the Laurentian margin between the Late Triassic and Early Jurassic, during east-dipping subduction (Allan et *al*., 2013; Nelson et *al*., 2013). This subduction event emplaced the regionally extensive Long Lake suite and Minto suite plutons. Porphyry-type systems, such as Minto (60 Mt at 1% Cu and 0.4 g/t Au; Allan et *al*., 2013) and Carmacks Copper (15.69 Mt oxide at 1% Cu, 0.4 g/t Au, and 4 g/t Ag; 8.07 Mt sulphide at 0.7% Cu, 0.2 g/t Au, and 2.3 g/t Ag; Kovacs et *al*., 2017), formed around the Late Triassic (Kovacs et *al*., *in press*).

Renewed east dipping subduction led to the emplacement of the *ca*. 105 Ma Dawson Range batholith (Whitehorse plutonic suite; 112–98 Ma) and the coeval Mount Nansen volcanic package in the mid-Cretaceous (115–110 Ma; Klöcking et *al*., 2016). Continued east-dipping subduction in the Late Cretaceous led to the emplacement of the Casino plutonic suite (78–74 Ma) and related cluster of porphyry-epithermal systems (Casino, Cash, Nucleus, Revenue, Sonora Gulch) within the Dawson Range belt (Allan et *al*., 2013; Nelson et *al*., 2013). The Casino plutonic suite is less voluminous than the Whitehorse suite, although it occurs regionally throughout the Dawson Range gold belt in the form of porphyritic dikes and stocks. The most economically important of these is the Patton porphyry, which is associated with the Casino porphyry deposit (1057 Mt at 0.2% Cu, 0.23 g/t Au and 0.022% Mo; Allan et *al*., 2013). Quartz-feldspar-porphyry (QFP) dikes yielding ages of 77–74 Ma are also reported at Sonora Gulch, the Freegold district, and the Mount Nansen district (Allan et *al*., 2013; Bennett, 2010; Bineli-Betsi and Bennett, 2010; Bineli-Betsi et *al*., 2013; Mortensen et *al*., 2016).

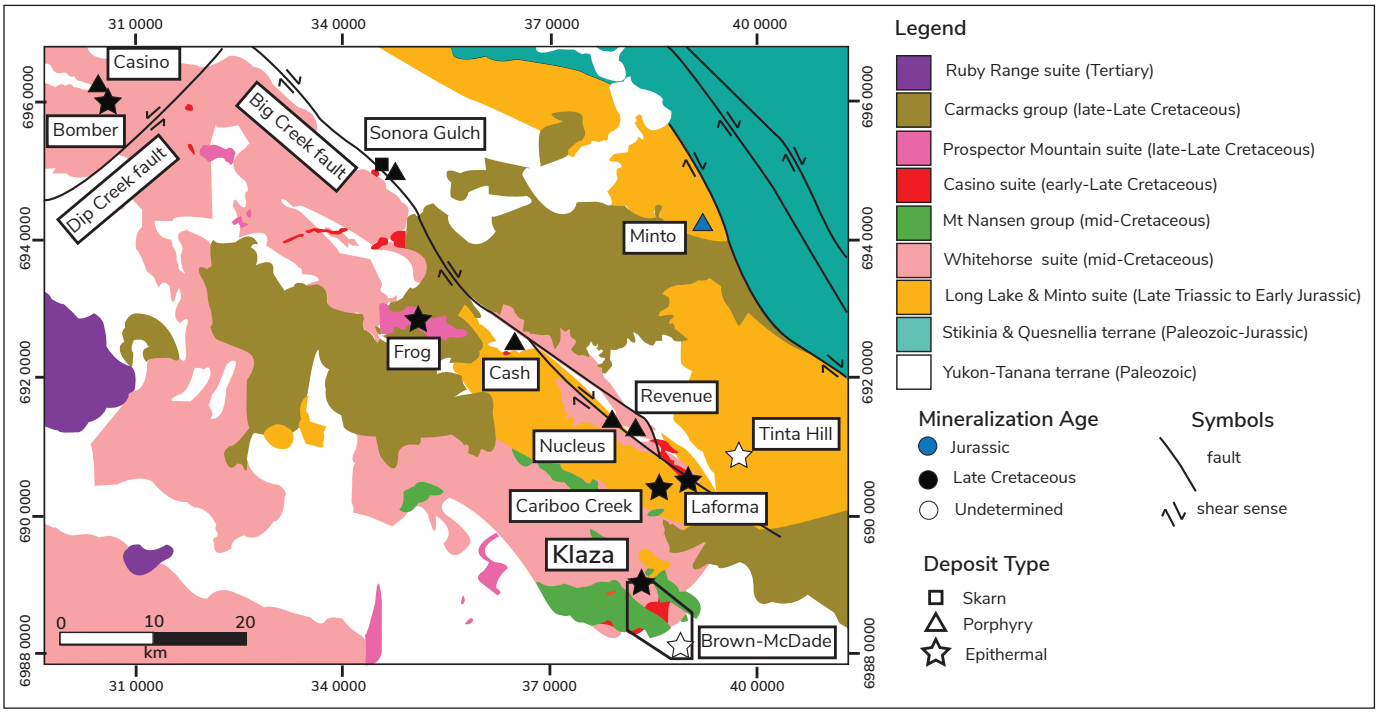


Figure 2. *Regional geologic map of the mid to southern Dawson Range, Yukon. UTM Zone 08, Datum: NAD 83. Map modified from Yukon Geological Survey digital map version April 2018.*

Soon after emplacement of the Casino suite, the composition of the magma became slightly more alkalic; it consists of both volcanic (Carmacks group) and shallow plutonic (Prospector Mountain suite) components. The Prospector Mountain suite and the coeval porphyry-epithermal prospects of Frog and Lilipad were emplaced from 69–67 m.y. (Allan et *al.*, 2013). Several porphyry-epithermal systems of Late Cretaceous age are localized on, or near, the Big Creek fault, a northwest trending transcrustal structure located on the northern margin of the Dawson Range batholith. Systems farther away from the fault, such as Casino, Tinta Hill and Klaza–Mt. Nansen display the same northwest structural trends.

Methodology

Ten days of fieldwork were conducted in August 2019 comprising: (1) re-logging and sampling of Cu-rich archival drill core from the eastern part of the deposit; and (2) traverses to the northeast and southwest extents of the Klaza property. Representative samples of least altered and altered intrusive rocks were cut and stained for K (*i.e.*, K-feldspar, biotite, sericite) using cobaltinitrite staining at a commercial lab. Least altered and weathered intrusive rock samples were from core drilled far from mineralization or found in trenches across the property. Images of the stained rocks were processed utilizing Image J software to estimate abundance of plagioclase, quartz, and K-feldspar. A preliminary classification of the intrusive rocks is made based on the modal mineralogy. Sulphide paragenesis and element distribution in vein stages were investigated using a combination of optical microscopy, SEM-EDS, and LA-ICP-MS analysis, the detailed results of which will be presented elsewhere.

We present an updated geologic map for the Klaza area in Figure 3a. Structure is constructed from a combination of drillhole constraints and VLF-IP data (very low frequency electromagnetic survey and induced polarization survey; Fig. 3b). Limitations in geological and geophysical information are highlighted in Figure 3c. Outcrop and subcrop information from Klöcking et *al.* (2016) and Ryan et *al.* (2016) were combined with data from this study. Outcrop and subcrop data are highlighted in bold colours whereas interpretive geology is indicated in pale colours. Magnetic (reduced to pole, first vertical derivative,

and magnetic susceptibility; Ross *et al.*, 2018), electromagnetic (very-low-frequency-EM; Fig. 3b), and induced polarization (IP) geophysical data from Ross *et al.* (2018) were utilized to define lithologic boundaries and faults/lineation. The first unit intersected in diamond drill holes were also used to construct this surface map within drilling extents.

Deposit geology

The area around the Klaza deposit was not subjected to Pleistocene glacial erosion and thus the landscape is mostly deeply weathered rolling hills with >20–30 m of overburden in valleys. The Klaza deposit is entirely buried and only "outcrops" in exploration trenches. Hart and Langdon (1997) propose that the Klaza deposit sits within an uplifted block of a horst structure, with mid-Cretaceous Mount Nansen volcanic rocks preserved on either side. Bounding faults of the horst block run parallel to mineralized trends as well as regional structural trends and are inferred to be pre-mineralization faults (Klöcking *et al.*, 2016). The Hart and Langdon (1997) model also highlights northeast-trending faults that crosscut and offset the host block with its associated bounding faults. Ryan *et al.* (2016) proposed a map that showed the NW-trending faults as the dominant structure in the Klaza area but showed little evidence of the NE-faults.

The geological map in Figure 3 shows northwest and northeast structural trends. The NW trend comprises dikes and faults in the main deposit and includes the composite veins. The veins occupy Riedel splays from dextral strike-slip movement on the faults. The NE-trending faults cut and sinistrally displace the NW trends, thus dividing the deposit into the western, central and eastern blocks. The eastern block and the western block are interpreted to be uplifted relative to the central block. The magnitude of this vertical displacement is unknown.

The Klaza polymetallic veins spatially coincide with 77–76 Ma quartz-feldspar porphyritic (QFP) dikes (Mortensen *et al.*, 2016; Turner and Dumala, 2017). The QFP dikes and the Klaza veins are hosted in the mid-Cretaceous (*ca.* 107 Ma) Whitehorse suite granodiorite, part of the regionally extensive Dawson Range batholith emplaced between 115 and 105 Ma (Allan *et al.*, 2013). The deposit is divided into four main resource zones: Central Klaza, Central BRX, Western Klaza and Western BRX respectively. The epithermal type mineralization seen in base-metal-rich veins transitions into Au-Cu-Mo-rich stock work veins and veinlets towards the Kelly and Cyprus porphyry prospects in the southeast.

Intrusive and extrusive rocks

The intrusive suites discussed below are assigned a map unit, whereas each intrusive phase intersected in drill core is assigned a short-form numbered code (i1–i5) for simple referencing to the observed paragenetic sequence.

Minto suite (LTrEJgM)

Intrusive rocks from this suite are observed in outcrop north-northeast of the Klaza deposit where they unconformably underlie Mt. Nansen Group volcanic rocks and are intruded by Whitehorse suite plutonic rocks. Slightly older (*ca.* 211 Ma) rocks of the Minto suite are also documented to unconformably underlie the Mt. Nansen Group rocks to the west and southwest of the Klaza deposit, where they intrude the Snowcap assemblage (Klöcking *et al.*, 2016). The composition of these of rocks varies between quartz monzodiorite and tonalite, and contain coarse to medium-grained, foliated hornblende and biotite (Allan *et al.*, 2013; Kovacs *et al.*, 2016). The outcrop of this suite, observed to the northeast of the Klaza deposit (Fig. 3a), is medium to coarse-grained porphyritic foliated hornblende-granodiorite with K-feldspar phenocrysts. Magnetic susceptibility for this suite ranges from ~15 to 25 nT.

Mt. Nansen group (mKN)

The Mt. Nansen volcanic complex outcrops to the east and west of the Klaza deposit, often forming knobs, tors and talus slopes. Exposure to the east and southeast of the Klaza deposit was mapped at 1:15 000-scale by Klöcking *et al.* (2016). Klöcking *et al.* (2016) suggest the volcanic stratigraphy is upright, undeformed, and dips at an angle of ~45–60° to the northeast. This volcanic package consists of andesitic flows, breccia, and rhyolite tuffs. Constrained to a minimum thickness of 450 m, significant uplift is interpreted to have occurred with the emplacement of the Whitehorse

suite plutonic rocks (Klöcking et *al.*, 2016). Mt. Nansen group rocks are characterized by dark blocky, rock piles resistant to weathering. The andesite flows are porphyritic with large plagioclase phenocrysts and fine-grained pyroxene-bearing groundmass. Outcrops on Victoria Mountain suggest flat-lying stratigraphy in this package to the east of the Klaza deposit (Fig. 3a). Magnetic susceptibility for the Mt. Nansen group rocks ranges between ~20 and 50 nT, making it highly pronounced in magnetic surveys. A detailed description of this volcanic package is documented in Klöcking et *al.* (2016).

Whitehorse suite (mKWg)

i1: Biotite-hornblende granodiorite to tonalite

The Whitehorse suite granodiorite, dates at *ca.* 107.9 Ma on the property (Mortensen et *al.*, 2016), is the most abundant rock type observed in drill core, and is the main host to the epithermal mineralization.

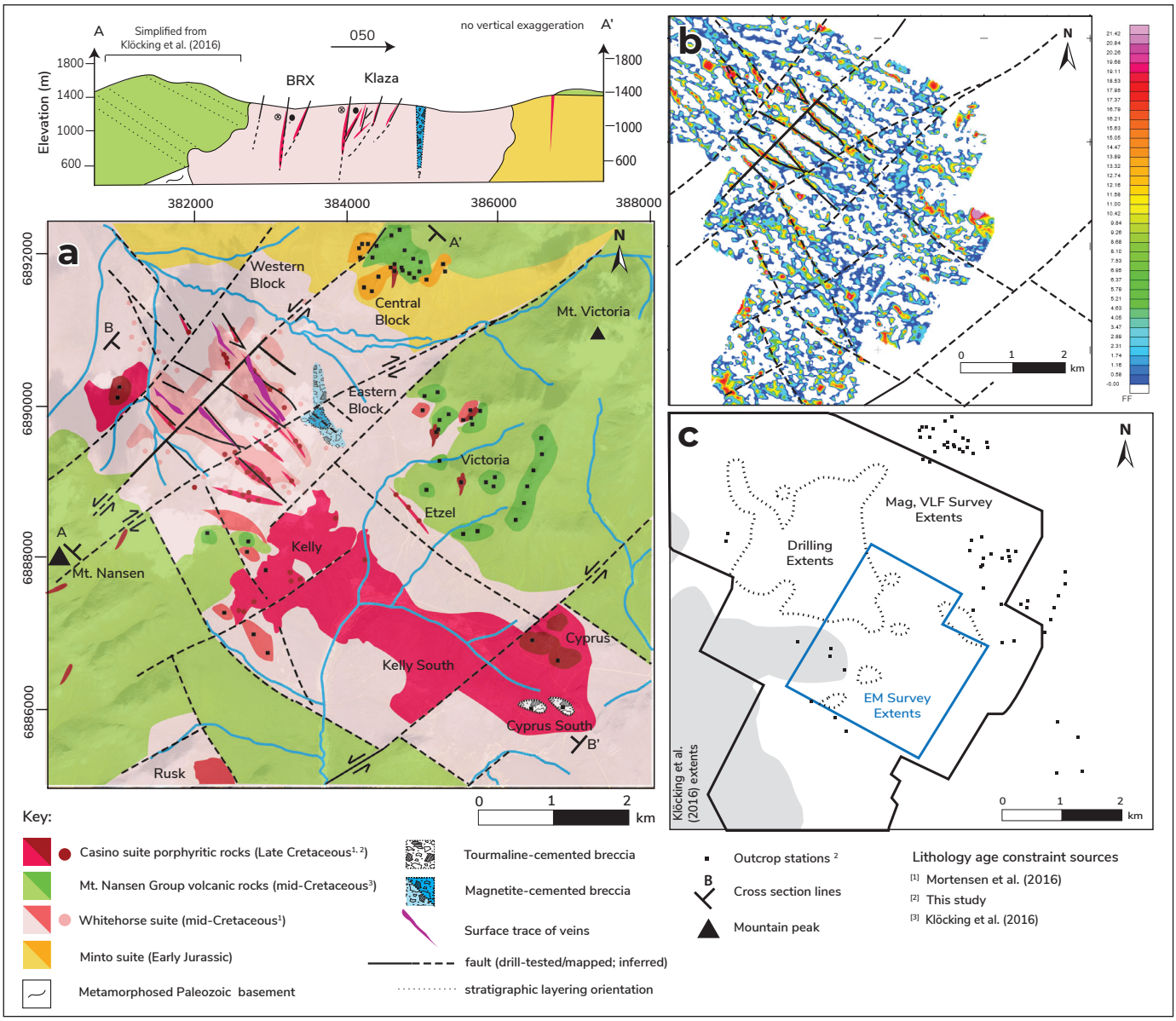


Figure 3. (a) *Geologic map of the Klaza deposit. Outcrop traces and "top of drillhole" intercepts are highlighted in bold colours while interpretative geology is indicated by pale colours. UTM Zone 08, Datum: NAD 83.* ***(b)*** *VLF-IP map highlighting shallow conductors and permeable fault zones. Interpretive and drill-tested faults are overlain on the geophysical map.* ***(c)*** *A limits of confidence map indicating sources of information for constraining the geological map.*

It is a composite intrusion and two dominant phases are identified: (1) a biotite-amphibole phyric granodiorite (Fig. 4a,b); and (2) biotite tonalite (Fig. 4c,d). Both phases consist of large, euhedral plagioclase (30–45%) phenocrysts in addition to subhedral quartz (25–40%) which has a bimodal size range, subhedral K-feldspar (0–20%) and intergranular biotite (10–15%) and amphibole (0–8%). Dioritic autoliths are a common occurrence in this suite. In two of these phases, there are larger subround (*i.e.*, corroded) quartz phenocrysts. Petrography shows accessory zircon, epidote, titanite and chlorite after biotite. This suite is commonly altered exhibiting a light propylitic overprint of chlorite, epidote and carbonate. Magnetic susceptibility for this suite ranges from ~15 to 20 nT.

Leucogranite/ Aplite dikes

This phase, which is seen in outcrop and drill core, consists of dikes crosscutting the i1 phase. The dikes consist of a massive, fine-grained pinkish K-feldspar-quartz-rich assemblage, and are 10 cm to 1 m thick. These aplite dikes match descriptions of a similar phase in Friend et *al.* (2018) and are inferred to be a late stage of the mid-Cretaceous Dawson Range batholith.

Casino suite (LKpC)

Casino suite rocks at the Klaza deposit occur as a composite dike swarm having a minimum of four phases (i2 to i4, see below). Magnetic susceptibility for Casino suite rocks at Klaza are between 1 and 5 nT, which manifests as mag-lows in geophysical surveys. The majority of the Casino suite rocks in the deposit record phyllic alteration as reflected by the growth of muscovite uniformly seen throughout samples studied petrographically. The consequence of the latter is the addition of K to the system, which resulted in a pervasive yellow colour to the stained rocks.

i2: Monzogranite to granodiorite

This phase occurs in the southeastern part of the Klaza property and is seen to be in sharp contact with the i1 phase. It is leucocratic, medium-grained, containing plagioclase (40%), quartz (30%) and K-feldspar (30%). It generally has a seriate texture, but plagioclase is slightly coarser and partly porphyritic (Fig. 5a). It has moderate to intense phyllic (muscovite-quartz-pyrite) and potassic (K-feldspar) alteration.

i3a: Biotite-plagioclase porphyritic granodiorite (80–78 Ma)

This phase is constrained to ca. 79 Ma (Lee et *al.*, in prep), and also occurs in the southeastern part of the Klaza property. A phase having similar texture and mineralogy is observed at the Cyprus porphyry prospect (Figs. 1 and 3). It consists of euhedral to subrounded, partially resorbed phenocrysts of plagioclase (20%), quartz (30%), and euhedral biotite (8%) phenocrysts, in a fine-grained K-rich (40%), quartz-plagioclase groundmass (Fig. 5b). The plagioclase crystals also display variable degrees of albitization. This phase maintains both sharp and gradational contacts with i2 and i3b (see below) and shows a mutual intrusive relationship with i3b as both occur in each other (Fig. 6a,b,c). Therefore, it is likely that i3a and i3b are comagmatic. This phase is variably altered and when altered can look like i4 (see below).

i3b: Hornblende-plagioclase diorite

This phase is also found in the southeastern part of the Klaza property. It is medium-grained and equigranular, and consists of plagioclase (50%), hornblende (30%) and variable biotite (5–11%). Biotite has an acicular habit (Fig. 5c). Phase i3b has variable phyllic alteration (muscovite-quartz-pyrite) and can be strongly sulphidized (*i.e.*, increase in sulphide mineral phases) due to the high amount of mafic minerals in the groundmass.

i4: Feldspar-quartz-biotite porphyritic granodiorite dikes (77–76 Ma)

This dike phase is the most commonly intersected phase of the Casino suite and is ca. 77 Ma (Mortensen et *al.*, 2016; Lee et *al.*, in prep). It is found throughout the Klaza property. Importantly, this phase is commonly co-spatial with, and cut by, composite epithermal-type veins. Phase i4 is texturally and mineralogically similar to the i3a phase, has partially resorbed plagioclase (25–30%) and quartz (15%) phenocrysts in a fine-grained K-rich (30–55%) groundmass of plagioclase

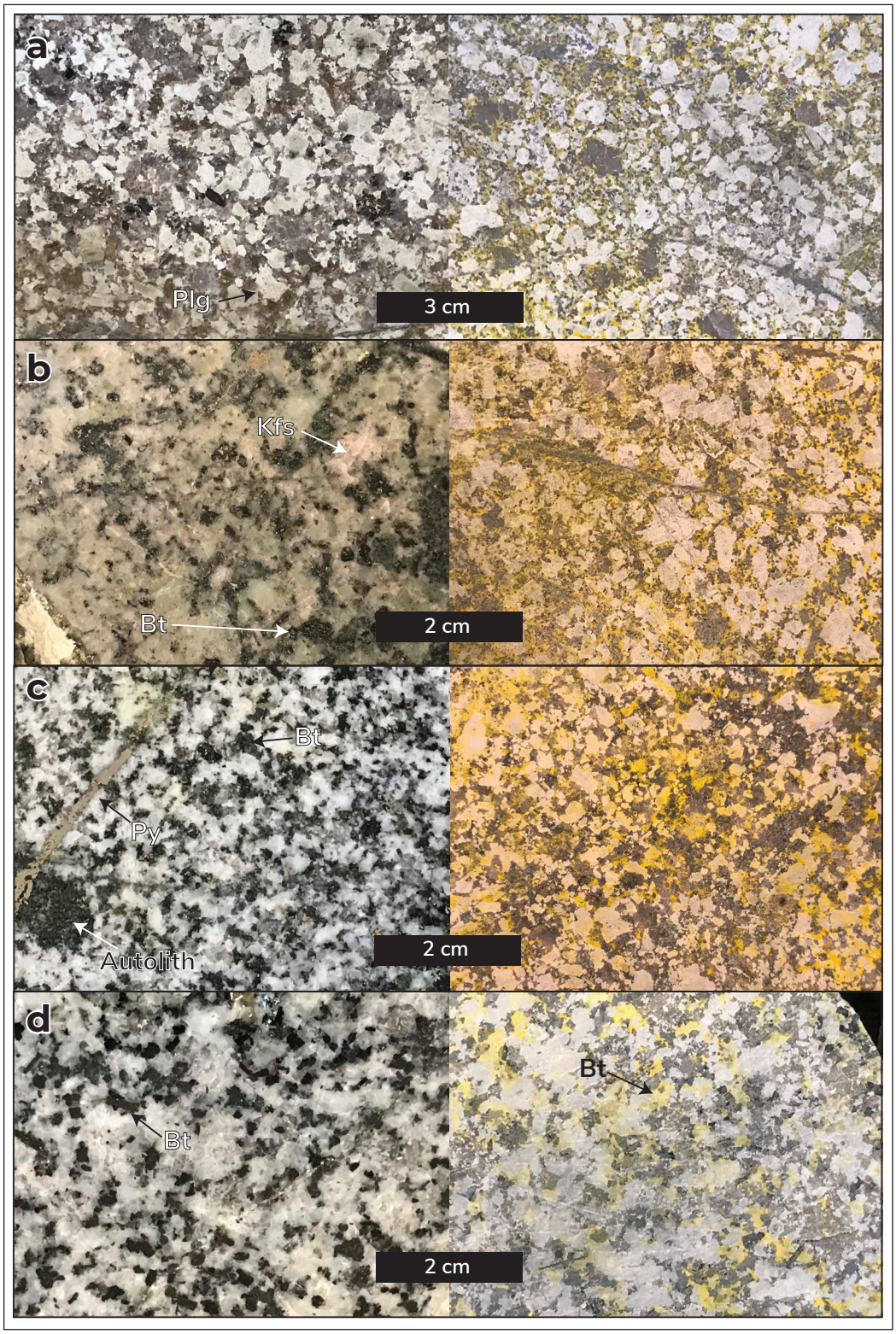


Figure 4. *Variations of the Whitehorse plutonic suite (i1 phase) at the Klaza deposit. Polished slabs are displayed on the left whereas potassium-stained slabs are displayed on the right. Note that a significant proportion of potassium staining is attributed to biotite in addition to K-feldspar.* **(a)** *Hornblende-biotite granodiorite showing significant clay-alteration.* **(b)** *Hornblende-biotite granodiorite shows light propylitic overprint.* **(c)** *Biotite-hornblende tonalite. shows light potassic (biotite) overprint.* **(d)** *Least altered biotite-hornblende tonalite. Mineral abbreviations in accordance with Whitney and Evans (2010).*

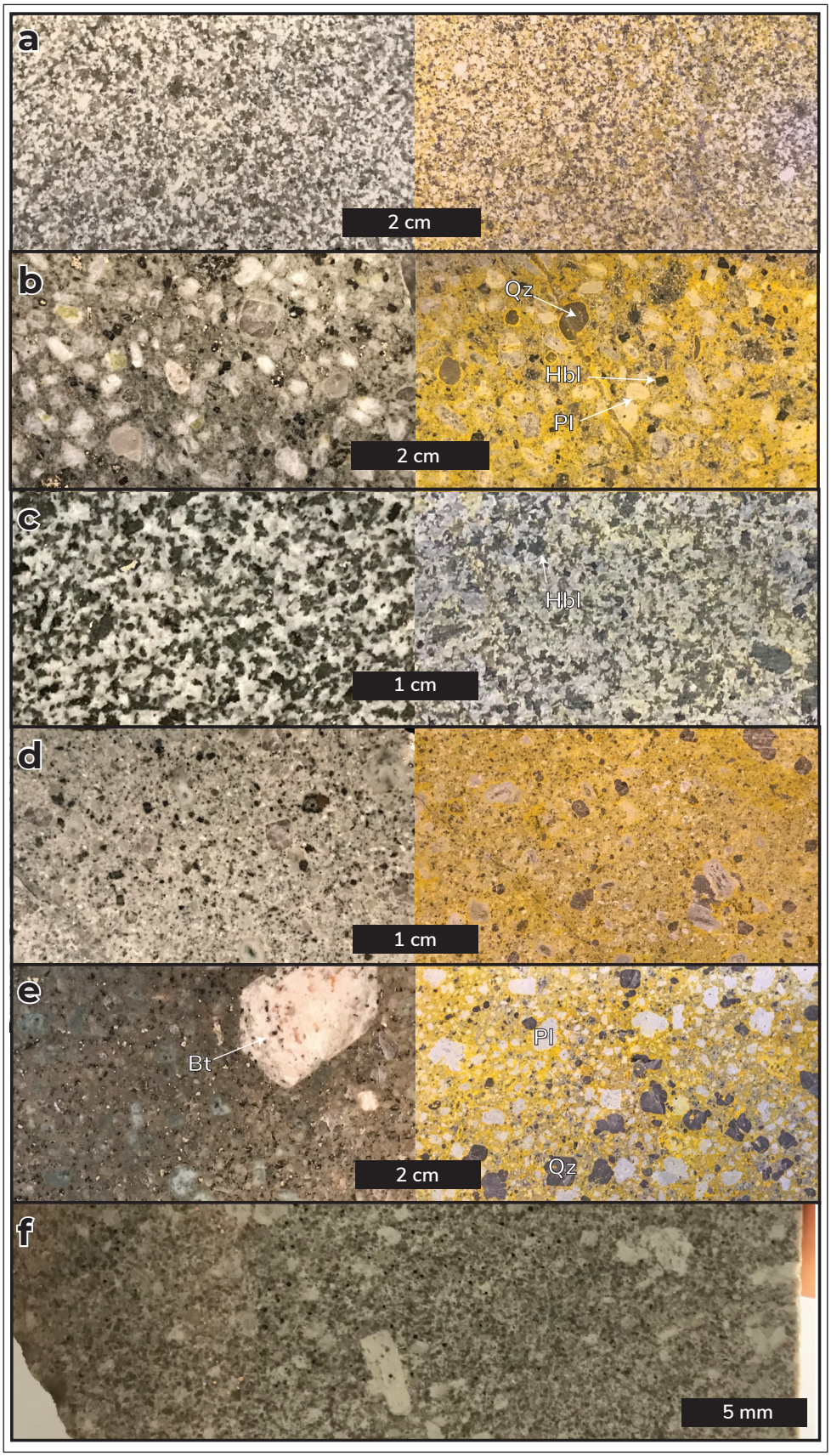


Figure 5. *Casino suite intrusive rocks. Polished slabs are displayed on the left whereas potassium-stained slabs are displayed on the right.* ***(a)*** *Monzogranite (i2 phase).* ***(b)*** *Biotite-plagioclase porphyritic granodiorite to monzogranite (i3a phase).* ***(c)*** *Hornblende-plagioclase diorite (i3b phase).* ***(d and e)*** *Feldspar-quartz-biotite porphyritic andesite dikes (i4 phase).* ***(f)*** *Feldspar-biotite porphyritic andesite dikes (i5 phase). Mineral abbreviations in accordance with Whitney and Evans (2010).*

and biotite (3–8%; Fig. 5d,e). There are localized, large (2–3 cm) plagioclase phenocrysts (Fig. 5e). Phase i4 contains more quartz but less biotite than i3a. It commonly exhibits greater phyllic/argillic alteration, forming an illite-muscovite-clay, due to its close proximity to epithermal veins and large fault zones. The alteration is texturally destructive, and results in the preservation of bleached, tan coloured dikes. The dikes are commonly barren but do host pyrite after biotite due to the phyllic overprint. This phase cuts the i3 phases and porphyry-type veins, and are in turn cut by i5 and epithermal mineralization.

Prospector Mountain suite (LKyP)

i5: Feldspar-biotite porphyritic diorite dikes (72–71 Ma)

This phase is significantly less common than the i4 phase but is found throughout the Klaza property. Identification is challenging due to the texturally destructive phyllic and argillic alteration. Current observations highlight a quartz-poor mineralogy having dominantly equant feldspar (plagioclase) and biotite phenocrysts in a fine-grained groundmass (Fig. 5f). This phase contains clasts of i4 (Fig. 6d) and is constrained to *ca.* 71 Ma (Mortensen *et al.*, 2016; Lee *et al.*, in prep).

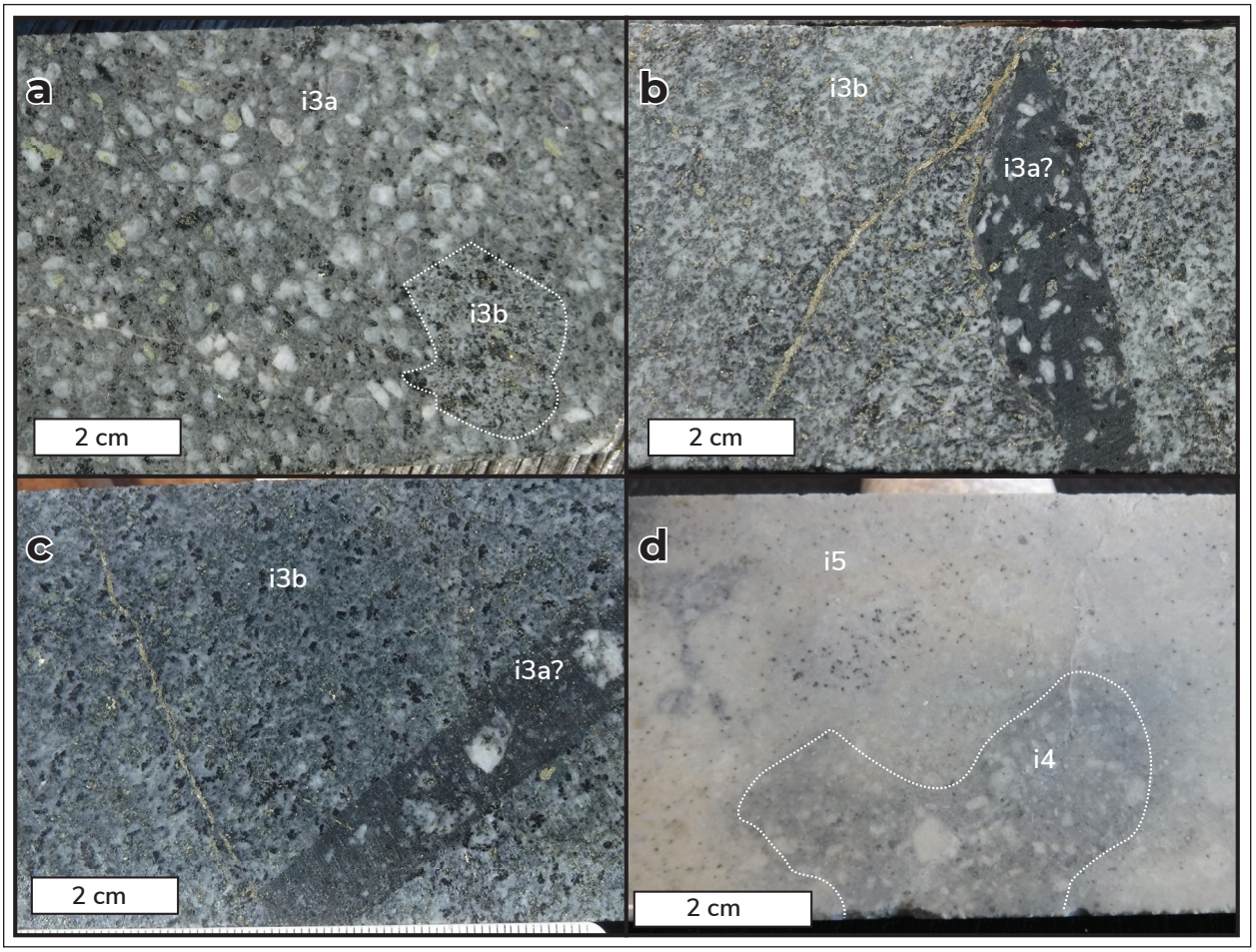


Figure 6. *Crosscutting relationships between intrusive dikes.* ***(a)*** *i3b phase clast within i3a phase.* ***(b)*** *i3a phase clast within i3b phase.* ***(c)*** *i3a phase injection within i3b phase.* ***(d)*** *i4 phase clast in i5 phase.*

Alteration

Phyllic alteration (Porphyry stage)

Quartz-muscovite-pyrite assemblages are associated with Stage 1 (porphyry-type, see below) mineralization in the Klaza system. This alteration can be pervasive and is up to 80 m wide in the southeast part of the deposit. Pyrite and muscovite, the latter verified by X-ray diffraction (XRD), replace biotite and hornblende, whereas K-feldspar is only replaced by muscovite. Plagioclase is minimally altered in this process. Pyrite in this alteration assemblage can be significantly enriched in gold, as seen from elemental mapping (Lee *et al.*, in prep), and may relate to the epithermal fluid overprint. Phyllic alteration in the central Klaza zone yields an ^{40}Ar-^{39}Ar muscovite age of *ca.* 78 Ma (Lee *et al.*, in prep).

Potassic alteration (Porphyry stage)

Potassic alteration is only observed in the southeast part of the deposit in spatial association with stockwork veins related to Stage 1. Potassium staining of altered rocks suggests the addition of hydrothermal-related potassium through growth of minerals such as muscovite, K-feldspar, and biotite; however, detailed mineralogy is needed to verify the potassic alteration minerals, and thus extent in the system.

Epithermal vein-related propylitic alteration

The composite epithermal veins at Klaza are associated with a distinct propylitic alteration halo. This halo, which is wider in the hanging wall of the veins, consists of Fe-carbonate, epidote, and muscovite-illite (both verified by XRD). An important observation of the past field season is that Fe-carbonate, which is now obvious due to oxidation, was not noted in the fresh drill core when originally logged. As the presence of Fe-carbonate reflects proximity to epithermal veins, this observation is significant. It is recommended that carbonate staining (see Hitzman, 1999 for protocol) be used in the future for immediate identification of Fe-carbonate alteration, enabling informed drilling decisions in real time.

Hydrothermal mineralization styles

Stage 1: EDM, A, B, and D-type veins

Several types of veins commonly associated with high temperature magmatic-hydrothermal systems are observed in drill core. Nomenclature used is adapted from Seedorf *et al.* (2005) and Sillitoe (2010) to match observations at the Klaza deposit. Veins are placed in a paragenesis based on relative crosscutting relationships among hydrothermal and magmatic events. Several generations or cycles between the veins are noted and described below.

The earliest veins have two variants: (1) early biotite-pyrite having a K-feldspar selvage (EB-type, Fig. 7a); and (2) early dark micaceous (EDM) infill of quartz ± pyrite ± chalcopyrite having dark haloes (chlorite-biotite; Fig. 7b,c). The haloes are between 4 and 10 cm wide; these veins are only seen in phases i1, i3a and i3b.

A-type veins consist of milky quartz containing pyrite-muscovite, and rarely chalcopyrite. These veins are sinuous and occur in i1 and i3b phases (Fig. 7c). Later A-type veins are planar, sheeted or stockworks, and have an assemblage of granular quartz-pyrite ± chalcopyrite and occur in phase i3a.

B-type veins occur as centre-line pyrite-chalcopyrite veins containing narrow quartz gangue (~1 cm wide) and a distinct K-feldspar (potassic) alteration halo. They occur as planar veins and are present in phases i2, i3a and i3b (Fig. 7d).

D-type veins are common and have many variants in terms of mineral assemblage: (i) pyrite ± quartz ± chalcopyrite; (ii) quartz-tourmaline-muscovite-pyrite ± rhodochrosite; and (iii) quartz-pyrite-muscovite (Fig. 7e). The vein assemblages have distinctive K-feldspar destructive sericite haloes of 8 to 15 cm width. The tourmaline-bearing variant of D-type veins is manifested as a hydrothermal breccia in Central Klaza zone, where intensely sericitized clasts of intrusive rock are cemented by an assemblage of acicular, radial, black tourmaline-muscovite-pyrite-quartz.

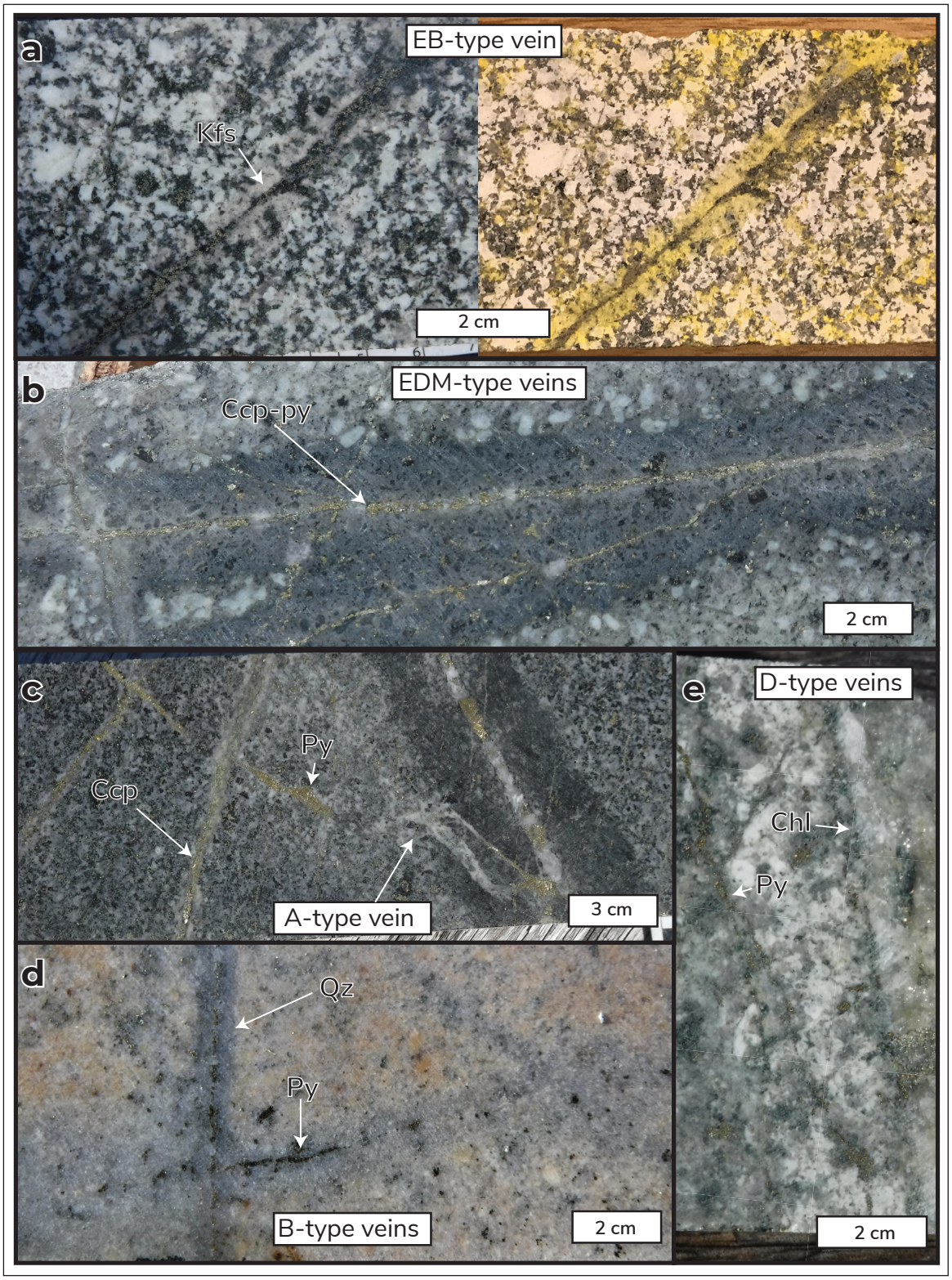


Figure 7. *Porphyry-type veins.* ***(a)*** *Early biotite (EB)-type veins in potassic (biotite) altered i1 phase. Potassium stained slab on the right.* ***(b)*** *Early dark micaceous (EDM) veins hosted in i3a phase.* ***(c)*** *Pyrite-chalcopyrite-bearing A-type veins cutting an EDM vein hosted in i3b phase.* ***(d)*** *B-type pyrite-granular quartz vein with in potassic (K-feldspar) altered i2 phase.* ***(e)*** *D-type quartz-pyrite-sericite veins with texturally destructive muscovite haloes hosted in i1 phase. Mineral abbreviations in accordance with Whitney and Evans (2010).*

Late generation chalcopyrite-only sheeted veinlets cut all vein generations. It is unclear which vein type this generation is associated with; however, it is spatially coincident with disseminated and blebby chalcopyrite mineralization, which occurs by replacing biotite and hornblende in the host intrusive rock. Semi-massive chalcopyrite is also present, which appears to co-precipitate with pyrite (see Stage 2a below).

Molybdenite-bearing veins

Quartz-molybdenite veins are present in the Whitehorse suite granodiorite and have varying alteration haloes. A sample of core from drill hole KL-16-309 is flanked by a strong chlorite-sericite alteration halo; it yielded a Re-Os age of *ca.* 77 Ma (Lee *et al.*, in prep.). A sample from the Cyprus porphyry prospect is flanked by a strong sericitic alteration halo and yielded a Re-Os age of *ca.* 71 Ma (Lee *et al.*, in prep.). One sample obtained from core from drill hole KL-16-314 is cut by epithermal-stage mineralization and is flanked by a narrow carbonate alteration halo; Re-Os geochronological data are pending for this sample.

Stage 2–4: Composite polymetallic veins and breccia

The Klaza composite epithermal veins show a strong structural control. Reactivation of large fault zones is considered to have been an important structural component in creating wide breccia-vein intervals up to 8 m in width. The main breccia-types in the Klaza system are documented below using modified breccia classification systems after Davies *et al.* (2008) and Byrne and Tosdal (2014). The breccia-types are integrated into vein stage descriptions and paragenesis.

Stage 2a veins

Massive fine-grained pyrite-arsenopyrite-quartz ± chalcopyrite veins, 10 cm to 2 m wide, cut Stage 1 veins, and i1, i3a and i4 phases (Fig. 8a). In general, these banded veins have milky white prismatic quartz that is followed by massive sulphide deposition. Pyrite and arsenopyrite from the sulphide substage show equilibrium textures and reflect growth in open space. Gold occurs as: (1) micron-scale electrum inclusions in pyrite, arsenopyrite, and quartz; and (2) lattice-hosted gold in pyrite and arsenopyrite as determined in LA-ICP-MS analysis (Lee *et al.*, in prep). Chalcopyrite, which co-precipitated in this substage, increases in abundance in the Central and Eastern BRX zones.

Stage 2b veins and breccia

This substage is manifested as both banded veins and hydrothermal breccia (C-Bx) — a breccia type characterized by a cement of hydrothermal minerals (quartz, carbonate, sulphide minerals) hosting mono or polymictic clasts. In stage 2b, an assemblage of euhedral arsenopyrite-pyrite-sphalerite nucleated and grew on available surfaces, which are commonly wallrock and clasts of Stage 2a and i4 phase (Fig. 8b). The brecciation event is commonly hydraulic; forming angular jigsaw fit clasts with little displacement or high energy (clast-supported). This substage forms intervals between 5 cm and 1 m wide but can also increase in width as more banding develops (as seen in large vein intersections in the Western BRX zone). This assemblage is followed by cloudy, prismatic quartz, which filled open-space. The cyclical nature of this substage resulted in a banded nature to the composite veins (Fig. 8c).

Stage 2c veins

The final stage of syn-mineralization veins is characterized by prismatic cloudy quartz (possibly from stage 2b), followed by open-space-filling euhedral sphalerite, galena, tetrahedrite-freibergite, minor chalcopyrite and minor dark grey quartz (Fig. 8d). Sphalerite from this substage and Stage 2b is Fe-rich containing compositional zoning, as determined from scanning electron microscopy energy-dispersive X-ray spectroscopy (SEM-EDS) and laser ablation inductively coupled plasma mass spectroscopy (LA-ICP-MS) analysis (Lee *et al.*, in prep). The diversity of sulfosalt minerals in this substage contributes to a large portion of the silver budget in the Klaza system, with significantly higher amounts of sulfosalts present in the Western Klaza Zone; consequently, it is the zone containing the highest Ag:Au ratios on the property.

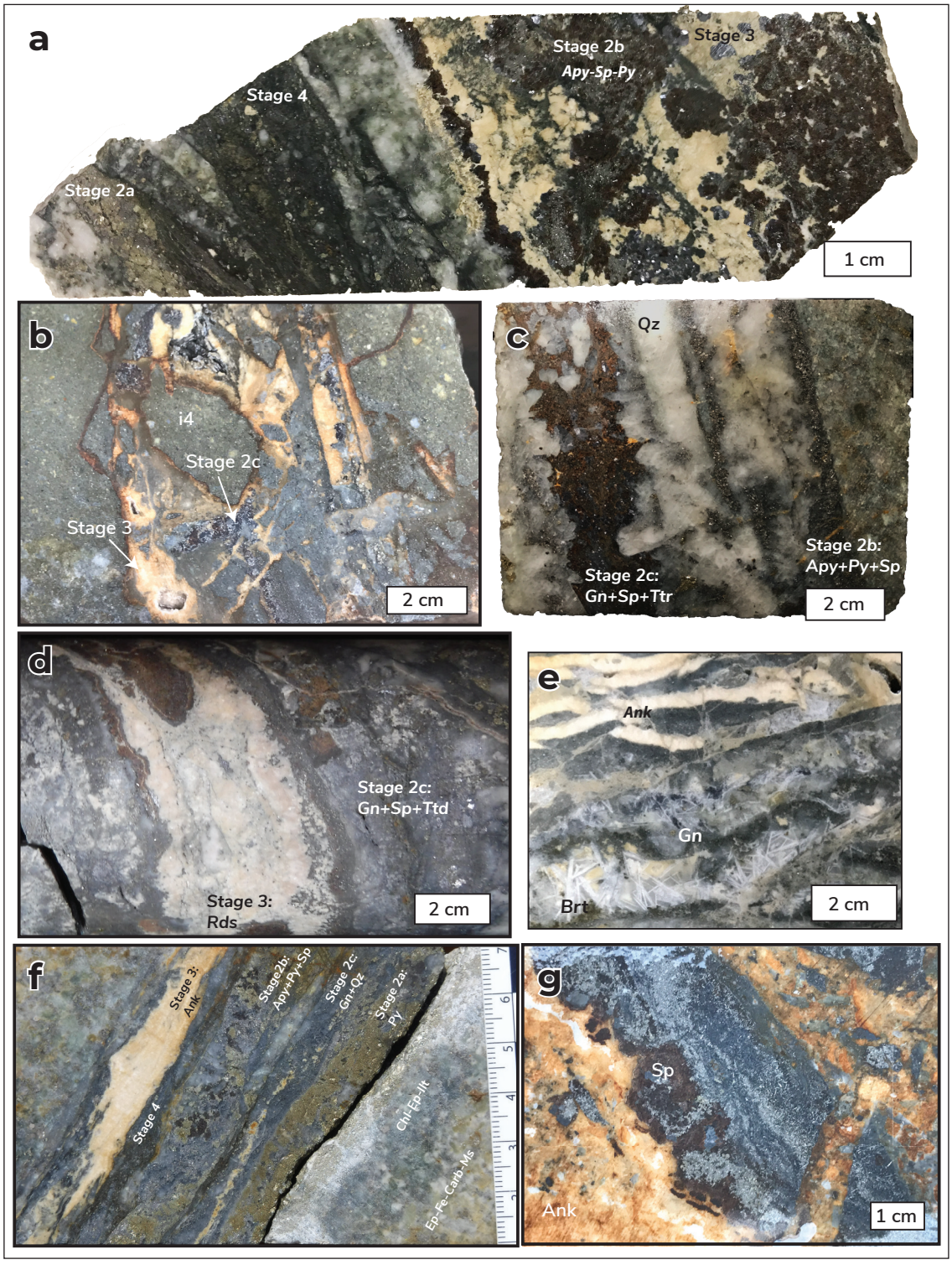


Figure 8. *Epithermal-type composite veins.* ***(a)*** *Western BRX zone Composite vein displaying sphalerite-rich vein stages.* ***(b)*** *i4 phase dikes cemented by Stage 2c and Stage 3 mineralization in the Western Klaza zone.* ***(c)*** *Stage 2b and Stage 2c composite vein form Central Klaza zone in contact with i1 host. Note the banding in Stage 2b and open space fill textures in Stage 2c.* ***(d)*** *Western BRX zone Stage 2c vein cut by Stage 3 rhodochrosite vein.* ***(e)*** *Stage 3 vein from Central Klaza zone displaying banded ankerite and bladed barite.* ***(f)*** *Central Klaza zone composite vein displaying Stage 2 to Stage 4 vein generations generated through reactivation of one structure.* ***(g)*** *Sphalerite–galena–freibergite from Stage 2c brecciated and cemented by Stage 3 ankerite in the Western Klaza zone. Mineral abbreviations in accordance with Whitney and Evans (2010).*

Stage 3 veins and breccia

The carbonate-rich stage cuts and brecciates (C-Bx) all previous vein stages (Fig. 8a,b,d,e,f,g**).** The carbonate in this generation is a solid solution between Fe-rich carbonate (ankerite) to dolomite (Fe, Mg-rich) to rhodochrosite (Mn-rich), as determined by SEM-EDS. This stage contributes minimal base metals to the system and does not display boiling textures (with the exception of bladed barite at ~100 m present depth; Fig. 8e). Brecciation in this stage can be hydraulic (*i.e.*, jigsaw fit; Fig. 8b,g) or high energy, forming small (sub-centimeter sized) subrounded clasts (cement-supported; Fig. 8d).

Stage 4 tectonic breccia-veins

The Klaza epithermal veins show strong evidence of post-mineral fault reactivation, displacement, and brecciation. This matrix-rich breccia (M-Bx) is characterized by the presence of rock flour forming interstitial to clasts of intrusive phases mentioned above, vein material, and other rock types. In the Klaza system, matrix-rich breccia occurs syn to post mineralization (Fig. 9a,b,c), inferred to be tectonic-related breccia and cataclasite. Stage 4 alternates between carbonate-quartz-rich pulses and matrix-rich components, and can result in a combination of matrix-rich and cement-rich breccia (*CM-Bx*). Poorly consolidated fault breccia is also observed within composite veins and in unmineralized fault zones (Fig. 9d).

Other features at Klaza

Magmatic breccia (IG-Bx)

This clast-supported breccia is characterized by an igneous matrix hosting subrounded, monomict to polymictic clasts of intrusive phases noted above plus other clast types. Intrusive breccia has been identified in this study between intrusive generations (i5 containing subrounded clasts of i4; i4 containing rounded clasts of i1) and more uncommon magmatic-hydrothermal composite-type breccia comprising a groundmass of anhydrite, quartz, biotite and feldspar (Fig. 9e). The later breccia-type displays an ambiguous relationship to the main paragenetic vein and intrusive stages defined above.

Tourmaline breccia pipe

A tourmaline breccia pipe is observed in the Cyprus porphyry prospect to the southeast of Klaza (Figs. 1 and 3), where sericitized clasts of porphyritic rock are cemented by black tourmaline-pyrite-quartz-biotite cement (Fig. 9f). This breccia pipe is interpreted to be a hydrothermal breccia related to the Cyprus porphyry complex.

Genetic model

The current compilation of field observations supplemented with a nominal amount of analytical data for the Klaza deposit suggests the composite epithermal veins are part of a much larger scale, continental arc-related magmatic-hydrothermal intrusive complex. Several lines of evidence are discussed below to suggest the presence of a buried Cu-Au porphyry system at Klaza.

1. Magmatic-hydrothermal paragenesis

The magmatic-hydrothermal sequence of events is summarized in Figure 10. Field and supporting petrographic observations suggest cyclical pulses of magmatic and hydrothermal nature analogous to that seen in protracted porphyry systems (Redmond and Einaudi, 2010; Sillitoe *et al.*, 2010). The presence of high-temperature hydrothermal veins (*e.g.*, EDM, A, and B-types) early in the paragenesis conform to classic vein descriptions for porphyry Cu-Au systems (Sillitoe, 2010). In contrast, the epithermal vein substages show a transition from massive sulphide phases, an inferred high temperature massive-sulphide assemblage dominated by pyrite ±arsenopyrite ± chalcopyrite (Stage 2a) to a later, lower-temperature, base metal-rich stage (Stage 2c).

A compilation of currently available geochronological data constrains magmatism (U-Pb zircon), some mineralization (Re-Os molybdenite), and alteration (K-Ar and Ar-Ar for hydrothermal K-feldspar and muscovite) in the Klaza-Mt. Nansen district. The data cluster into two age ranges, both associated with hydrothermal alteration ages (Fig. 11). Initial magmatism between 80 and 76 Ma coincides with the Casino intrusive suite,

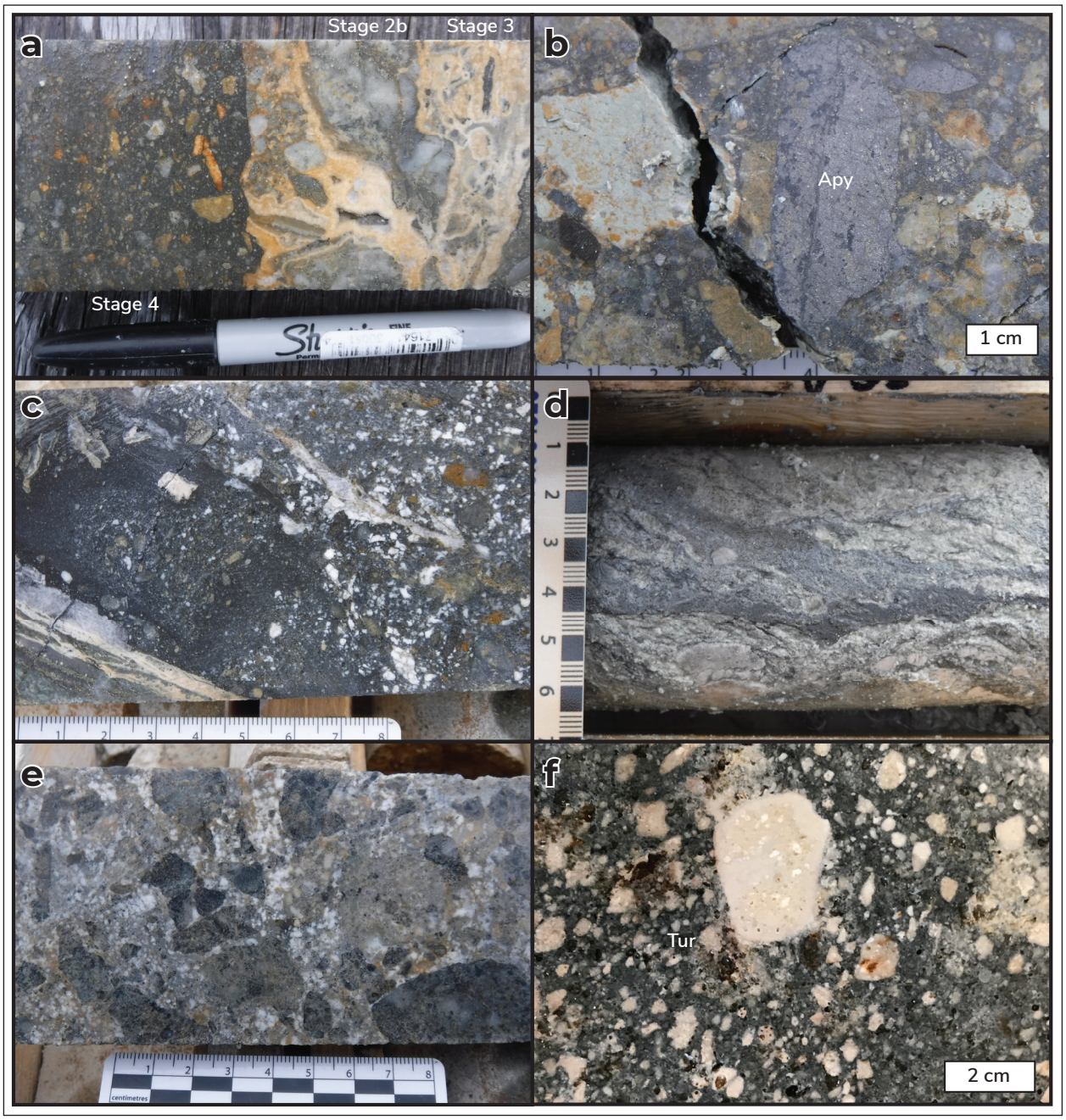


Figure 9. *Breccia types at the Klaza deposit.* ***(a)*** *Stage 4 cement-matrix-breccia cutting a composite breccia of Stage 2b mineralization cut cemented by Stage 3 ankerite.* ***(b)*** *Stage 4 cement-matrix-breccia with polylithic clasts of sericitized porphyritic dike material, i1 host, and massive arsenopyrite from Stage 2a.* ***(c)*** *Cataclasite containing rock flour and barite-carbonate clasts from the Central Klaza Zone.* ***(d)*** *Fault gouge with a brecciated and mechanically sheared sulphide vein.* ***(e)*** *Magmatic-hydrothermal breccia with feldspar-anhydrite cement and polymictic clasts.* ***(f)*** *Tourmaline-cemented breccia from the Cyprus South occurrence with clasts of sericitized porphyritic rock. Mineral abbreviations in accordance with Whitney and Evans (2010).*

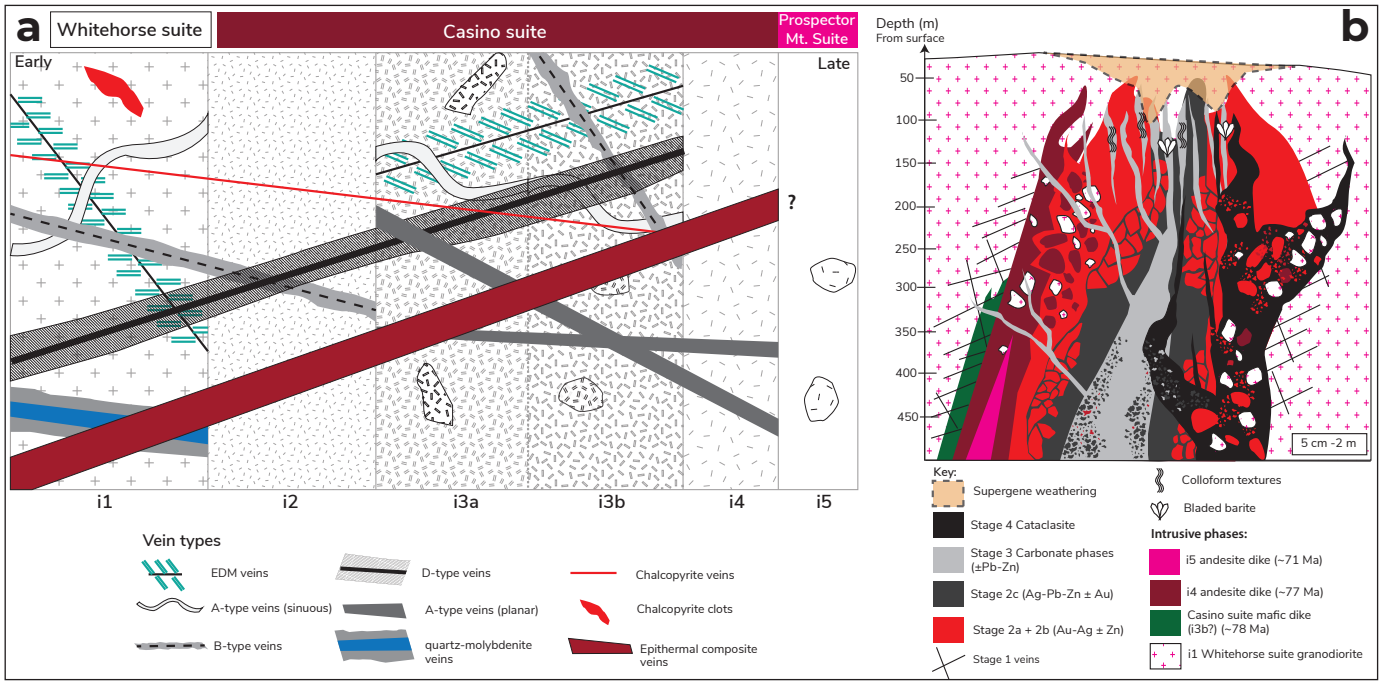


Figure 10. *Magmatic–hydrothermal paragenesis diagrams for the Klaza system.* ***(a)*** *Timeline with crosscutting relationships between magmatic phases and high to low temperature vein types.* ***(b)*** *A schematic diagram of the Klaza composite vein substages and their relationship to magmatic and high-T vein phases.*

which is constrained to ca. 79–72 Ma (Allan et *al.*, 2013). This age range overlaps the 77 Ma molybdenite age for the Kelly prospect and muscovite ages of ca. 79 Ma and ca. 77 Ma for phyllic alteration and tourmaline-pyrite-muscovite vein formation, respectively, at the Central Klaza (Mortensen et *al.*, 2016; Lee et *al.*, in prep). A second magmatic pulse at 72.5 to 71 Ma coincides with the upper age limit for the Prospector Mountain suite, which is constrained to ca. 72–67 Ma (Allan et *al.*, 2013; Friend et *al.*, 2018). The age of this magmatic event overlaps with that of two molybdenite ages of ca. 71 Ma from the Cyprus prospect (Mortensen et *al.*, 2016; Selby and Creaser, 2001a; Lee et *al.*, in prep). K-Ar dates for hydrothermal K-feldspar (*i.e.*, adularia) from an unspecified location in the Mt. Nansen district yielded younger ages of 69 to 68 Ma (Selby et *al.*, 2001b), which also overlaps with the age for the Prospector Mountain suite. In summary, the available age data show a magmatic-hydrothermal system comprising ~10 m.y. arc-related magmatism and an apparent 2 m.y. hiatus. The data support two pulses of porphyry-type mineralization at two locations in the Klaza system, whereby Kelly forms the older, Casino-age porphyry event and Cyprus forms the younger, Prospector Mountain-age porphyry event.

2. Local intrusive rocks

Intrusive rocks of the Casino suite comprise mafic to intermediate compositions that are typical in volcanic arcs. The partially resorbed plagioclase and quartz phenocrysts in the porphyritic rocks (i3a, i4) are indicative of variable P-T-X conditions in the magma chamber, a common feature of productive arc environments and magmatic processes (e.g., Bingham Canyon, Utah; Maughan et *al.*, 2002; Santa Rita, New Mexico; Audetat and Pettke, 2006). The comagmatic mingling of the porphyritic i3a phase and the mafic equigranular diorite (i3b) reflects a dynamic replenishing magma chamber, which is also an important feature of porphyry deposits (Caricchi et *al.*, 2014; Chiaradia and Caricchi, 2017; Putirka, 2017). Thus, there is evidence that the Kelly magmatic system likely experienced chemical changes related to the addition of mafic magma to the magma chamber. The abundance of

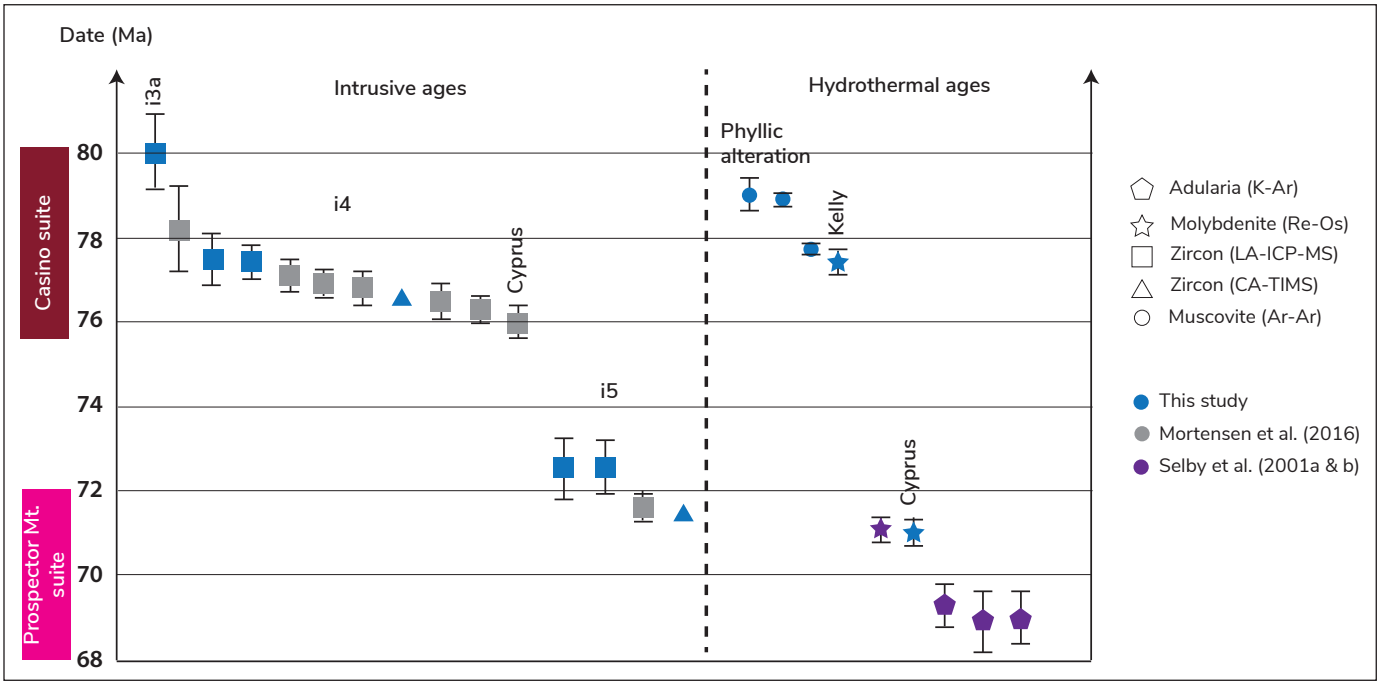


Figure 11. *Summary compilation of geochronologic data from the Klaza deposit area with sources indicated. Casino suite and Prospector Mt. suite boundaries are drawn based on intrusive ages in the Klaza area and in accordance with definitions from Allan et al. (2013). Note that the Selby et al. (2001b) K-Ar data consists of samples with unspecified locations within the Mt. Nansen district.*

hydrous phases, such as hornblende and biotite, in the Casino suite rocks at the Kelly prospect and at Klaza is also characteristic of a fertile (wet) magma chamber and one conducive to form porphyry deposits (Burnham, 1979; Richards, 2011; Richards et al., 2012). Lastly, the variety of porphyritic phases is also a feature typical of many productive porphyry systems (Burnham, 1979; Seedorff et al., 2005; Redmond and Einaudi, 2010; Sillitoe, 2010; D'Angelo et al., 2017).

3. Downhole lithogeochemistry

Three holes drilled southeast of the Klaza deposit resource zone intersected porphyry-type mineralization, and a simplified graphic log for one of these holes (KL-16-314) is summarized in Figure 12. The geochemical signatures of Au, Ag, Cu, K, and Na are split into three domains: (1) epithermal domain (0–200 m); (2) less-altered domain (200–350 m); and (3) porphyry-type domain (350–end of hole).

Distinct, highly anomalous Au, Ag, Cu values that correspond to intersections of composite sulphide-rich veins categorize the epithermal domain. The increase in K and complementary depletion in Na is attributed to muscovite and illite formation in phyllic and propylitic alteration zones related to the epithermal veins. Some barren pyrite-bearing B-type veins were observed in this domain. The less-altered domain displays background values for Au and Cu whereas the uniform K and Na contents reflect least-altered i1 composition. Silver values correspond to minor base-metal bearing veins in this domain. The porphyry-type domain corresponds to an overall above-background Cu-Au response, which correlates to increased vein density (EDM, A, B and D-type veins) and disseminated pyrite-chalcopyrite. It is noted that the potassic (biotite-K-feldspar) alteration assemblage observed in this domain is partially overprinted by phyllic alteration.

Observations of core from drill holes KL-16-314, KL-16-309, and KL-12-134 suggest the current maximum drilling depth (475 m) in the Kelly prospect area intersects the phyllic pyrite ± chalcopyrite bearing shell of a deeper porphyry system.

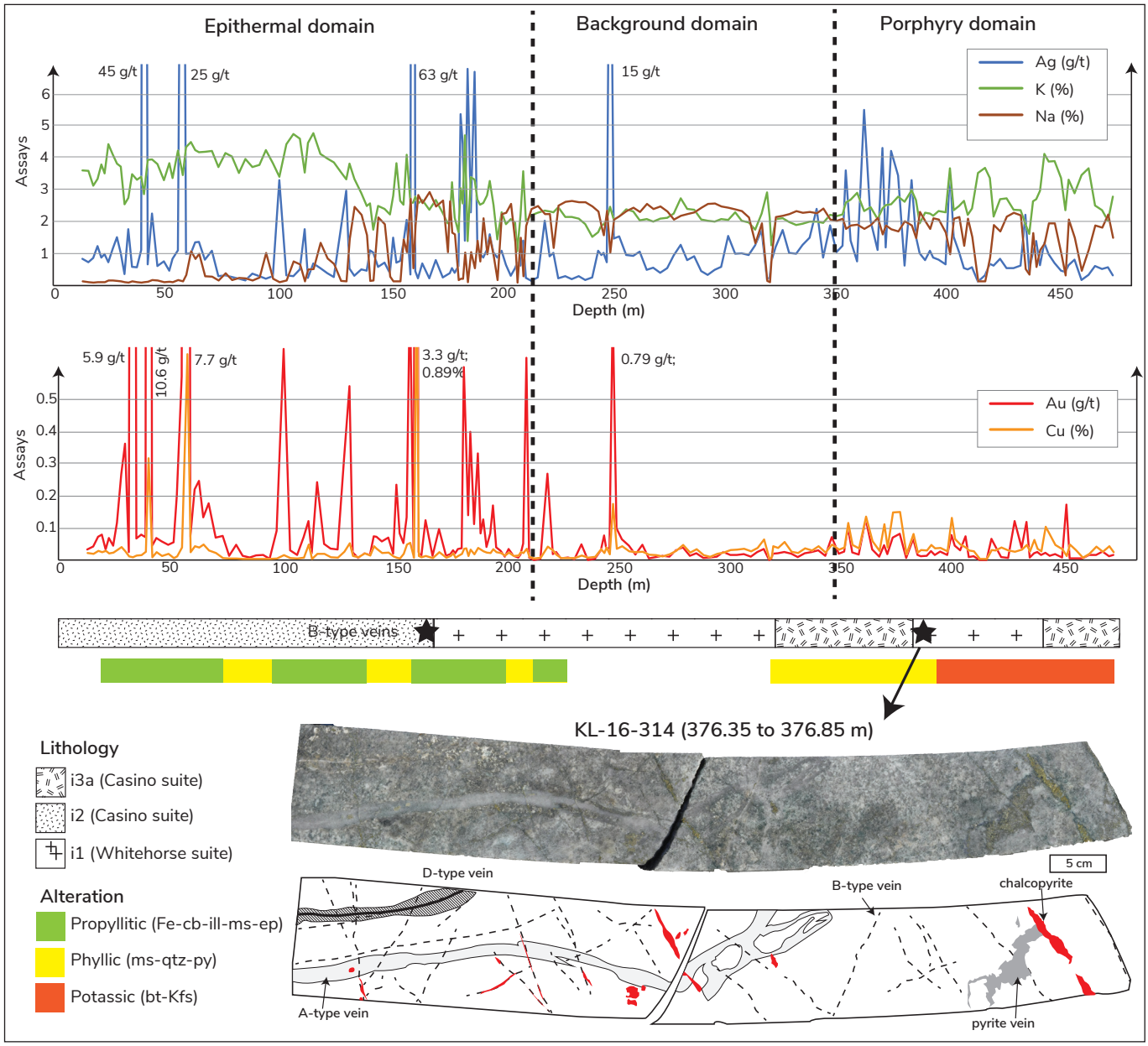


Figure 12. *Graphic log of drill hole KL-16-314 consisting of Au-Ag-Cu-K-Na assay data from Rockhaven Resources Ltd., simplified lithology and alteration re-logs. A representative sample of a A-type vein with crosscutting copper mineralization is also depicted here.*

4. Deposit-scale metal zonation and geophysical data

A schematic summary of the various intrusive suites, mineralization, and geochemistry is illustrated in Figure 13. As seen in Figure 13b, the ca. 76 Ma Casino and later ca. 72 Ma intrusive suites consisting of varied porphyry dike stocks invade the host ca. 105 Ma Whitehorse composite intrusive complex; spatially related to this dike swarm are the epithermal and porphyry-type mineralized zones. The geochemical data from Klaza drill holes display a metal zonation trending from Cu-Au-rich in the southeast (*i.e.*, porphyry-type) to Ag-Pb-Zn-rich (*i.e.*, epithermal-type) in the northwest (Fig. 13b,c). This trend is reflected in the sulphide mineralogy of the composite vein intercepts across the deposit. Intercepts in the

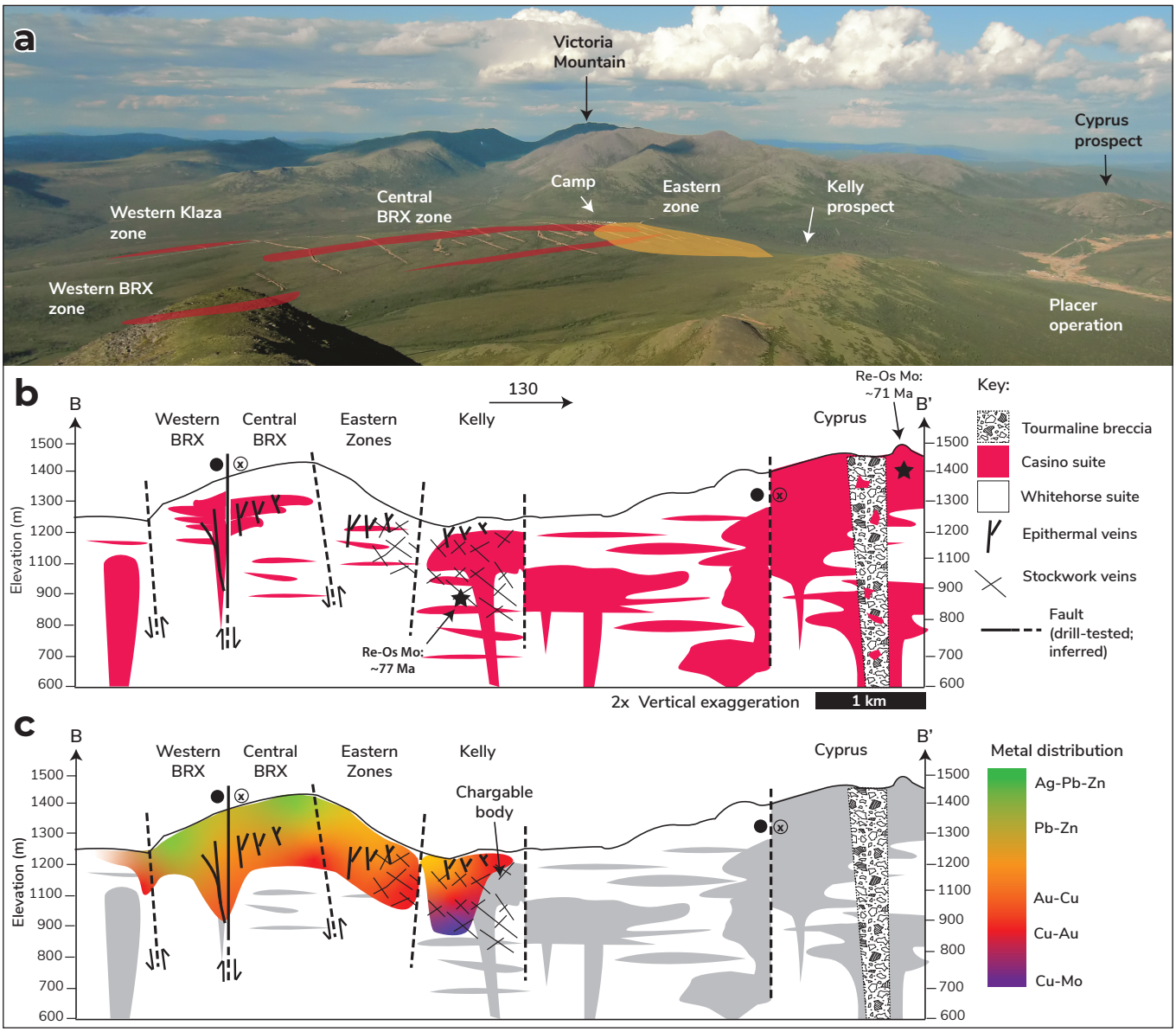


Figure 13. (a) *View of the Klaza deposit looking northeast from the top of Mt. Nansen. Mineralization traces are highlighted in red. Stockwork and sheeted vein mineralization is highlighted in orange.* ***(b)*** *Schematic cross section through B-B' (from Fig. 3a). Relative motion of faults is indicated and inferred based on drill hole and surface data.* ***(c)*** *Section highlighting precious and base metal distribution in the main deposit. Zonation data were obtained from leapfrog models of assay data. The data displayed here are limited to current drilling extents. The location of the chargeable body identified in IP surveys is indicated here and has not been drill-tested. Note that the metal distribution data for the Kelly fault block is only constrained by four drill holes.*

Eastern and Central BRX zones contain significant chalcopyrite hosted in Stage 2a veins, which grades into massive arsenopyrite-pyrite assemblages in the Central Klaza and Western BRX zones. Stage 2a is not present in the Western Klaza zone, and instead contains wider Stage 2c veins with increased sulfosalt abundance and diversity of sulphide minerals.

Induced polarization (IP) geophysical surveys across the Kelly prospect area display donut-shaped high chargeability areas (Fig. 14) coinciding with north-south trending low-resistivity zones (Ross et *al.*, 2018). The high chargeability zones are interpreted to be pyrite-shells while low resistivity zones are interpreted to be clay-altered fault zones.

Exploration Implications

We present a generalized genetic model in Figure 13. The Kelly prospect displays Cu-Au-Mo porphyry potential and requires deeper drill-testing to verify the true economic potential of the inferred underlying system. Archived drill core, on the periphery of current drill pattern, requires relogging by an experienced geologist familiar with porphyry-type geology and mineralization placing an emphasis on generating an updated geological model. This will also generate an appropriate logging scheme to consistently capture relevant information. Thus in regards to this, the new logging scheme should: (1) capture the Whitehorse, Minto, and Casino intrusive suites with the aid of a rock library; (2) record vein types and mineralization on a porphyry-scale in addition to an epithermal scale; (3) record mineralogy-based alteration assemblages; and (4) differentiate between breccia types to aid in resource and metallurgical domain modelling.

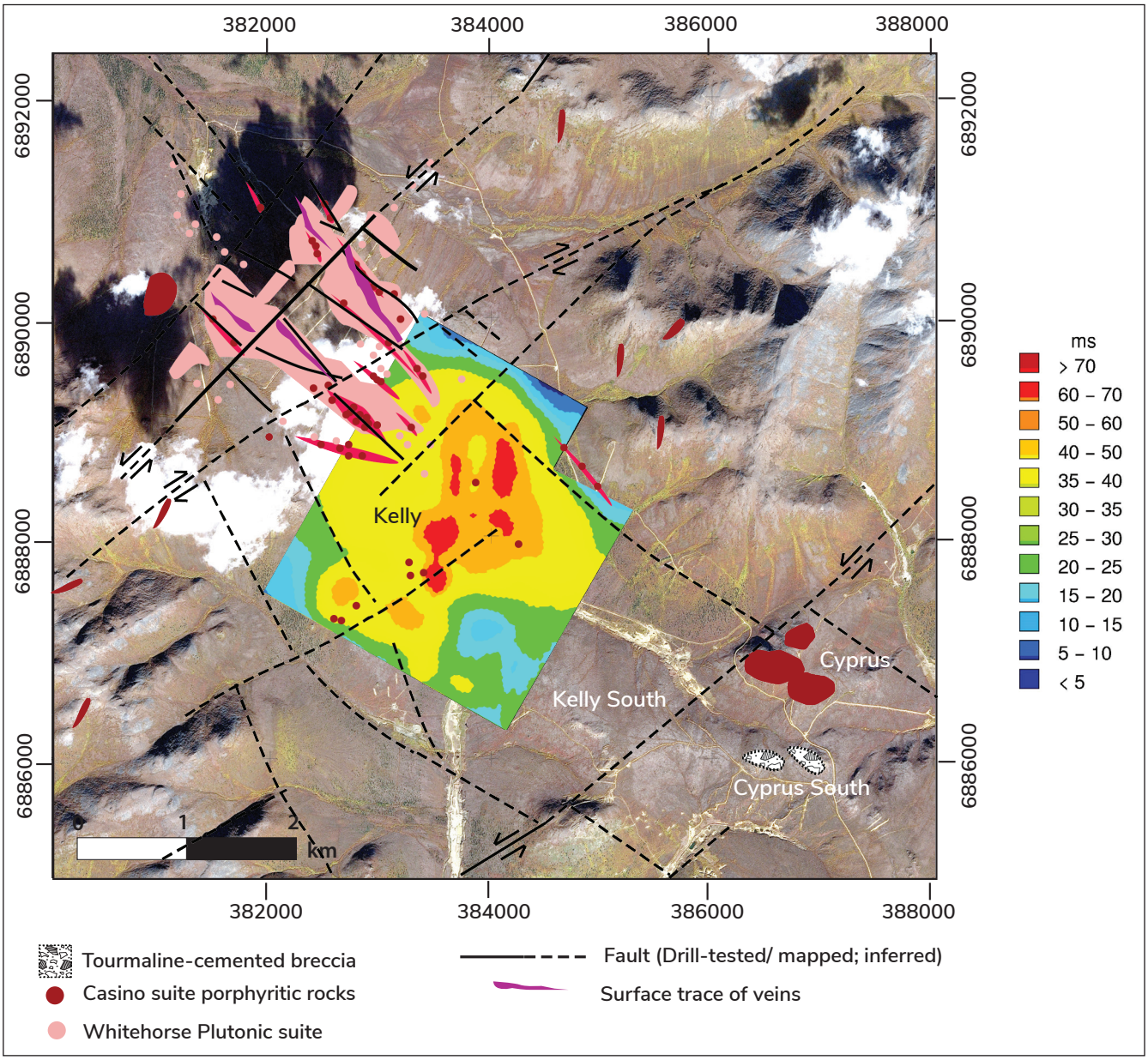


Figure 14. *Induced polarization survey data (chargeability; Ross et al., 2018) from the Kelly zone overlain on an airphoto of the Klaza property. Outcrop and drilling lithologic information is also illustrated for reference to Figure 3.*

IP surveys coupled with airborne magnetic surveys remain important tools for: (1) exploring undercover for large structures, alteration zones, and buried intrusive rocks; and (2) aiding in the reconstruction of geologic maps in outcrop poor areas. The magnetic susceptibilities of the intrusive suites in the Klaza-Nansen area show distinguishable differences, which prove valuable for said map-reconstructions. Note however that fault-related alteration can also significantly lower the magnetic response of these rocks.

Further exploration in the Dawson Range should not discount intrusive rocks outside the prospective 76–75 Ma range from considerations, particularly if said intrusive rocks are porphyritic, contain appropriate abundances of hydrous-mineral phases (hornblende-biotite) and show textural evidence of magma mixing and mingling.

Regional Implications

The longevity and overprinting nature of the magmatic-hydrothermal system at the Klaza deposit also carries implications for understanding the relationship between the Casino (early Late Cretaceous) and Prospector Mountain (late Late Cretaceous) metallogenic events. Although the age of epithermal mineralization at Klaza is currently not directly dated, it is constrained to <76 Ma. Current results show evidence for two overprinting porphyry mineralization events five million years apart. Two contending hypothesis regarding the genesis of the Klaza epithermal veins are to be tested in future work: (1) The Klaza epithermal veins are Casino-age (76–72 Ma) and overprint *ca.* 77 Ma Casino-age Kelly porphyry mineralization during the collapse of the porphyry hydrothermal system, resulting in an epithermal and phyllic overprint of potassic-zone porphyry veins. This is then followed by an overprint from the younger Prospector Mountain-age (72–67 Ma) Cyprus porphyry; or (2) The Klaza epithermal veins are genetically related to the younger Prospector Mountain-age Cyprus porphyry, and form the distal extension of the Cyprus porphyry complex, overprinting the Casino-age Kelly porphyry. Both hypothesis highlight the importance of the late-Late Cretaceous metallogenic event as a significant contributor to precious and base metal endowment in the Dawson Range, Yukon.

Acknowledgements

We are grateful for financial and logistical support from the Yukon Geological Survey (YGS) to conduct fieldwork at the Klaza property. We would like to extend our thanks to Patrick Sack of the YGS for his valuable time, insight and knowledge throughout our time in and out of the field. We also thank Rockhaven Resources Ltd. (RK) for permission to visit and sample at the Klaza property in 2017 and 2019. Matt Turner (RK), Kelson Willms, and Matt Van Loon of Archer, Cathro & Associates are thanked for their time and insight. This paper has greatly benefited from reviews by Patrick Sack and Matt Turner. Work presented in this paper is resultant of the lead-author's on-going PhD thesis at Laurentian University. We acknowledge financial support from the Targeted Geoscience Initiative for the early phase of this study. We also honour the contributions from Jeremy Richards whom is a post-humous co-author, esteemed supervisor, colleague, friend, and technical advisor to RK at the time of his passing.

References

Allan, M. M., Mortensen, J. K., Hart, C. J. R., Bailey, L. A., Sánchez, M. G., Ciolkiewicz, W., McKenzie, G. G. and Creaser, R. A., 2013. Magmatic and metallogenic framework of west-central Yukon and eastern Alaska: Tectonics, Metallogeny, and Discovery: The North American Cordillera and Similar Accretionary Settings. Society of Economic Geologists, Special Publication, vol. 17, p. 111–168.

Audetat, A. and Pettke, T., 2006. Evolution of a Porphyry-Cu Mineralized Magma System at Santa Rita, New Mexico, USA. Journal of Petrology. vol. 47, p. 2021–2046.

Bennett, V., Schulze, C., Ouellette, D. and Pollries, B., 2010. Deconstructing complex Au-Ag-Cu mineralization, Sonora Gulch project, Dawson Range: A Late Cretaceous evolution to the epithermal environment. *In:* Yukon Exploration and Geology 2009, K.E. MacFarlane, L.H. Weston and L.R. Blackburn (eds.), Yukon Geological Survey, p. 23–45.

Bineli Betsi, T. and Bennett, V., 2010. New U-Pb age constraints at Freegold Mountain: Evidence for multiple phases of polymetallic mid to Late Cretaceous mineralization. *In:* Yukon Exploration and Geology 2009, K.E. MacFarlane, L.H. Weston and L.R. Blackburn (eds.), Yukon Geological Survey, p. 57–84.

Bineli Betsi, T., Lentz, D., Chiaradia, M., Kyser, K., and Creaser, R. A., 2013. Genesis of the Au-Bi-Cu-As, Cu-Mo ± W, and base-metal Au-Ag mineralization at the Mountain Freegold (Yukon, Canada): Constraints from Ar-Ar and Re-Os geochronology and Pb and stable isotope compositions. Mineralium Deposita, vol. 48, p. 991–1017.

Burnham, C.W., 1979. Magmas and hydrothermal fluids. Geochemistry of hydrothermal ore deposits, 2nd edition, John Wiley and Sons, p. 71–136.

Byrne, K. and Tosdal, R. M., 2014. Genesis of the Late Triassic Southwest Zone Breccia-Hosted Alkalic Porphyry Cu-Au Deposit, Galore Creek, British Columbia, Canada. Economic Geology, vol. 109, p. 915–938.

Caricchi, L., Annen, C., Blundy, J., Simpson, G. and Pinel, V., 2014. Frequency and magnitude of volcanic eruptions controlled by magma injection and buoyancy. Nature Geoscience Letters, https://doi.org/10.1038/NGEO2041.

Chiaradia, M. and Caricchi, L., 2017. Stochastic modelling of deep magmatic controls on porphyry copper deposit endowment. Scientific Reports 7, article 44523, https://doi.org/10.1038/srep44523.

D'Angelo, M., Miguel, A., Hollings, P., Byrne, K., Piercey, S. and Creaser, R.A., 2017. Petrogenesis and Magmatic Evolution of the Guichon Creek Batholith: Highland Valley Porphyry Cu ± (Mo) District, South-Central British Columbia. Economic Geology, vol. 112, p. 1857–1888.

Davies, A.G.S., Cooke, D.R., Gemmell, J.B. and Simpson, K.A., 2008. Diatreme Breccias at the Kelian Gold Mine, Kalimantan, Indonesia: Precursors to Epithermal Gold Mineralization. Economic Geology, vol. 103, p. 689–716.

Friend, M.A., Allan, M.M. and Hart, C.J.R., 2018. New contributions to the bedrock geology of the Mount Freegold district, Dawson Range, Yukon (NTS 115I/2, 6 and 7). *In:* Yukon Exploration and Geology 2017, K.E. MacFarlane (ed.), Yukon Geological Survey, p. 47–68.

Hart, C.J.R. and Langdon, M., 1998. Geology and mineral deposits of the Mount Nansen camp, Yukon. *In:* Yukon Exploration and Geology 1997, Exploration and Geological Services Division, Yukon, Indian and Northern Affairs Canada, p. 129–138.

Hitzman, M.W., 1999. Routine staining of drill core to determine carbonate mineralogy and distinguish carbonate alteration textures. Mineralium Deposita, vol. 39, p. 794–798.

Klöcking, M., Mills, L., Mortensen, J. and Roots, C., 2016. Geology of mid-Cretaceous volcanic rocks at Mount Nansen, central Yukon, and their relationship to the Dawson Range batholith. Yukon Geological Survey, Open File 2016-25, 37 p. plus appendices.

Kovacs, N., Allan, M.M., Zagorevski, A., Milton, J.E. and Hart, C.J.R., 2017. New geological insights into the Carmacks Copper Cu-Au-Ag deposit, central Yukon (Yukon MINFILE 115I 008). *In:* Yukon Exploration and Geology 2016, K.E. MacFarlane and L.H. Weston (eds.), Yukon Geological Survey, p. 117–140.

Maughan, D. T., Keith, J. D., Christiansen, E.H., Pulsipher, T., Haitori, K. and Evans, N.J., 2002. Contributions from mafic alkaline magmas to the Bingham porphyry Cu-Au-Modeposit, Utah, USA. Mineralium Deposita, vol. 37, p. 14–37.

Mortensen, J.K., Appel, V.L. and Hart, C.J.R., 2003. Geological and U-Pb age constraints on base and precious metal vein systems in the Mount Nansen area, eastern Dawson Range, Yukon. *In:* Yukon Exploration and Geology 2002, D.S. Emond and L.L. Lewis (eds.), Exploration and Geological Services Division, Yukon Region, Indian and Northern Affairs Canada, p. 165–174.

Mortensen, J.K., Hart, C.J.R., Tarswell, J. and Allan, M.M., 2016. U-Pb zircon age and Pb isotopic constraints on the age and origin of porphyry and epithermal vein mineralization in the eastern Dawson Range, Yukon. *In:* Yukon Exploration Geology 2015, K.E. MacFarlane and M.G. Nordling (eds.), Yukon Geological Survey, p. 165–185.

Nelson, J. L., Colpron, M. and Israel, S., 2013. Chapter 3. The Cordillera of British Columbia, Yukon, and Alaska: Tectonics and Metallogeny. *In:* Tectonics, Metallogeny, and Discovery: the North American Cordillera and Similar Accretionary Settings, M. Colpron, T. Bissig, B.G. Rusk and J.F.H. Thompson (eds), Society of Economic Geologists Special Publication 17, p. 53–109, https://doi.org/10.1017/CBO9781107415324.004.

Putirka, K.D., 2017. Down the crater: where magmas are stored and why they erupt. Elements, vol. 13, p. 11–16.

Redmond, P.B. and Einaudi, M.T., 2010. The Bingham Canyon Porphyry Cu-Mo-Au Deposit. I. Sequence of Intrusions, Vein Formation, and Sulfide Deposition. Economic Geology, vol. 105, p. 43–68.

Richards, J.P., 2011. High Sr/Y arc magmas and porphyry Cu ± Mo ± Au deposits: Just add water. Economic Geology, vol. 106, p. 1075–1081.

Richards, J.P., Spell, T., Rameh, E., Razique, A. and Feltcher, T., 2012. High Sr/Y Magmas Reflect Arc Maturity, High Magmatic Water Content, and Porphyry Cu ± Mo ± Au Potential: Examples from the Tethyan Arcs of Central and Eastern Iran and Western Pakistan. Economic Geology, vol. 107, p. 295–332.

Ross, A.A., Kirchner, I., Martin, C.J., Dumala, M.R. and Methven, G., 2018. Technical Report Describing Updated Diamond Drilling, Metallurgical Testing and Mineral Resources on the Klaza Property, Yukon, Canada. NI 43-101, https://doi.org/10.1016/j.cagd.2003.08.001.

Ryan, J.J., Westberg, E.E., Williams, S.P. and Chapman, J.B., 2016. Geology, Mount Nansen–Nisling River area, Yukon. Geological Survey of Canada, Canadian Geoscience Map 292 (preliminary), scale 1:100 000, https://doi.org/10.4095/298835.

Seedorf, E., Dilles, J.H., Proffett, J.M., Einaudi, M.T., Zurcher, L., Stavast, W.J.A., Johnson, D.A. and Barton, M.D., 2005. Porphyry Deposits: Characteristics and Origin of Hypogene Features. In: Economic Geology 100th Anniversary Volume, J.W. Hedenquist, J.F. Thompson, R.J. Goldfarb and J.P. Richards (eds.), Society of Economic Geologists, Inc., p. 251–298.

Selby, D. and Creaser, R.A., 2001. Late and mid-Cretaceous mineralization in the Northern Canadian Cordillera: Constraints from Re-Os molybdenite dates. Economic Geology, vol. 96, p. 1461–1467.

Selby, D., Nesbitt, B.E., Creaser, R.A., Reynolds, P.H. and Muehlenbachs, K., 2001. Evidence for a nonmagmatic component in potassic hydrothermal fluids of porphyry Cu-Au-Mo systems, Yukon, Canada. Geochimica et Cosmochimica Acta, vol. 65, p. 571–587.

Sillitoe, R., 2010. Porphyry Copper Systems. Economic Geology, vol. 105, p. 3–41.

Turner, M. and Dumala, M., 2017. Klaza project: An expanding high-grade Au and Ag resource in the Mount Nansen gold camp (Yukon MINFILE 115I 067). *In:* Yukon Exploration and Geology Overview 2016, K.E. MacFarlane (ed.), Yukon Geological Survey, p. 89–96.

Whitney, D.L. and Evans, B.W., 2010. Abbreviations for names of rock-forming minerals. American Mineralogist, vol. 95, p. 185–187.

Geochronologic and Pb-isotopic constraints on gold mineralization at the Plateau South property (Yukon MINFILE 105N 034, 035, 036), central Yukon

P. Sack*
Yukon Geological Survey

J. Gabites
University of British Columbia

J. Crowley
Boise State University

J. Benowitz
University of Alaska Fairbanks

C. McFarlane
University of New Brunswick

M. Gobadi
Activation Laboratories Ltd.

D. Ferraro
Goldstrike Resources Ltd.

Sack, P., Gabites, J., Crowley, J., Benowitz, J., McFarlane, C., Gobadi, M. and Ferraro, D., 2020. Geochronologic and Pb-isotopic constraints on gold mineralization at the Plateau South property (Yukon MINFILE 105N 034, 035, 036), central Yukon. *In:* Yukon Exploration and Geology 2019, K.E. MacFarlane (ed.), Yukon Geological Survey, p. 99–119.

Abstract

Quantitative mineralogy, U-Pb geochronology of zircon and monazite, $^{40}Ar/^{39}Ar$ geochronology of muscovite and sericite, and Pb isotopes from galena in veins and feldspar in plutons provide insight into the age of metamorphism, mineralization, intrusion emplacement and the sources of metals at the Plateau South (MINFILE 105N 034, 035, 036) occurrences in central Yukon. Orogenic mineralization and metamorphism is *ca.* 110 Ma to 100 Ma, and possibly as old as *ca.* 130 Ma. Following deformation and regional metamorphism, two biotite-muscovite plutons, the Russell stock and Armstrong pluton, were emplaced at 95.39 ± 0.03 Ma and 95.51 ± 0.03 Ma, respectively. These plutons are here reassigned to the Tungsten suite based on mineralogy, chemistry and age. Coeval with these plutons are contact metamorphism and possibly intrusion-related mineralization. Lead isotopic data from galena cluster into two groups: Group 1 is enriched in thorogenic Pb with $^{206}Pb/^{204}Pb$ values between 18.31 and 18.14, $^{207}Pb/^{204}Pb$ between 15.62 and 15.55 and $^{208}Pb/^{204}Pb$ between 38.77 and 38.30. Group 2 is isotopically evolved with $^{206}Pb/^{204}Pb$ values between 19.13 nd 18.91, $^{207}Pb/^{204}Pb$ between 15.78 and 15.63 and $^{208}Pb/^{204}Pb$ between 39.24 and 39.07. We suggest that late Early Cretaceous mineralization is related to large-scale orogenic fluids that tapped primitive (deep?) metal sources and early Late Cretaceous mineralization, coeval with local intrusions, sourced isotopically distinct metals from the intrusions. Alternatively, all mineralization could relate to Early Cretaceous orogenic fluids but with heterogeneous, locally derived metal sources and thermal resetting of Ar ages near the intrusions.

* patrick.sack@gov.yk.ca

Introduction

The Plateau South property was initially staked in 2011 and since then more than 20 breccia and vein gold showings have been found across a 50 km area; the veins and property geology are described in more detail in Sack et *al.* (2018). The Plateau South showings often contain visible gold and are reminiscent of orogenic gold veins though previous work points out that mineralization also shares similarities with reduced-intrusion related gold deposits (Sack et *al.*, 2018) which are well known in the Selwyn basin area (e.g., Hart et *al.*, 2004). To help discriminate between an orogenic and intrusion-related origin for the veins in the Plateau area, a suite of samples was collected in 2016 and 2017 for geochronology and Pb isotopic analyses. Here, we present and discuss these data and use them to constrain the age of metamorphism, mineralization, intrusion emplacement and the sources of metals in the veins at the Plateau property in central Yukon.

Geology

The Plateau property lies within basinal ancestral North America rocks of the northern Canadian Cordillera (Fig. 1). The property is mostly underlain by Neoproterozoic to Cambrian rocks of the Hyland Group, mostly the Yusezyu Formation (Fig. 2). The Yusezyu Formation rocks are coarse to fine-grained sandstone and siltstone with pebble conglomerate interbeds that have been regionally metamorphosed to greenschist facies and are now phyllite to schist (Sack et *al.*, 2018).

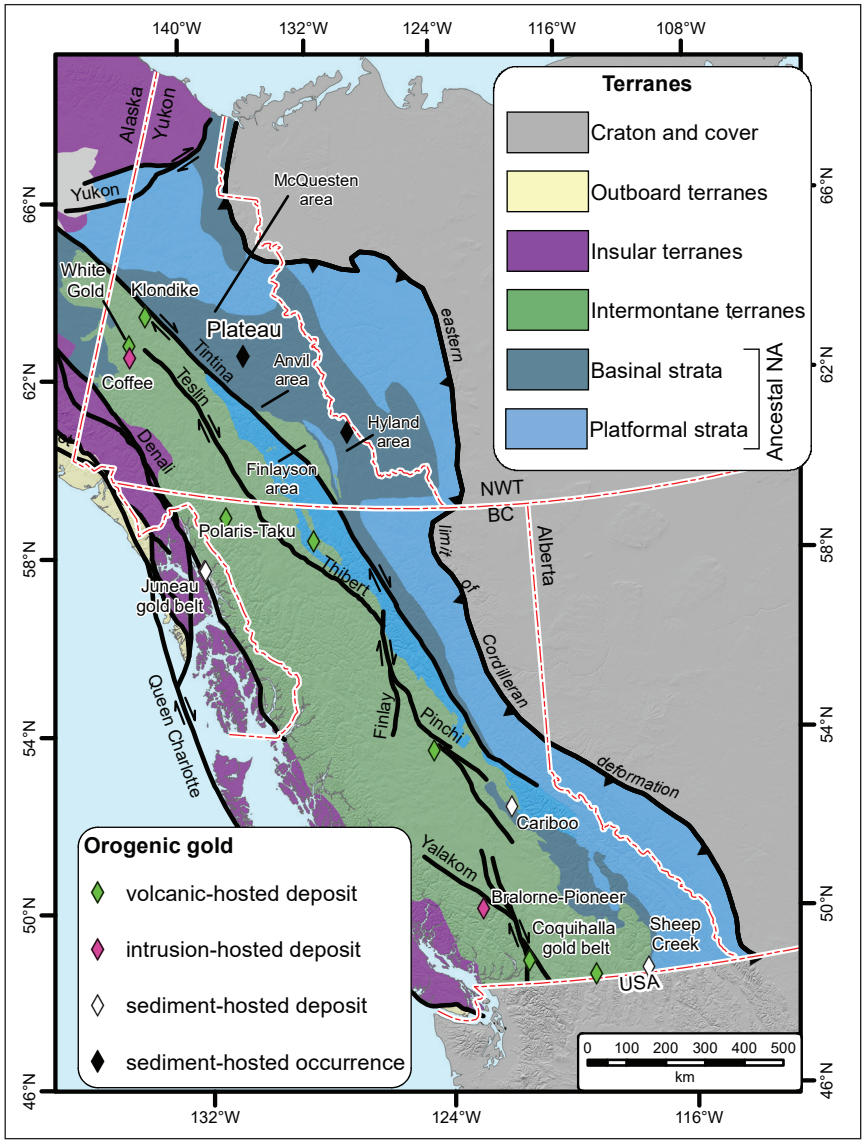


Figure 1. *Terranes, regional faults, significant orogenic gold deposits and camps of British Columbia and Yukon. Deposits from Goldfarb et al. (2005), Dubé and Gosselin (2007) and YGS (2018a). Terranes from Colpron and Nelson (2011). NA = North America. Note location of Hyland, Anvil, McQuesten and Finlayson areas used to frame regional geochronology discussion.*

At the property scale, the Yusezyu Formation is subdivided into units that are dominantly psammite and pelite (Roach, 2013; Stubley, 2017; Vanwermeskerken, 2017) with all of the known veins hosted in the psammite unit. A thin, concordant body of chloritic phyllite in the Big Bang zone (Fig. 2) is interpreted as a mafic volcanic rock or sill (Stubley, 2017), possibly correlating with the Old Cabin Formation of Cecile (2000); mafic rocks are also found 30 km to the south (Roots, 2003). Paleozoic shale of the Gull Lake, Road River and Earn groups, as well as the Mt Christie, Tsichu and No Gold formations (Roots, 2003) is found to the northeast and southwest of the area. The Yusezyu Formation is intruded by the Russell stock and Armstrong pluton. These plutons are medium-grained, equigranular, and biotite-muscovite ± hornblende ± garnet bearing granite to granodiorite intrusions having low magnetic susceptibility (<0.1 × 10^{-3} SI units; Sack et *al*., 2018).

The Plateau property mostly lies within the Tombstone strain zone (Murphy, 1997), the southern (upper) boundary of which is approximated by the thick dashed line on Fig. 2 (Roots et *al*., 1995; Roots, 1998). This boundary broadly subdivides the property into two structural domains and is coincident with many of the vein showings (Sack et *al*., 2018). The southern domain has upright folds with steep axial planar cleavage and the northern domain comprises inclined to recumbent folds with low-angle axial planar cleavage (Stubley, 2017). The upright domain structurally overlies the shallow domain. Though the detailed structural history varies slightly between the domains, they each have a well developed early axial planar cleavage developed around broadly NW or SE fold axes and a later, less intense crenulation cleavage (Sack et *al*., 2018). Mineralized breccia in the Goldstack zone forms an elongate body, as defined by limited diamond drilling,

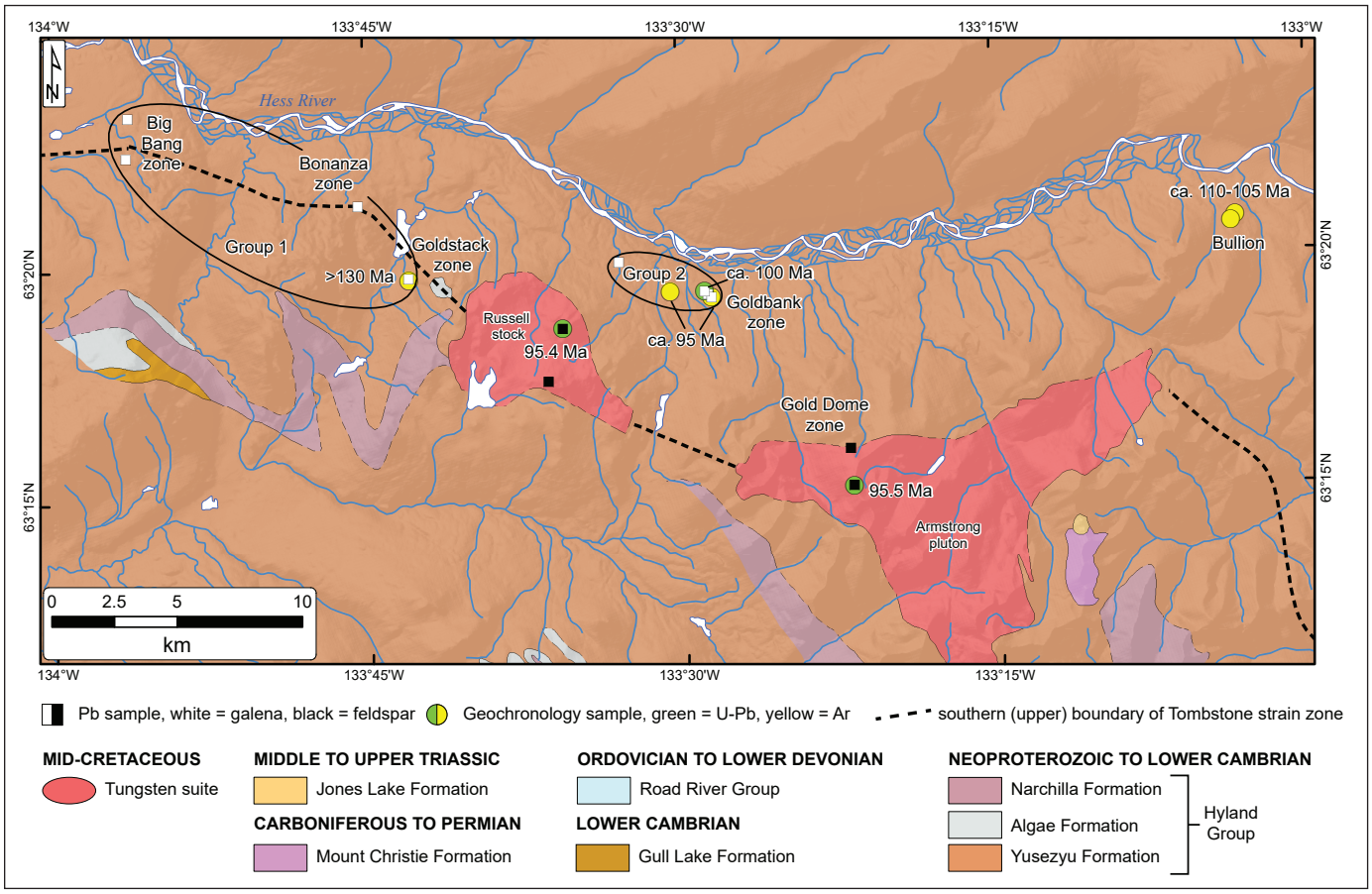


Figure 2. *Simplified Plateau property geology from YGS (2018b). Geochronology labels are those cited in text and Table 1. Groups 1 and 2 are based on Pb isotopic data from Table 3. For more information on the detailed geology, showings and claim boundaries in this area see Fig. 4 of Sack et al. (2018).*

that strikes NW, and appears to be in the antiformal hinge of a fold in the upright domain; the orientation of other breccia showings is not known. Mineralized veins are dominantly NE striking extensional veins that crosscut all earlier structures and fabrics but are variably deformed and recrystallized suggesting formation late in the ductile deformation history (Sack et *al*., 2018). Plutons in the area are undeformed and have contact aureoles that overprint foliation, thus indicating emplacement after ductile deformation (Fig. 3; Sack et *al*., 2018).

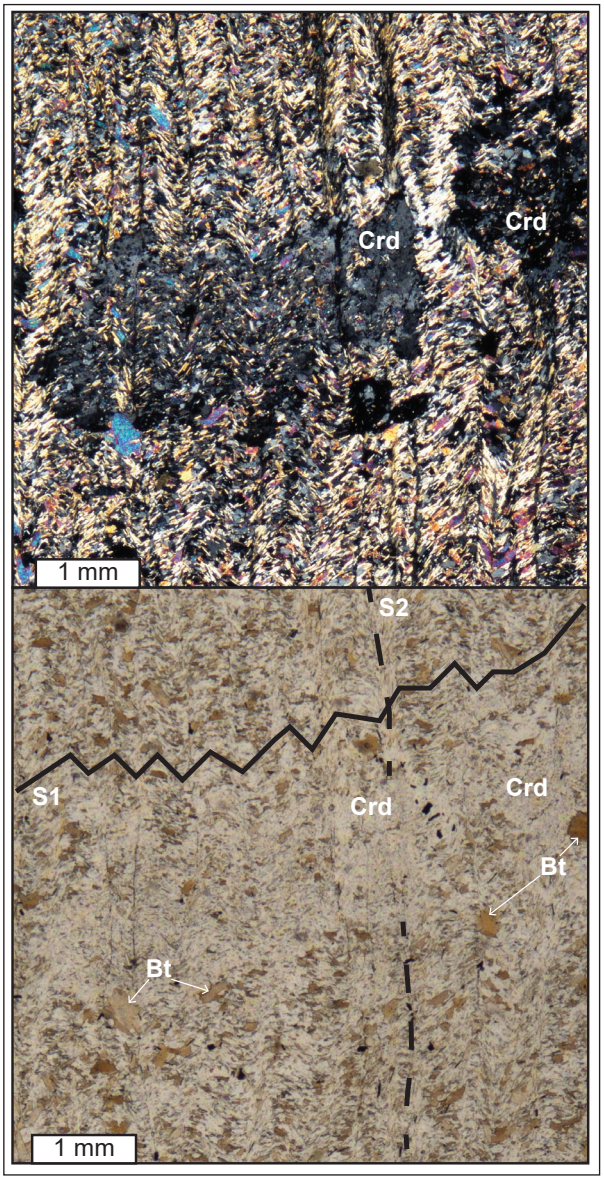


Figure 3. *Cross-polarized* ***(upper)*** *and plain polarized* ***(lower)*** *photomicrographs of cordierite overgrowing two generations of foliation in pelite (17PS009-1) (Sack et al., 2018). Birefringent mineral is muscovite. Crd = cordierite, Bt = biotite.*

Mineralization on the Plateau South property can be broadly divided into breccia bodies that may strike NW and massive, discrete, white quartz veins that strike NE. The Goldstack, Big Bang zones and possibly Gold Dome have breccia style showings but most of the showings are individual, or sets of, discrete NE striking veins (Sack et *al*., 2018). In both styles of mineralization, the earliest quartz is massive and recrystallized, commonly with reduced grain boundaries and strong undulatory extinction (Fig. 4a). Associated coarse-grained euhedral arsenopyrite is typically fractured (Fig. 4b). Later quartz-sulphide ± muscovite ± carbonate ± plagioclase (albite?) veins crosscut earlier veins. Gold is associated predominantly with arsenopyrite (Fig. 4c) but also with pyrite and pyrrhotite. Minor galena and chalcopyrite are noted locally (Richards, 2015).

Despite the different orientation and appearance, the similar mineralogy and paragenesis has lead previous workers to infer a shared origin for vein and breccia type showings (Barr, 2017; Farquharson, 2017; Sack et *al*., 2018). Galena in the vein showings occurs as anhedral fracture-fill in arsenopyrite or as anhedral masses within the veins (Fig. 6) and is interpreted as a pargenetically late mineral. Where galena fits in the paragenesis of the breccia showings is not constrained in thin section. Correlation coefficient (r^2) values between Au and Ag, As, Pb and Sb for all showings range between 0.6 and 0.1, consistent with the presence of arsenopyrite in all gold bearing veins and galena in some (Sack et *al*., 2018).

Methods

We use five data sets in this paper: (1) whole-rock geochemistry; (2) quantitative mineralogy; (3) U-Pb zircon geochronology for plutons and U-Pb monazite for psammitic schist; (4) Ar geochronology of muscovite from psammitic schist and sericite from veins; and (5) Pb isotopes from galena in veins and feldspar in plutons. A brief method summary for each data set is given below; further details for each method are in the appendices or in cited references.

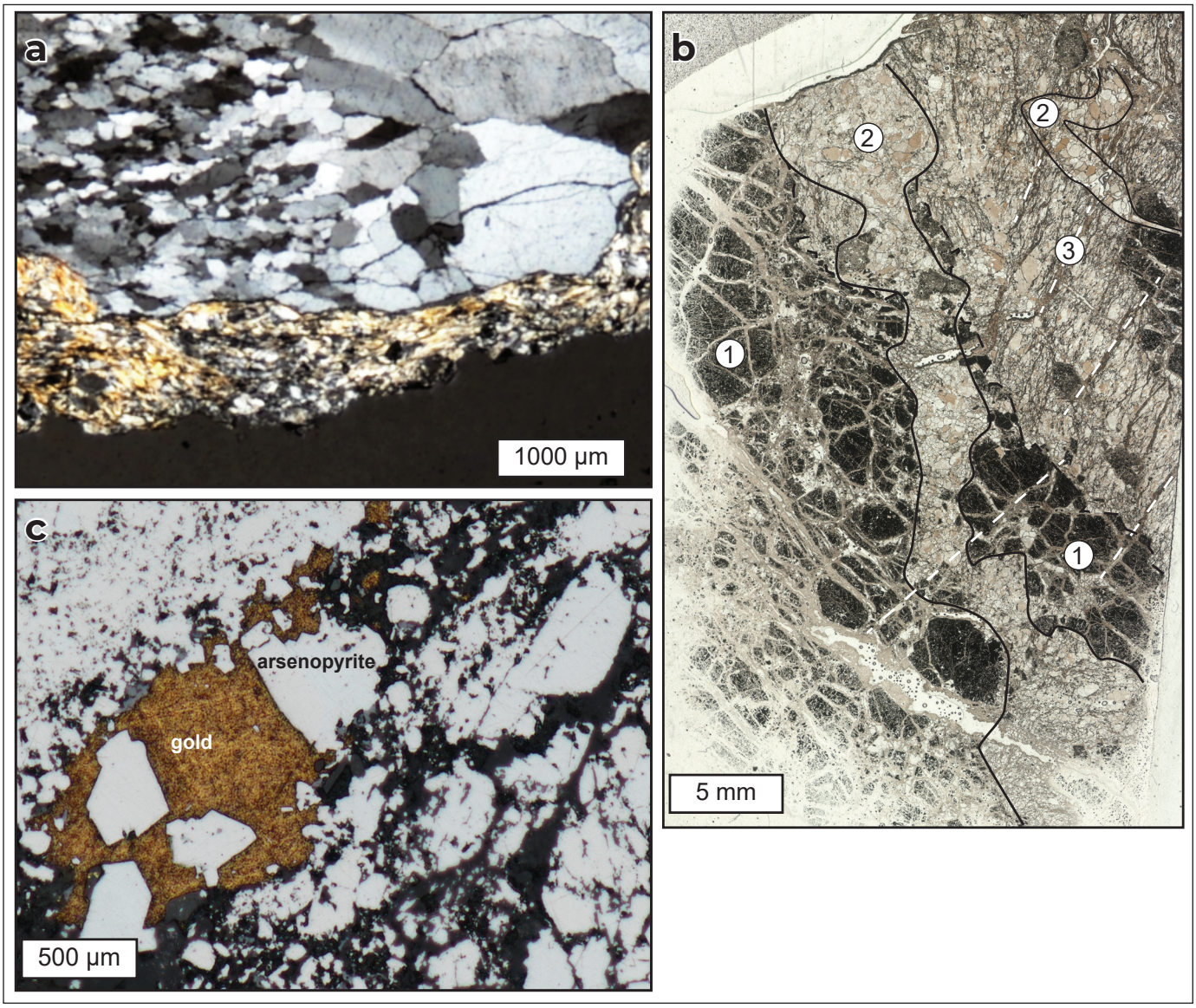


Figure 4. *Mineralized veins on the Plateau South property.* ***(a)*** *Breccia style with early recrystallized quartz cut by later, thin quartz-sericite-carbonate veinlet, Bonanza zone, 16PS001-1 (Sack et al., 2018).* ***(b)*** *Plane polarized light thin section scan illustrating paragenesis for vein style mineralization at the Ron Stack vein, Goldbank zone (17PS028-2): 1 – early brittle deformed arsenopyrite vein; 2 – folded and variably recrystallized quartz veins that cut 1; and 3 – foliation that penetrates 1 and 2.* ***(c)*** *Native gold intergrown with arsenopyrite PSGS1502-37.60m, Goldstack zone.*

Whole-rock geochemistry

Whole-rock analysis of four pluton and five country rock samples was conducted at Activation Laboratories Ltd. The analytical package was 4Lithoresearch, a lithium metaborate/tetraborate fusion followed by Inductively Coupled Plasma Mass Spectrometry (ICPMS). For major elements, the quality of these data meet or exceeds fusion x-ray fluorescence data. For trace elements, the fusion process provides total dissolution of refractory minerals such as zircon, sphene and monazite, and gives accurate rare earth and high field strength element data. Precision for major elements is typically <5%; trace and rare earth element precision is typically <10%. Major and rare earth element accuracy is <10%; trace element accuracy is <20%. Data are in Appendix 1.

Mineralogy

Quantitative mineralogy and mineralogical mapping using QEMSCAN (quantitative evaluation of materials by scanning electron microscopy) were conducted at Activation Laboratories on three parallel cut thin sections from one breccia style showing and one vein style showing. Data are in Appendix 1

U-Pb geochronology

Two plutonic samples underwent U-Pb zircon geochronological analysis at Boise State University. Data include cathodoluminescence (CL) images of zircon, and results of laser ablation-inductively coupled plasma mass spectrometry (LA-ICPMS) and chemical abrasion-thermal ionization mass spectrometry (CA-TIMS). We use the more precise weighted mean date of CA-TIMS analyses to determine the crystallization age of each sample. Errors are reported at 2σ. Data are in Appendix 2

U-Th-Pb monazite geochronology for one wall rock sample was carried out at the University of New Brunswick. Monazite grains were located using QEMSCAN and were imaged with a scanning electron microscope in backscatter emission mode (SEM-BSE). U-Th-Pb data were collected using LA-ICPMS with a laser crater diameter of 13 µm, a laser pulse rate of 3 Hz, 3 J/cm^2 laser fluence, and 30 seconds of ablation after 30 seconds of gas background collection. Errors are reported at 2σ. Data are in Appendix 2

Ar geochronology

Argon geochronology for five samples was completed at the Geochronology Laboratory at the University of Alaska Fairbanks; two muscovite samples from country rock and three sericite samples from mineralized rocks. Samples were crushed, sieved, washed and hand-picked for pure muscovite and sericite separates. Samples were irradiated and subsequently analyzed for $^{40}Ar/^{39}Ar$ using step-heating and mass spectrometry. Analysis for each sample consists of eight steps and ages are primarily interpreted from plateau or pseudo-plateau ages. An isochron age determination is not possible for any of the samples because of disturbance to all Ar spectra. Argon ages quoted in text and Table 1 are at 2σ to facilitate comparison with other data. Data were collected at 1σ and are reported as such in Appendix 3 tables.

Pb isotopes

Lead isotopic composition of galena from veins, and feldspar from plutons, was determined at the Pacific Centre for Isotopic and Geochemical Research at the University of British Columbia. Mineral separates were washed and dissolved in dilute hydrochloric acid, then prepared and analyzed using the TIMS method described by Mortensen and Gabites (2002). Errors are reported at 2σ. Data are in Table 3.

Results

Mineralogy

Breccia showings comprise recrystallized quartz-plagioclase and wall-rock fragments within quartz-muscovite-carbonate-pyrite cement cut by later, relatively simple quartz-arsenopyrite-calcite veins (Fig. 5). The quartz in these later veins is variably recrystallized. Vein showings have at least two generations of veining: 1) early recrystallized quartz-sulphide (pyrite?) veins at a high angle to foliation; and 2) veins oblique to the dominant foliation with variably recrystallized quartz-arsenopyrite-galena-pyrite (Fig. 6). In both styles of mineralization, where observed in thin section, gold is most closely associated with arsenopyrite (Fig. 4; Sack *et al.*, 2018).

U-Pb zircon geochronology

Table 1 summarizes the geochronological results for the Plateau South area.

Sample 16PS011-1 is a medium-grained, equigranular biotite-muscovite granodiorite collected from the core of the Russell stock (Fig. 2). It yielded euhedral, concentrically zoned zircons with a 3:1 aspect ratio; one grain has an inherited core (Fig. 7a). Forty-eight LA-ICPMS spot analyses yielded $^{206}Pb/^{238}U$ dates between 108 and 86 Ma, the one inherited core is 1200 Ma. The weighted mean of 41 LA-ICPMS dates is 95.95 ± 0.76 Ma (n = 41 of 48; Fig. 7b). Five zircons from 16PS011-1 were analyzed by CA-TIMS and

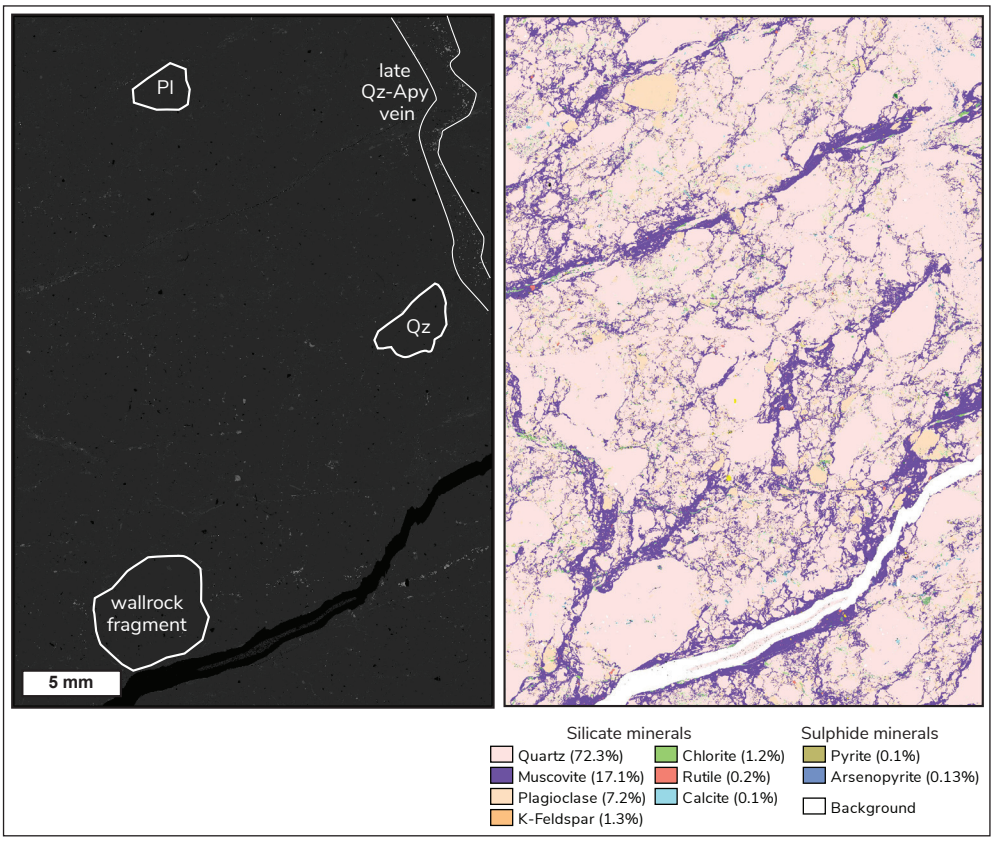


Figure 5. *Mineralogy of sample PSGS1501-31.36 m, Goldstack breccia. SEM-BSE image* ***(L)*** *and QEMSCAN particle map* ***(R)****. Minerals in the legend below QEMSCAN particle map make up 99.7% of sample by surface area. Qz = quartz, Pl = plagioclase, Apy = arsenopyrite.*

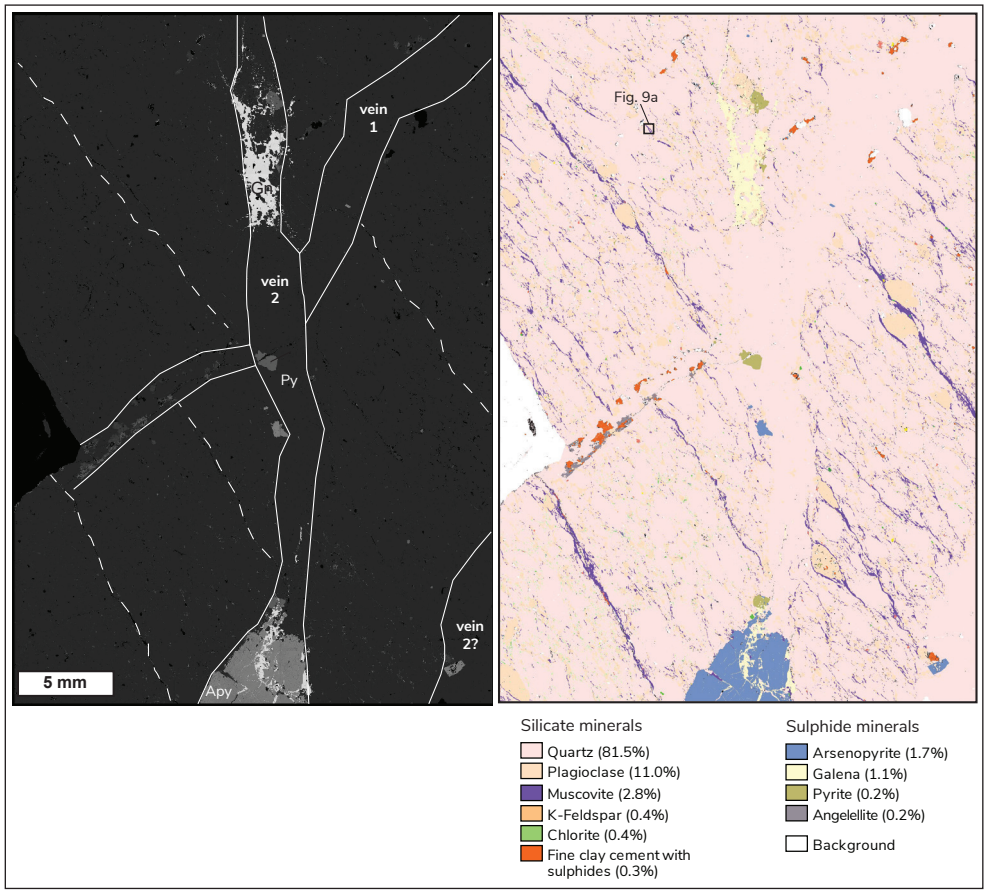


Figure 6. *Mineralogy of sample 16PS006-1, Stack West vein in the Goldbank zone. SEM-BSE image* ***(L)*** *and a QEMSCAN particle map* ***(R)****. Minerals in the legend below QEMSCAN particle map make up 99.6% of sample by surface area. Note approximate location of Fig. 9a, which is from a parallel cut thin section. Mineral abbreviations same as Fig. 5; Gn = galena.*

Table 1. *Summary table listing geochronological results.*

Sample	Zone	Showing	Latitude	Longitude	Age	Error (2σ)	MSWD	Method	Mineral	Comment	Interpretation
17PS025-1	Bullion	Bullion vein	63.345774	-133.057198	103.2	5.2	0.14	Ar/Ar	Ser	Ar loss - 77% release in 4 of 8 fractions; integrated age = 107.0±5.4	mineralization
PSGS1501-25.19m	Goldstack	Goldstack breccia	63.328847	-133.716292	130.1	6.0	0.48	Ar/Ar	Ser	excess Ar - 62% release in 4 of 8 fractions; integrated age = 196.2±5.0	regional metamorphism; possibly mineralization
17PS023-1	Bullion	Bullion schist	63.343608	-133.060891	107.0	5.2	0.84	Ar/Ar	Ms	Ar loss - 37% release in 2 of 8 fractions; integrated age = 103.9±5.0	regional metamorphism
17PS028-2	Goldbank	Ron Stack vein	63.320613	-133.475433	95.5	6.2	0.4	Ar/Ar	Ser	excess Ar - 73% release in 5 of 8 fractions; integrated age = 112.0±6.8	contact metamorphism
17PS026-1	Goldbank	Goldbank schist	63.32282	-133.508163	93.9	4.6	2.76	Ar/Ar	Ms	Ar loss - 54% release in 2 of 8 fractions; integrated age = 91.4±4.6	contact metamorphism
16PS006-1	Goldbank	Stack west vein	63.32274	-133.48071	98.8	4.0	1.8	U/Pb	Mnz	n=12; weighted mean age; small isolated grains and trains in anastomosing fabric; U/Th 0.012	regional metamorphism
16PS011-1	Russell stock	Russell stock	63.3104	-133.59449	95.4	0.03	1.3	U/Pb	Zrn	n=5 of 5; pof = 0.27; 1 inherited 1200 Ma grain	igneous crystallization
16PS013-1	Armstrong pluton	Armstrong pluton	63.25193	-133.36551	95.5	0.03	0.8	U/Pb	Zrn	n=5 of 5; pof = 0.55; no inherited grains	igneous crystallization

Ser = sericite, Ms = muscovite, Mnz = monazite, Zrn = zircon

yielded equivalent $^{206}Pb/^{238}U$ dates ranging from 95.34 ± 0.07 to 95.45 ± 0.07 Ma (Table 2), with a weighted mean age of 95.39 ± 0.03 Ma (MSWD = 1.3, n = 5; Fig. 7c). This is the best estimate of the crystallization age of the Russell stock.

Sample 16PS013-1 is a medium-grained, equigranular biotite-muscovite granite collected from an area near the north margin of the Armstrong pluton (Fig. 2). It also yielded euhedral, concentrically zoned zircons that are either stubby (~1:1 aspect ratio) or elongate (>3:1 aspect ratio; Fig. 8a). Forty-eight LA-ICPMS spot analyses yielded $^{206}Pb/^{238}U$ dates between 110 and 86 Ma; there are no inherited cores. The weighted mean of 38 LA-ICPMS dates is 93.73 ± 0.57 Ma (n = 38 of 48; Fig. 8b). Five zircons from 16PS013-1 were analyzed by CA-TIMS and yielded equivalent $^{206}Pb/^{238}U$ dates ranging from 95.54 ± 0.07 to 95.48 ± 0.07 Ma (Table 2), with a weighted mean age of 95.51 ± 0.03 Ma (MSWD = 0.8, n = 5; Fig. 8c). This is the best estimate of the crystallization age for the Armstrong pluton.

U-Th-Pb monazite geochronology

Sample 16PS006-1 is from the Stack West vein in the Goldbank area (Fig. 2) and the thin section includes both psammite wall rock and quartz-sulphide veins (Fig. 6). The *in situ* dated monazite are small (<50 µm) anhedral grains along foliation within the wall rock and are intergrown with muscovite (Figs. 6 and 9a). We interpret the monazite as metamorphic in origin. The inverse isochron age, anchored at a common-Pb $^{207}Pb/^{206}Pb$ value of 0.825 ± 0.005, for 14 of 21 analyses gives a lower intercept age of 89.8 ± 8.8 Ma (MSWD = 1.7; Fig. 9b). The ^{204}Pb-corrected weighted mean $^{208}Pb/^{232}Th$ age for 12 of these analyses is 98.8 ± 4.0 (MSWD = 1.8; Fig. 9c) which is within error of the anchored inverse isochron lower intercept age and is the best estimate for the age of regional metamorphism in the Goldbank zone.

$^{40}Ar/^{39}Ar$ geochronology

Sample 17PS023-1 is of psammitic schist that hosts veins in the Bullion zone (Fig. 2). Muscovite in this sample is predominantly related to an early bedding parallel foliation; minor new muscovite is associated

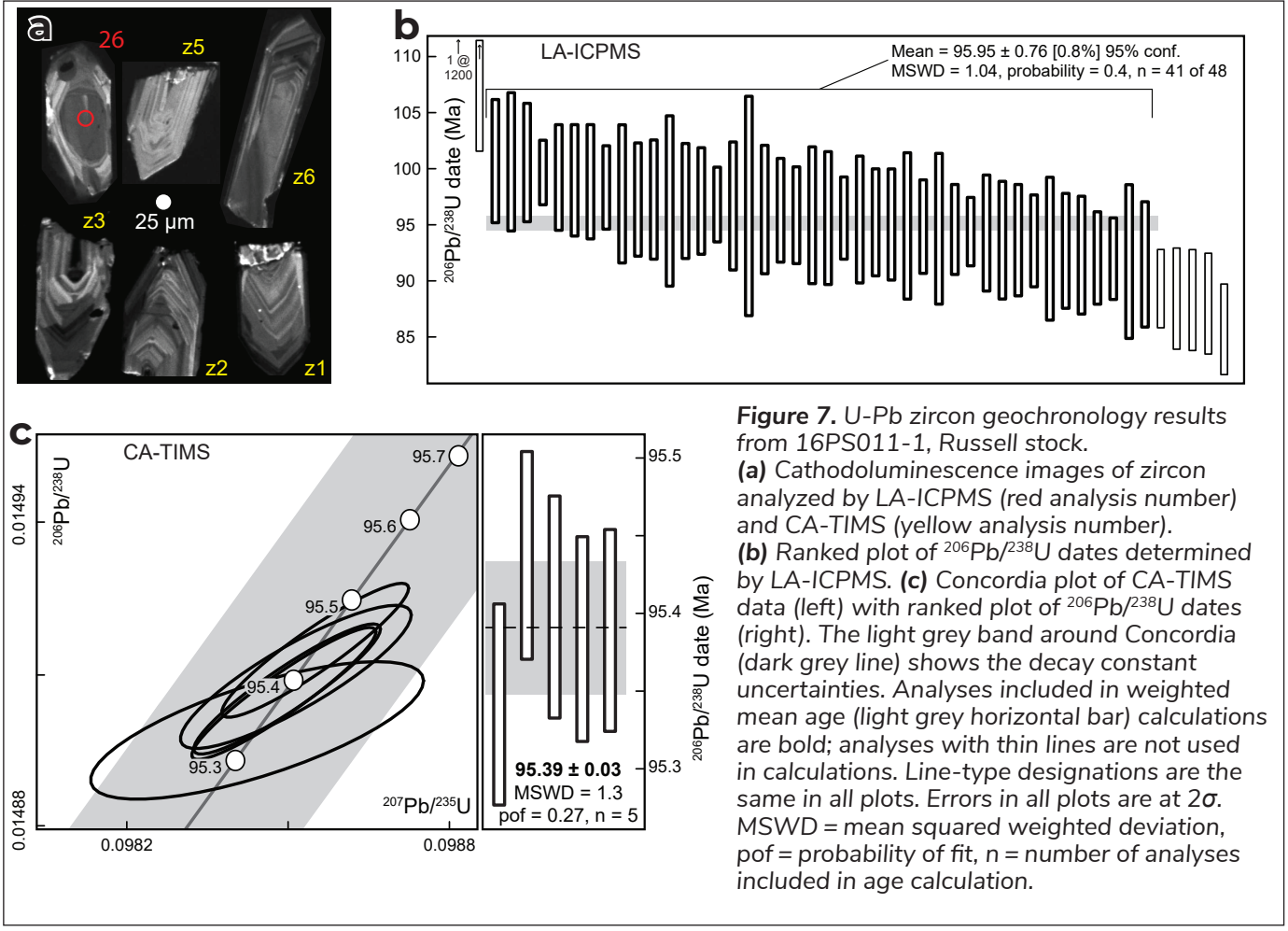


Figure 7. *U-Pb zircon geochronology results from 16PS011-1, Russell stock.* ***(a)*** *Cathodoluminescence images of zircon analyzed by LA-ICPMS (red analysis number) and CA-TIMS (yellow analysis number).* ***(b)*** *Ranked plot of ^{206}Pb/^{238}U dates determined by LA-ICPMS.* ***(c)*** *Concordia plot of CA-TIMS data (left) with ranked plot of ^{206}Pb/^{238}U dates (right). The light grey band around Concordia (dark grey line) shows the decay constant uncertainties. Analyses included in weighted mean age (light grey horizontal bar) calculations are bold; analyses with thin lines are not used in calculations. Line-type designations are the same in all plots. Errors in all plots are at 2σ. MSWD = mean squared weighted deviation, pof = probability of fit, n = number of analyses included in age calculation.*

with a subsequent foliation. A muscovite separate gave an integrated age of 103.9 ± 5.0 Ma and a weighted mean age from two overlapping, but non-sequential, steps of 107.6 ± 5.2 Ma (2 of 8 steps, 36.9% ^{39}Ar release MSWD = 0.84; Fig. 10). The spectra have a 'stepping-up' age pattern where the higher temperature steps had older ages than the lower temperature steps. This pattern is indicative of gas loss due to alteration or reheating and suggests the oldest step (109.65 ± 0.8 Ma) may be a minimum age. The spectra do not meet the sequential overlapping criteria for a plateau age; hence, a weighted average age of steps 6 and 8 is presented. The integrated and weighted average age are within error of each other. We interpret the weighted average age of 107.0 ± 5.2 Ma as the minimum age of significant regional metamorphism recording the end of ductile deformation and metamorphism ca. 110 to 105 Ma.

Sample 17PS026-1 is psammitic schist that hosts veins in the Goldbank zone (Fig. 2). The same two generations of muscovite recognized in 17PS023-1 are also recognized in this sample. A muscovite separate gave an integrated age for all steps of 91.4 ± 4.6 Ma and a pseudo-plateau age of 93.7 ± 7.0 Ma (3 of 8 steps, 63.6% ^{39}Ar release MSWD = 2.19; Fig. 10). The spectra have a 'stepping-up' age pattern indicative of gas loss due to alteration or reheating. The integrated and pseudo-plateau ages are within error. We interpret the plateau age of 93.7 ± 7.0 Ma as reset by the nearby 95.5 Ma intrusions.

Sample PSGS1501-25.19m is from a mineralized and recrystallized quartz-sericite-sulphide breccia in the Goldstack area. A sericite separate from the sample gave an integrated age for all steps of 196.2 ± 5.0 Ma and a plateau age of 130.1 ± 6.0 Ma (4 of 8 steps, 62.3% ^{39}Ar release MSWD = 0.48; Fig. 11).

Table 2. *CA-TIMS U-Pb zircon data table. The data and calculations for this table are available in Appendix 2.*

Sample	Th/U	$^{206}Pb^*$ x10^{-13} mol	mol% $^{206}Pb^*$	Pb^*/Pb_c	Pb_c (pg)	$^{206}Pb/^{204}Pb$	$^{208}Pb/^{206}Pb$	$^{207}Pb/^{206}Pb$	% err	$^{207}Pb/^{235}U$	% err	$^{206}Pb/^{238}U$	% err	corr. coef.	$^{207}Pb/^{206}Pb$	±	$^{207}Pb/^{235}U$	±	$^{206}Pb/^{238}U$	±	include in weighted mean
(a)	(b)	(c)	(c)	(c)	(c)	(d)	(e)	(e)	(f)	(e)	(f)	(e)	(f)		(g)	(f)	(g)	(f)	(g)	(f)	
16PS11-1																					
z1	0.226	2.7152	99.84%	177.9	0.35	11647	0.072	0.0480	0.080	0.0986	0.142	0.0149	0.071	0.940	98.14	1.90	95.49	0.13	95.38	0.07	x
z2	0.403	2.0437	99.86%	210.3	0.24	13030	0.129	0.0480	0.082	0.0987	0.144	0.0149	0.072	0.932	99.59	1.93	95.61	0.13	95.45	0.07	x
z3	0.456	1.1147	99.65%	85.8	0.32	5269	0.146	0.0480	0.118	0.0986	0.178	0.0149	0.077	0.867	97.48	2.79	95.49	0.16	95.41	0.07	x
z5	0.565	0.6973	99.55%	68.2	0.26	4066	0.181	0.0479	0.210	0.0985	0.257	0.0149	0.074	0.719	96.08	4.97	95.36	0.23	95.34	0.07	x
z6	0.312	2.6767	99.91%	303.3	0.21	19223	0.100	0.0480	0.084	0.0986	0.144	0.0149	0.070	0.923	98.46	1.98	95.51	0.13	95.39	0.07	x
16PS13-1																					
z1	0.250	8.0530	99.97%	955.7	0.20	61561	0.080	0.0480	0.065	0.0987	0.129	0.0149	0.070	0.965	97.13	1.53	95.60	0.12	95.54	0.07	x
z2	0.200	6.8267	99.96%	719.7	0.22	47103	0.064	0.0480	0.065	0.0987	0.130	0.0149	0.071	0.966	97.75	1.53	95.59	0.12	95.50	0.07	x
z3	0.251	5.9637	99.96%	663.5	0.21	42764	0.080	0.0480	0.067	0.0988	0.131	0.0149	0.071	0.960	98.52	1.58	95.65	0.12	95.54	0.07	x
z5	0.354	2.9896	99.90%	294.8	0.24	18516	0.113	0.0480	0.079	0.0987	0.140	0.0149	0.070	0.937	97.69	1.86	95.56	0.13	95.48	0.07	x
z6	0.387	2.8976	99.89%	274.2	0.26	17079	0.124	0.0480	0.079	0.0987	0.141	0.0149	0.071	0.936	97.85	1.87	95.57	0.13	95.48	0.07	x

(a) z1, z2, etc. are labels for analyses composed of single zircon grains that were annealed and chemically abraded (Mattinson, 2005). Labels in bold denote analyses used in weighted mean calculations or discordia regressions.
(b) Model Th/U ratio calculated from radiogenic $^{208}Pb/^{206}Pb$ ratio and $^{207}Pb/^{235}U$ date.
(c) Pb* and Pbc are radiogenic and common Pb, respectively. mol% $^{206}Pb^*$ is with respect to radiogenic and blank Pb.
(d) Measured ratio corrected for spike and fractionation only. Fractionation correction is 0.16 ± 0.03 (1 sigma) %/amu (atomic mass unit) for single-collector Daly analyses, based on analysis of EARTHTIME 202Pb-205Pb tracer solution.
(e) Corrected for fractionation and spike. Common Pb in zircon analyses is assigned to procedural blank with composition of $^{206}Pb/^{204}Pb$ = 18.04 ± 0.61%; $^{207}Pb/^{204}Pb$ = 15.54 ± 0.52%; $^{208}Pb/^{204}Pb$ = 37.69 ± 0.63% (1 sigma). $^{206}Pb/^{238}U$ and $^{207}Pb/^{206}Pb$ ratios corrected for initial disequilibrium in $^{230}Th/^{238}U$ using a D(Th/U) of 0.20 ± 0.05 (1 sigma).
(f) Errors are 2 sigma, propagated using algorithms of Schmitz and Schoene (2007) and Crowley et al. (2007).
(g) Calculations based on the decay constants of Jaffey et al. (1971). $^{206}Pb/^{238}U$ and $^{207}Pb/^{206}Pb$ dates corrected for initial disequilibrium in $^{230}Th/^{238}U$ usinga D(Th/U) of 0.20 ± 0.05 (1 sigma).

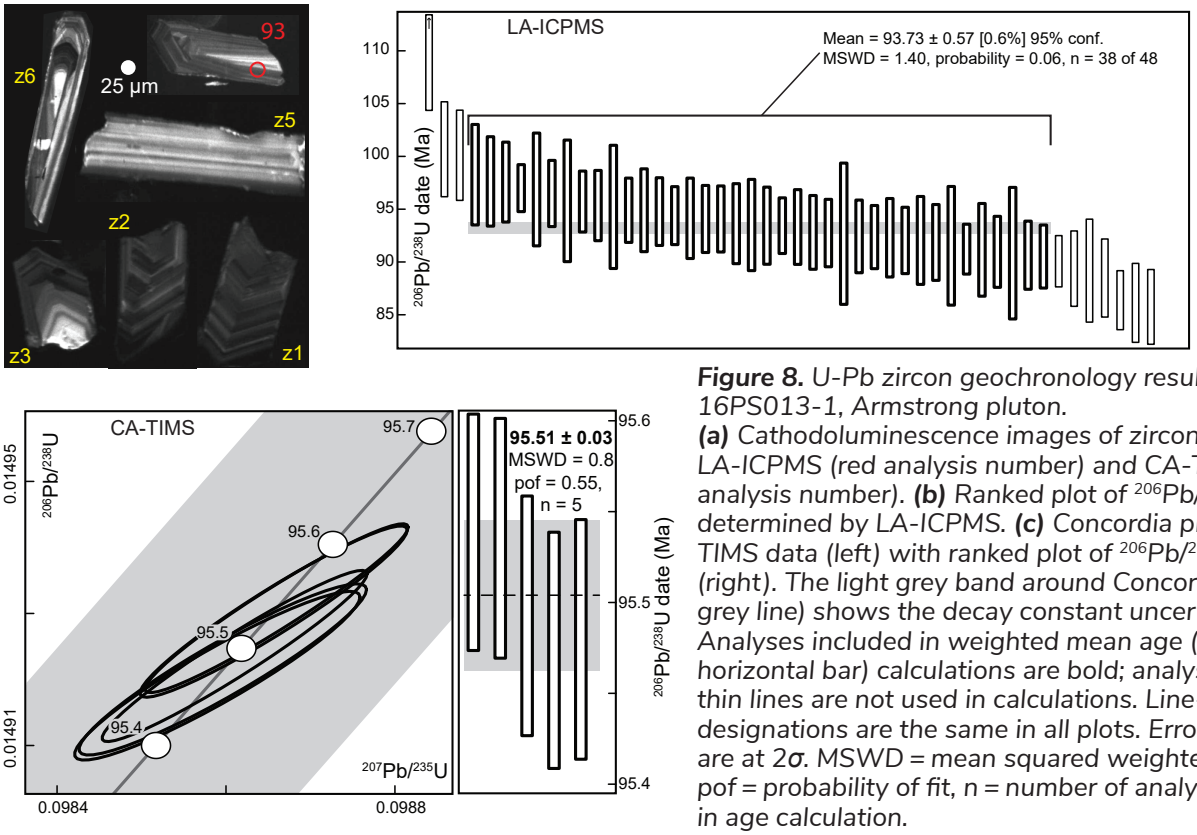


Figure 8. *U-Pb zircon geochronology results from 16PS013-1, Armstrong pluton.* ***(a)*** *Cathodoluminescence images of zircon analyzed by LA-ICPMS (red analysis number) and CA-TIMS (yellow analysis number).* ***(b)*** *Ranked plot of $^{206}Pb/^{238}U$ dates determined by LA-ICPMS.* ***(c)*** *Concordia plot of CA-TIMS data (left) with ranked plot of $^{206}Pb/^{238}U$ dates (right). The light grey band around Concordia (dark grey line) shows the decay constant uncertainties. Analyses included in weighted mean age (light grey horizontal bar) calculations are bold; analyses with thin lines are not used in calculations. Line-type designations are the same in all plots. Errors in all plots are at 2σ. MSWD = mean squared weighted deviation, pof = probability of fit, n = number of analyses included in age calculation.*

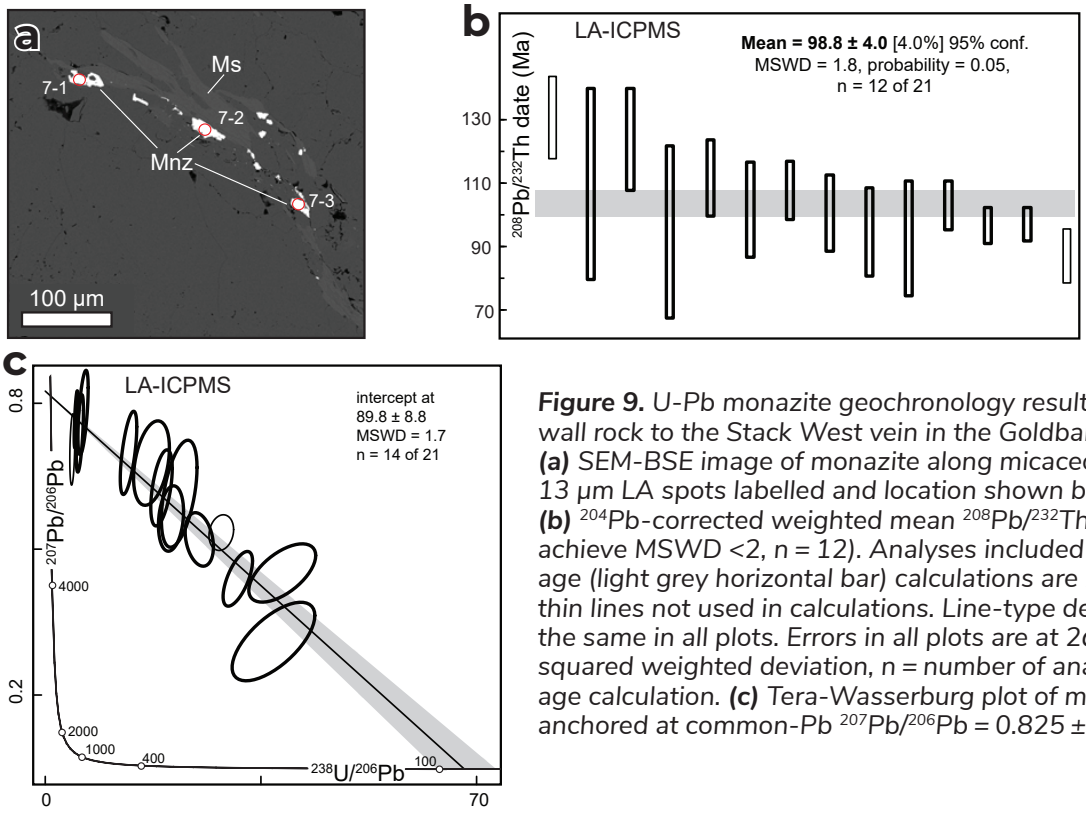


Figure 9. *U-Pb monazite geochronology results from 16PS006-1, wall rock to the Stack West vein in the Goldbank zone.* ***(a)*** *SEM-BSE image of monazite along micaceous foliation plane; 13 µm LA spots labelled and location shown by open red circle.* ***(b)*** *^{204}Pb-corrected weighted mean $^{208}Pb/^{232}Th$ age (refined to achieve MSWD <2, n = 12). Analyses included in weighted mean age (light grey horizontal bar) calculations are bold; analyses with thin lines not used in calculations. Line-type designations are the same in all plots. Errors in all plots are at 2σ. MSWD = mean squared weighted deviation, n = number of analyses included in age calculation.* ***(c)*** *Tera-Wasserburg plot of monazite data, n = 14, anchored at common-Pb $^{207}Pb/^{206}Pb = 0.825 \pm 0.005$.*

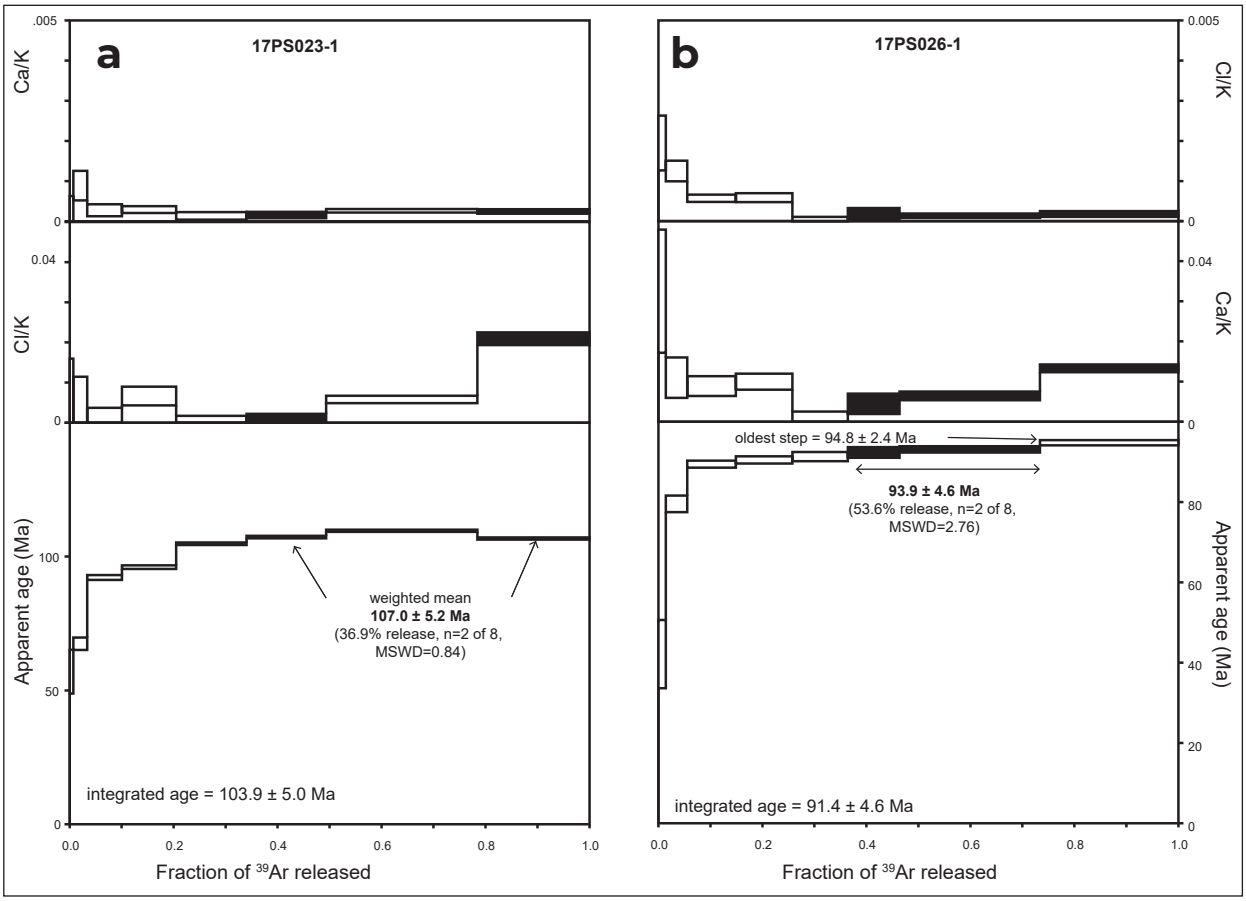


Figure 10. *^{40}Ar/^{39}Ar spectra for muscovite from schist in the* ***(a)*** *Bullion zone, 17PS023-1, and* ***(b)*** *Goldbank zone, 17PS026-1. Steps in black were used to calculate the age.*

Excess Ar released in the youngest and oldest steps have resulted in anomalously old ages (up to 1.4 billion years old) and therefore the Ar spectra is 'U-shaped'. This showing exhibits strongly recrystallized quartz suggesting the sericite in the sample was also recrystallized and mineralization was pre to syn-deformation. Due to the unquantifiable influence of excess Ar we interpret the age of this sample as a maximum age; the actual age could be significantly younger.

Sample 17PS025-1 is from a vein in the Bullion zone. A sericite separate from the sample gave an integrated age for all steps of 107.0 ± 5.4 Ma and a plateau age of 103.2 ± 5.2 Ma (4 of 8 steps, 77.1% ^{39}Ar release MSWD = 0.14; Fig. 11). The spectra have a 'stepping-up' age pattern indicative of gas loss. The integrated and plateau ages are within error. We interpret the plateau age of 103.2 ± 5.2 Ma as the age of mineralization in this sample.

Sample 17PS028-2 is from the Ron Stack vein, Goldbank zone. A sericite separate gave an integrated age for all steps of 112.0 ± 6.8 Ma and a plateau age of 95.5 ± 6.2 Ma (5 of 8 steps, 72.8% ^{39}Ar release MSWD = 0.40; Fig. 11). The spectra have a slight 'U-shaped' age pattern indicative of excess Ar. The integrated and the plateau ages are not within error. We interpret the plateau age of 95.5 ± 6.2 Ma as a maximum age, due to either resetting by contact metamorphism or reflecting mineralization, an interpretation elaborated on in the discussion.

Pb isotopes

Radiogenic Pb isotopes ^{206}Pb, ^{207}Pb and ^{208}Pb were analyzed from galena in eight vein samples and feldspar from four pluton samples; two vein samples and one pluton were analyzed twice (Table 3). Two groupings are apparent in the data, (1) a more isotopically primitive,

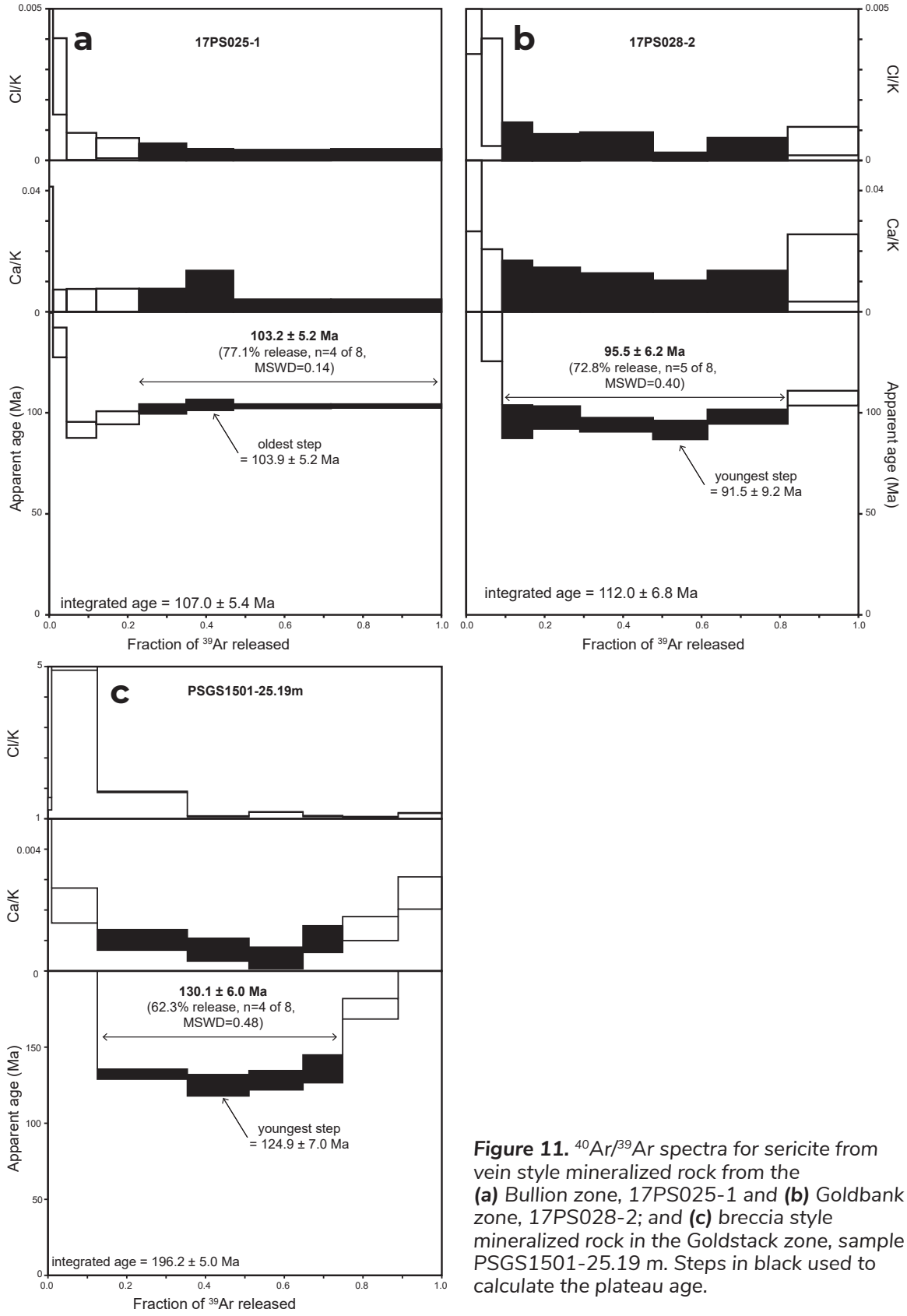


Figure 11. *$^{40}Ar/^{39}Ar$ spectra for sericite from vein style mineralized rock from the* ***(a)*** *Bullion zone, 17PS025-1 and* ***(b)*** *Goldbank zone, 17PS028-2; and* ***(c)*** *breccia style mineralized rock in the Goldstack zone, sample PSGS1501-25.19 m. Steps in black used to calculate the plateau age.*

Table 3. Lead isotope data table.

Sample	Zone	Showing	Grp	Latitude	Longitude	Mineral	$^{206}Pb/^{204}Pb$	Error abs (2σ)	$^{207}Pb/^{204}Pb$	Error abs (2σ)	$^{208}Pb/^{204}Pb$	Error abs (2σ)	$^{207}Pb/^{206}Pb$	Error abs (2σ)	$^{208}Pb/^{206}Pb$	Error abs (2σ)
17PS017-1	Big Bang vein	Big Bang	1	63.3739	-133.9397	Gn	18.301	0.0004	15.581	0.0002	38.499	0.0008	0.8514	0.0000	2.104	0.0000
17PS018-1	Big Bang vein	Big Bang	1	63.3882	-133.9379	Gn	18.135	0.0029	15.555	0.0024	38.302	0.0062	0.8577	0.0000	2.112	0.0001
16PS007-3	Bonanza vein	Bonanza	1	63.3555	-133.7555	Gn	18.309	0.0028	15.618	0.0020	38.512	0.0064	0.8530	0.0001	2.103	0.0002
Goldstack01	Goldstack	Goldstack breccia	1	63.3291	-133.7162	Gn	18.168	0.0048	15.569	0.0029	38.772	0.0114	0.8569	0.0002	2.134	0.0003
Goldstack01	Goldstack	Goldstack breccia	1	63.3291	-133.7162	Gn	18.146	0.0021	15.559	0.0017	38.731	0.0050	0.8574	0.0000	2.134	0.0001
17PS027-1	Goldbank	Astro vein	2	63.3215	-133.4782	Gn	19.035	0.0012	15.712	0.0007	39.189	0.0029	0.8254	0.0000	2.059	0.0001
17PS028-3	Goldbank	Lewis vein	2	63.3206	-133.4754	Gn	19.112	0.0007	15.729	0.0005	39.299	0.0016	0.8230	0.0000	2.056	0.0000
16PS006-1	Goldbank	Stack west vein	2	63.3227	-133.4807	Gn	19.010	0.0015	15.728	0.0007	39.225	0.0033	0.8273	0.0001	2.063	0.0001
PSGR1702-20m	Goldbank	Gold Bar vein	2	63.3336	-133.5486	Gn	18.939	0.0061	15.656	0.0044	39.100	0.0141	0.8267	0.0001	2.065	0.0003
PSGR1702-20m	Goldbank	Gold Bar vein	2	63.3336	-133.5486	Gn	18.911	0.0013	15.679	0.0010	39.142	0.0032	0.8291	0.0000	2.070	0.0001
16PS013	Armstrong pluton	Armstrong pluton	2	63.2519	-133.3655	Kfs	19.245	0.0015	15.696	0.0007	39.204	0.0043	0.8156	0.0000	2.037	0.0002
16PS015	Armstrong pluton	Armstrong pluton	2	63.2654	-133.3672	Kfs	19.145	0.0142	15.626	0.0115	39.069	0.0291	0.8162	0.0001	2.041	0.0002
16PS009	Russell stock	Russell stock	2	63.2915	-133.6063	Kfs	19.323	0.0222	15.775	0.0174	39.442	0.0464	0.8164	0.0003	2.041	0.0005
16PS009	Russell stock	Russell stock	2	63.2915	-133.6063	Kfs	19.358	0.0157	15.765	0.0107	39.375	0.0335	0.8144	0.0004	2.034	0.0005
16PS11	Russell stock	Russell stock	2	63.3104	-133.5945	Kfs	19.244	0.0068	15.726	0.0054	39.328	0.0140	0.8172	0.0001	2.044	0.0001

abs = absolute

thorogenic Pb-enriched group of five analyses that clusters along the 'orogene curve' of Zartman and Doe (1981), and (2) a more isotopically evolved group of 10 analyses which clusters around the 'Selwyn shale curve' of Godwin and Sinclair (1982). Group 1 comprises galena from mineralized rocks in the Goldstack, Bonanza and Big Bang zones on the western side of the property and has $^{206}Pb/^{204}Pb$ values between 18.31 and 18.14, $^{207}Pb/^{204}Pb$ between 15.62 and 15.55 and $^{208}Pb/^{204}Pb$ between 38.77 and 38.30 (Table 3). Group 2 comprises galena from the Goldbank zone as well as feldspar from the Russell and Armstrong plutons and has $^{206}Pb/^{204}Pb$ values between 19.13 and 18.91, $^{207}Pb/^{204}Pb$ between 15.78 and 15.63 and $^{208}Pb/^{204}Pb$ between 39.24 and 39.07 (Table 3).

Discussion

Tungsten plutonic suite

The Russell stock and Armstrong pluton have previously been assigned to the Tombstone suite (Roots, 2003) and Mayo suite (Rasmussen, 2013). Roots (1998) described the plutons in the Lansing map sheet area (105N) as biotite dominant over hornblende granodiorite intrusions of mid-Cretaceous age. Mid-Cretaceous plutons in the Selwyn basin area share many similarities and suites are challenging to separate (Rasmussen, 2013). In fact, the *ca.* 98 to 90 Ma Tungsten, Mayo, and Tombstone suite plutons are often referred to together as the Tungsten - Tombstone belt (*e.g.*, TTB in Hart *et al.*, 2004). The ages of these three suites are close, and mineralogy and geochemistry are useful for differentiating the suites (Hart *et al.*, 2004; Rasmussen, 2013). Tungsten suite plutons (98 to 94 Ma) are biotite ± hornblende ± muscovite ± garnet intermediate plutons with low magnetic character (0.2×10^{-3} SI units) and are peraluminous. Mayo suite plutons (96 to 93 Ma) are hornblende ± biotite intermediate plutons with low magnetic character (0.1×10^{-3} SI units) and are metaluminous. Tombstone suite plutons (92 to 90 Ma) are hornblende ± biotite intermediate plutons with moderate magnetic character (1.8×10^{-3} SI units) and are mainly metaluminous with fewer examples of peralkaline and peraluminous intrusions.

We did not observe hornblende in four thin sections from the Russell and Armstrong plutons and noted only minor hornblende in the field (Sack *et al.*, 2018). Both plutons have similar geochemistry and are ferroan, calcic and peraluminous using the criteria of Frost *et al.* (2001; Fig. 12). These characteristics combined with the presence of minor muscovite and garnet and the new 95.5 Ma ages presented in this paper, better match the description of the Tungsten suite in Rasmussen (2013). The tungsten skarn occurrence (Tongue, Yukon MINFILE 105N 014) on the south margin of the Armstrong pluton is another hallmark of Tungsten suite intrusions (Rasmussen, 2013). We suggest reassigning the Russell stock and Armstrong pluton to the Tungsten suite. This would make these intrusions the farthest west examples of the Tungsten suite.

Plateau breccia and vein showings

Quantitative mineralogy confirms thin section observations that both vein and breccia style showings have at least two generations of mineralization, both of which seem to have been recrystallized to some extent. The vein mineralogy and paragenesis is similar for both styles and based on these characteristics the two types seem best described as structural variations on the same veining event(s).

The age of mineralization at the Plateau South property is an important constraint on the deposit model used to describe mineralization (Sack *et al.*, 2018). While the U-Pb zircon data presented here are considered easy to interpret, the U-Pb monazite and Ar data are less so; with that in mind, we identify two events in the geochronologic data (Fig. 13). The oldest is a protracted period of orogenic mineralization and metamorphism from a maximum of *ca.* 130 Ma to *ca.* 100 Ma. Shortly afterwards, there is a well-constrained intrusive event at 95.5 Ma with coeval mineralization or thermal resetting of sericite in veins near plutons. Our monazite and muscovite geochronologic data suggest that the end of ductile deformation in the Plateau area was *ca.* 110 to 100 Ma. Ductile deformation and regional metamorphism were complete by 95.5 Ma when undeformed cordierite and andalusite porphyroblasts associated with intrusion of the Russell stock overgrew regional metamorphic fabrics (Fig. 3; Sack *et al.*, 2018).

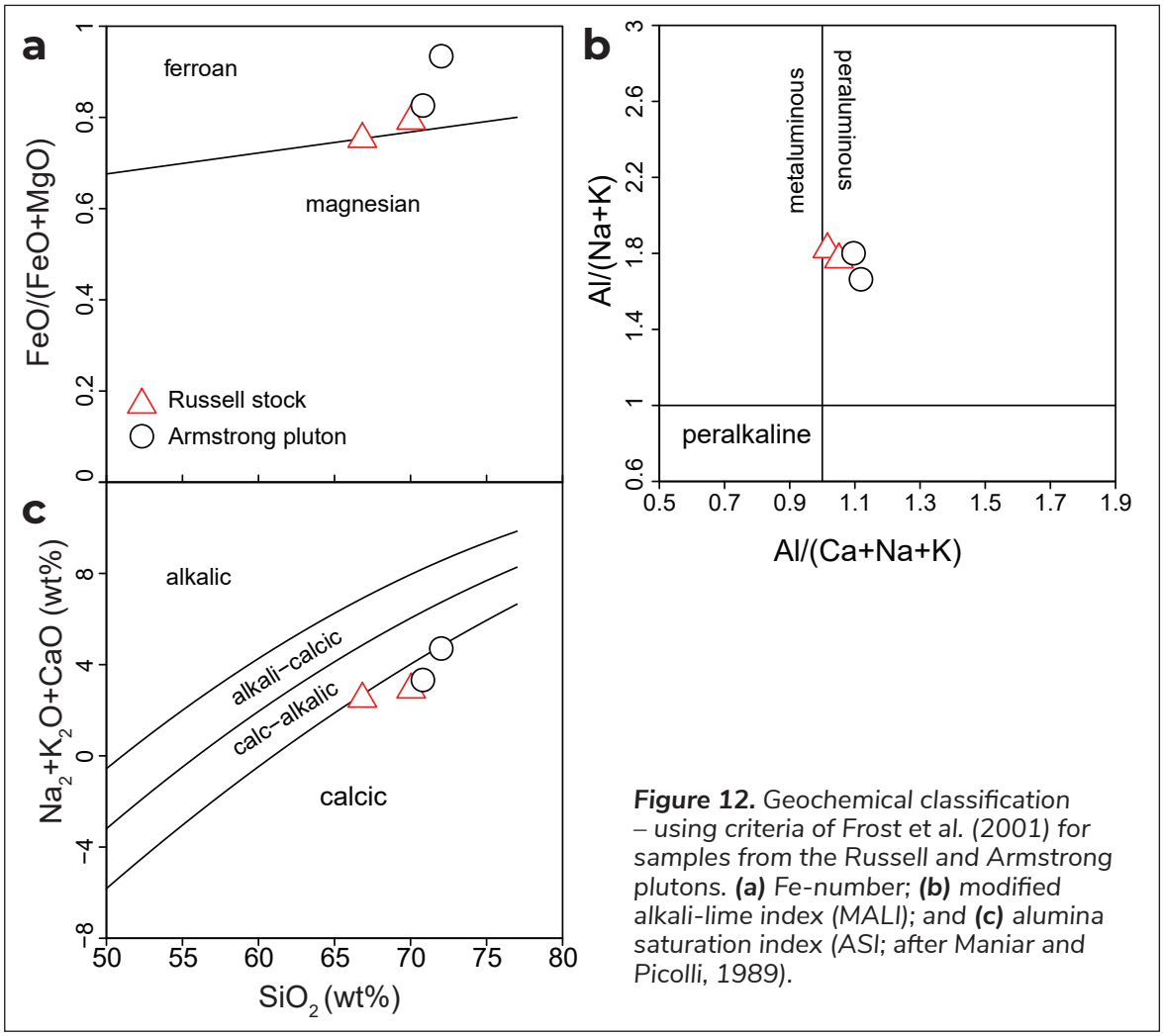


Figure 12. *Geochemical classification – using criteria of Frost et al. (2001) for samples from the Russell and Armstrong plutons.* ***(a)*** *Fe-number;* ***(b)*** *modified alkali-lime index (MALI); and* ***(c)*** *alumina saturation index (ASI; after Maniar and Picolli, 1989).*

This late Early Cretaceous end to regional metamorphism is relatively consistent throughout the Selwyn basin area (Fig. 1). For example, in the Hyland area 112 Ma dikes are deformed whereas, 106 Ma intrusions (Heffernan and Mortensen, 2000) are undeformed (Moynihan pers comm, 2019). In the Anvil area 50 km south of Plateau, deformation is constrained to as young as ca. 109 to 104 Ma based on early Anvil batholith dikes that are weakly deformed and weak foliation in parts of the Anvil batholith (Pigage, 2004). In the McQuesten area, $^{40}Ar/^{39}Ar$ cooling ages of ca. 104 to 100 Ma metamorphic muscovite provide a lower age constraint for Tombstone strain zone deformation (Mair et al., 2006). The onset of Jura-Cretaceous deformation is less well constrained throughout the Selwyn basin area of Yukon. The nearest reliable estimate is from *in situ* monazite dating in the Finlayson Lake area, 300 km southeast of the Plateau area, where the regional metamorphic age is as young as 142 Ma (Staples et al., 2014). For comparison, the Cariboo and Sheep Creek orogenic gold camps of southern British Columbia have regional metamorphic ages of Late Jurassic to Early Cretaceous and protracted orogenic mineralization ages from ca. 143 Ma to 133 Ma (Allan et al., 2017). We suggest a similar sequence of events in the Plateau area though we interpret our data as indicating a slightly younger Early Cretaceous (ca. 130 to 100 Ma) orogenic mineralization event.

The Pb isotopic composition of sulphides precipitated from magmatic or hydrothermal fluids reflects the Pb isotopic composition of the metal source(s) (Tosdal et al., 1999) and thus helps constrain genetic models.

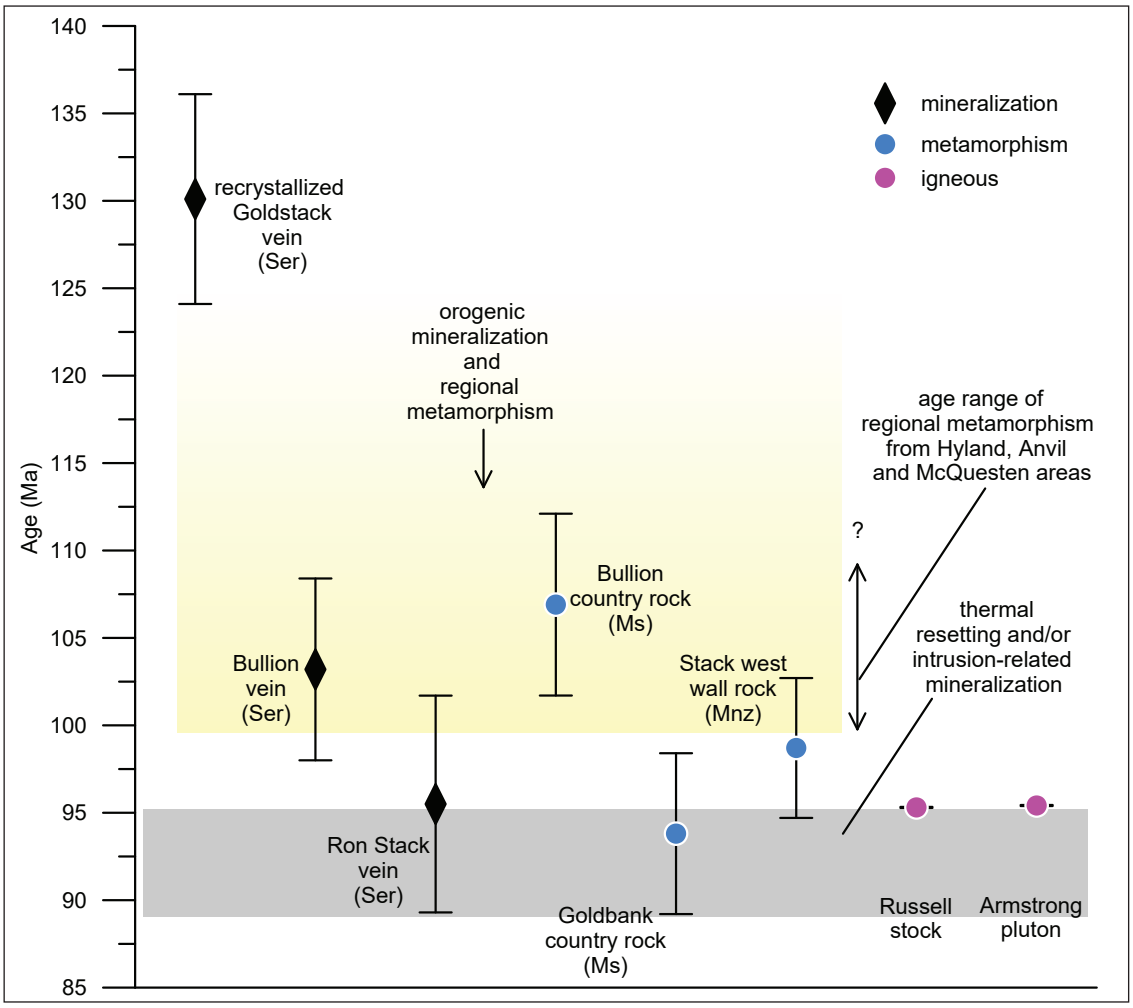


Figure 13. *Geochronology summary for the Plateau area. Regional metamorphism for the Hyland area from Moynihan (pers. comm), the Anvil area from Pigage (2004) and the McQuesten area from Mair et al. (2006). Errors 2σ.*

For example, in intrusion-related systems, the sulphide Pb isotopic composition is similar to those of igneous feldspar within genetically related intrusions (Tosdal et *al.*, 1999). The close spatial and genetic association between galena and arsenopyrite and arsenopyrite and gold in the Plateau occurrences (Sack et *al.*, 2018) suggests Pb, As and Au were in the same hydrothermal fluid and Pb is a useful proxy for gold source at Plateau. We do note that while the paragenesis of galena in discrete vein showings is relatively well constrained to later than arsenopyrite, similar constraints are not known for the breccia showings.

One breccia showing, and two vein showings on the western side of the property are enriched in thorogenic Pb (Group 1) indicative of Pb sources from relatively isotopically primitive rocks (Zartman and Doe, 1981; Tosdal et *al.*, 1999). This may indicate the early orogenic mineralizing fluids were sourced relatively deep in the lower crust, the 'orogene' of Zartman and Doe (1981), or that they interacted locally with rocks such as the mafic volcanic Old Cabin Formation. The Pb isotopic signature from primitive rocks is relatively easily overwhelmed by evolved rocks due to lower Pb concentrations overall in primitive rocks (Tosdal et *al.*, 1999). Whole-rock Pb for one sample from the chloritic phyllite in the Big Bang area is <5 ppm (detection limit), country rocks are between 7 and 26 ppm Pb, and intrusions have 30 to 42 ppm Pb (Appendix 1). This suggests that the Group 1 Pb signature is from fluid that did not interact with the relatively Pb-rich country rock or intrusions.

The Pb isotope signature of vein showings in the Big Bang area (Group 2) is distinct from Group 1. Group 2 Pb isotopic data are similar to that of feldspar in mid-Cretaceous intrusions of the Selwyn basin area and to the country rocks (Fig. 14). Data from the Russell and Armstrong plutons overlap entirely with that of other mid-Cretaceous plutons across the Selwyn basin area (Fig. 14). Country rock Pb isotopic composition for the Selwyn basin area is best estimated from syngenetic massive sulphide deposits throughout the stratigraphy and is presented as the 'Selwyn shale' curve of Godwin and Sinclair (1982). These data are corroborated by limited whole-rock Pb isotopic data from widespread samples of Yusezyu Formation shale (Ben Cave written comm., 2018). The similar Pb isotopic composition for mid-Cretaceous plutons and country rock suggests a fundamental, regional basement control on the composition of lead in the area. From the point of view of mineralization at Plateau, it is not possible to distinguish between plutons and country rock as a source of Pb in hydrothermal fluids. Thus, the more isotopically evolved signature is compatible with metals sourced from either the plutons or the country rock. However, it is worth restating, that Pb isotopic data show two distinct sources of Pb in the Plateau deposits and any genetic model must account for this.

The above data are internally consistent in that each data set suggests at least two mineralizing events: (1) mineralogy and petrography show at least two stages of veining or brecciation; (2) geochronologic data broadly cluster into two ranges; and (3) Pb isotopic data clearly show two distinct metal sources. Unfortunately, these data do not allow a unique solution as to which deposit model best explains mineralization on the Plateau property. Below, we present what we consider the two most likely options.

1. Initial mineralization relates to Early Cretaceous (ca. 130 to 100 Ma) orogenic fluids and later mineralization is intrusion-related (ca. 95 Ma). In this interpretation, Early Cretaceous regional-scale orogenic fluids are envisioned to have tapped a primitive (deep?) Pb source with minimal interaction with surrounding rocks and intrusion-related mineralization sourced Pb from mid-Cretaceous plutons.

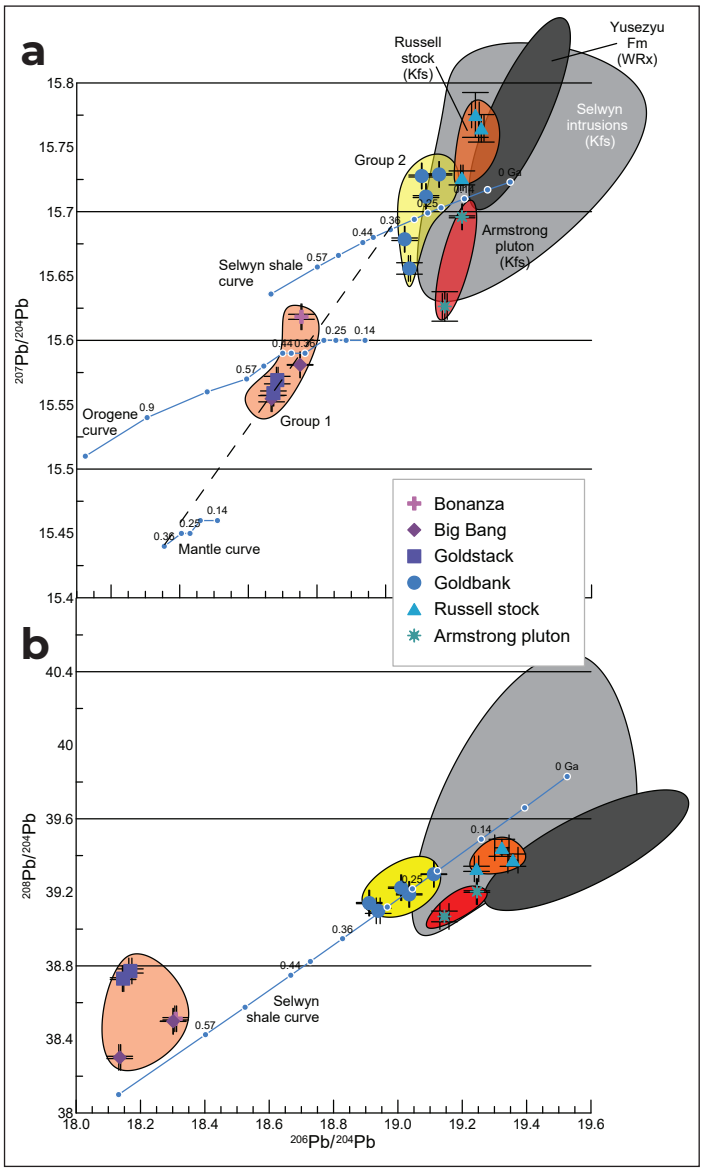


Figure 14. *Plot of* ***(a)*** *Uranogenic lead and* ***(b)*** *Thorogenic lead for galena and feldspar from the Plateau area. Included are previously published feldspar data from 'Selwyn basin area' plutons compiled in Rasmussen (2013) and whole-rock Pb isotope analyses from the Yusezyu Formation courtesy of Ben Cave (written communication, 2018). Mantle and orogene curves are from Zartman and Doe (1981) and the Selwyn shale curve is from Godwin and Sinclair (1982). Dashed line ties ca. 360 Ma mantle, orogene and Selwyn shale curves together.*

2. All mineralization relates to Early Cretaceous (*ca.* 130 to 100 Ma) orogenic fluids. In this interpretation, the younger muscovite and sericite ages in the Goldbank area are a result of thermal resetting by intrusions and the bimodal nature of Pb isotopic data is the result of local (<10 km?) metal sources. Primitive lead could have come from mafic rocks such as those mapped on the western portion of the property (Stubley, 2017) and the more isotopically evolved Pb would reflect hydrothermal circulation in country rocks without a primitive component.

Discussion and further work

This is an initial attempt to constrain the origin of gold mineralization in the Plateau area. We present evidence for orogenic gold mineralization but consider the identification of intrusion-related gold mineralization subjective. Better understanding of the age of regional metamorphism and mineralization would boost confidence in the interpretation of mineralization associated with both regional metamorphism and pluton emplacement. For example, *in situ* muscovite dating may constrain the age of individual ductile deformation events in the area, breaking mineralization into discrete events as opposed to our current suggestion of a single protracted event. Similarly, if additional Pb isotope data with well-constrained paragenesis could be petrographically linked to deformation or intrusive events, a stronger interpretation on the importance of intrusion-related mineralization would be possible.

References

Allan, M., Rhys, D.A. and Hart, C.J.R., 2017. Orogenic gold mineralization of the eastern Cordilleran gold belt, British Columbia: Structural ore controls in the Cariboo (093A/H), Cassiar (104P) and Sheep Creek (082F) mining districts. Geoscience BC, Report 2017-15, 108 p.

Barr, T., 2017. Fluid inclusion analysis of the Plateau Gold project, Yukon, Canada. BSc thesis, University of Alberta, 27 p.

Cecile, M.P., 2000. Geology of the northeastern Niddery Lake map area, east-central Yukon and adjacent Northwest Territories. Geological Survey of Canada, Bulletin 553, 128 p.

Colpron, M. and Nelson, J.L., 2011. A digital atlas of terranes for the northern Cordillera. Yukon Geological Survey, also, BC Geological Survey, GeoFile 2011-11.

Dubé, B. and Gosselin, P., 2007. Greenstone-hosted quartz-carbonate vein deposits *In*: Mineral Deposits of Canada: A Synthesis of Major Deposit-types, District Metallogeny, the Evolution of Geological Provinces, and Exploration Methods, W.D. Goodfellow (ed.), Special Publication 5, Mineral Deposits Division, Geological Association of Canada, p. 49–73.

Farquharson, J., 2017. A microstructural analysis of Goldstrike's Plateau property, Yukon. BSc thesis, Lakehead University, 67 p.

Frost, B.R., Barnes, C.G., Collins, W.J., Arculus, R.J., Ellis, D.J. and Frost, C.D., 2001. A geochemical classification for granitic rocks. Journal of Petrology, vol. 42, no. 11, p. 2033–2048.

Godwin, C.I. and Sinclair, A.J., 1982. Average lead isotope growth curves for shale-hosted zinc-lead deposits, Canadian Cordillera. Economic Geology, vol. 77, no. 3, p. 675–690.

Goldfarb, R.J., Baker, T., Dube, B., Groves, D.I., Hart, C.J.R. and Patrice, G., 2005. Distribution, character, and genesis of gold deposits in metamorphic terranes *In*: Economic Geology: One Hundredth Anniversary Volume, J.W. Hedenquist, J.F.H. Thompson, R.J. Goldfarb and J.P. Richards (eds.), Society of Economic Geologists, p. 407–450.

Hart, C.J.R., Mair, J.L., Goldfarb, R.J. and Groves, D.I., 2004. Source and redox controls on the metallogenic variations in intrusion-related ore systems, Tombstone-Tungsten Belt, Yukon Territory, Canada. Transactions of the Royal Society of Edinburgh: Earth Sciences, vol. 95, p. 339–356.

Heffernan, S. and Mortensen, J.K., 2000. Age, geochemical and metallogenic investigations of Cretaceous intrusions in southeastern Yukon and southwestern NWT: A preliminary report *In*: Yukon Exploration and Geology 1999, D.S. Emond and L.H. Weston (eds.), Exploration and Geological Services Division, Yukon, Indian and Northern Affairs Canada, p. 145–149.

Mair, J.L., Hart, C.J.R. and Stephens, J.R., 2006. Deformation history of the northwestern Selwyn Basin, Yukon, Canada: Implications for orogen evolution and mid-Cretaceous magmatism. Geological Society of America Bulletin, vol. 118, no. 3/4, p. 304–323.

Maniar, P.D. and Picolli, P.M., 1989. Tectonic discrimination of granitoids. Geological Society of America Bulletin, vol. 101, no. 5, p. 635–643.

Mortensen, J.K. and Gabites, J.E., 2002. Lead isotopic constraints on the metallogeny of southern Wolf Lake, southeastern Teslin and northern Jennings River map areas, Yukon and British Columbia: Preliminary results *In*: Yukon Exploration and Geology 2001, D.S. Emond, L.H. Weston and L.L. Lewis (eds.), Exploration and Geological Services Division, Yukon Region, Indian and Northern Affairs Canada, p. 179–188.

Murphy, D., 1997. Geology of the McQuesten River region, northern McQuesten and Mayo map areas, Yukon Territory (115P/14, 15, 16; 105M/13, 14). Indian and Northern Affairs Canada, Exploration and Geological Services Division, Yukon, Bulletin 6, 122 p.

Pigage, L.C., 2004. Bedrock geology compilation of the Anvil district (parts of NTS 105K/2, 3, 5, 6, 7 and 11), central Yukon. Yukon Geological Survey, Bulletin 15, 103 p.

Rasmussen, K.L., 2013. The timing, composition and petrogenesis of syn- to post-accretionary magmatism in the northern Cordilleran miogeocline, eastern Yukon and southwest Northwest Territories. PhD thesis, University of British Columbia, 810 p.

Richards, J.P., 2015. Petrographic and paragenetic relationships of seventeen samples from the Goldstack and Gold Dome zones, Plateau Gold deposit, Yukon. Internal company report.

Roach, S., 2013. Report of 2012 surface exploration and diamond drill program on the Plateau South project. Yukon Energy, Mines and Resources Assessment Report AR096441.

Roots, C.F., 1998. Progress report on bedrock geology of Lansing map area, central Yukon Territory. Geological Survey of Canada, Current Research 1998-A, p. 19–28.

Roots, C.F., 2003. Bedrock geology of Lansing Range map area (NTS 105N), central Yukon (scale). Yukon Geological Survey and Geological Survey of Canada, Geoscience Map 2003-1, scale 1:250 000.

Roots, C.F., Abbott, J.G., Cecile, M.P., Gordey, S.P. and Orchard, M.J., 1995. New stratigraphy and structures in eastern Lansing map area, central Yukon Territory. Geological Survey of Canada, Current Research 1995-A, p. 141–147.

Sack, P.J., Kruse, S. and Ferraro, D., 2018. Gold occurrences on the Plateau South property (Yukon MINFILE 105N 034, 035, 036), central Yukon. *In*: Yukon Exploration and Geology Overview 2017, K.E. MacFarlane (Ed.), Yukon Geological Survey, p. 75–91.

Staples, R.D., Murphy, D.C., Gibson, H.D., Colpron, M., Berman, R.G. and Ryan, J.J., 2014. Middle Jurassic to earliest Cretaceous mid-crustal tectono-metamorphism in the northern Canadian Cordillera: Recording foreland-directed migration of an orogenic front. Geological Society of America Bulletin, vol. 126, no. 11-12, p. 1511–1530.

Stubley, M., 2017. Structural architecture of the Plateau property: Some preliminary comments (NTS 105N). Internal company report.

Tosdal, R.M., Wooden, J.L. and Bouse, R.M., 1999. Pb isotopes, ore deposits, and metallogenic terranes *In*: Reviews in Economic Geology, Volume 12, D.D. Lambert and J. Ruiz (eds.), Society of Economic Geology, p. 1–28.

Vanwermeskerken, M., 2017. Detailed geologic mapping at Goldstack, Goldstack Lake and Bonanza zones *In*: 2016 diamond drilling, geological mapping and structural analysis on the Plateau Property, D. Ferraro, Yukon Energy, Mines and Resources Assessment Report 097024.

Yukon Geological Survey, 2018a. Yukon MINFILE - A database of mineral occurrences, https://data.geology.gov.yk.ca, [accessed April 23, 2018].

Yukon Geological Survey, 2018b. Yukon Digital Bedrock Geology, http://data.geology.gov.yk.ca/Compilation/3, [accessed April 25, 2018].

Zartman, R.E. and Doe, B.R., 1981. Plumbotectonics–The model. Tectonophysics, vol. 75, p. 135–162.

Appendices

The appendices are only available as digital files. They are included in a .zip file that accompanies this document, and are available from https://data.geology.gov.yk.ca.

Appendix 1. Plateau geochemistry and QEMSCAN.

Appendix 2. U-Pb geochronology.

Appendix 3. Ar geochronology.

Upper Triassic to Lower Jurassic stratigraphy of the Faro Peak formation, southern Tay River map area, central Yukon (NTS 105K)

A.C. Wiest, L.P. Beranek* and M.J. Manor
Department of Earth Sciences, Memorial University of Newfoundland

Wiest, A.C., Beranek, L.P. and Manor, M.J., 2020. Upper Triassic to Lower Jurassic stratigraphy of the Faro Peak formation, southern Tay River map area, central Yukon (NTS 105K). *In:* Yukon Exploration and Geology 2019, K.E. MacFarlane (ed.), Yukon Geological Survey, p. 121–139.

Abstract

The lower and upper members of the Faro Peak formation comprise Upper Triassic and Lower Jurassic successions, respectively, that are assigned to the Yukon-Tanana terrane in the southern Tay River map area (NTS 105K). The lower member is ~650 m-thick and contains a basal conglomerate overlain by argillite, limestone, basalt, and lithic feldspathic wacke to arenite that represents part of an overlap assemblage and regionally covers Paleozoic rocks of the Yukon-Tanana terrane, Slide Mountain terrane, and ancestral Cordilleran margin. The upper member has >800 m of massive conglomerate and sandstone that overlies different stratigraphic levels of the lower member and locally sits on Yukon-Tanana basement. The upper member is coeval with Whitehorse trough strata of central Yukon and similarly records Early Jurassic exhumation of the northern Intermontane terranes. The two members are lithologically distinct, of mappable extent, and have unconformable contacts, and therefore should be separated into two new formations.

* lberanek@mun.ca

Introduction

The late Permian to Early Jurassic was a time of significant change along the northwestern margin of North America. The deposition of multiple syn to post-orogenic sedimentary successions from eastern Alaska to northern British Columbia (Fig. 1; Mihalynuk et *al.*, 1994; Beranek and Mortensen, 2011; Colpron et *al.*, 2015; Golding et *al.*, 2016) was related to arc accretion, outward stepping of the continental margin, new arc development, and crustal thickening and exhumation of the Intermontane terranes (e.g., Yukon-Tanana, Slide Mountain, Stikinia, Quesnellia, Cache Creek). Middle to Upper Triassic overlap assemblages were deposited across the Yukon-Tanana and Slide Mountain terranes and former Cordilleran margin after late Permian closure of a marginal ocean basin (Beranek and Mortensen, 2011). Yukon-Tanana terrane basement rocks were locally metamorphosed to eclogite facies during this ocean closure and contain late Permian white mica cooling ages in the Faro area of central Yukon (Erdmer et *al.*, 1998). Subsequent Late Triassic to Early Jurassic arc collision and intra-arc shortening along the composite margin resulted in regional crustal thickening and burial of Stikinia and Yukon-Tanana basement to mid-crustal depths (Johnston et *al.* 1996; Topham et *al.*, 2016; Clark, 2017). This crustal thickening in central Yukon was followed by ~15-20 km of tectonic exhumation (Knight et *al.*, 2013) and resulted in Sinemurian and later deposition of Laberge Group strata in the Whitehorse trough (Fig. 1; Colpron et *al.*, 2015; Staples et *al.*, 2016). Dusel-Bacon et *al.* (2002) similarly documented Early Jurassic exhumation in the Yukon-Tanana terrane of eastern Alaska after regional crustal thickening. Constraining the timing and depositional setting of Late Triassic to Early Jurassic basin-filling events is critical to investigate these existing models and further constrain the tectonic evolution and growth of the Canadian Cordillera.

Isolated exposures of Upper Triassic to Lower Jurassic rocks assigned to the Faro Peak formation by Pigage (2004) crop out along the Yukon-Tanana–Slide Mountain terrane boundary near the town of Faro (Fig. 2a,b) in the southern Tay River map area (NTS 105K). Colpron et *al.* (2015) reported 200–180 Ma detrital zircon grains in conglomerate units of the Faro Peak formation and correlated these rock units with synorogenic strata of the Laberge Group in central Yukon and northern British Columbia. A two-year project was initiated in 2018 to test these hypotheses (Wiest and Beranek, 2019) and investigate the depositional age, regional correlation, and tectonic setting of the Faro Peak formation.

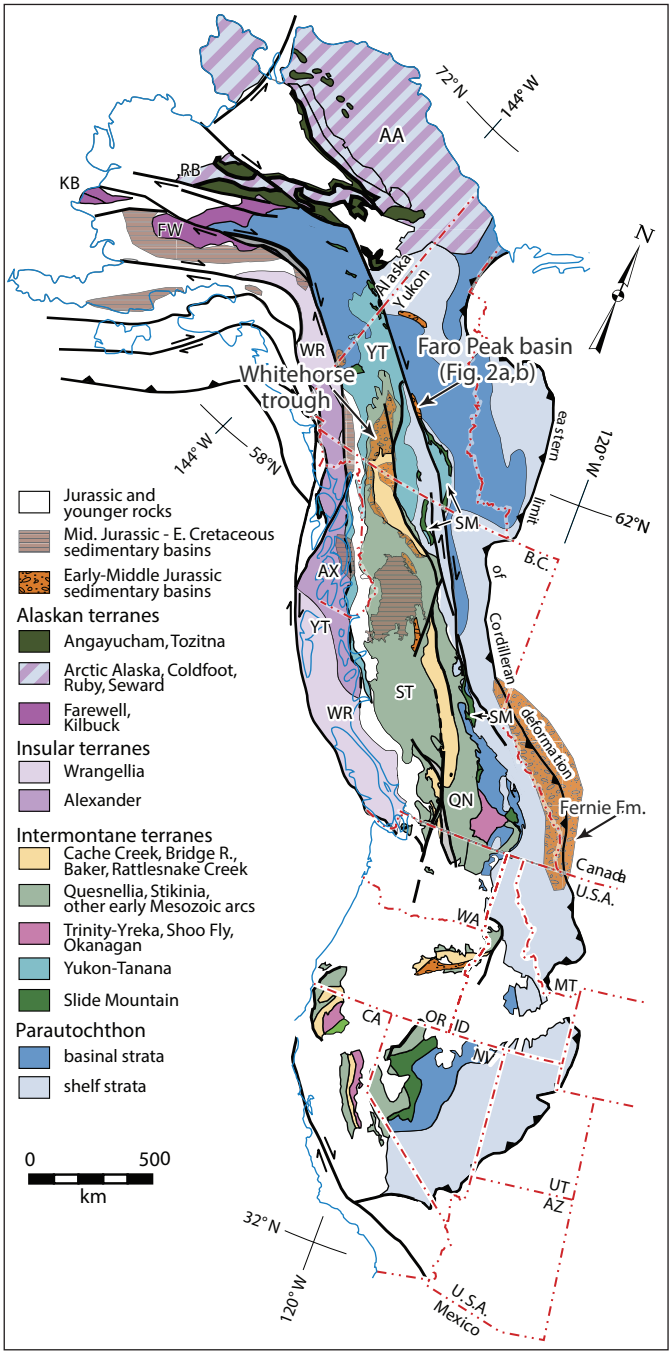


Figure 1. *Paleozoic to early Mesozoic terrane map of the North American Cordillera and associated Jurassic basins modified from Colpron et al. (2015). Terrane abbreviations: AA–Arctic Alaska; AX–Alexander; FW–Farewell; KB–Kilbuck; QN–Quesnellia; RB–Ruby; SM–Slide Mountain; ST–Stikinia; YT–Yukon-Tanana.*

In this article, we summarize our 2019 field studies and current understanding of the Faro Peak formation as originally defined by Pigage (2004). The internal character of the lower member of the Faro Peak formation is documented in a new stratigraphic section west of Rose Mountain. The contact between the upper and lower members of the Faro Peak formation appears to be transitional in at least two localities. The observation that upper member conglomerate overlies multiple units of the lower member and quartzite and schist units of the Yukon-Tanana terrane suggests, however, that the base of the upper member is an unconformity. Finally, we speculate on the basis of lithological differences and unconformable contacts that some or all rocks previously included in the lower Faro Peak formation should be re-assigned to a new formation. It is currently uncertain if all lower member units of Pigage (2004) should be included in this new formation. Ongoing detrital zircon U-Pb-Hf isotope and petrographic investigations of Faro Peak formation rock units will assist in future stratigraphic correlations and help guide a new formation designation.

Geological background

The town of Faro is located at the eastern edge of the Intermontane belt near the suture between the Yukon-Tanana and Slide Mountain terranes (Fig. 2a,b). In this area, the Intermontane terranes are separated from parautochthonous North American continental margin strata along the Inconnu thrust to the northeast and Cassiar terrane along the Tintina fault to the southwest (Fig. 2a,b; Pigage, 2004). Dextral movement along the Tintina fault accommodated at least 430 km of

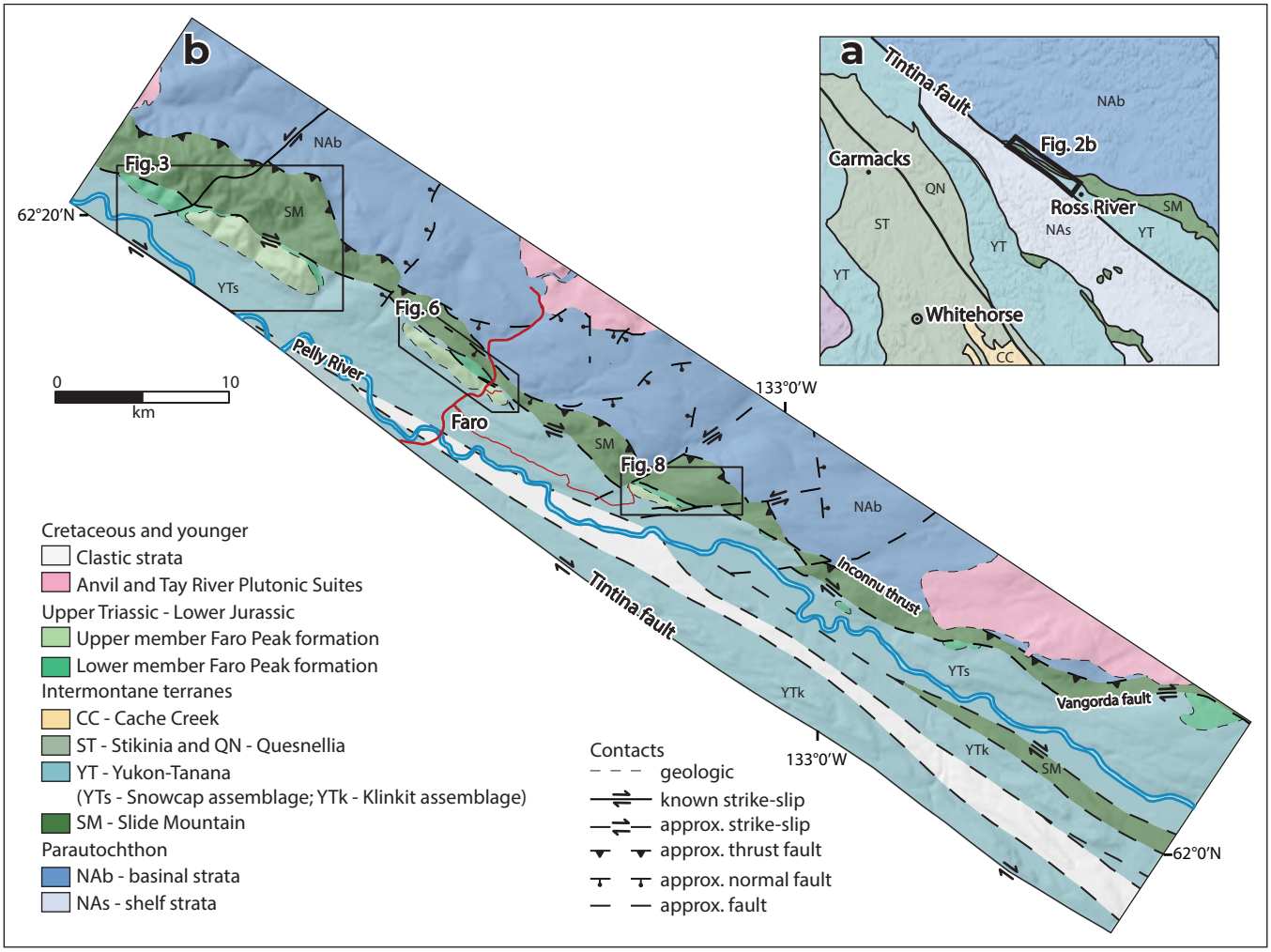


Figure 2. (a) *Terrane map of central Yukon modified from Yukon Geological Survey (2019).* ***(b)*** *Simplified bedrock geology of the southern Tay River map area modified from Pigage (2004).*

post-Cretaceous displacement (Gabrielse et *al*., 2006). Restoration of the Tintina fault places Faro near the present day region of Eagle, Alaska. In the Faro area, the Yukon-Tanana and Slide Mountain terranes are separated by the Vangorda fault (Fig. 2b), a northern equivalent to the Jules Creek fault in the Finlayson Lake map area (Murphy et *al*., 2006).

The Faro Peak formation crops out along a northwest-trending belt that parallels the Tintina Trench near Faro. Faro Peak formation strata were first described by Tempelman-Kluit (1972, 1979) as argillaceous limestone, silty slate, and polymictic conglomerate that unconformably overlies quartzite, schist, and other metasedimentary rocks of what is now called the Snowcap assemblage (*e.g.* Colpron et *al*., 2006) of the Yukon-Tanana terrane. Pigage (2004) informally named the Faro Peak formation and defined a lower member of basal basalt overlain by interbedded argillite, chert, greywacke, limestone, and conglomerate, and an upper member of massive, polymictic conglomerate. Wiest and Beranek (2019) documented that these lower and upper member units were deposited in contrasting environments. Lower member units ~3 km northeast of the Faro township exhibit normally graded, tabular, and convolute bedding characteristics that are generally consistent with deposition by turbulent, concentrated density flows. Petrographic results indicate that some lower member sandstone units have mafic to intermediate volcanic provenance (Wiest and Beranek, 2019). Massive, upper member conglomerate and channelized sandstone units from Faro Peak and adjacent ridges are consistent with deposition by non-concentrated debris flows. Typical clasts in the upper member conglomerate units include schist, quartzite, chert, and mafic to felsic intrusive rocks, which suggests that the upper Faro Peak formation has provenance from Intermontane terrane basement assemblages and may be linked to depositional events along the Vangorda fault or its predecessor (*c.f.* Tempelman-Kluit, 1972).

2019 field observations

Lower member of the Faro Peak formation

Rose Mountain

The lower member of the Faro Peak formation near Rose Mountain, ~20 km northwest of Faro, is ~650 m-thick and generally undeformed (Figs. 3 and 4). Lower member units at this location unconformably overlie micaceous quartzite and schist of the Snowcap assemblage (Fig. 5a). The basal unconformity is defined by well-silicified, pebble to cobble conglomerate that contains clasts of schist, quartzite, black to grey chert, and tan volcanic rocks (Fig. 5b). This basal conglomerate is overlain by interbedded graphitic to calcareous shale and tan weathering, dark grey micrite (Fig. 5c). Limestone from this succession yields Late Triassic conodont elements (Late Norian to Rhaetian *M. ex gr. Polygnathiformis*, Late Carnian *Epigondolella cf. mosheri* and *Norigondolella steinbergensis*; Pigage, 2004; Orchard, 2006). Conformably above this limestone is an ~4 m-thick exposure of grey basalt and green lithic feldspathic wacke units that become sheared upsection (Fig. 5d,e). Shearing at this locality is interpreted to be intraformational bedding plane movement that occurred along the resistant basalt-wacke contact (cf., Tempelman-Kluit, 1979). Poorly exposed argillaceous to silty micrite beds that show cross-stratification overlie this sheared section (Fig. 5f). Along strike ~1 to 2 km to the southeast, limestone units are mapped as being interbedded with basalt and wacke units (Jennings et *al*., 1978; Pigage, 2004). Exposures above the cross-stratified limestone units are rare. Small outcrop of thinly laminated, dark grey micrite and micaceous siltstone were observed directly against the Vangorda fault, which separates the lower member from foliated serpentinite and gabbro of the Slide Mountain terrane (Fig. 3).

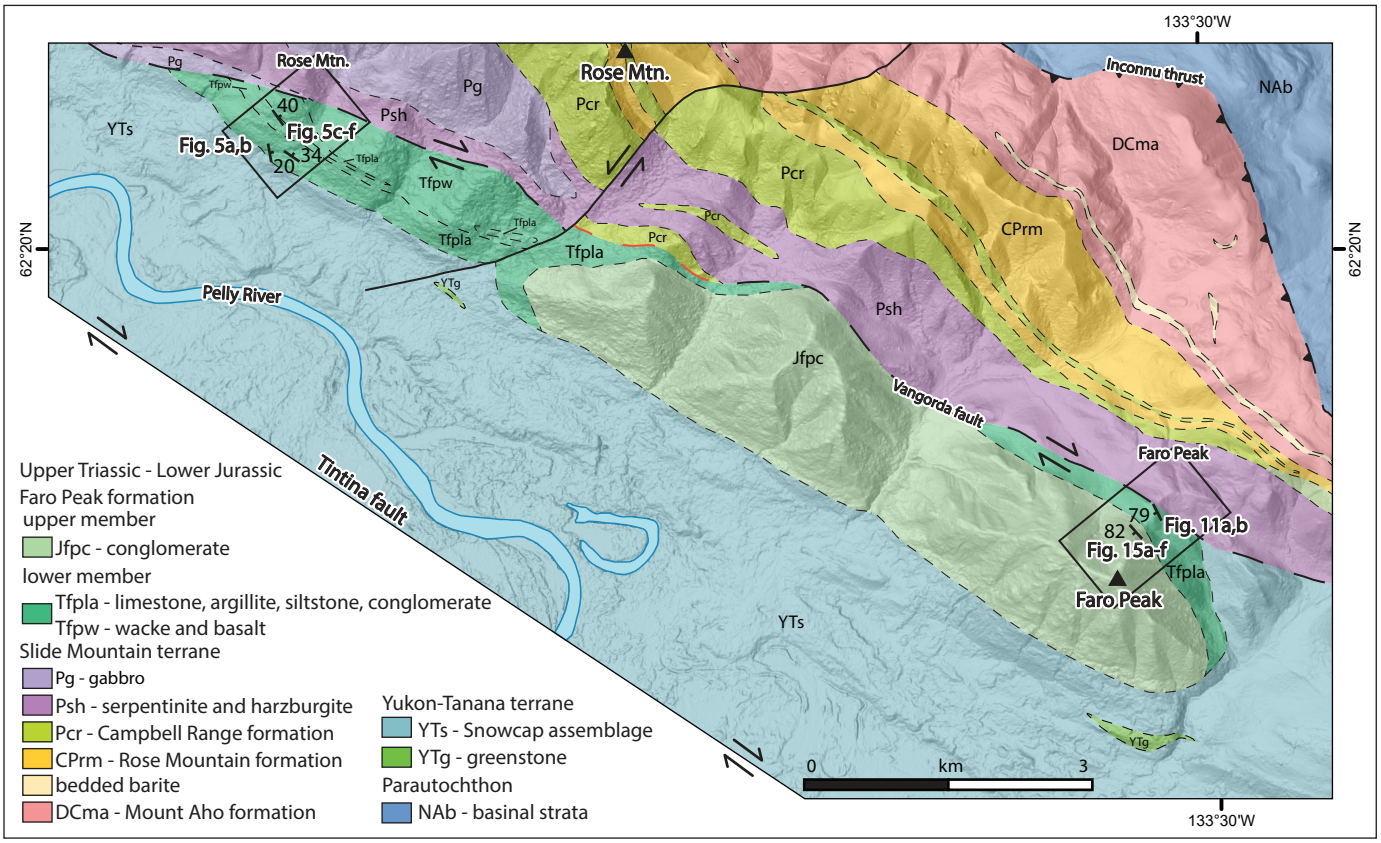


Figure 3. *Simplified bedrock geology map of the Rose Mountain and Faro Peak areas discussed in the text (modified from Pigage, 2004 and Jennings et al., 1978). Red dashed line indicates modified Vangorda fault location due to reassignment of basalt unit to Campbell Range formation. Contact symbols same as Figure 2. Basemap DEM (digital elevation model) obtained from the University of Minnesota Polar Geospatial Center (2018) and Porter et al. (2018).*

Repeater Hill

Late Triassic conodont elements (late Norian; *Epigondolella quadrata*; Orchard, 2006) are reported in dark grey micrite to wackestone units below the NorthwesTel repeater at the top of Repeater Hill, ~22 km to the southeast of Rose Mountain and ~2.5 km northwest of Faro (Fig. 6). Upper Triassic limestone units are interbedded with siltstone and argillite units similar to those at Rose Mountain, however, at Repeater Hill these fine-grained strata are strongly foliated along a fault that cuts out the basal conglomerate and juxtaposes younger lower member rocks with the Snowcap assemblage (Fig. 7a,b).

Blind Creek–Dena Cho Trail

The Blind Creek–Dena Cho Trail localities are ~10 km southeast of the Faro townsite (Fig. 8). Near the trace of the Vangorda fault, mineral exploration trenches provide access to lower member outcrops in otherwise unexposed areas. The lower member typically consists of foliated, thin-bedded, dark grey micrite, siltstone, and argillite units (Fig. 9a,b). There are no reported fossil constraints on the limestone units in this area.

Eastern Whiskey Mountain

Lower member strata exposed along the eastern ridge of Whiskey Mountain, ~3 km northeast of Faro (Fig. 6), are generally more coarse-grained than the argillite and limestone-dominated units at the Rose Mountain and Repeater Hill localities. Stratigraphic relationships along the eastern ridge of Whiskey Mountain are uncertain because of poor exposure and variable bedding. Rock units along the north fork of Vangorda Creek appear highly deformed and contain east-verging folds and small-scale west-dipping faults (Fig. 10a,b).

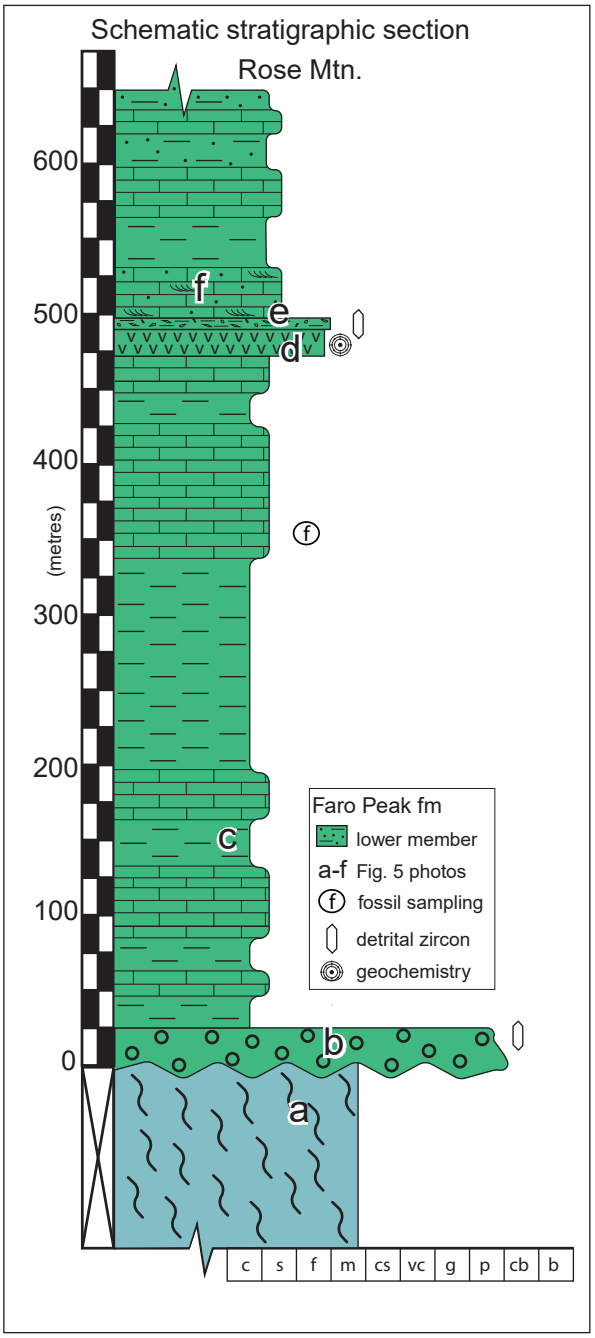


Figure 4. *Schematic stratigraphic section of the lower member of the Faro Peak formation at Rose Mountain. The fossil location is approximate. Samples are from the 2019 field season. Abbreviations: c–clay; s–silt; f–fine sand; m–medium sand; cs–coarse sand; vc–very coarse sand; g–gravel; p–pebble; cb–cobble; b–boulder.*

Green to grey volcanic lithic feldspathic wacke and feldspathic arenite units characterize this locality. Along the north fork of Vangorda Creek, thin to medium beds of orange to tan, fine to medium-grained, feldspathic arenite are interbedded with siltstone and argillite (Fig. 10c). Slightly coarser sandstone layers show evidence of slump structures or convolute bedding (Fig. 10d). Argillite is green to grey, thin bedded to massive, and locally contains minor white mica (Fig. 10e). A unit of green lithic feldspathic wacke reported by Wiest and Beranek (2019) is interpreted to be a sheet sand above isoclinally folded beds that are the result of soft sediment deformation. This same sheet sand was observed during this field season to overlie tabular to slightly undulatory, thin-bedded argillite and siltstone indicating that soft sediment deformation was local (Fig. 10f). The highest elevation exposures along the eastern ridge of Whiskey Mountain consist of tabular, medium to thick-bedded sheets of steeply dipping, medium to very coarse grained, feldspathic to lithic feldspathic arenite and siltstone interbeds (Fig. 10g,h).

Faro Peak

Northeast of Faro Peak, ~10 km northeast of Faro, the Vangorda fault separates serpentinite and harzburgite units of the Slide Mountain terrane from the lower member Faro Peak formation (Fig. 3). Lower member units at this locality consist of subvertical, grey to brown, thin-bedded, locally wavy laminated, micaceous argillite, siltstone, and feldspathic arenite units (Fig. 11a). These siliciclastic rock units grade upwards into resistant, tabular siltstone (Fig. 11b).

Interpretation

The lower member consists of three lithological groups: (1) interbedded shale/argillite and limestone units from Rose Mountain, Repeater Hill, and Blind Creek–Dena Cho Trail; (2) basalt, wacke, and lithic feldspathic arenite units from Rose Mountain and eastern Whiskey Mountain; and (3) micaceous siltstone, argillite, and feldspathic to lithic feldspathic arenite units from Faro Peak.



Figure 5. *Field photographs of the Snowcap assemblage (Sa) and lower member of the Faro Peak formation (FPf) at Rose Mountain.* **(a)** *Highly deformed micaceous schist and quartzite (Sa);* **(b)** *cut section of basal conglomerate unit (FPf);* **(c)** *interbedded shale and limestone (FPf);* **(d)** *grey basalt overlain by green wacke (FPf);* **(e)** *sheared green wacke; and* **(f)** *cross-stratified silty limestone. Yellow-handled hammer (55 cm) and brown-handled hammer (33 cm) for scale.*

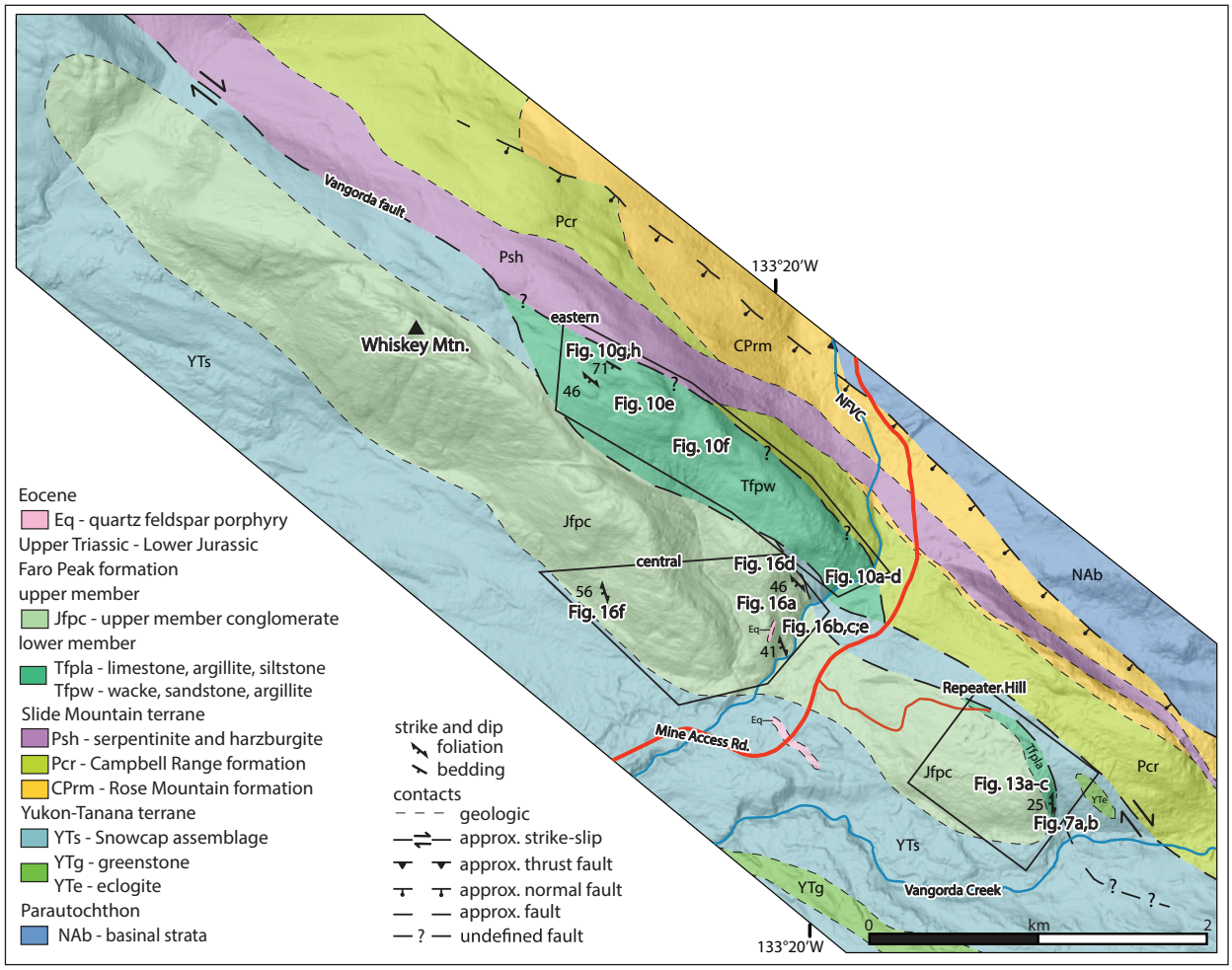


Figure 6. *Simplified bedrock geology of the eastern and central Whiskey Mountain and Repeater Hill areas (modified from Pigage, 2004). Abbreviations: NFVC–north fork Vangorda Creek. Basemap DEM (digital elevation model) obtained from the University of Minnesota Polar Geospatial Center (2018) and Porter et al. (2018).*

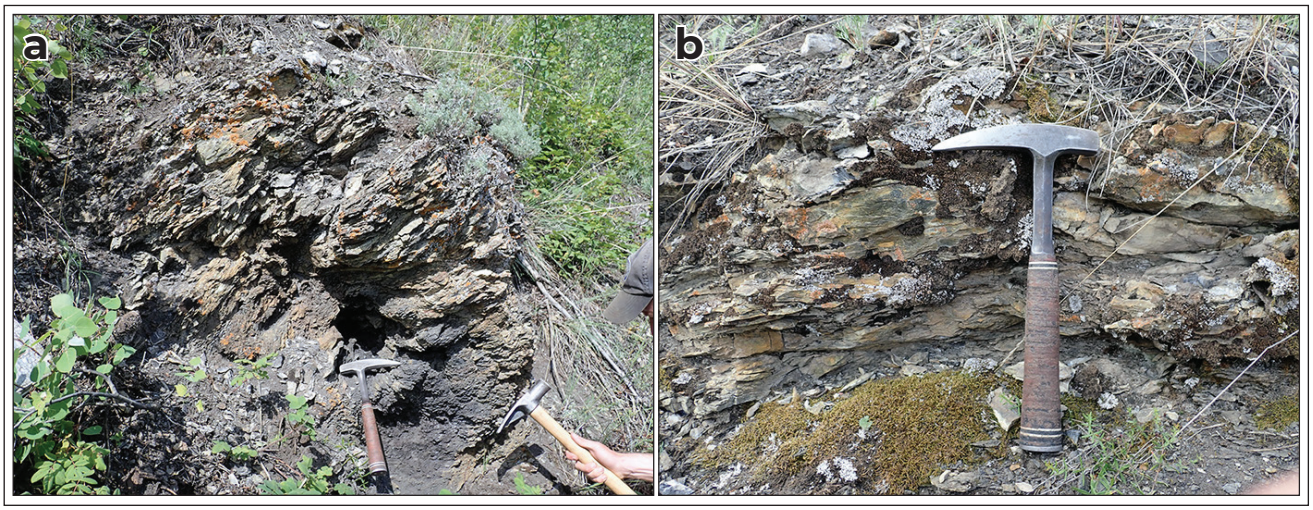


Figure 7. *Field photographs of the lower member of the Faro Peak formation at Repeater Hill.* ***(a)*** *Strongly foliated argillite and siltstone; and* ***(b)*** *thin-bedded, tan weathered, dark grey micrite. Yellow-handled hammer (55 cm) and brown-handled hammer (33 cm) for scale.*

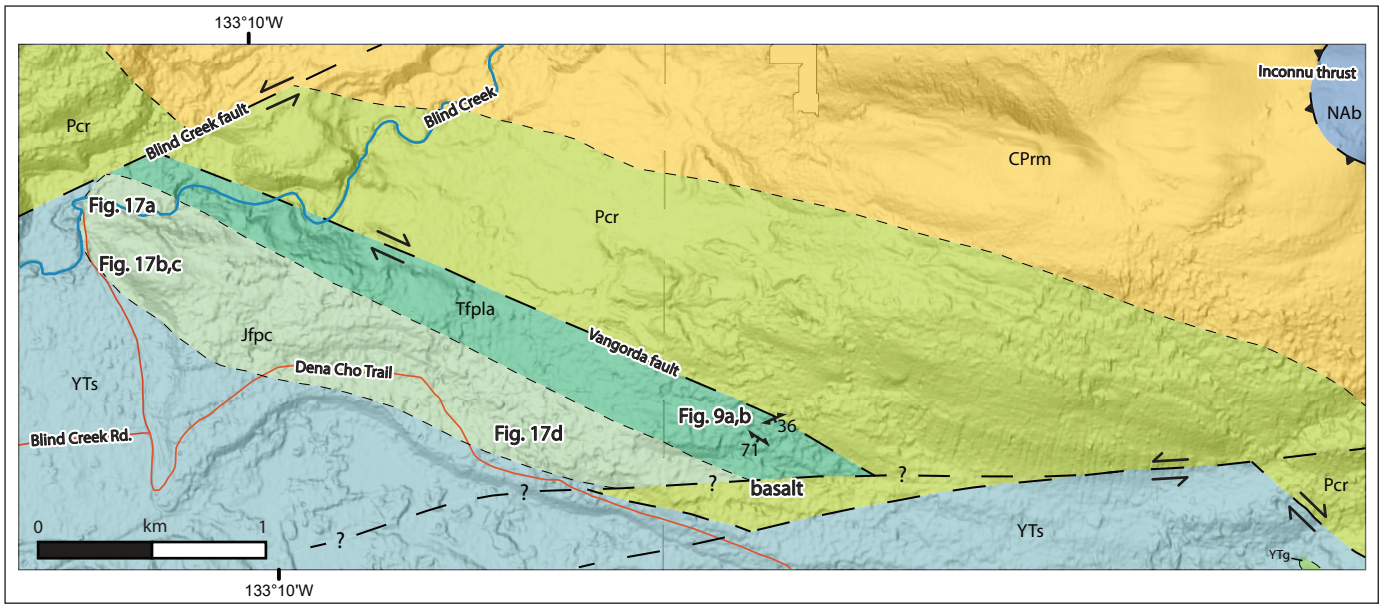


Figure 8. *Simplified bedrock geology of the Blind Creek and Dena Cho Trail area (modified from Pigage, 2004). Symbols same as Figure 6. Basemap DEM obtained from the University of Minnesota Polar Geospatial Center (2018) and Porter et al. (2018).*

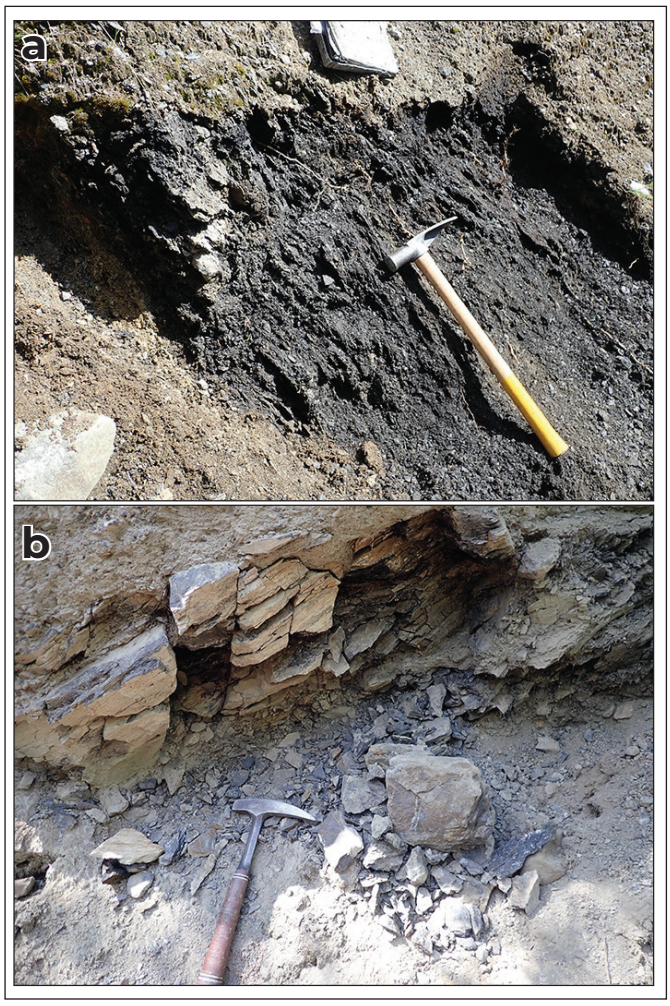


Figure 9. *Field photographs of the lower member of the Faro Peak formation near the Dena Cho Trail and Vangorda fault.* ***(a)*** *Trenched outcrop of foliated argillite; and* ***(b)*** *trenched outcrop of tan weathered, dark grey micrite.*

Upper Triassic limestone and shale units are age-constrained by conodont fossils in the lower part of the Rose Mountain section and sit unconformably on metasedimentary rocks of the Snowcap assemblage. These basal units are interpreted to correlate with Upper Triassic argillite and fossil-bearing limestone units that crop out at the Repeater Hill locality. The overlying basalt-wacke succession at Rose Mountain is likely correlative with green wacke and arenite units along the eastern ridge of Whiskey Mountain (Fig. 12), suggesting that the latter comprise the upper portion of the lower member. The basalt-wacke succession at Rose Mountain apparently indicates a shift from earlier, argillite-limestone deposition to proximal derivation from mafic to intermediate volcanic rocks. For example, Wiest and Beranek (2019) reported that lithic feldspathic arenite units along the eastern ridge of Whiskey Mountain contain angular mafic to intermediate volcanic rock fragments and suggest local, first-cycle sources. The uppermost parts of the lower member at Rose Mountain include micrite and micaceous siltstone that potentially correlate with micaceous argillite,

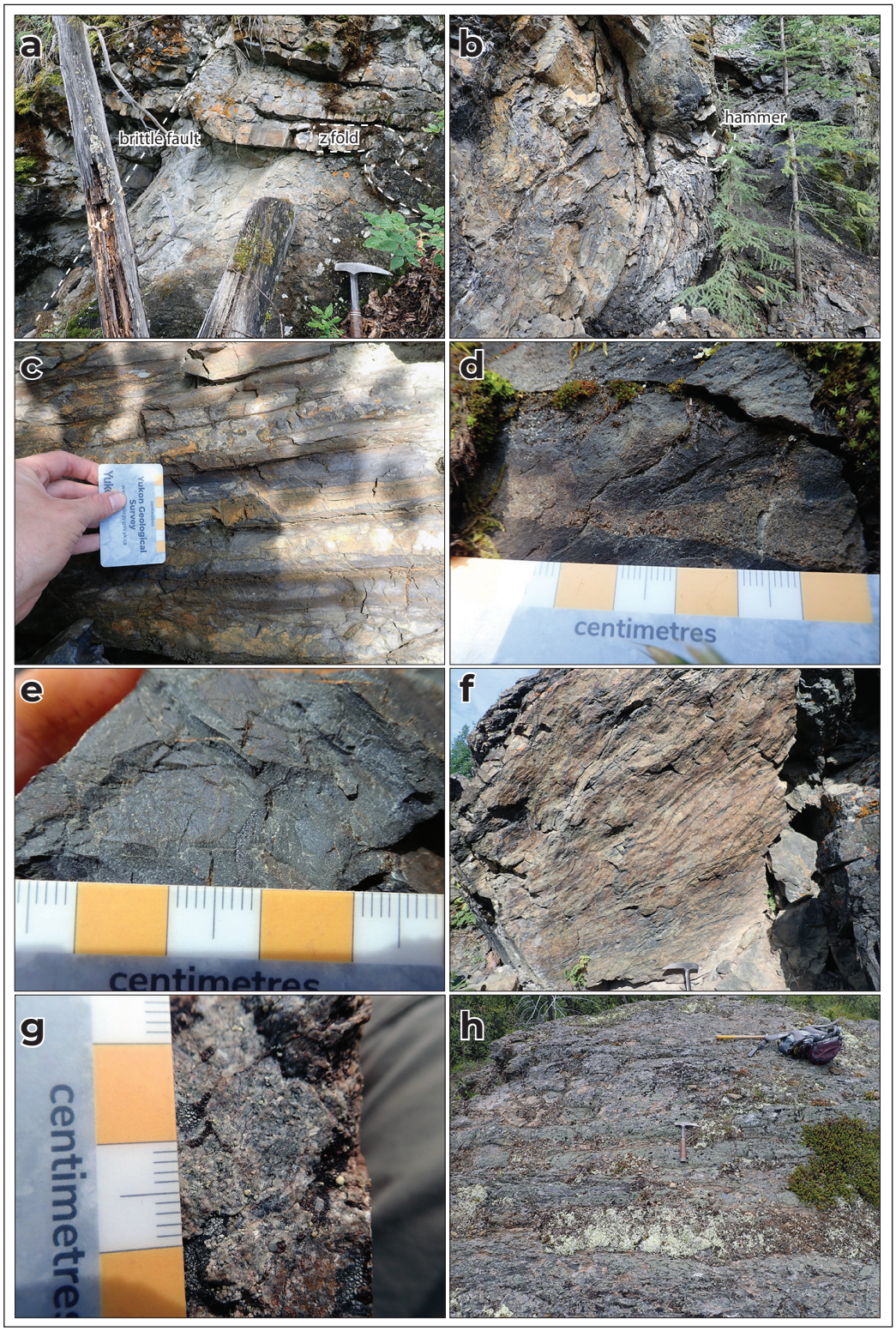


Figure 10. *Field photographs of the lower member of the Faro Peak formation at eastern Whiskey Mountain.* **(a)** *West-dipping brittle fault in argillite and medium-grained tabular sandstone with z-fold;* **(b)** *west-dipping brittle fracture in thin-bedded siltstone and fine-sandstone with east-vergent box-fold;* **(c)** *tabular bedded siltstone and argillite with local scouring* **(d)** *slump structure in coarse sandstone and argillite;* **(e)** *massive green argillite;* **(f)** *tabular, undulatory-bedded argillite and siltstone;* **(g)** *immature coarse-grained feldspathic arenite; and* **(h)** *steeply-dipping, tabular-bedded sandstone and siltstone. Brown-handled hammer (33 cm) for scale.*

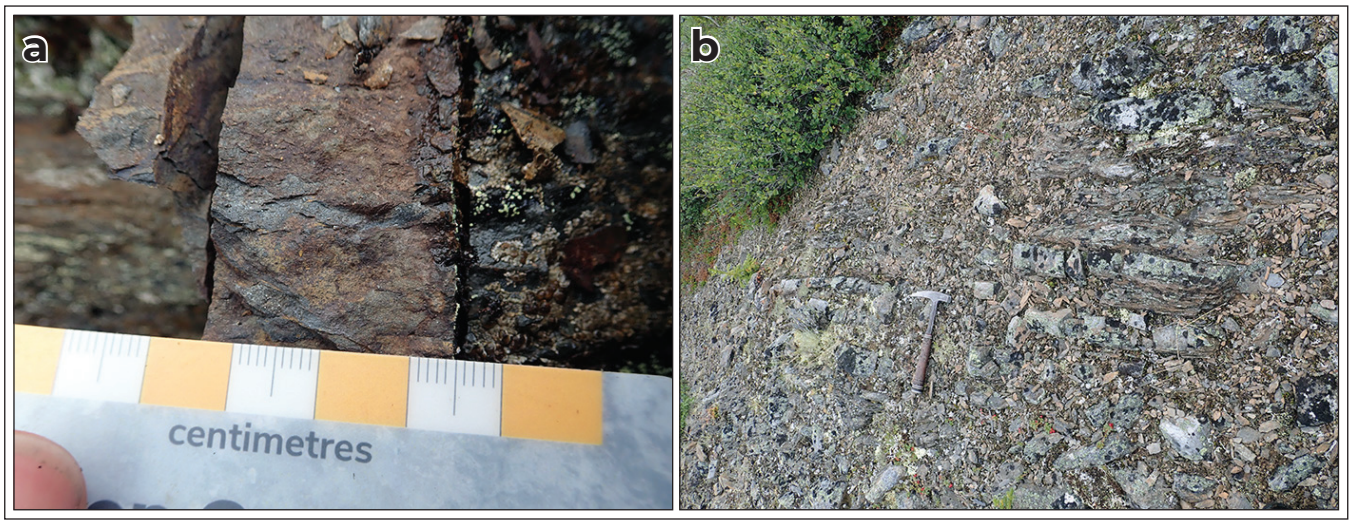


Figure 11. *Field photographs of the lower member of the Faro Peak formation at Faro Peak.* ***(a)*** *Micaceous siltstone; and* ***(b)*** *tabular-bedded micaceous siltstone. Brown-handled hammer (33 cm) for scale.*

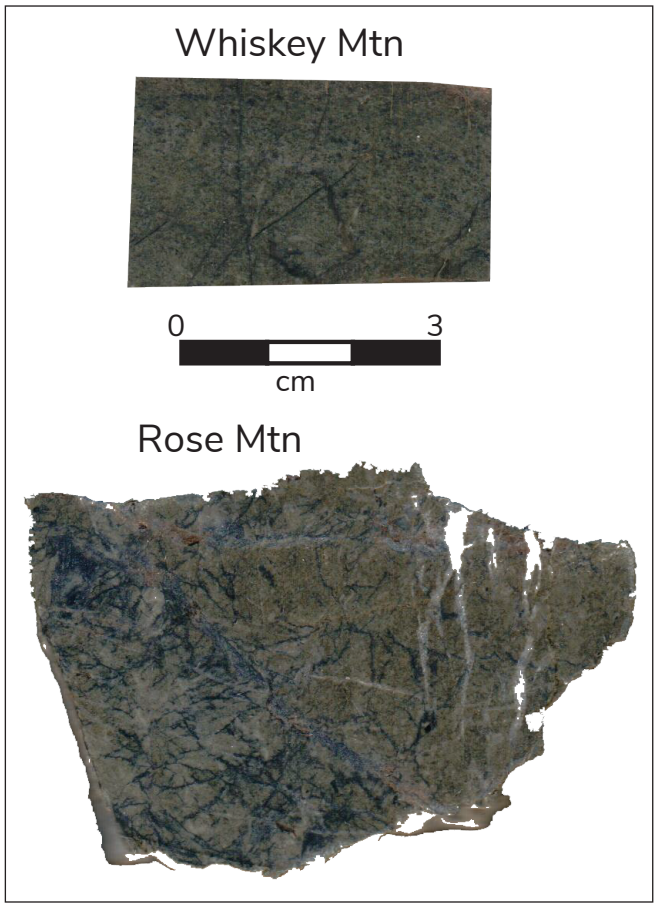


Figure 12. *Comparison between green wacke at eastern Whiskey Mountain area* ***(upper)*** *and unsheared green wacke overlying basalt at Rose Mountain area* ***(lower)****.*

siltstone, and feldspathic arenite at the Faro Peak locality. Micaceous strata are characteristic of Upper Triassic overlap assemblage units in association with Yukon-Tanana terrane, Slide Mountain terrane, and ancestral Cordilleran margin from eastern Alaska to northern British Columbia (Beranek and Mortensen, 2011).

Lower member basalt from Rose Mountain is lithologically distinct from that of the Permian Campbell Range formation to the northeast of the Vangorda fault and its apparent conformable nature above Carnian to Rhaetian limestone units indicates a Late Triassic depositional age. The lack of epidote streaking and green chlorite-alteration also suggests it is distinct from basalt mapped as basal Faro Peak formation by Pigage (2004) and Jennings *et al.* (1978) south of Rose Mountain (Fig. 3). Pigage (2004) speculated that this 'basal basalt' is unrecognized Campbell Range formation as the N-MORB (normal mid-ocean ridge basalt) whole-rock geochemical compositions of this unit are indistinguishable from Permian units in the Faro area. The geochemical signatures of Campbell Range formation rocks in the Finlayson Lake area are also similar (e.g., Piercey *et al.*, 2012). Therefore, based on the mineralogical and geochemical similarities between the 'basal basalt' of Faro Peak formation and Campbell Range formation from the Faro and Finlayson Lake areas, the 'basal basalt' locality south of Rose Mountain outlined in Pigage (2004) is herein reassigned to Campbell Range formation.

An outcrop of green basalt reported by Wiest and Beranek (2019) near the Dena Cho Trail was investigated in summer 2019 to understand its relationship with the Faro Peak and Campbell Range formations (Fig. 8). This green basalt contains epidote streaking and local to pervasive chlorite-carbonate alteration suggesting an affiliation with the Permian Campbell Range formation. Its location near lower and upper member units of the Faro Peak formation suggests it may be the result of an east-northeast trending fault splay in the area (Fig. 8).

Lower member–upper member contact relationships

Repeater Hill

The contact between lower member and upper member units at Repeater Hill is well constrained (Fig. 6). Upper Triassic limestone and argillite units of the lower member crop out directly below a bed of pebble to cobble, matrix-supported, polymictic conglomerate that contains clasts of micaceous quartzite, schist, grey and black chert, green to tan volcanic rocks, and sedimentary rocks (Fig. 13a). This conglomerate marks the base of the upper member and is consistent with the map interpretations of Pigage (2004). Above this conglomerate, micaceous argillite separates these units from massive, matrix to clast-supported conglomerate that comprises the bulk of Repeater Hill and locally contains porphyry and intrusive rock clasts (Fig. 13b,c; Wiest and Beranek, 2019).

Faro Peak

At least 800 m of upper member stratigraphy is exposed above the lower member–upper member contact at Faro Peak (Fig. 14). Subvertical, tan to brown, massive to thin-bedded, medium to very coarse grained arenite units scour into, and are interbedded with, wavy laminated, micaceous siltstone to argillite (Fig. 15a–d) above the saddle ~600 m northeast of Faro Peak. This saddle separates these upper member units from tabular, lower member micaceous siltstone. The contact between the lower and upper members is drawn at the first occurrence of coarse-grained sandstone (Fig. 3) and is consistent with the map interpretations of Pigage (2004).

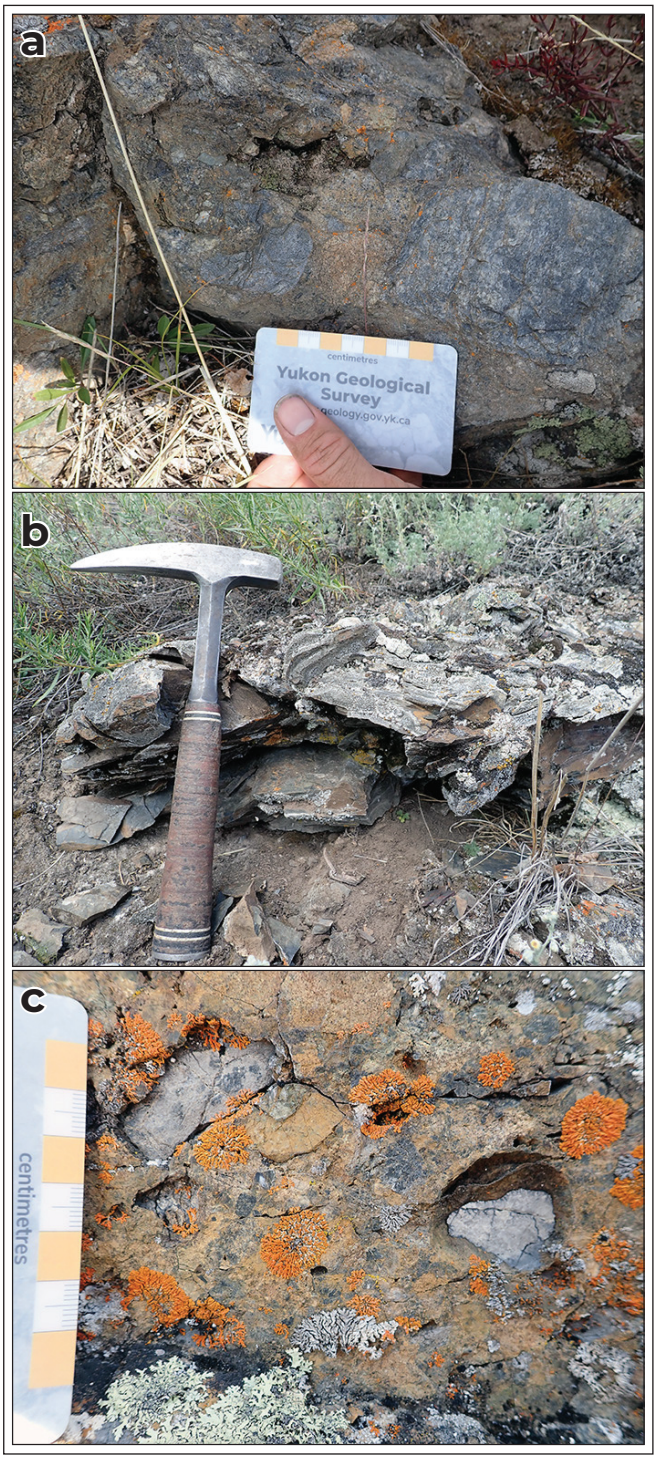


Figure 13. *Field photographs of upper member of the Faro Peak formation at Repeater Hill.* ***(a)*** *Matrix-supported conglomerate with quartzite, volcanic, and sedimentary clasts;* ***(b)*** *weakly folded micaceous argillite; and* ***(c)*** *normally graded bed in matrix-supported conglomerate. Brown-handled hammer (33 cm).*

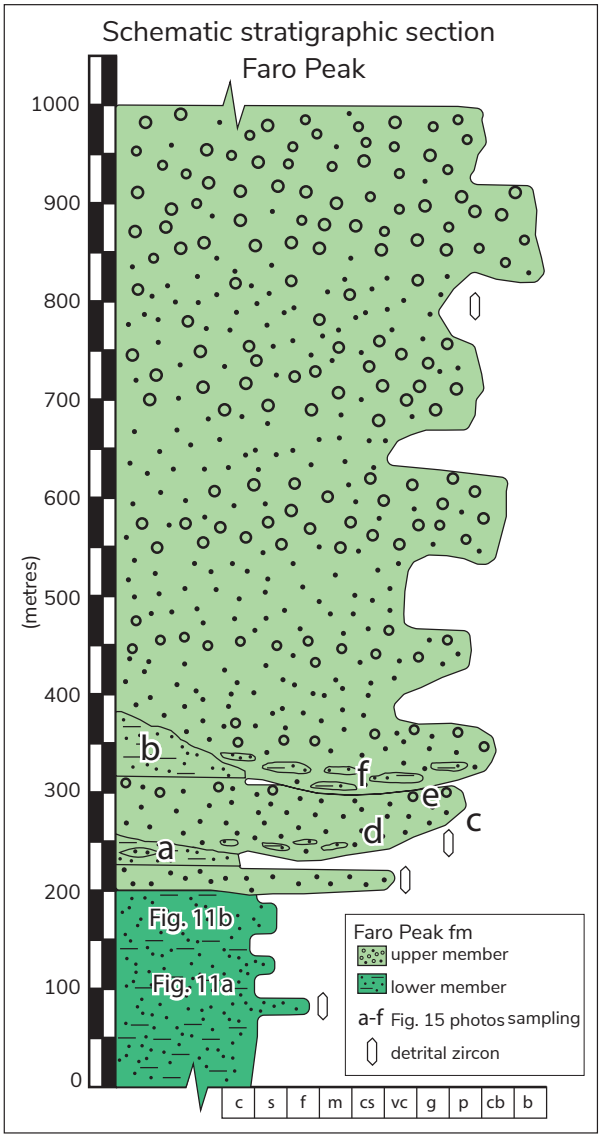


Figure 14. *Schematic stratigraphic section of the lower and upper members of the Faro Peak formation at Faro Peak. Samples are from the 2018 and 2019 field seasons. Abbreviations same as Figure 4.*

Coarse-grained beds of feldspathic to lithic feldspathic arenite at the Faro Peak locality contain wavy laminated, micaceous argillite rip-up clasts and are locally overlain by conglomerate with clasts of grey and black chert, grey quartzite, tan volcanic rocks, and limestone (Fig. 15e). Upsection, these rip-up clasts become coarser (>10 cm) and suggest more intense scouring of argillaceous interbeds (Fig. 15f). The increase in coarse-grained sandstone, conglomerate, and rip-up clast size suggests an overall coarsening-upward sequence that continues to the summit of Faro Peak. Wiest and Beranek (2019) reported granule to cobble, matrix to clast-supported, polymictic conglomerate units containing clasts of porphyry and felsic intrusive rocks that are intercalated with very coarse grained to granule feldspathic and lithic arenite units upsection at the summit of Faro Peak and an adjacent peak ~4 km to the northwest.

Central Whiskey Mountain

The upper member of the Faro Peak formation consists of tightly folded, thin to medium-bedded, locally calcareous, micaceous feldspathic to lithic feldspathic arenite and micaceous siltstone units near the center of Whiskey Mountain, ~2.5 km northeast of Faro (Fig. 16a,b). These units occur both above and below matrix-supported conglomerate that dips gently to moderately towards the Tintina Trench and shows normally graded bedding (Fig. 16c). Conglomerate clasts include quartzite, schist, limestone, tan volcanic rocks, and pyroxenite. Below the conglomerate beds, fine-grained rocks are pervasively sheared by a fault that juxtaposes the upper member with the Snowcap assemblage (Fig. 16d). Locally, polymictic conglomerate was observed in faulted contact with these finer-grained units (Fig. 16e). It appears that fine-grained strata accommodated the majority of strain at this locality, whereas conglomerate facies are more resistant, generally appear less deformed, and contain a slight to moderate foliation (Fig. 16f) and local brittle fracturing and faulting.

Blind Creek–Dena Cho Trail

The contact between the lower and upper members is not exposed near the Blind Creek–Dena Cho Trail locality (Fig. 8). Outcrops along the southern bank of Blind Creek consist of matrix-supported conglomerate that overlies limestone and/or calcareous argillite, possibly indicating its stratigraphic position in the upper member, similar to calcareous units near central Whiskey Mountain (Fig. 17a). Upper member exposures at this locality mostly consist of matrix to clast-supported polymictic conglomerate. Clast components include green to grey quartzite, schist, black and grey chert, intermediate to mafic volcanic and intrusive rocks, and subordinate limestone, basalt, and sedimentary rocks that resemble the lower member of the Faro Peak formation (Fig. 17c,d).



Figure 15. *Field photographs of the upper member of the Faro Peak formation at Faro Peak.* ***(a)*** *Sandstone channel in interbedded micaceous argillite and siltstone;* ***(b)*** *wavy laminated argillite;* ***(c)*** *outcrop of sheet sandstone (s) and conglomerate (c) interbeds;* ***(d)*** *coarse-grained lithic feldspathic arenite (s bed from Fig. 15c);* ***(e)*** *matrix-supported conglomerate (c bed from Fig. 15c); and* ***(f)*** *disk-shaped rip-up clasts of wavy laminated argillite in very-coarse sandstone. Brown-handled hammer (33 cm) and geologist (180 cm) for scale.*



Figure 16. *Field photographs of the upper member of the Faro Peak formation at central Whiskey Mountain.* ***(a)*** *Recumbent fold in fine-grained, micaceous sandstone and siltstone;* ***(b)*** *calcareous sandstone;* ***(c)*** *Normally graded bedding in coarse-grained sandstone and matrix-supported conglomerate;* ***(d)*** *uniformly sheared fine-grained, micaceous sandstone and siltstone;* ***(e)*** *west-dipping fault separating conglomerate and fine-grained units; and* ***(f)*** *well foliated, clast-supported conglomerate. Brown-handled hammer (33 cm) for scale.*

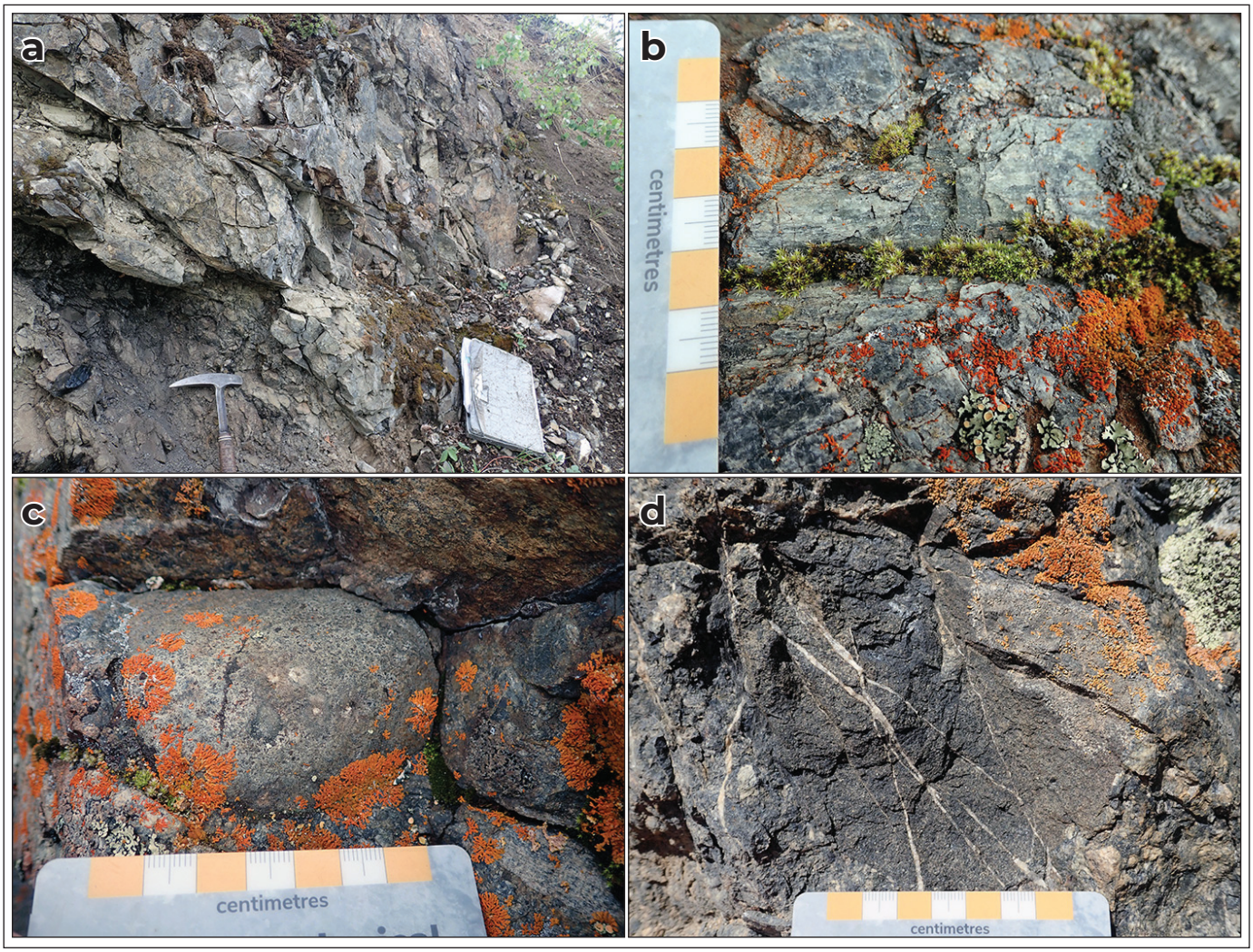


Figure 17. *Field photographs of the upper member of the Faro Peak formation at Blind Creek and Dena Cho Trail.* ***(a)*** *Calcareous unit overlain by normally graded, matrix-supported conglomerate;* ***(b)*** *green quartzite clast;* ***(c)*** *equigranular gabbro clast; and* ***(d)*** *dark grey sandstone clast. Brown-handled hammer (33 cm) for scale.*

Interpretation

The upper member of the Faro Peak formation overlies Upper Triassic limestone units that correlate with the base of the Rose Mountain section, micaceous siltstone and feldspathic arenite units that are potentially the upper part of the lower member, and Snowcap assemblage metasedimentary and eclogitic rocks that crop out below the lower member. These observations suggest that the basal contact of the upper member is an unconformity, however, the interbedded micaceous argillite and conglomerate at Repeater Hill, and interbedded micaceous siltstone, argillite, and coarse-grained sandstone to conglomerate at Faro Peak, suggest a transitional contact between the lower and upper members. A potential third occurrence of a transitional contact is located at central Whiskey Mountain where locally calcareous micaceous siltstone and feldspathic arenite units of the upper member (e.g., Pigage, 2004) are interbedded with upper member conglomerate facies.

There are a few working hypotheses that explain the transitional and unconformable contact relationships between the lower and upper members: (1) micaceous units at Faro Peak and Repeater Hill are fine-grained parts of the upper member and do not belong to the lower member. This compares well with central Whiskey Mountain where micaceous siltstone and feldspathic arenite units have previously been mapped

as the upper member (Pigage, 2004); (2) lower and upper member units comprise part of a syndepositional synform. Bedding is moderately to steeply dipping and the contact with lower member and upper member units appears transitional only near the trace of the Vangorda fault. Towards the Tintina Trench, lower member units are not exposed and massive, polymictic conglomerate units of the upper member sit unconformably on Snowcap assemblage; and (3) lower member units are not laterally continuous and Upper Triassic limestone and argillite beds are correlative with micaceous siltstone and feldspathic arenite units. This last hypothesis requires that micaceous sedimentary rocks in the Faro area are not laterally continuous, suggesting that different units contain a different provenance and became interfingered in the Faro Peak basin(s).

Discussion and future work

The lower member of the Faro Peak formation should be reassigned to a new formation because it is lithologically distinct and its lower and upper contacts are defined by unconformities. This new formation likely consists of a lower, limestone-argillite unit and an upper, basalt-wacke-feldspathic arenite unit. It is uncertain if micaceous units currently mapped as the lower member of the Faro Peak formation at central Whiskey Mountain, Repeater Hill, and the base of the Faro Peak section are part of this new formation, or, if they instead represent fine-grained parts of the upper member of the Faro Peak formation. It is also uncertain if basalt and wacke units at Rose Mountain correlate with the wacke and feldspathic arenite units along the eastern ridge of Whiskey Mountain. Future detrital zircon U-Pb-Hf studies will assist in identifying the stratigraphic position of these units and determine if some, or all, of the lower member of the Faro Peak formation should be assigned to a new formation.

Preliminary conclusions

Field investigations of Upper Triassic to Lower Jurassic rock units near Faro have uncovered new details about the regional stratigraphy of the southern Tay River map area. The lower member of the Faro Peak formation likely represents part of an Upper Triassic overlap assemblage that covered the Yukon-Tanana and Slide Mountain terranes and ancestral North American margin, similar to other Upper Triassic strata that crop out along the eastern edge of the Intermontane terranes from eastern Alaska to northern British Columbia (Beranek and Mortensen, 2011; Golding *et al.* 2016). Basal conglomerate units of the lower member near Rose Mountain sit unconformably on the Snowcap assemblage and indicate that Yukon-Tanana terrane basement was locally exhumed to the surface by Late Triassic time. Black and grey chert clasts furthermore indicate that lower member sand and gravel were also partially sourced from Paleozoic rock units of the adjacent Slide Mountain terrane. These observations suggest that the suture between the Yukon-Tanana and Slide Mountain terranes accommodated early Late Triassic subsidence during regional plate convergence, initiation of a new east-dipping subduction zone, and collisional processes along the outboard edge of northwestern North America (*e.g.*, Nelson *et al.*, 2013).

The lithology and stratigraphic character of upper member strata are consistent with synorogenic deposition related to Early Jurassic exhumation of the northern Intermontane terranes in central Yukon (Colpron *et al.* 2015). The upper member is massively bedded, >800 m-thick, and its basal units are dominated by pebble to cobble-sized clasts of limestone, argillite, and volcanic rocks, whereas the exposed top also contains up to boulder-sized clasts of mafic to felsic intrusive rocks. These observations are consistent with progressive unroofing and suggest proximity to a basin-bounding structure, such as the proto-Vangorda fault (cf. Tempelman-Kluit, 1972). Faro Peak basin subsidence and exhumation of the Snowcap assemblage was likely controlled by major extensional to transcurrent structures (*e.g.*, Colpron *et al.*, 2015) similar to the Willow Lake fault in central Yukon (Knight *et al.*, 2013) that accommodated the Early Jurassic exhumation of Yukon-Tanana basement. Clasts in upper member conglomerate (Wiest and Beranek, 2019) also suggest that basin-filling along the Yukon-Tanana and Slide Mountain suture that initiated during the early Late Triassic persisted until or became active again during the Early Jurassic. Lower and upper member strata of the Faro Peak formation

are cut by the Vangorda fault (see Fig. 8) and confirm that this terrane-bounding fault underwent post-Early Jurassic motion. The Jules Creek fault in the Finlayson Lake area is the southern equivalent to the Vangorda fault and is similarly suggested to have accommodated subsidence and strike-slip motion that occurred until early Mesozoic time (Murphy *et al.*, 2006). Future studies of the Faro Peak formation will further assess the potential correlations between clastic units in the Finlayson Lake and southern Tay River map areas. These results combined with continued investigations into the stratigraphic relationships between lower and upper member units will provide new insights into the evolution of the Yukon-Tanana–Slide Mountain terrane boundary and further constrain plate tectonic models for the early growth of the Canadian Cordillera.

Acknowledgements

This is a product of the Geo-mapping for Energy and Minerals (GEM) program at Natural Resources Canada. A special thanks to the Yukon Geological Survey for field logistics and helicopter support to the Rose Mountain area. Thank you to reviewer Don Murphy for thoughtful and constructive comments that significantly improved this manuscript.

References

Beranek, L.P. and Mortensen, J.K., 2011. The timing and provenance record of the Late Permian Klondike orogeny in northwestern Canada and arc-continent collision along western North America. Tectonics, vol. 30, TC5017.

Clark, A.D., 2017. Tectonometamorphic history of mid-crustal rocks at Aishihik Lake, southwest Yukon. Unpublished MSc thesis, Simon Fraser University, British Columbia, Canada, 153 p.

Colpron, M., Crowley, J.L., Gehrels, G.E., Long, D.G.F., Murphy, D.C., Beranek, L.P. and Bickerton, L., 2015. Birth of the northern Cordilleran orogen, as recorded by detrital zircons in Jurassic synorogenic strata and regional exhumation in Yukon. Lithosphere, vol. 7, p. 541–562.

Colpron, M., Nelson, J.L. and Murphy, D.C., 2006. A tectonostratigraphic framework for the pericratonic terranes of the northern Canadian Cordillera. In: Paleozoic Evolution and Metallogeny of Pericratonic Terranes at the Ancient Pacific Margin of North America, Canadian and Alaskan Cordillera, M. Colpron and J.L. Nelson (eds.), Geological Association of Canada Special Paper 45, p. 1–23.

Dusel-Bacon, C., Lanphere, M.A., Sharp, W.D., Layer, P.W. and Hansen, V.L., 2002. Mesozoic thermal history and timing of structural events for the Yukon-Tanana Upland, east-central Alaska: $^{40}Ar/^{39}Ar$ data from metamorphic and plutonic rocks. Canadian Journal of Earth Sciences, vol. 39, p. 1013–1051.

Gabrielse, H., Murphy, D.C. and Mortensen, J.K., 2006. Cretaceous and Cenozoic dextral orogen-parallel displacements, magmatism, and paleogeography, north-central Canadian Cordillera. In: Paleogeography of the North American Cordillera: Evidence For and Against Large-Scale Displacements, Haggard, J.W., Enkin, R.J. and Monger, J.W.H. (eds.), Geological Association of Canada, Special Paper 46, p. 255–276.

Golding, M.L., Mortensen, J.K., Ferri, F., Zonneveld, J.-P. and Orchard, M.J., 2016. Determining the provenance of Triassic sedimentary rocks in northeastern British Columbia and western Alberta using detrital zircon geochronology, with implications for regional tectonics. Canadian Journal of Earth Sciences, vol. 53, p. 140–155.

Jennings, D.S., Jilson, G.A., Hanson, D.J. and Franzen, J.P., 1978. Geology Anvil District map area, Unpublished Cyprus Anvil Mining Corporation internal company report 1:50 000 scale.

Johnston, S.T., Mortensen, J.K. and Erdmer, P., 1996. Igneous and metaigneous age constraints for the Aishihik metamorphic suite, southwest Yukon. Canadian Journal of Earth Sciences, vol. 33, p. 1543–1555.

Knight, E., Schneider, D.A. and Ryan, J.J., 2013. Thermochronology of the Yukon-Tanana terrane, west-central Yukon: Evidence for Jurassic extension and exhumation in the northern Canadian Cordillera. Journal of Geology, vol. 121, p. 371–400.

Mihalynuk, M.G., Nelson, J.A. and Diakow, L.J., 1994. Cache Creek terrane entrapment: Oroclinal paradox within the Canadian Cordillera. Tectonics, vol. 13, p. 575–595.

Murphy, D.C., Mortensen, J.K., Piercey, S.J., Orchard, M.J. and Gehrels, G.E., 2006. Mid-Paleozoic to early Mesozoic tectonostratigraphic evolution of the Yukon-Tanana and Slide Mountain terranes and affiliated overlap assemblages, Finlayson Lake massive sulphide district, southeastern Yukon. In: Paleozoic Evolution and Metallogeny of Pericratonic Terranes at the Ancient Pacific Margin of North America, Canadian and Alaskan Cordillera, M. Colpron and J.L. Nelson (eds.), Geological Association of Canada Special Paper 45, p. 75–105.

Nelson, J.L., Colpron, M. and Israel, S. 2013. The Cordillera of British Columbia, Yukon, and Alaska: Tectonics and Metallogeny. In: Tectonics, Metallogeny and Discovery: The North American Cordillera and Similar Accretionary Settings, M. Colpron, T. Bissig, B.G. Rusk and J.F.H. Thompson (eds.), Society of Economic Geologists, Special Publication 17, p. 53–109.

Orchard, M.J., 2006. Late Paleozoic and Triassic conodont faunas of Yukon and northern British Columbia and implications for the evolution of the Yukon-Tanana terrane. In: Paleozoic Evolution and Metallogeny of Pericratonic Terranes at the Ancient Pacific Margin of North America, Canadian and Alaskan Cordillera, M. Colpron and J.L. Nelson (eds.), Geological Association of Canada Special Paper 45, p. 229–260.

Piercey, S.J., Murphy, D.C. and Creaser, R.A., 2012. Lithosphere-asthenosphere mixing in a transform-dominated late Paleozoic backarc basin: Implications for northern Cordilleran crustal growth and assembly. Geosphere, vol. 8, no. 3, p. 716–739.

Pigage, L.C., 2004. Bedrock geology compilation of the Anvil District (parts of NTS 105K/2, 3, 5, 6, 7, and 11), central Yukon. Yukon Geological Survey, Bulletin 15, 103 p.

Porter, C., Morin, P., Howat, I., Noh, M-J., Bates, B., Peterman, K., Keesey, S., Schlenk, M., Gardiner, J., Tomko, K., Willis, M., Kelleher, C., Cloutier, M., Husby, E., Foga, S., Nakamura, H., Platson, M., Wethington, M. Jr., Williamson, C., Bauer, G., Enos, J., Arnold, G., Kramer, W., Becker, P., Doshi, A., D'Souza, C., Cummens, P., Laurier, F. and Bojesen, M., 2018. ArcticDEM, https://doi.org/10.7910/DVN/OHHUKH, Harvard Dataverse, vol. 1 [accessed November, 2019].

Staples, R.D., Gibson, H.D., Colpron, M. and Ryan, J.J., 2016. An orogenic wedge model for diachronous deformation, metamorphism, and exhumation in the hinterland of the northern Canadian Cordillera. Lithosphere, vol. 8, no. 2, p. 165–184.

Tempelman-Kluit, D.J., 1972. Geology and origin of the Faro, Vangorda, and Swim concordant zinc-lead deposits, central Yukon Territory. Geological Survey of Canada, Bulletin 208, 73 p.

Tempelman-Kluit, D.J., 1979. Five occurrences of transported synorogenic clastic rocks in Yukon Territory. Geological Survey of Canada, Paper 79-1A, p. 1–12.

Topham, M.J., Allan, M.M., Mortensen, J.K., Hart, C.J.R., Colpron, M. and Sack, P.J., 2016. Crustal depth of emplacement of the Early Jurassic Aishihik and Tatchun batholiths, west-central Yukon. *In:* Yukon Exploration and Geology 2015, K.E. MacFarlane (ed.), Yukon Geological Survey, p. 233–251.

University of Minnesota, 2018. Polar Geospatial Center, https://www.pgc.umn.edu [accessed November, 2019].

Wiest, A.C., Beranek, L.P., 2019. Stratigraphy of the Faro Peak formation, central Yukon: New field observations of Jurassic synorogenic sedimentation along the Yukon-Tanana–Slide Mountain terrane boundary. In: Yukon Exploration and Geology 2019, K.E. MacFarlane (ed.), Yukon Geological Survey, p. 127–142.

Yukon Geological Survey, 2019. Yukon Digital Bedrock Geology. Yukon Geological Survey, http://data.geology.gov.yk.ca/Compilation/3, [accessed November, 2019].

Yukon Geological Survey

Yukon Geological Survey staff are located in two buildings in Whitehorse: the Elijah Smith Building at 300 Main Street, room 102, and the H.S. Bostock Core Library at Mile 918 on the Alaska Highway.

Branch Director

H.S. Bostock Core Library

Relf, Carolyn – Director, (867) 667–8892 carolyn.relf@gov.yk.ca

Operations

H.S. Bostock Core Library

Minor, Julie – Manager, Finance & Operations, (867) 667–8508 julie.minor@gov.yk.ca

Outreach

H.S. Bostock Core Library

Weston, Leyla – Outreach Geologist, (867) 393–7187 leyla.weston@gov.yk.ca

Regional Geology

H.S. Bostock Core Library

Colpron, Maurice – Head, Regional Geology, (867) 667–8235 maurice.colpron@gov.yk.ca
Ambrose, Tyler – Project Geologist, (867) 667–5175 tyler.ambrose@gov.yk.ca
Cobbett, Rosie – Project Geologist, (867) 455–2802 rosie.cobbett@gov.yk.ca
Fraser, Tiffani – Petroleum Geologist, (867) 667–3228 tiffani.fraser@gov.yk.ca
Moynihan, David – Project Geologist, (867) 455–2805 david.moynihan@gov.yk.ca
Skipton, Diane – Project Geologist, (867) 667–5175 diane.skipton@gov.yk.ca

Surficial Geology

Elijah Smith Building

Bond, Jeffrey – Head, Surficial Geology, (867) 667–8514 jeff.bond@gov.yk.ca
van Loon, Sydney – Placer Geologist, (867) 667–3408 sydney.vanloon@gov.yk.ca

H.S. Bostock Core Library

Kennedy, Kristen – Surficial Geologist, (867) 393–7188 kristen.kennedy@gov.yk.ca
Lipovsky, Panya – Surficial Geologist, (867) 667–8520 panya.lipovsky@gov.yk.ca

Minerals Geology

Elijah Smith Building

Casselman, Scott – Head, Minerals Geology, (867) 667–8192 scott.casselman@gov.yk.ca
Lewis, Lara – Economic Geologist, (867) 667–8518 lara.lewis@gov.yk.ca
Torgerson, Derek – Yukon Mineral Exploration Program, (867) 456–3828 derek.torgerson@gov.yk.ca

H.S. Bostock Core Library

Emberley, Justin – Core Library Manager, (867) 393–6492 justin.emberley@gov.yk.ca
Sack, Patrick – Economic Geologist, (867) 667–3203 patrick.sack@gov.yk.ca

Editorial & Technical Services

Elijah Smith Building

MacFarlane, Karen – Head, Technical Services, (867) 667–8519 karen.macfarlane@gov.yk.ca
Bruce, Olwyn – Geological Spatial Data Administrator, (867) 393–7186 olwyn.bruce@gov.yk.ca
Elliot, Brett – Geological Spatial Database Administrator, (867) 667–8481 brett.elliot@gov.yk.ca
Staffen, Bailey – GIS Technician/Web Manager, (867) 456–6801 bailey.staffen@gov.yk.ca

Yukon Geological Survey
Energy, Mines and Resources
Government of Yukon